Simulating Brain Resting-State Activity
What Matters?

Jonathan Hadida

University College

University of Oxford

A thesis submitted for the degree of

Doctor of Philosophy

Michaelmas 2017

Acknowledgements

Personal

Imagine that you are to embark on a long cruise across an ocean. You have packed your suitcase neatly and carefully, and put your hands on a book appropriately titled “What makes a good skipper?” to cover the basics — perhaps you have even sailed on your own before, lucky you! Feeling emboldened by the knowledge that skipper comes from the Dutch word “*schipper*”, you embark with confidence. Before long, your earliest memory of this trip becomes that of waking up alone in a life-boat without any coast in sight and the words "head west" bouncing lightly inside your head. Anything before that is a blur, but you remember that you keep forgetting to reconnect with that other life. Oh well, at least there is a satphone to call if you need help; although, it is becoming less and less clear what to ask, and you sometimes wonder why anyone would care anyway. As the months pass by, you start having clever ideas, like trying to reach your destination faster by remembering the first constellation behind the sunset and following it into the night. Constellations are pretty stable “skymarks”, aren’t they? On cloudy days, you find yourself chasing after occasional bird flocks thinking that they must be going *somewhere*. But in truth, the more time passes, and the more dubious it seems that you’ll be reaching the destination you headed off towards; wait, where was that again?

I hope this allegory of the doctorate was to your liking; it is a fairly relevant description of my personal experience in the first two years of my DPhil, though of course there are better days than others. I know younger me would have liked to read similarly honest accounts in the preamble of the theses I skimmed over during my previous studies; so here it is, for future like-minded fellows!

My first thanks must go to my supervisors: Mark Woolrich, Saad Jbabdi and Stamatios Sotiropoulos. If you are reading this thinking that you have seen such thanks in literally every thesis that you opened, and that based on your recollection of “The PHD Movie” I *must* be writing this bitterly, then let me tell you that you couldn’t be more wrong. All three of my supervisors were simply exceptional, each in their own way, and working with them over the past four years has been an immense privilege. In particular, I would like to thank them for their patience with me, for always finding time to talk, for the time they devoted to proof-reading this thesis, and for pushing me gradually to become the captain of my own ship. If I had to do it all over again, the only things I would change would be about myself.

To my wonderful partner and best friend Hannah, I would like to say that none of this would have been the same without you. It wasn’t easy, but we both made it, and we made it together. I admire you for so many reasons, but I would like to say that your determination has been an endless source of inspiration to me, and I would like to thank you for finding beauty and happiness in the simplest aspects of life.

To my parents, I would like to apologise for my absence over the past four years. Thank you for always being there, and for making me feel at home no matter where we meet. To my sister and brothers, I am so proud of the paths you have chosen for yourselves, and I cannot wait to spend more time with my niblings.

Finally I would like to thank all my friends at the Doctoral Training Centre, FMRIB and OHBA, and in particular: Citlali, Jakub, Emma, Alexa, Moises, Anderson, Sam, Oiwi, Hanna, Diego, Andrew and Giles. And last but not least, all my other friends who made Oxford a very special place for me, and in particular: Armin, Konrad, Debbie, Niko, Alex, Thibaut, Aleks, Philippa, Sanja, Eamon and Sook.

So long, and thanks for all the fish!

Institutional

I would like to thank my examiners Steve Smith and Steve Coombes, for taking the time to read this thesis and reviewing the corrections, for making me feel at ease during the oral examinations, and more generally for being the role-models that they are in their respective fields. Your willingness to examine this work means a lot to me.

None of this would have been possible without the financial support that I have received from the EPSRC and the Oxford-Radcliffe scholarship. I feel indebted to University College and to the Doctoral Training Centre for allowing me to complete this work, and for their guidance during my time in Oxford; in particular, I would like to thank David Gavaghan, Charlotte Deane, Gail Preston, Peter Jezzard, Jotun Hein and Sir Ivor Crewe.

Abstract

Large-scale biophysical modelling is an ongoing effort in computational neuroscience, and has been advocated as a bottom-up approach for studying the interaction between structure and function in the human brain. The dynamical activity generated by these models can be compared to functional imaging data (*e.g.* resting-state), allowing different modelling hypotheses to be ranked in accordance with their ability to explain the data. Of particular relevance is the fast oscillatory activity measured in magneto-encephalography (MEG); the high temporal resolution of these electro-physiological measurements (compared to functional MRI) matches the typical time-scales in models of populations of neurons, and therefore makes for an ideal point of comparison in the development of such models.

In practice however, these models are computationally expensive (due to their size and mathematical form), and methods to infer their capabilities efficiently, without strong assumptions, and considering multiple parameters simultaneously are currently lacking. In particular, and although the phenomenon is widely recognised, there is currently no general framework to predict the emergence of patterns of activity resulting from complex interactions between multiple dynamical systems. This is due in part to the chaotic nature of the dynamics, but also to the lack of analytic results for the qualitative study of non-linear coupled delay-differential systems.

Instead, the emerging characteristics of such systems need to be assessed numerically through simulations. This comes with many challenges, which are presented in the body of this work, and we address some of them. Specifically, we characterise the oscillatory properties of two neuronal models of increasing complexity (and biophysical relevance), which are used as the building blocks of whole-brain networks of neuronal populations with delays. We propose several parametrisations of these networks, encompassing both local and global scales, and introduce an efficient optimisation method to infer those parameters, by matching a set of empirical features from real resting-state MEG. This method is borrowed from the latest advances in the field of Bayesian optimisation, and we further propose and demonstrate improvements to this method.

Contents

List of Figures

List of Abbreviations

AC . . . . . Anatomical connectivity

AP . . . . . Action-potential **or** Anterior-posterior

BA . . . . . Brodmann area

BFS, BFT . . . Breadth-first search/traversal

BOLD . . . . . Blood oxygenation-level dependent (contrast/signal)

CB . . . . . Conductance-based

CSF . . . . . Cerebro-spinal fluid

CWC . . . . . Coherence-weighted correlation

CWT . . . . . Continuous wavelet transform

DDE . . . . . Delay-differential equation(s)

DFT . . . . . Discrete Fourier Transform

DK . . . . . Desikan-Killiany

DMN . . . . . Default-mode network

DOF . . . . . Degree(s) of freedom

DTI . . . . . Diffusion-tensor imaging

EC . . . . . Envelope correlation

EEG . . . . . Electro-encephalography

EMD . . . . . Empirical mode decomposition

EPSC, IPSC . . Excitatory or inhibitory post-synaptic current

EPSP, IPSP . . . Excitatory or inhibitory post-synaptic potential

FC . . . . . Functional connectivity

FFT . . . . . Fast Fourier transform

FIR . . . . . Finite impulse response

fMRI . . . . . Functional MRI

GM . . . . . Grey-matter

GP, GPR . . . . Gaussian-process (regression)

GPSO . . . . . Gaussian-process surrogate optimisation

HCP . . . . . Human connectome project

HMM . . . . . Hidden Markov model

IH . . . . . Inter-hemispheric

IMF . . . . . Intrinsic-mode function

IMGPO . . . . Infinite-metric GP optimisation

LCMV . . . . . Linearly constrained minimum variance

LSBM . . . . . Large-scale biophysical model

MEG . . . . . Magneto-encephalography

MNI . . . . . Montreal neurological institute

MR, MRI . . . . Magnetic-resonnance imaging

NMM . . . . . Neuronal-mass model

ODE . . . . . Ordinary differential equation(s)

ODF . . . . . Orientation distribution function

OFC . . . . . Orbito-frontal cortex

PBS . . . . . Partial barycentric subdvision

PCA . . . . . Principal component analysis

PET . . . . . Positron emission tomography

PSD . . . . . Power spectral density

PSP . . . . . Post-synaptic potential

RF . . . . . Radio-frequency

RMS . . . . . Root-mean-square

ROI . . . . . Region of interest

RSN . . . . . Resting-state network(s)

SDE . . . . . Stochastic differential equation(s)

SH . . . . . Spherical harmonic

SI . . . . . Superior-inferior

SNR . . . . . Signal-to-noise ratio

SPD . . . . . Symmetric positive definite

WC . . . . . Wilson-Cowan

WM . . . . . White-matter

– Some say that while the 20th century was the century of physics, we are now entering the century of biology. What do you think of this?

– I think the 21st century will be the century of complexity. We have already discovered the basic laws that govern matter and understand all the normal situations. We don't know how the laws fit together, and what happens under extreme conditions. But I expect we will find a complete unified theory sometime this century. There is no limit to the complexity that we can build using those basic laws.

— Stephen Hawking

1

Introduction

Contents

1.1 Motivation

Perhaps the most distinctive features of human behaviour, when compared to other life-forms, are: our ability to **think**, either to make choices, or to reason abstractly; our ability to store and reflect on the **memories** of past events, and assign meaning to them so they can fit within our sense of *self*; and our ability to **communicate**, either through language,

or more freely through music and arts. These behaviours and abilities have been examined for millennia, but despite the knowledge accumulated and formalised through various disciplines, we do not yet understand how our brains *enable* them.

If it is easy to conceive with modern knowledge that, due to their biochemical properties, cell-tissues could facilitate large-scale chemical reactions such as digestion, or convert chemical energy into large-scale mechanical forces in the case of muscle contraction, it is much more difficult to imagine how these reactions could encode thoughts or ideas, and allow them to influence each other and evolve coherently over the course of an entire lifetime.

The advent of non-invasive imaging techniques, and in particular functional magnetic-resonance imaging (fMRI), allowed human brain activity to be measured *in vivo* with exquisite spatial resolution. This not only supported prior observations that specific brain regions would systematically "activate" in response to particular tasks (*e.g.* finger-tapping, listening to music or voices, recognising faces, *etc.*), also known as **functional segregation**; but indeed prompted the endeavour of mapping different parts of the brain with the various tasks that triggered them, often referred to as *functional mapping*.

However, in order for the brain to function as a coherent information processing system, functional segregation is not sufficient; these different specialised regions need to communicate information dynamically, and in an orchestrated manner, in order to perform complex tasks like talking with someone else for example. This cooperation is known as **functional integration**, and prompted the task of characterising the interactions between different brain regions, as if organised into a network in which the connections would vary depending on the context, hence the name of *functional connectomics*.

Studying the emergence of complex behaviour transcending the capabilities of the various parts involved through their cooperation pertains to the field of **complexity science**. Within the life-sciences, the paradigm of segregation-integration provides a mechanism

of evolution through recursion; in other words, the idea that functional integration is itself a form of segregation, only at a higher level of complexity.

In the case of computational neuroscience, the goal is to eventually propose a mechanistic theory of brain activity, by shedding light on the relationship between **structure** (organisational properties) and **function** (actionable capabilities).

1.1.1 Default Mode

The advent of positron-emission tomography (PET) and fMRI as non-invasive tools for functional mapping led to the development of methods to locate and quantify regional "activations" in medical images. A successful and now-predominant method to do so is using a so-called block-design, whereby the subject or patient repeats the same (or related) task multiple times while in the scanner, and the data is analysed *a posteriori* in a statistical manner, comparing the activity measured during versus in-between individual trials at several points in space (typically the voxels of a regular grid).

Naturally this prompted investigations into the baseline activity, and in 1995 the first study reporting systematic activations in distributed brain areas during rest-periods using PET was published by (Andreasen et al. 1995); this was the discovery of the **default mode** of brain activity (Raichle et al. 2001; Buckner 2012).

1.1.2 Resting-State Activity

At about the same time, research aiming at characterising the temporal dynamics of blood oxygen-level dependent contrasts (BOLD) in fMRI during rest was published in two papers (Biswal et al. 1995; Biswal et al. 1997), which reported strong correlations between hemispheres in the sensory-motor areas, characterised by slow fluctuations ($<$ 0.1 Hz) of the BOLD signal. This demonstrated that the cooperation between spatially segregated regions in the brain was not limited to a task-context.

Subsequent studies (Greicius et al. 2003; De Luca et al. 2006) showed that patterns of functional connectivity at rest was not only widespread and replicable across individuals (and modalities, see Brookes et al. 2011b), but also that it varied over time as a sequence of transient but consistent brain networks; the so-called **resting-state networks** (RSNs). Fig. 1.1 (reproduced from Heuvel et al. 2010) illustrates commonly reported RSNs.

From this point forward, the related literature can be classified into three main streams of research, each concerned with a different task:

1. Studying the physiological basis of resting-state activity.
2. Developing methods to measure and characterise this activity.
3. Evaluating the replicability across subjects and modalities.

The first stream leads to research mainly in biophysical modelling and the structure-function interaction (Honey et al. 2009; Wang 2010; Ashwin et al. 2016; Breakspear 2017), while the second stream leads to research in signal processing and network science (Damoiseaux et al. 2006; Baker et al. 2014; Bullmore et al. 2009; Smith et al. 2011). The work presented in this thesis follows the first stream, with a brief excursion into the second stream (see §4.3).

1.1.3 Biophysical Models

Throughout the various disciplines in sciences, mathematical models formalise our understanding of observed phenomena, at a level of detail usually sufficient to capture a range of conditions encountered in practice, but making simplifying assumptions where possible in order to reduce the complexity of the model.

From a biological point of view, brain activity is enabled by the functional properties of neuron cells, and in particular their ability to fire action-potentials. A seminal modelling work of this behaviour is that of Hodgkin and Huxley (Hodgkin et al. 1952), which was

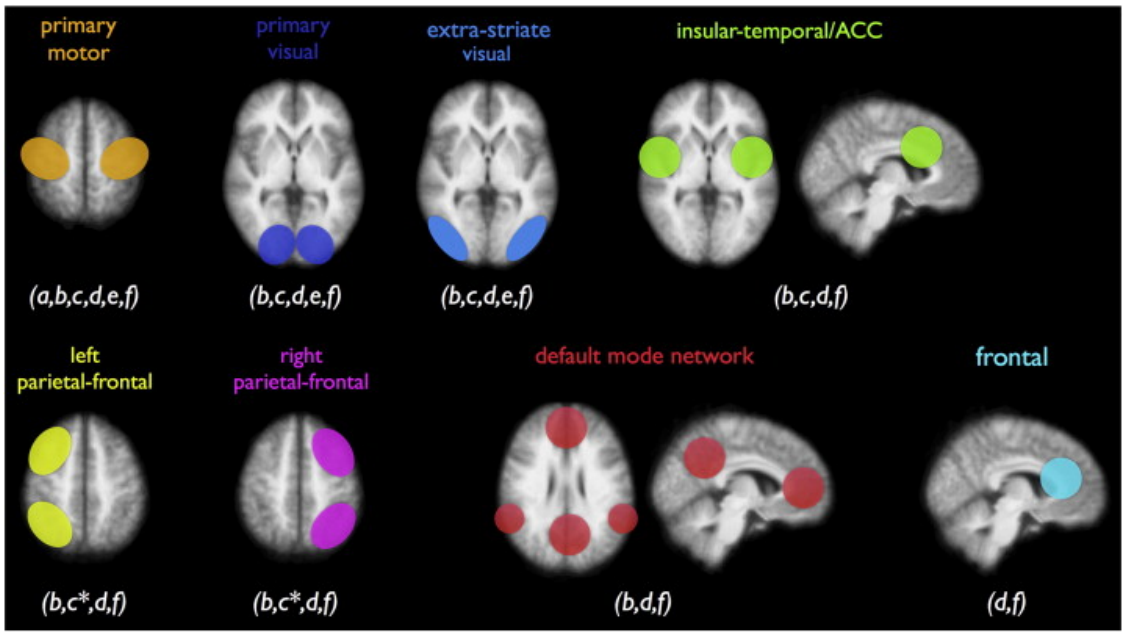

Figure 1.1: The so-called resting-state networks each consist of one or several remote brain regions, in which the activity is found to co-fluctuate (at the time-scale of a few minutes) consistently across subjects, and across a range of different MRI acquisition protocols (in fact, even across modalities (Brookes et al. 2011b)), and choice of analysis methods. This figure illustrates the regions reported in the following published works: (a) (Biswal et al. 1995), (b) (Beckmann et al. 2005), (c) (De Luca et al. 2006) (*: the parietal network was reported as bi-lateral), (d) (Damoiseaux et al. 2006), (e) (Salvador et al. 2005), (f) (Heuvel et al. 2008).

Reproduced with permission from (Heuvel et al. 2010).

rewarded by a Nobel Prize in Physiology or Medicine in 1963. Their model described the mechanisms of ionic flows through the membranes of neuron-cells, and the ensuing chain-reaction enabling propagation along the axon, in terms of an equivalent electrical circuit. This analogy allowed to express quantitatively the evolution of the membrane potential over time in terms of **differential equations**, and laid the theoretical foundation for a large family of so-called **conductance-based models** (we will come back to this in §3.4).

Although studying the physiological properties of individual neurons is essential in order to remain empirically grounded; and that the formal analysis of networks of individual neurons is needed to understand the principles underlying neural computations (Izhikevich 2006), and more generally how modelling choices at the micro-scale (*e.g.* synaptic plasticity or wiring-patterns) can result in functional properties at the macro-scale (*e.g.* homeostasis or functional specialisation, see Hafting et al. 2005; Vogels

et al. 2011); such level of detail may not be suitable to study *whole-brain* activity. This is because the resulting complexity is too great to make predictions about the behaviour of the entire system.

Instead, large-scale biophysical models (LSBMs) typically consider interactions between large populations of neurons (*e.g.* ranging from 10^6 to 10^8 neurons), the activity of which is summarised by mean-field equations (Breakspear 2017). In practice, these simplified models are still sufficiently complex to produce realistic simulations of brain dynamical activity (Coombes 2010; Freyer et al. 2011; Cabral et al. 2014a; Hansen et al. 2015).

Ultimately, biophysical models are attractive in computational neuroscience because they are the only tool to provide a mechanistic explanation of brain activity that is, at least in principle, biologically plausible (Woolrich et al. 2013). The work presented in this thesis focuses on the development of methods and tools to reliably and efficiently fit these models to empirical data, and doing so, compare the performance of different models, and assess the relevance of certain modelling assumptions.

1.2 Contents

1.2.1 Organisation

This thesis is organised as follows (chapters marked with a star * can be read independently):

- Chapter 2*: we present the empirical data that was used in our experiments (either as a reference for comparison, or to inform our models). The corresponding modalities are introduced briefly, and we illustrate the features of interest in resting-state magneto-encephalography (MEG).
- Chapter 3*: we present our work on biophysical modelling, as well as the methods and software created to run our simulation. In particular, our analysis of the models

focuses on characterising the influence of the various parameters on the resulting dynamics in oscillatory regimes.

- Chapter 4: covers the main methods used to analyse and compare simulations and empirical data, with a focus on oscillatory dynamics and functional connectivity.

- Chapter 5*: we present a Bayesian optimisation method designed for problems in which the objective function is very costly to evaluate, and we propose several improvements to this method.

- Chapters 6 and 7: we present the results obtained by applying the previous optimisation method to infer the parameters of several models of increasing complexity.

The essential material is in chapters 3 and 5, and for a quick glance, the bare minimum required to understand the results are §3.3 and §5.2. Chapters 2 and 4 are about data analysis, and we recommend reading them in that order. The results can be found in chapters 6 and 7.

In terms of reading-time, chapter 3 is by far the longest, though it is split into three loosely dependent parts (Wilson-Cowan model §3.3, conductance-based model §3.4, and software implementation §3.5). Chapter 5 is shorter in length, but may take just as long to read, in order to properly integrate the concepts introduced. Chapters 2 and 4 are relatively short and easy reads.

The results chapters 6 and 7 each present a different experiment using the methods and data covered in the previous chapters. They follow the same internal organisation, namely: purpose, assumptions, controlled parameters, definition of the objective, and results. Familiarising with the format of those results, and their meaning, may require some time; in particular, it is important to understand the figures in §6.4 before moving on to the last chapter.

1.2.2 Contributions

The work presented in this thesis is the result of three years of research as a post-graduate student. Our main contributions are listed below:

- Chapter 2: detailed comparison of tract-lengths vs Euclidean distances;
- Chapter 3: detailed analysis of the effects of model parameters on the oscillatory dynamics, derivation of a stochastic Wilson-Cowan network model, new formulation of a conductance-based model, numerical methods and software for the efficient simulation of large-scale models;
- Chapter 4: new measure of functional connectivity (improves replicability), new Riemannian similarity metric;
- Chapter 5: improved formulation of Gaussian-Process Surrogate Optimisation (GPSO), new partition function (improves convergence), new software implementation;
- Chapters 6 and 7: parametrisations and results are new, and we achieve high scores of similarity with MEG in terms of band-specific functional connectivity and spectral contents.

Dogs can't operate MRI scanners. But CAT-scan.

2

Imaging Data

Contents

2.1 Introduction

The main purpose of modelling brain activity is to provide a mechanistic and biologically plausible relationship between **structure and function** (Woolrich et al. 2013). In general, structural information relates to the *spatial* organisation across scales (hemispheres, lobes, subcortical structures, cortical layers, tissue properties, *etc*.); whereas functional information relates to *temporal* characteristics of brain activity (oscillations, spectral contents, co-activations, stimulus-response, *etc*.).

Any scientific model starts with **observations**: what does the empirical data look like; are there caveats to the acquisition method(s); and what are the main features that the model should either exploit or explain? From this perspective, there are several modalities measuring information about brain *function*: electro-encephalography (scalp potential), magneto-encephalography (dendritic currents), functional MRI (blood oxygenation), arterial spin labelling (blood perfusion), *etc*. And there are also several *structural* modalities: T_1-weighted MRI (tissue contrast), susceptibility-weighted MRI (venous blood), diffusion MRI (fibre orientation), computed tomography (tissue density), *etc*. Importantly, all of these modalities are **non-invasive**, meaning that they provide information about internal tissues and biological processes *in vivo*, without the need of interventions, or otherwise interfering with the body's "normal" function.

In this thesis, we used diffusion MRI as our principal source of structural information, and magneto-encephalography as our source of functional information, specifically in the context of resting-state activity (see §1.1.2). In this chapter, we introduce briefly these modalities in order to explain what they measure, and present the key properties of the empirical data (post-processing) that are relevant to our modelling endeavour.

Temporal Lobe	**Regions (10)**
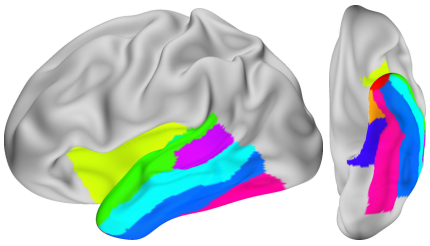	Temporal-pole, Enthorinal, Insula, Superior, Transverse, Middle, Inferior, Para-hippocampal, BankSTS, Fusiform
Occipital Lobe	**Regions (4)**
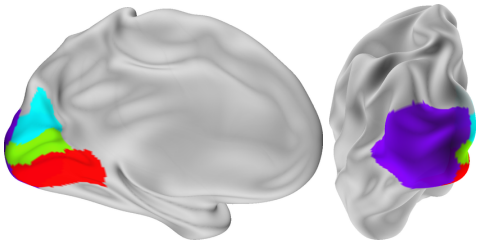	Lingual, Pericalcarine, Cuneus, Lateral-occipital
Parietal Lobe	**Regions (9)**
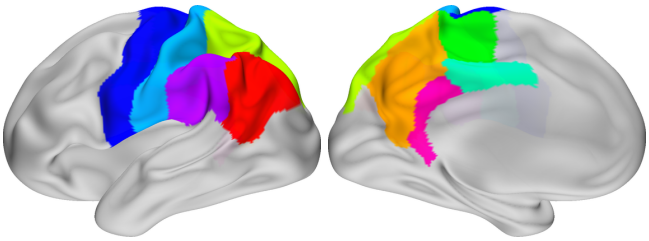	Inferior, Precuneus, Superior, Para-central, Posterior-Cglt, Post-central, Pre-central, Supra-marginal, Isthmus-Cglt
Frontal Lobe	**Regions (11)**
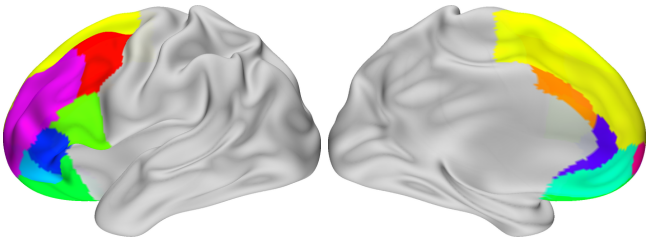	Caudal-middle, Caudal-anterior-Cglt, Superior, Pars-opercularis, Lateral-orbito-F, Medial-orbito-F, Pars-orbitalis, Pars-triangularis, Rostral-anterior-Cglt, Rostral-middle, Frontal-pole

Figure 2.1: The Desikan-Killiany cortical parcellation (Desikan et al. 2006), grouped by lobe. The regions within each lobe are shown on the left, and the names of those regions are shown on the right with corresponding colours. This parcellation is identical for both left and right hemispheres, with 34 regions in each. The directions of the surfaces for each lobe are: L-R and I-S (temporal), R-L and P-A (occipital), L-R and R-L (parietal and frontal), where L=left, R=right, I=inferior, S=superior, P=posterior, A=anterior.

2.2 Connectivity and Parcellation

Before diving into the different modalities, and the information they provide, it is important to introduce the idea of **connectivity**. Throughout this thesis, and in the literature, this term relates to a measure of dependency (either structural or functional) between certain entities (Jbabdi et al. 2015). These entities can either be sensors, individual voxels, groups of voxels or brain regions for example, but they need to be clearly defined. The associated measure(s) of connectivity, and any analysis deriving from them, will usually be highly dependent on this definition (Smith et al. 2011; Fornito et al. 2013).

In our experiments, we used the Desikan-Killiany (DK) cortical parcellation (Desikan et al. 2006) to define a set of 68 brain regions. This parcellation is mirrored across hemispheres, and relies on anatomical considerations (automated gyral-based labelling method); an illustration is proposed in Fig. 2.1.

We emphasize that this choice is by no means a gold-standard; in our case, it was simply a pragmatic choice given the data already available for analysis. The task of defining brain regions that are relevant across modalities is a difficult problem, and one that is still being researched (Glasser et al. 2016). We are conscious that the results presented in Chapters 6 and 7 might change with a different parcellation, and this will be investigated in future work.

Nevertheless, **the tools and methodologies exposed throughout this thesis are insensitive to the choice of a parcellation**, although they may require certain structural properties (*e.g.* hemispheric symmetry in §6.2.1). Indeed, this is because the material in chapters 3 through 5 operates at a theoretical level where, for example:

- The brain is modelled as a dynamical system composed of brain regions connected into a network (see Fig. 3.1). What those regions are, or how strong is a particular connection, are irrelevant questions at this level. They can only be answered by considering specific values for the *parameters* of the model, without which the

model itself is only a template waiting to be instantiated. And yet, however abstract, there are valuable insights that contribute to the design of such templates.

- The problem of fitting such models to real brain activity consists in finding the parameter values which lead to the most realistic simulations. Deciding on the exact meaning of "realistic" — in other words, defining physiologically meaningful criteria in order to quantify the similarity between real and simulated data — is an entirely separate problem to that of searching for the best parameters. The optimisation method presented in chapter 5 treats the particular problem at hand as a "black-box", and focuses instead on formulating a search-strategy which iteratively *adapts* to the problem, as more knowledge is acquired through exploration.

We will come back to this in due course.

2.3 Diffusion Imaging

Diffusion imaging is a modality of magnetic-resonance (MR) capable of detecting the presence, and estimating the orientation, of **white-matter tracts** (*i.e.* bundles of axons) *in vivo* (Basser et al. 1994; Behrens et al. 2013; Jones 2011). In the following sections, we briefly summarise the relevant aspects of the modality itself, and present the information derived from this modality that was used in our work.

2.3.1 Modality

Diffusion imaging (Le Bihan et al. 1986) relies on the phenomenon of molecular diffusion; the fact that particles in a fluid move seemingly randomly over time due to thermal energy. A fundamental assumption behind this modality is that the resulting motion, in places where multiple axons align, is hindered in the cross-sectional plane (due to the cell-membranes) more than it is along the axons.

Figuratively then, if we were able to *tag* the position of diffusing particles at time t, and recognize those tags by taking a snapshot at time $t + dt$, we should observe a net displacement which is smaller across the tracts, and larger along them.

Although it is not possible to individually and instantaneously locate all particles in a living brain, let alone recognise them at a different timepoint, it is possible (see Pooley 2005 for a short introduction to MR physics) to: encode the position of these particles along a specific direction in space, by varying the rate of nuclear precession using magnetic gradient fields; and ensure that the nuclei precess initially synchronously, or "in-phase", by exciting them with a radio-frequency (RF) pulse.

The fact that nearby nuclei precess at different rates eventually leads to a local dispersion of the signal's phase, characterised by the T_2 relaxation-time. If the particles do not move, then it is possible to *refocus* the phase by reversing the nuclei's spins[1] shortly after the initial excitation — a method used in **spin echo** acquisitions. However, if the particles moved incoherently (*i.e.* not in bulk) between the initial excitation and the spin-reversal, then the phase cannot be entirely refocused (due to locally incoherent precession rates), which results in signal attenuation (Stejskal et al. 1965). This attenuation is the basis of MR diffusion-imaging.

Diffusion is not always constrained to a principal direction; in the ventricles for instance, the diffusion of water molecules within the cerebro-spinal fluid (CSF) is unconstrained, and we should expect high attenuations in every direction. Furthermore, because the imaging resolution is typically on the order of a cubic millimetre, most voxels contain tracts going in different directions. Generally then, the fibre orientation within each voxel should be seen as a **spherical distribution** (possibly multi-modal or uniform), called the orientation distribution function (ODF). This distribution is estimated in practice by measuring diffusion in as many directions as possible (given time, cost and

[1] This is intuitively equivalent to inverting the direction of rotation, *e.g.* from clockwise to anti-clockwise.

ethical constraints), and subsequently inverting a biophysical model that links diffusion measurements to fibre orientations.

This orientational information can be used to assess the local structure of white-matter tracts, and serve as a basis for statistical comparisons across subjects and/or patients for example (Smith et al. 2006). Importantly, it can also be used to estimate the *connections* between different brain regions (Jbabdi et al. 2015). For this purpose, the local orientation estimates need to be integrated across space in order to form pathways between those regions (or **streamlines**), and the set of all pathways can be summarised in the form of a three-dimensional map (or tractogram). This is the aim of **diffusion tractography**.

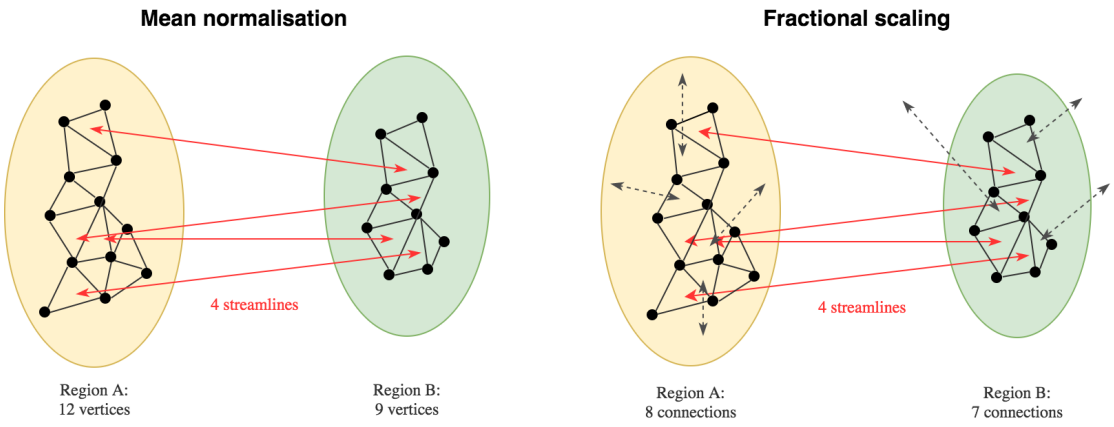

Figure 2.2: Anatomical connectivity estimation from streamline-counts can be done in several ways; two different normalisation methods are illustrated here. Note that tractography cannot infer the directionality of the connections between regions, hence the double-ended arrows. Mean-normalisation divides the number of streamlines between two regions by the total number of vertices in both regions; whereas fractional scaling divides by the total number of streamlines reaching either region (Donahue et al. 2016).

2.3.2 Anatomical connectivity

In this thesis, we rely on probabilistic diffusion tractography (as implemented in ProbTrackX, see Behrens et al. 2007) to estimate the so-called **anatomical connectivity** (AC) between different brain regions (a.k.a. structural connectome), and inform our biophysical network models (*c.f.* Chapter 3).

Probabilistic methods proceed to integrating the diffusion space by sampling large numbers of streamlines in a random fashion (*i.e.* Monte-Carlo sampling). The computation of a streamline can be summarised in a few simple steps (Behrens et al. 2003):

1. Select a seed point z as the start of the streamline (*e.g.* in the white-matter);
2. Draw a sample direction $\vec{d}$, with $\left\|\vec{d}\right\| = 1$, from the ODF at point z;
3. Make a step of length s, such that $z \leftarrow\!\shortmid z + s\vec{d}$;
4. Go to step 2, unless a stopping criterion is met (*e.g.* reaching a target region).

As apparent from the previous description, this process depends on the definition of a set of **seed and target points**, as well as a set of terminal constraints. The constraints aim at avoiding unrealistic streamlines (*e.g.* making sharp turns, or stepping outside the white-matter), and the set of target points is typically taken as the boundary between white-matter (WM) and grey-matter (GM).

However, the choice of seed points is not straightforward: it seems equally reasonable to start from the WM/GM boundary (as with the target points), or to draw two half-streamlines from any point within the WM for example. Furthermore, it is also unclear how this information should be used to quantify the connectivity between two brain *regions* (*e.g.* when using a cortical parcellation); for instance, simply counting the number of streamlines connecting points within one region to the other would lead to connectivity strengths correlated with the region's sizes. These are still open problems (Sotiropoulos et al. 2017), to which we refer below respectively as **seeding** and **normalisation**.

In our experiments, we used distortion corrected data (Glasser et al. 2013) from the Human Connectome Project (HCP, see Van Essen et al. 2012b) in order to estimate the fibre orientations required for tractography (Jbabdi et al. 2012). Two different seeding methods were used: the `conn1` method considered streamlines starting from the WM/GM boundary; whereas the `conn3` method considered every brain voxel as a seed.

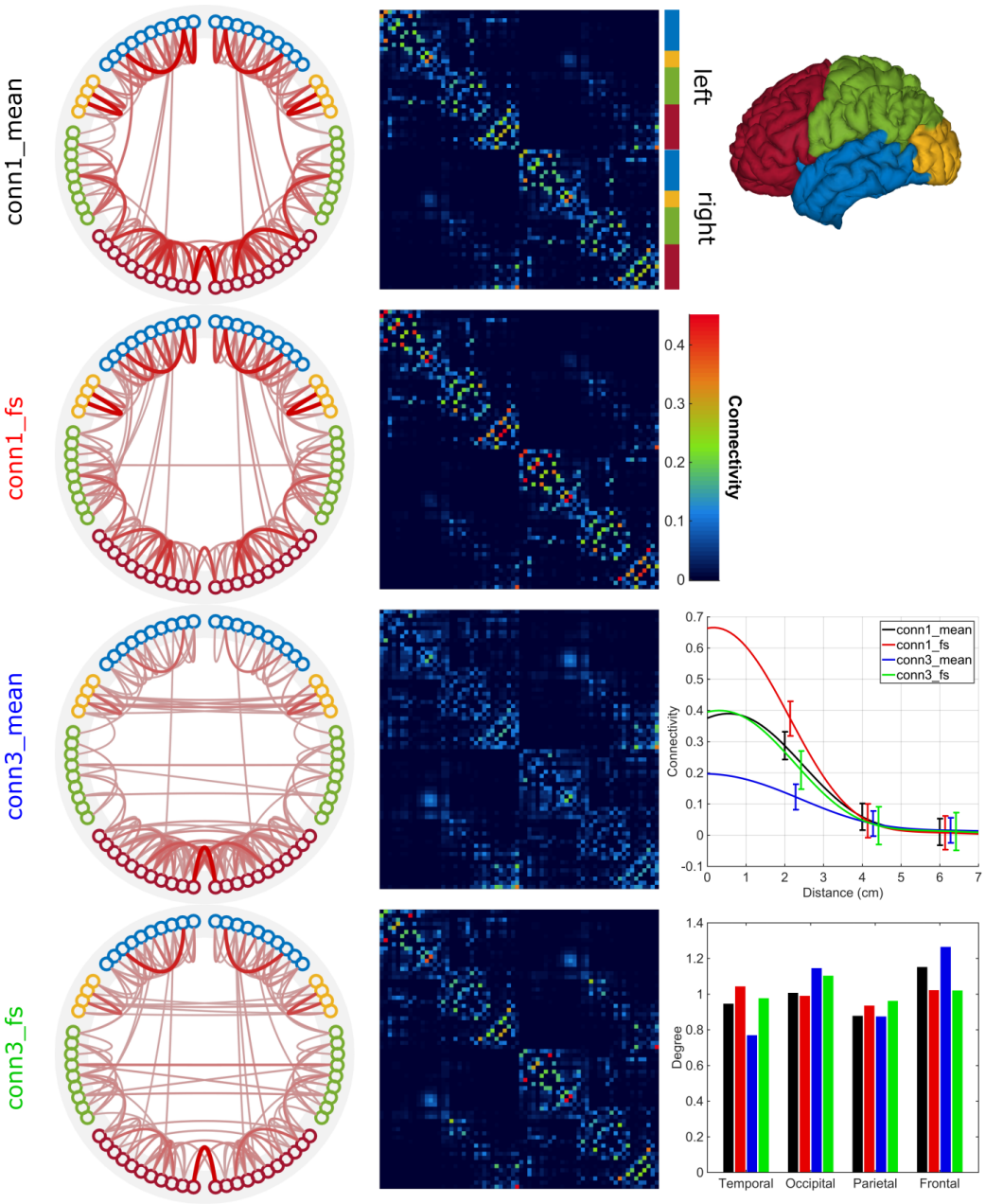

Figure 2.3: Anatomical connectivity (AC) derived from diffusion tractography, averaged across 10 subjects from the HCP (Van Essen et al. 2012a). **Columns 1&2.** AC matrices on the right, using different seeding and normalisation methods (see §2.3.2); and corresponding thresholded networks (90^{th} percentile) showing strongest edges. Brain regions corresponding to each row/column are grouped by lobe (see colours at the top-right). `conn3` seeding favours homotopic connections, whereas `conn1` favours anterior-posterior connections, and `mean` normalisation shows stronger frontal connectivity. **Bar-plot.** Average connectivity strength for each method (colour) and within each hemisphere (x-axis): connectivity is higher in the frontal and occipital lobes; fractional scaling (`fs`) reduces frontal connectivity, while increasing temporal and and parietal ones; and `conn1` seeding yields higher temporal and lower occipital connectivity. **Line-plot.** GP regression of connectivity strength vs. corresponding tract-lengths (see §2.3.3), showing predicted mean and 95% confidence intervals; connectivity decreases sharply with the distance.

Thousands of streamlines were computed for each seeding method (10k/seed for `conn1`, 3k per seed for `conn3`), and the number of streamlines reaching locations on the WM/GM boundary (~60k vertices in standard MNI space) were recorded for each pair of target points. The connectivity between regions in the DK parcellation (*c.f.* §2.2) was estimated by summing the streamlines connecting vertices within two different regions (self-connectivity was set to zero), and normalising the resulting matrices using two different methods:

- with the `mean` method, each aggregated streamline-count was divided by the total number of vertices within both regions;
- and with fractional scaling (Donahue et al. 2016), denoted `fs`, each count was divided by the total number of streamlines reaching either region. This mimics the normalisation performed on chemical tracing measurements (Markov et al. 2014).

Both methods are illustrated in Fig. 2.2. Conceptually, the first normalisation accounts for differences in *size* between different regions, while the second method accounts for differences in *connectivity* between pairs of regions instead (which indirectly accounts for differences in size as well). Finally, each normalised matrix was made symmetric by arithmetic average with its transpose, and rescaled such that the average degree (sum of rows or columns) be unitary.

The resulting AC matrices are shown in Fig. 2.3, along with elements of analysis highlighting the characteristic features of this information. In particular, it is worth noting that the connectivity strength between two regions decreases sharply with the length of the streamlines connecting them; probabilistic tractography methods have an inherent bias towards shorter connections, because uncertainty is accumulated with the distance from the seed, and as a result longer streamlines are less probable (Sotiropoulos et al. 2017). This may reflect a biological reality(Ercsey-Ravasz et al. 2013), but whether or not the decrease predicted by these methods is accurate is an open question.

In addition, we note that the difference between `conn1` and `conn3` is that the latter emphasises homotopic connections; this is because seeding from the WM makes it easier to reconstruct longer connections, but also causes a bias towards them, as they are then sampled more frequently.

2.3.3 Tract-length

Another important information derived from probabilistic diffusion tractography is the distance between different regions along the streamlines connecting them, or **tract-lengths**. These distances are used mainly to estimate the delays between two connected regions in our biophysical models (see §3.3.2), which arise due to the finite conduction velocity in neuronal tissue. This velocity is known to be affected by a range of factors, including axon diameter (Ritchie 1982), myelination (Purves 2004, p.63), and temperature (Sabatini et al. 1999).

Although the knowledge about brain temperature regulation is presently limited (Wang et al. 2016), it is unlikely that variations of temperature between different areas would be large enough to affect conduction delays significantly, due to the severe damage that such variations could cause (Childs 2008). With regards to axon diameter and myelination, the question is more delicate. There is a near-linear relationship between the axon diameter and the conduction velocity for myelinated fibres in the peripheral nervous system, which leads to a range of velocities between roughly 10 and 120 m/s (Ritchie 1982). The relationship between axon diameter and myelin sheath thickness is described by the so-called **g-ratio**, which is almost constant in the central nervous system (Behrens et al. 2013 section 7.2.2.2); therefore measuring variations in either axon diameter or myelin thickness should lead to the same conclusions in terms of conduction velocity modulation.

Recent research (Liewald et al. 2014) suggests that the distribution of axon diameter in the human brain follows a gamma distribution, with a peak near $0.5\mu m$ and most of the

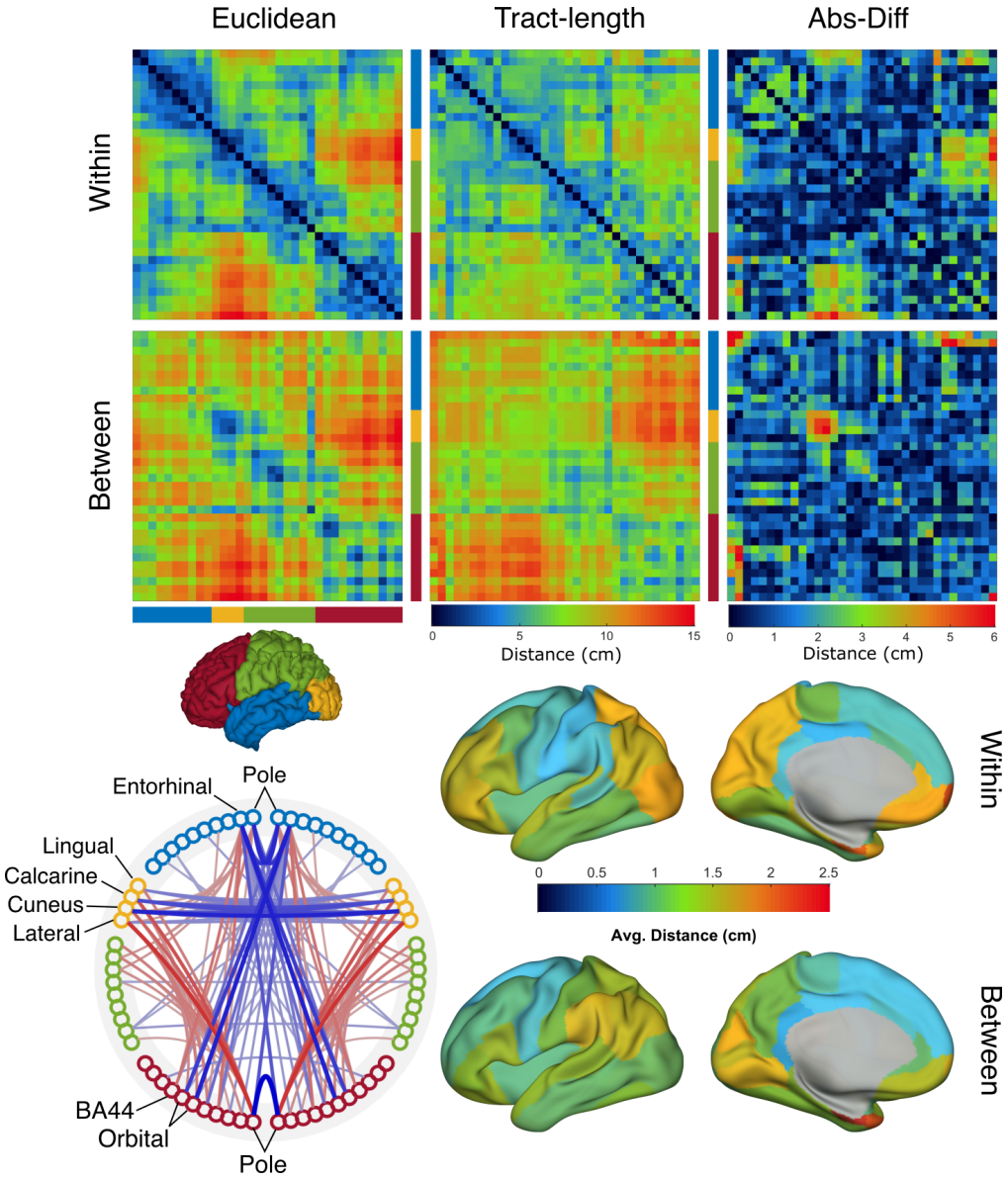

Figure 2.4: Comparison of pairwise Euclidean distances between regions, with corresponding average tract-lengths from tractography (averaged across 10 subjects from the HCP). **Matrices.** Comparing pairwise distances within/between hemispheres (first/second row). **Surfaces.** Average absolute difference between Euclidean distances and tract-lengths, from each brain region to others within (top) and between (bottom) hemispheres, shown on the cortical surface. **Network.** Visualisation of largest absolute differences (95^{th} percentile), within and between hemispheres (in red and blue, respectively). The most pronounced differences are between frontal and inferior temporal areas (both within and between hemispheres), as well as between homotopic regions (mainly occipital), and occipital-frontal within hemispheres. Note that BA44 refers to the 44^{th} Brodmann area, a.k.a. *pars opercularis*.

mass below $1\mu m$. Extrapolation from the known linear relationship in the peripheral nervous system places the corresponding conduction velocities roughly between 1 and 10 m/s, leading to delays varying between 1 and 10 ms per centimetre travelled. These estimates suggest that variations of axonal diameter throughout the brain is potentially a major cause of delay modulation between brain areas, and assuming a constant g-ratio, these could potentially be estimated by MRI myelin maps (Laule et al. 2007).

In this thesis, **we assumed a constant propagation velocity throughout the brain**, and considered the distance between different brain areas as a proxy for estimating the delays between them. Additional information about conduction velocity modulation (*e.g.* derived from myelin maps) will be used in future work.

The effects on the simulated dynamics of varying delays between brain areas is not trivial; small differences in the distribution of delays can cause qualitative differences in the simulated dynamics (Deco et al. 2009; Lücken et al. 2015). From a theoretical standpoint, this is because non-linear delay-systems are very likely to be chaotic; as we will see later in §3.5.2.2, delay-systems are infinite-dimensional, and non-linear rules of evolution often lead to a complex organisation of the phase-space, which affects the sensitivity to initial conditions.

In our experiments, tract-lengths were estimated from diffusion tractography on a cortical mesh with 1627 vertices per hemisphere (downsampled from the standard HCP mesh with 32k vertices, see Glasser et al. 2013). The pairwise distances between regions in the DK parcellation was taken as the average length of the streamlines connecting vertices within two different regions (self-distances were set to zero). A comparison of the matrices obtained after averaging across 10 subjects from the HCP, using either tract-lengths or Euclidean distances between the region's barycentres, is illustrated in Fig. 2.4. We found relatively large differences (up to 6cm) in the distances between:

- the occipital and frontal lobes (within hemisphere);
- homotopic regions within the occipital lobes (between hemispheres);

- and between inferior-temporal (enthorinal and temporal-pole) and orbito-frontal areas (between hemispheres).

The magnitude of these differences (and the regions involved) suggest that using tract-lengths instead of Euclidean distances may be important for the simulation of bio-physical models.

2.4 Magneto-Encephalography

Magneto-encephalography (MEG) is an imaging technique capable of measuring directly the magnetic-fields induced by electro-physiological activity in the brain. In this section, we briefly summarise the biophysical origin of the MEG signal, and discuss the typical processing pipeline and characteristic features of resting-state data.

2.4.1 Modality

The ability of neurons to fire action potentials (APs) in response to inputs is a defining feature of their biological function. This function is chemically mediated by ionic pumps and voltage-gated sodium channels located in the cell-membrane. In the absence of stimulation, the membrane-potential is maintained at approximately $-70\mathrm{mV}$, by keeping higher ionic concentrations of sodium, calcium and chloride outside the cell, and potassium inside. Stimulation from afferent neurons can raise the membrane-potential above a critical value (around $-40\mathrm{mV}$, see Fig. 3.3 p.47); this triggers a positive-feedback loop whereby voltage-gated sodium channels open near the soma, leading to a rapid influx of sodium ions into the cell, which locally increases the membrane potential, and allows nearby sodium channels to open in turn. As a result, a rapid depolarisation of the cell membrane travelling along the axon occurs (called *action potential*), and is followed by a closing of the sodium channels, and opening of the potassium channels, in order to restore the ionic concentrations to their resting values.

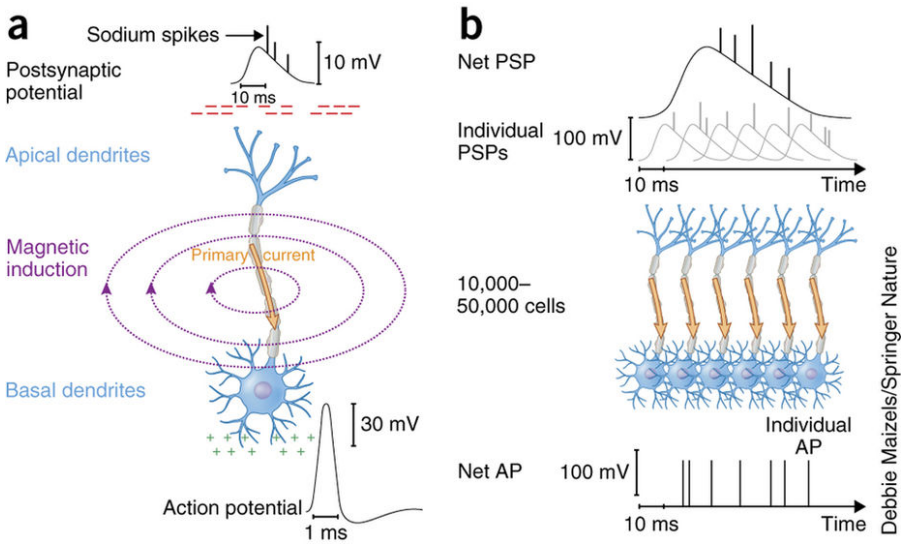

Figure 2.5: The MEG signal originates from the magnetic field induced by temporally overlapping post-synaptic potentials (PSPs) involving tens of thousands of cells. The propagation of an action potential (AP) along the axon of a neuron induces a short-lived electrical current (due to the imbalance of ionic concentrations between the soma and the axon terminals), denoted "*primary current*" in this figure. This current is very small for a single neuron, and the typical duration of an action potential (~1ms) is too short to allow large numbers of spikes to overlap temporally, and build-up a net current that can be measured at the macro-scale. Although dendritic currents induced by PSPs are weaker than axonal ones for individual neurons, their duration is long enough to allow for constructive temporal overlaps, which magnify the local activity. Computational models and empirical evidence show that the PSPs resulting from the activity of 10-50k neurons generate a magnetic field that can be detected with MEG (Murakami et al. 2006).

Reproduced with permission from (Baillet 2017).

The "stimulation" from afferent neurons occurs in the dendrites of the cell, where thousands of synaptic connections (on average, see Drachman 2005) are integrated, and contribute to changing the membrane-potential via so-called **post-synaptic potentials** (PSPs). The imbalance of ionic concentrations in different parts of the cell creates short-lived electrical currents, which induce small **magnetic-fields** governed by the Maxwell-Ampere law. These fields are too weak to be measured for individual cells, but they can add-up to larger fields if an entire population of neurons becomes synchronously active. The characteristic decay-time of axonal currents during an AP is on the order of a millisecond, which is too short to allow for sufficient temporal overlap. However, the effects of PSPs typically last longer than 10ms, which is long enough for a measurable signal to emerge in a population of 10k-50k neurons (Murakami et al. 2006).

We reproduce a figure from (Baillet 2017) to illustrate this point in Fig. 2.5; more details about the strengths and weaknesses of MEG for brain imaging can be found in this paper.

2.4.2 Source reconstruction

Brain activity is measured in MEG by an array of magnetic sensors (typically a few hundred) in close proximity with the head. Each sensor measures a particular weighted summation of all active sources within the brain (depending on its location); the corresponding set of raw measurements is said to be in **sensor-space**, as opposed to the **source-space**. Estimating the spatial location of active sources from the patterns of sensor measurements is a fundamentally ill-posed problem; in general, there are infinitely many spatial configurations that can result in a given pattern being measured by the sensors. This can also be understood by looking at the imbalance between the number of unknowns (*e.g.* each voxel within the brain), and the number of variables (a few hundred sensors), although we should expect some degree of spatial smoothness.

In principle, solving the reconstruction problem requires the inversion of a so-called **forward-model**, describing the propagation and interference of magnetic fields through various tissues in the brain (*e.g.* WM, GM, CSF, fat, skull and scalp). This is no small feat; the propagation of magnetic waves is governed by Maxwell's equations, which are analytically intractable (and likely computationally expensive) when considering arbitrary head shapes, cortical foldings, and non-uniform tissue distributions. In practice, methods attempting to invert the forward-model make strong simplifying assumptions (*e.g.* spherical head-shape with uniform conduction properties, small number of active sources) in order to remain tractable (Wipf et al. 2009; Hansen et al. 2010).

It is possible to avoid the complexity of model inversion to some extent by taking a different approach. **Beamforming** methods tackle the reconstruction problem using spatial filters that can be tuned to attenuate the signal everywhere, except in one particular

location. This is achieved by weighting the contribution of each sensor at this location, using the linearly constrained minimum variance (LCMV) approach developed by (Van Veen et al. 1997). As a result, it is possible to estimate the signal at each voxel within the brain as a linear combination of sensor measurements, with weights derived from the forward-model (Baillet et al. 2001).

2.4.3 Source leakage

One caveat of beamforming methods is that, for a limited number of sensors in close proximity to each other (as is the case with MEG), the correlation between the reconstructed signal at a particular location and points in its vicinity can be quite large. In essence, this is a consequence of the ill-posedness of source-reconstruction from a finite number of sensors. Although spatial correlations certainly reflect a biological reality (neuronal populations are not confined to a single point), in practice this vicinity can extend to several centimetres (especially with deeper sources), which becomes problematic when trying to estimate the connectivity between different regions. This is the so-called **source-leakage** problem.

For a given parcellation defining multiple regions as groups of voxels, the activity within each region can be summarised by simple averaging, or using more advanced methods like principal component analysis (PCA). Correlations between the summary activity in two specific regions may exist for several reasons, for example:

- because the corresponding neuronal populations are directly connected by WM tracts (causal dependence);
- because they affect each-other via shared neighbours (indirect dependence);
- because the regions overlap spatially (contamination);
- because they both contain parts of an indivisible functional unit (structural flaw);

- or because of information contamination introduced by the processing methods (analytic flaw).

What is considered "spurious" amongst the above can be a matter of perspective, depending on the meaning assigned to the "connectedness" between two regions. Although source leakage (which is an analytic flaw) is generally considered spurious, its effects cannot be easily distinguished from other potential sources of correlation, such as causal dependencies and structural flaws due to the choice of an imperfect parcellation. Therefore, correcting for spatial leakage using generic approaches like orthogonalisation methods (Colclough et al. 2015) may also remove "true" correlations — this should be kept in mind when comparing simulations to leakage-corrected empirical data.

2.4.4 Oscillatory dynamics

The activity measured with MEG is oscillatory in nature; the biophysical explanation for these oscillations relates to the interaction between populations of excitatory and inhibitory neurons (as will be explained in §3.3). The amplitude variations of these oscillations over time, which are believed to reflect the degree of stimulation of a given region, can be measured using the *analytic transform* (see §4.2.1), specifically looking at its magnitude, also called the **Hilbert envelope**.

In our experiments, we used the resting-state datasets of 28 healthy subjects from (Brookes et al. 2015; Robson et al. 2016). Details about acquisition and pre-processing can be found in these references. The sensor data were filtered between 4 and 40 Hz, and beamformed into MNI 8mm standard space (*i.e.* the source activity was estimated for each brain voxel in that space). Summary time-courses for each region in the DK cortical parcellation (see §2.2) were computed using PCA, rescaled to set the largest standard-deviation to 1, and orthogonalised to correct for spatial leakage using the method developed by (Colclough et al. 2015).

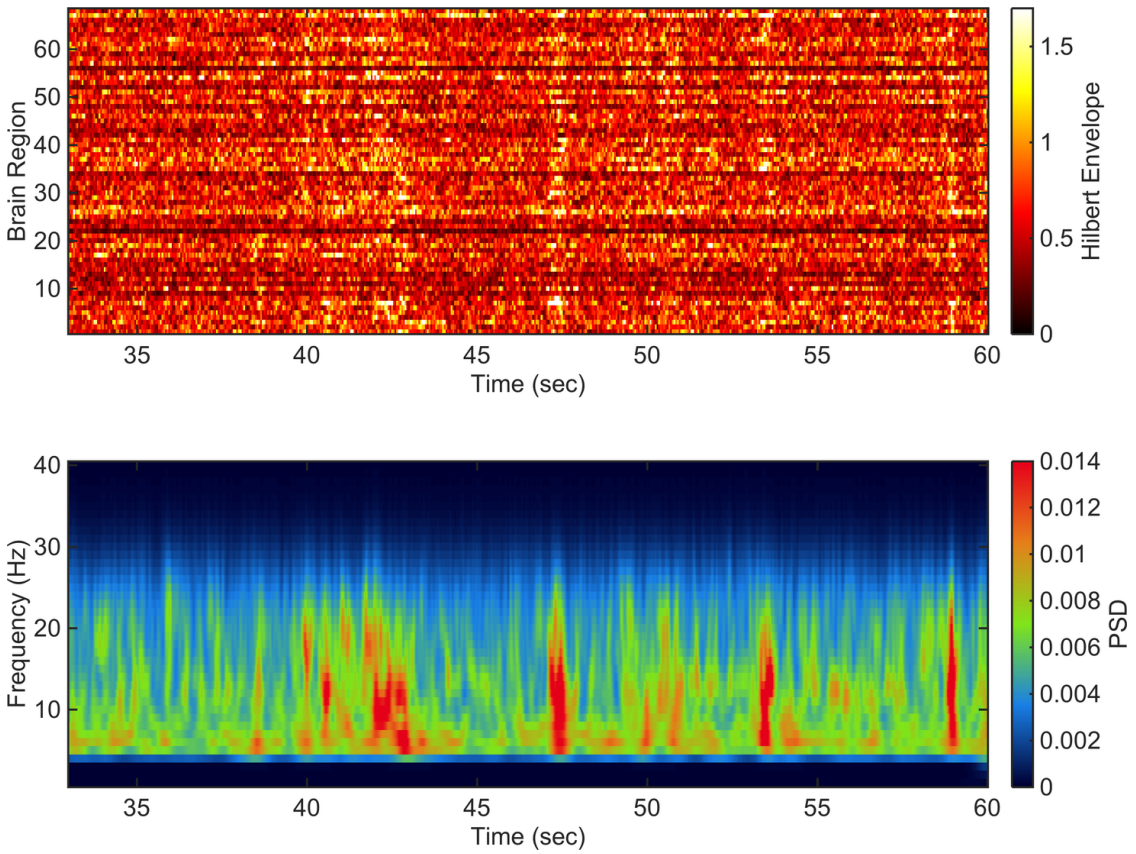

Figure 2.6: Example MEG resting-state activity (beamformed, parcellated into 68 regions, and orthogonalised). The Hilbert envelope of the signals is shown at the top, and the corresponding wavelet spectrogram (power spectral density (PSD), averaged across signals) is at the bottom. Band-pass filtering between 4-40 Hz was applied prior to beamforming. The spectrogram at the bottom (obtained with a continuous wavelet transform) reveals dynamics spanning multiple time-scales: there seems to be a regular baseline below 10 Hz, interrupted by bursts of activity spanning frequencies between 4-25 Hz (the upper-bound varies across subjects between 15-25 Hz) and re-occurring at a rate <1 Hz. Note that these bursts of spectral power are characterised by high-amplitude synchronous activity across regions (see brighter bands in the top plot around 40-43s, 47s and 59s).

An example of the corresponding Hilbert envelopes and time-frequency contents after this processing is shown in Fig. 2.6. The leakage correction altered significantly the amplitude of oscillations across brain regions, in particular the envelopes in the following regions have very low amplitudes after orthogonalisation: *posterior cingulate*, *isthmus cingulate*, *lateral orbito-frontal*, *medial orbito-frontal* and *pars-orbitalis*. In terms of frequency contents, most of the spectral power is below 30 Hz, with a relatively stable baseline below 10 Hz, interrupted by bursts of activity spanning frequencies between 4-25 Hz, corresponding to seemingly synchronous activations across the entire cortex.

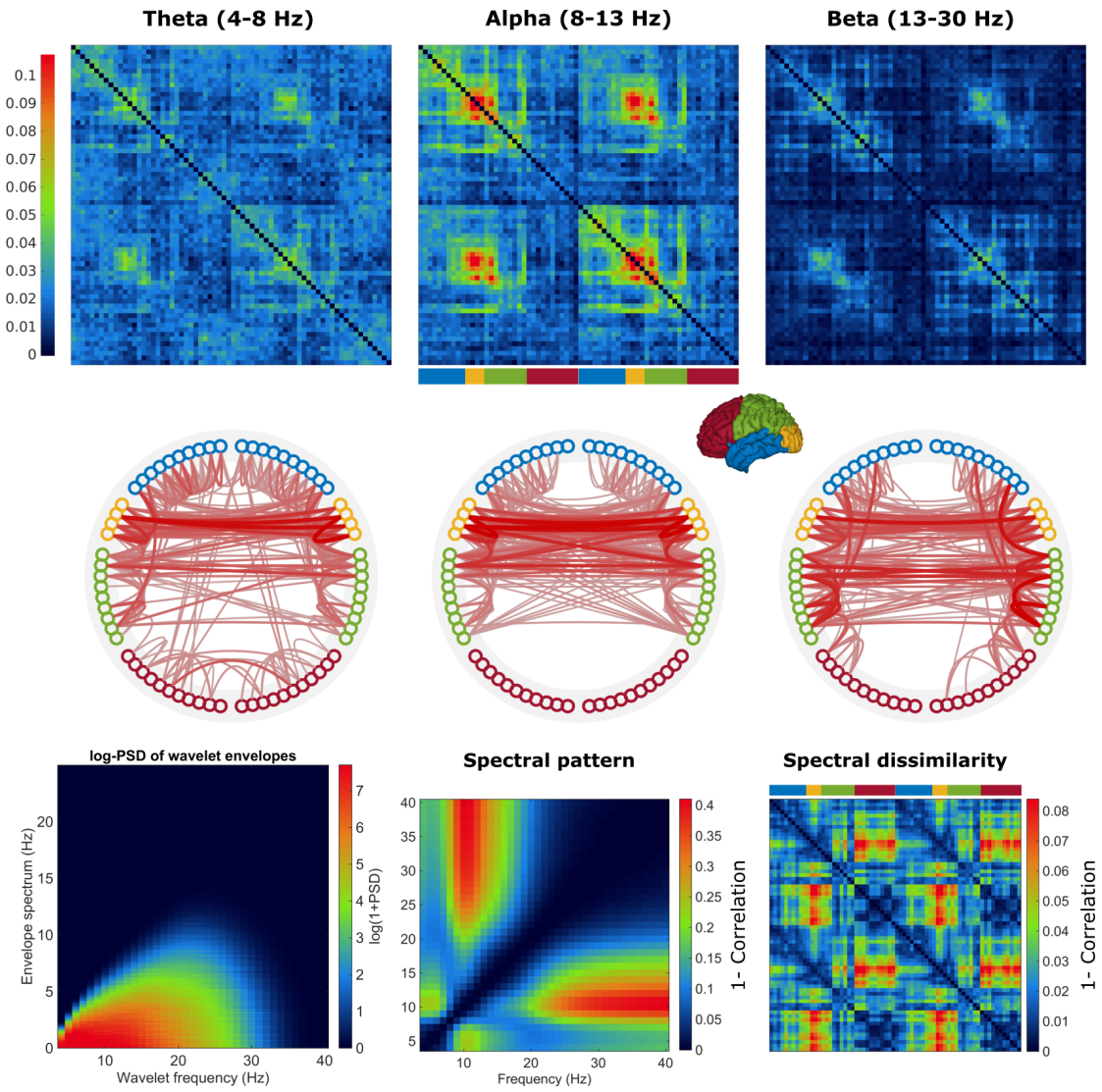

Figure 2.7: Summary of resting-state activity in MEG. **Rows 1& 2.** Functional connectivity (row 1) and corresponding thresholded networks (row 2, 90^{th} percentile) in frequency-bands theta, alpha and beta (left-to-right). The FC is visibly stronger in alpha band, almost symmetric between hemispheres, and involving mainly the occipital and parietal lobes. The networks show that connectivity is most widespread in theta band, notably with temporal-parietal and temporal-frontal connectivity; connectivity in alpha band is mainly within-lobe or homotopic, with notable cross-hemispheric links between the occipital and parietal lobes; and finally, beta connectivity is more pronounced in the parietal lobe, with notable temporal-parietal links within-lobe. **Last row.** Characterisation of spectral contents, from left to right: power spectral density (PSD) of wavelet magnitude time-courses between 4 and 40Hz; anti-correlation of PSD in each brain region, for pairs of frequencies between 4 and 40Hz; and anti-correlation of PSD between pairs of regions.

2.4.5 Functional Connectivity

The previous analysis allowed us to derive certain features of resting-state activity by characterising the activity within each brain region independently. Ultimately however, the brain functions as a coordinated system through the cooperation of these regions, and therefore it is crucial to look at the *relationships* between individual measurements. **Functional connectivity** (FC) aims at quantifying such relationships, by establishing pairwise statistical dependencies between different recordings of brain activity. Similarly to AC, it is typically visualised as a matrix or thresholded network (see Fig. 2.3).

MEG recordings have a very high temporal resolution (typically up to 500 Hz), and resting-state activity is spectrally complex (*i.e.* spanning a range of different frequencies with transient bursts of activity). Connectivity analyses in resting-state MEG data usually exploit this temporal resolution, by carrying out analyses in different frequency-bands. The relevant bands in resting-state are:

$$\text{Delta}: < 4\text{Hz} \quad \text{Theta}: 4-8\text{Hz} \quad \text{Alpha}: 8-13\text{Hz} \quad \text{Beta}: 13-30\text{Hz}$$

These definitions are not entirely arbitrary; by computing the power spectral density (PSD) of the activity in each region, and correlating pairs of *frequencies* (not regions), we find that the distribution of power across regions is similar between frequencies inside, and dissimilar with frequencies outside these bands[2]. This is shown as the "spectral pattern" in Fig. 2.7. We also correlated the PSD between *regions*, in order to probe for any spatial dependency to the frequency contents (labelled "spectral similarity"); we found very similar spectral contents overall across regions (see colour-scale), the largest differences being between the frontal and occipital lobes.

[2]Unfortunately, we could not go below 4 Hz in this dataset due to the filtering between 4-40 Hz applied in source-space as part of the pre-processing. This filtering, combined with the fact that we only computed wavelet time-courses for integer-frequencies between 4-40 Hz, also means that the "block" corresponding to the theta band is not visible in the spectral pattern.

Looking at the variations of spectral power over time in Fig. 2.6, another pertinent question is whether the temporal dynamics are specific to certain frequencies. To clarify, we are now talking about the spectral distribution of the wavelet-magnitude time-courses, for integer frequencies between 4 and 40 Hz. These distributions are shown in Fig. 2.7 (bottom-left), and reveal slow envelope dynamics (below 10 Hz) consistent across oscillatory frequencies between 4-40 Hz.

Interestingly, this picture likely reflects the discrepancy of time-scales between local oscillatory activity (due to densely connected populations of neurons), and long-range interactions between remote brain regions (constrained by propagation delays around 10-25 ms), which is consistent with the assumption that **Hilbert envelopes reflect the degree of stimulation in these regions**.

Hence, the FC was computed between regions in the DK parcellation as the correlation between Hilbert envelopes in each frequency-band mentioned previously. The resulting matrices are given in Fig. 2.7, along with corresponding thresholded networks (grouped by lobes) showing the 90^{th} percentile of strongest similarities. The FC is visibly stronger in alpha band (although overall with small correlation coefficients), and the connectivity between the occipital and parietal lobes is present across bands.

2.5 Comparing Structure and Function

We conclude this imaging chapter with a comparison between the structural and functional connectivity information presented above. The structural information consists of four AC matrices estimated from probabilistic diffusion tractography, as shown in Fig. 2.3; and the functional information is taken as the band-specific MEG resting-state FC matrices shown previously in Fig. 2.7.

We ask two questions, relating to previous research (Honey et al. 2009; Meier et al. 2016):

1. Does the comparison between structure and function improve by considering only "strongly" connected regions?

2. Does it improve if we consider so-called "poly-synaptic" connections?

To answer the first question, we thresholded the various AC matrices independently, filtering out the bottom 5% of the connections to start with, and up to the bottom 95%. For each thresholded matrix, we computed the correlation between the remaining edges, and the corresponding elements in each of the three band-specific FC matrix from MEG (in theta, alpha, and beta bands). As a result, we obtain a series of correlation values (for each threshold), for every pair of AC and band-specific FC, illustrated in Fig. 2.8. Our results show that the correlation between structural and functional information decreases systematically (across bands) as the thresholding becomes more stringent, suggesting that the two sources of information point to a different set of "main" connections.

Given the answer to the first question, we include all edges in our analysis for the second question. In order to determine whether poly-synaptic connections help improve the correspondence between structural and functional information, we consider a linear mixing between each AC matrix, and the corresponding squared matrix $\mathrm{AC} + m\ \mathrm{AC}^2$. Indeed, interpreting the connectivity information as the adjacency of a graph leads to the insight that the k^{th} power of the adjacency corresponds to paths of length up-to k connecting pairs of brain regions (*i.e.* connections with between 0 and $k-1$ intermediaries). By varying the mixing coefficient m between 0 and 5, and for each value comparing every pair of AC and band-specific FC (as previously), we obtain a new series of correlations, illustrated in Fig. 2.9.

Based on these results, there appears to be a noticeable difference between AC matrices obtained using `mean` versus `fs` normalisation (see Fig. 2.2 for a reminder). Namely, the inclusion of poly-synaptic connections does not seem to improve correspondence between structure and function when the `mean` normalisation is applied, but it does when using fractional scaling (`fs`) instead. It is tempting to conclude from these results, that fractional scaling is therefore a "better" normalisation method; but this would imply that we expect the dynamic activity to be linearly related to white-matter connectivity. Perhaps the choice of a different mixing would tell a different story, or improve both cases; and perhaps structure and function should not be compared directly, but rather through the use of a biophysical model of brain activity.

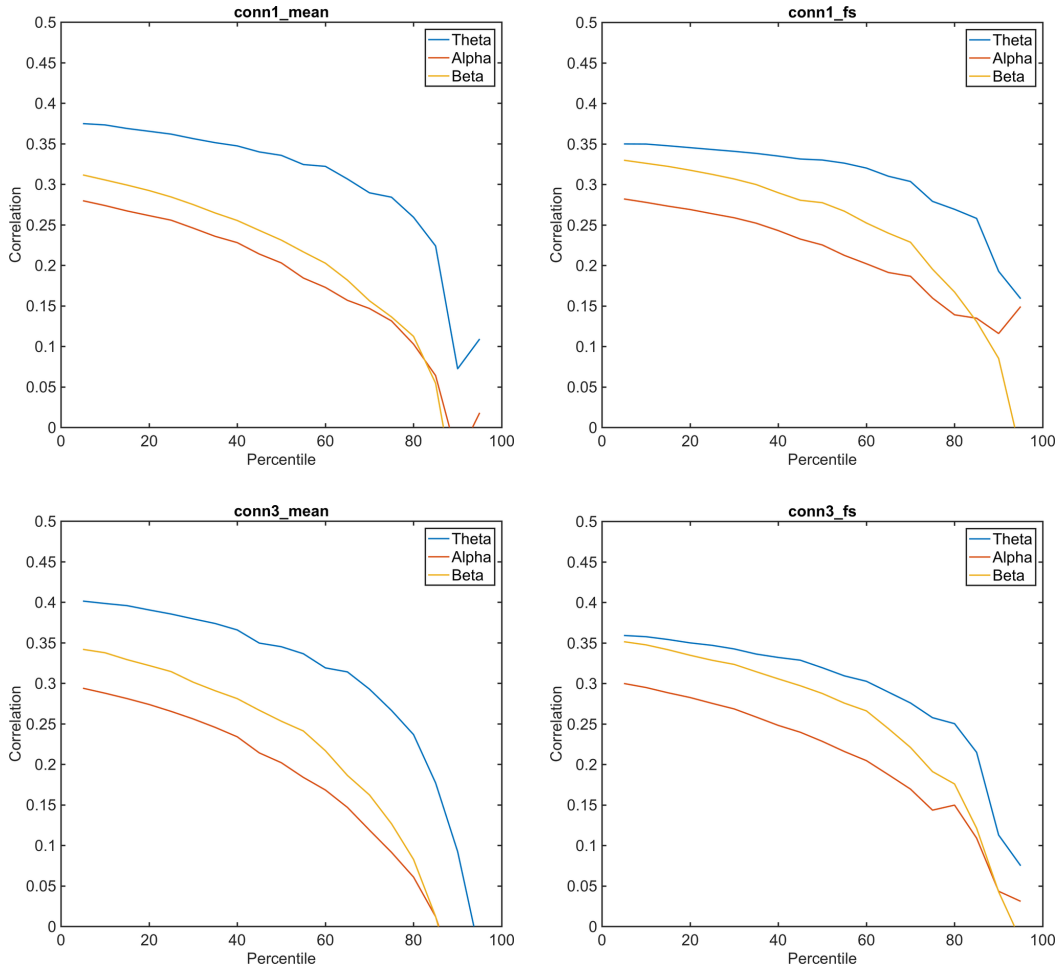

Figure 2.8: The comparison between structure and function is not improved by considering only those "strongly connected" regions. Each of the four panels corresponds to a different AC matrix, shown previously in Fig. 2.3; and each of the three curves within each panel corresponds to a different frequency-band. We show the evolution of the correlation between AC and band-specific MEG resting-state FC, when considering an increasingly small subset of the connections, obtained by thresholding the AC at a given percentile.

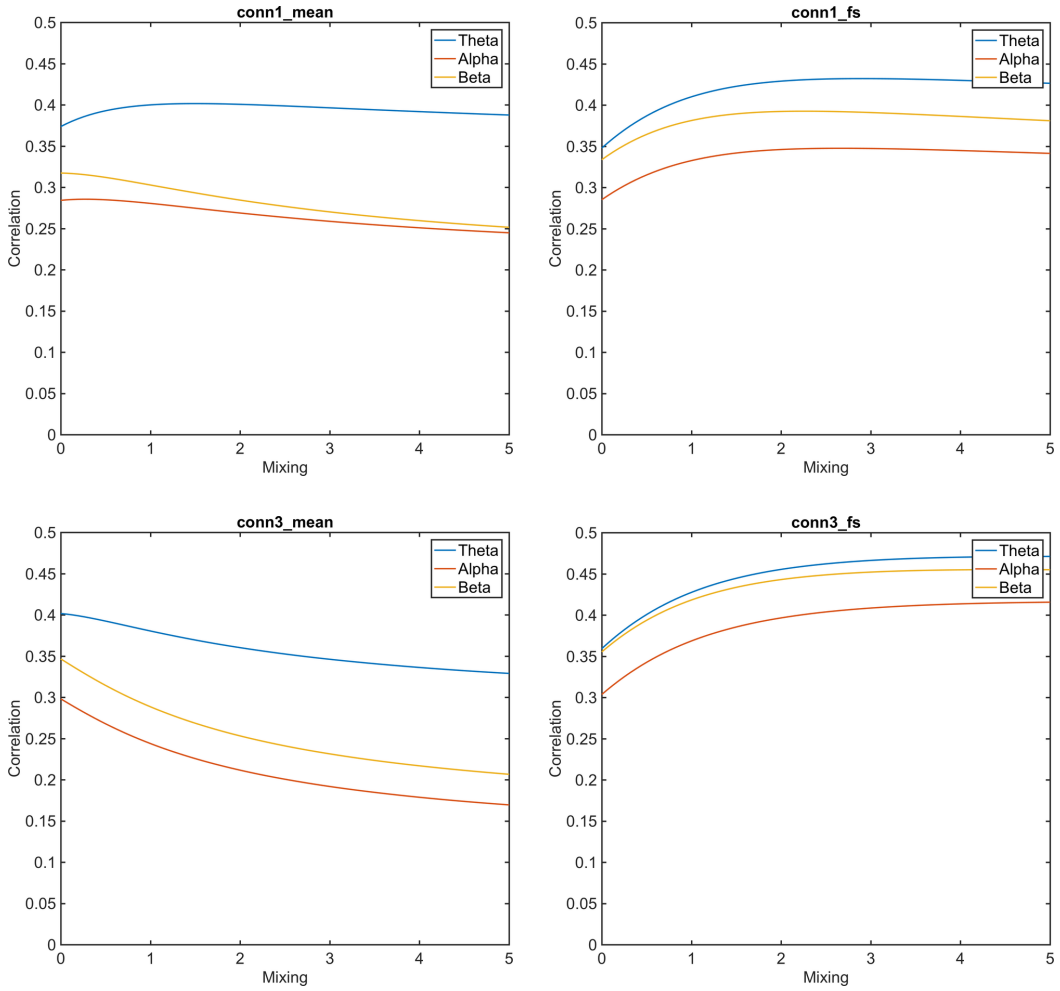

Figure 2.9: The comparison between structure and function improves when considering polysynaptic connections, but with fractional scaling. As previously, each panel corresponds to a different AC matrix, and each curve to a different frequency-band. We show the evolution of the correlation between band-specific MEG resting-state FC, and a structural matrix obtained by the linear mixing $\mathrm{AC} + m\ \mathrm{AC}^2$, where m varies between 0 and 5. Powers of the AC matrix correspond to connectivity scores considering paths with intermediaries between two regions.

3

Large-Scale Biophysical Models

Contents

3.1 Introduction

The purpose of phenomenological models, in a research context, is to formulate mechanistic hypotheses about the underlying causes of some observed phenomenon, in a mathematical form that can be used to generate predictions. These predictions can then be used to rank various hypotheses, depending on how well they match empirical data, and ultimately for a model to gain credence, if the predictions consistently match evidence across different experiments. In the case of resting-state activity (see §1.1.2), the running hypothesis is that it emerges at the macro-scale through the electro-physiological interactions between different brain regions; this is supported by empirical evidence (Greicius et al. 2009; Honey et al. 2009) as well as modelling work (Pinotsis et al. 2013a; Deco et al. 2013).

In this chapter, we present the biophysical models used in our experiments, as well as the methods used to run our simulations. Our main contributions are as follows:

- We provide an original formulation of a stochastic Wilson-Cowan model, and of a mean-field conductance-based model.
- We provide detailed analyses of these models, focusing on the influence of their parameters on key oscillatory features (frequency and amplitude). This perspective will be useful for parameter optimisation in chapters 6 and 7.
- We provide software and numerical methods for the simulation of these models, and we argue that the proposed framework is a lighter, simpler, more performant and more flexible alternative to currently existing software.

3.1.1 Neuronal masses and fields

In the literature, the different large-scale modelling approaches can be grouped into three main categories:

- **Data-driven approaches**: these methods usually borrow from digital signal processing, and summarise key aspects of the observed dynamics (*e.g.* spectral profiles) with few parameters. For example, auto-regressive methods (Harrison et al. 2003; Michalareas et al. 2013) formulate explicit lagged dependencies between successive timepoints, typically in a multivariate fashion in order to capture structural interactions between distant brain regions. Another example is the use of Hidden-Markov Models to study fast-paced "state"-transitions in electro-physiological data (Baker et al. 2014; Vidaurre et al. 2016). Although such approaches are designed to accurately reproduce the observed signals (often under linear assumptions), and can reveal structural dependencies in the data (Messe et al. 2014), they do not provide any insight into the underlying biophysical processes.

- **Neuronal-mass models**: these methods describe the average dynamics of large populations of densely connected neurons, with parametric systems of ordinary differential equations (Vogels et al. 2005; Pinotsis et al. 2014). In comparison with the previous data-driven approaches, these models are phenomenological in nature, and are therefore typically derived from empirical observations, with a concern to remain faithful to the (relevant) underlying biophysics. Importantly, these models are inherently *local*, because they neglect the spatial dependency of the dynamics (*e.g.* due to axonal conduction delays) in order to work with functions of time only. However, large-scale models can be constructed, by considering *networks* of neuronal masses, with vertices summarising the local activity in different brain regions, and with edges representing (delayed) interactions between these regions.

- **Neural-field models**: these methods extend the previous mass-models, by considering brain tissue as a spatial continuum, and brain activity (summarised by properties of interest such as firing-rates) as being governed by integro-differential equations (Bressloff 2003). For example, the activity at each point can be modelled uniformly on the cortical surface by convolution of some function summarising the activity at each point, with a spatial kernel representing the local coupling with neighbouring points (in which case, the kernel would typically be a decreasing function of the distance). More complex models may consider non-linear, non-local, non-uniform and non-instantaneous couplings instead (*e.g.* convolution within some non-linear response-function, and using maps of hyper-parameters for the coupling kernel). The activity of interest generated by such model typically exhibits wave-like phenomena, propagating over the cortical surface at speeds on the order of 10 cm/sec (Bressloff et al. 2015). However, the mathematical treatment of such models requires advanced analytical methods (see part I of Coombes et al. 2014), and their simulation requires more computational power than with (reasonably-sized) networks of neuronal masses. Although quantitative differences between the two have been demonstrated (Pinotsis et al. 2013b), it is unclear whether this added complexity is *required* in order to produce dynamics of interest (see §2.4.4) in large-scale models.

It is also worth noting that large-scale *spiking* models considering very large networks of individual neurons have been attempted (Izhikevich et al. 2008), and are the focus of ongoing research notably with the Human Brain Project (Markram et al. 2011), but their overwhelming complexity precludes any practical exploration of their capabilities.

In our work, we focused on the use of networks of neuronal-masses, as a reasonable compromise between complexity and biophysical pertinence. The general structure of these models is described in Fig. 3.1; in particular, the different brain regions are associated with network **units**, which may themselves be composed of several network

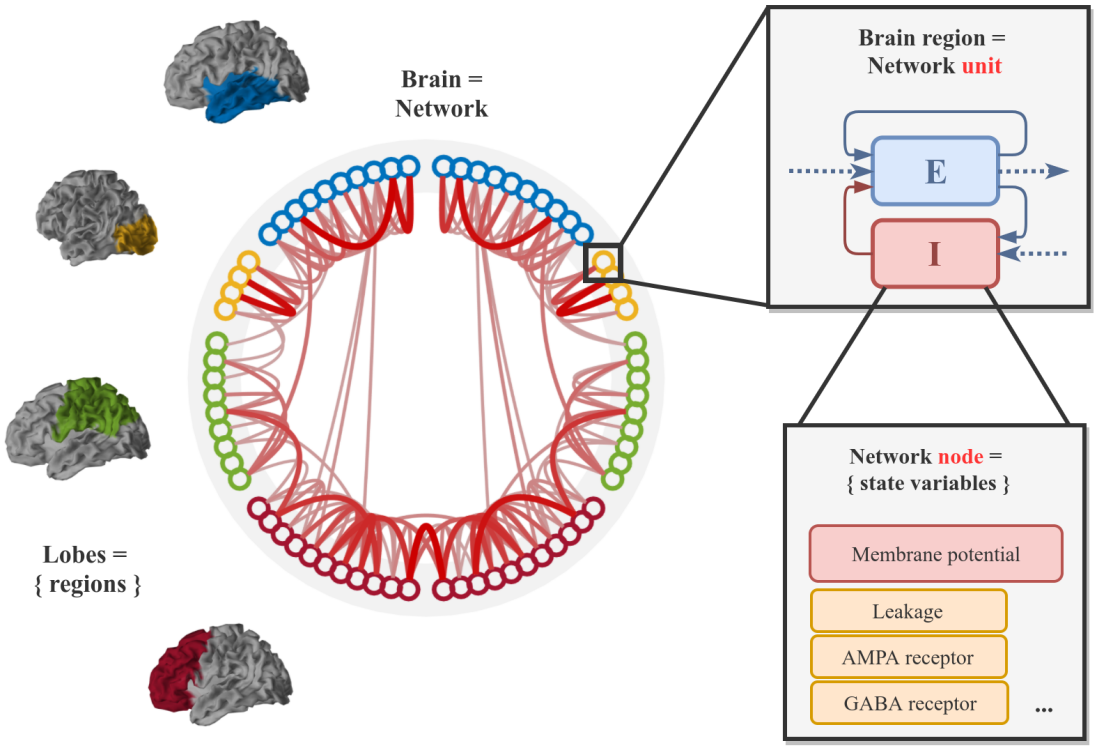

Figure 3.1: Structure of a biophysical network model of the brain. The radial graph at the centre is reproduced from Fig. 2.3, as an example, and shows the strongest anatomical connections in the network (90^{th} percentile, as evaluated by diffusion tractography). Each coloured ring corresponds to a brain region, and each colour corresponds to a lobe (temporal, occipital, parietal and frontal). In the models proposed, each brain region maps to a network *unit*, the dynamics of which are described by a local mass-model, which may consider multiple populations of neurons (*e.g.* excitatory and inhibitory). In turn, each population of neurons maps to a network *node*, the dynamics of which may depend on several *state variables*, describing the evolution of physiological quantities such as: membrane potential, synaptic conductances, *etc*.

nodes associated with different local cell populations.

The models presented below are formulated in terms of ordinary differential equations, which describe the temporal evolution of **state variables** (*e.g.* membrane potential or synaptic conductance) as a function of **inputs**. These inputs can arise either: locally from other cells or cell-populations; globally from distant brain regions; or externally from sensory inputs.

In addition, an artificial level of background-activity is usually included to account for further unknown sources, and to bring the system into (or close to) an oscillatory regime. The biophysical relevance of this artificial input, although usually not modelled

explicitly as such, has to do with the assumption of *homeostasis*; the fact that the brain constantly maintains a balance between spontaneous activity and sensitivity to sensory inputs, while avoiding extreme regimes of inactivity or epilepsy (Muresan et al. 2007; Vogels et al. 2011).

3.1.2 Standard analysis of dynamical systems

The models presented in this chapter are formulated as systems of ordinary differential equations (ODEs), describing the evolution of a set of state variables $X = \{x_1, .., x_n\}$ as a function of inputs $P = \{p_1, .., p_m\}$, where each element in these sets is a scalar function of time. Denoting the temporal derivative as $\partial_t \bullet$, these models can be written in the general form:

$$\partial_t X = F\Big(X, P; \theta\Big) \tag{3.1}$$

where F is the **differential map** (or "right-hand side"), and θ is a set of parameters.

If F is not linear with respect to its first argument X, which is the case for most neuronal models in the literature, the system is said to be **non-linear**. Furthermore in the previous equation, note that F does not depend explicitly on time (although it depends on functions of time); such systems of ODEs are called **autonomous**. In particular, it would be wrong to assume that X could be replaced with $X(t)$ in this equation, because the parameters θ may include delays, as we will see below when studying network models.

If there are multiple state-variables in Eq. 3.1 (*i.e.* if $n \geq 1$), any solution of this system is a multi-variate function of time, the value of which at timepoint t corresponds to the vector-valued **state** $\Big[x_1(t), .., x_n(t)\Big]$. For given inputs P and parameters θ, the function $F(X, P; \theta)$ maps the state-space to a vector field describing the **trajectories** of the solutions. The geometric properties of these trajectories are constrained by the **nullclines** of the system, which correspond to the state-subspaces in which individual

coordinates of $F(\bullet, P; \theta)$ are zero; therefore, when crossing a nullcline, one of the derivatives $\partial_t X_k$ changes sign for some k, and the corresponding trajectories reverse course with respect to the k^{th} state-variable.

Studying the behaviour of such a model consists in identifying qualitative changes in the trajectories of the solutions as a function of P and θ; that is, looking at how they affect the structural properties[1] of the vector field described by F.

The values of P and θ for which such structural changes occur are called **bifurcation points**, and can be determined via bifurcation analysis. These structural changes can either be local or global; that is, either confined to a particular region of the state-space, or extending throughout the entire space. The detection of global bifurcations is arduous and will not be discussed here; see section 2.3 of (Gros 2015) for an introduction, and chapter 8 of (Meiss 2007). Local bifurcations, on the other hand, can be detected relatively easily using stability analysis, which can be summarised as follows:

- Find the set of fixed-points $\mathcal{X}_0 = \{X_{0,1}, .., X_{0,p}\}$ of the system by solving $F(X, P; \theta) = 0$ for X;
- Evaluate the Jacobian matrix of the system, defined as $J = \left[j_{i,k}\right]$ with $j_{i,k} = \partial_{x_k}(\partial_t x_i)$, at the previous fixed points, and determine its (complex) eigenvalues;
- Find the values of P and θ for which the real part of any eigenvalue changes sign.

Although this analysis provides *some* characterisation of the dynamical behaviour of the model[2], by delineating the different regimes of the system in terms of controlled parameters, it does not offer any particular insight about the effect of these parameters on simple oscillatory features (when applicable), such as the frequency mode or amplitude of the oscillations. Therefore, it is of limited interest in the context of large-scale brain activity modelling.

[1] By "structural properties" here, we refer to the "shape" of the trajectories. For example, whether these trajectories describe a cycle, a parabola, a hyperbola, converge to a single point or diverge from it, *etc*. Such properties can be analysed with algebraic geometry in the case of linear systems for example.

[2] The MatCont toolbox (Dhooge et al. 2008) can be used in Matlab to carry out such analysis.

3.1.3 Analysis of oscillatory systems

As discussed previously in §2.4.4, the electro-physiological measurements of brain activity are oscillatory in nature. These oscillations result from interactions between excitatory and inhibitory populations of neurons, as we will see later on in this chapter. It is therefore relevant to introduce a suitable mathematical formalism for representing oscillatory signals.

For a given real-valued signal $s(t)$, the corresponding **analytic signal** is a complex-valued function of time:

$$\forall t, \quad s_a(t) = s(t) + i\,\mathcal{H}[s](t) = A(t)e^{i\varphi(t)} \tag{3.2}$$

where $i = \sqrt{-1}$, $\mathcal{H}[s](t)$ is the Hilbert transform[3] of s, A is the **envelope**, and φ the **instantaneous phase**.

The definition of the instantaneous phase can also be used to define the instantaneous *frequency* of the signal — we will come back to this in §4.2.1. For now, the point is that amplitude, frequency and phase are the main features of interest when dealing with oscillatory signals, and therefore we should analyse the influence of model parameters on these features. In the following sections, we provide a minimal analysis of the state-space for each model, looking at the nullclines and the trajectories of typical solutions, but we focus mainly on characterising the effects of controlled parameters on the oscillatory behaviour. Specifically, we look for mechanisms of frequency and amplitude modulation at the local level, which will be useful later on, when we optimise these parameters at the whole-brain level.

[3] For reference, the Hilbert transform of a signal s is defined as the convolution between s and the kernel $h(t) = 1/\pi t$. In practice, it is never computed as such, but rather by inverse Fourier transform, given the following property:

$$\mathcal{F}[\mathcal{H}[s]](\omega) = -i\ \mathrm{sign}(\omega)\ \mathcal{F}[s](\omega)$$

where $\mathcal{F}$ denotes the Fourier transform and ω denotes the frequency (in rad/sec).

3.2 Kuramoto Model

The Kuramoto oscillator is one of the simplest oscillatory systems in the literature (Kuramoto 1984). It was originally introduced to study synchronisation events in very large systems of coupled oscillators, during which the entire system would lock (on average) to a single oscillatory frequency (Strogatz 2000).

In its basic form, the model considers the interactions between N oscillators defined only by their phase θ (in radians), and parametrised with an intrinsic oscillatory rate ω (in rad/sec). This means that each oscillator spontaneously oscillates at $\omega/2\pi$ Hz, and interactions between oscillators are modelled as additive frequency-modulating perturbations[4]:

$$\forall 1 \leq k \leq N, \quad \partial_t \theta_k = \omega_k + \frac{K}{N} \sum_{i=1}^{N} c_{ik} \sin\left(\theta_i - \theta_k\right) \tag{3.3}$$

where K is a global coupling coefficient, and $c_{ik} \equiv c_{i \to k}$ is a coupling coefficient from unit i to unit k.

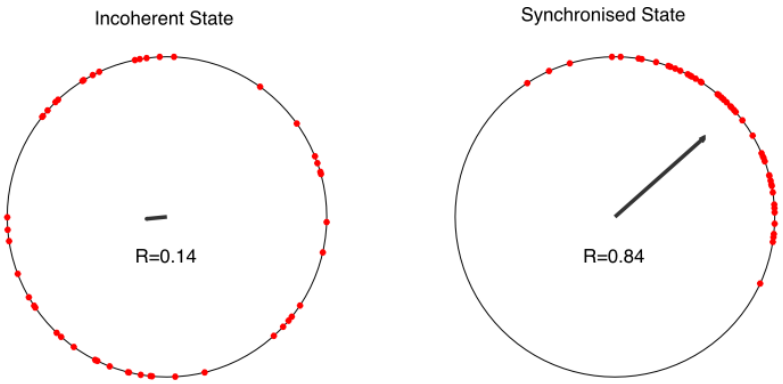

Figure 3.2: Illustration of the Kuramoto synchrony (see Eq. 3.4) in an incoherent and partially synchronised state (left and right, respectively). The red dots correspond to the points $e^{i\theta_k}$, where $k = 1..50$ in each case; we took $\theta \sim \mathcal{U}(0, 2\pi)$ on the left, and $\theta \sim \mathcal{N}(\frac{\pi}{4}, \left(\frac{2\pi}{10}\right)^2)$ on the right, as simple examples of phase distributions. Higher synchrony values correspond to more closely "clustered" phases.

[4]Note that when solving these equations, the state variables should be constrained to the interval $[0, 2\pi)$ to ensure numerical stability.

Synchronisation events in the previous system are studied using a measure of **synchrony** (also called the "order" parameter), defined as:

$$R = \left| \frac{1}{N} \sum_{k=1}^{N} e^{i\theta_k} \right| \tag{3.4}$$

In this sum, each term is a complex number with modulus 1, and can therefore be represented by a point on the unit circle at angle θ_k. Visually, R is then simply the magnitude of the barycentre of these points, which is 1 when the spread of $\{\theta_k\}$ around the circle is null (all oscillators are perfectly synchronised), and decreases towards zero when the spread increases, or if oscillators are in phase opposition. The state of the system for which no two oscillators are synchronised is called *incoherent*, and those for which not all oscillators are synchronised are called *partially synchronised*. An illustration of this is provided in Fig. 3.2.

3.2.1 Application to neural modelling

It is known (Schröder et al. 2017) that for a system of Kuramoto oscillators with all-to-all coupling (*i.e.* $c_{i,j} = 1$ for all i, j), and a unimodal symmetric distribution of frequencies, two critical coupling thresholds $K_L \geq K_C$ exist, such that at least two oscillators synchronise for $K \geq K_C$, and all oscillators synchronise for $K \geq K_L$. Synchronisation in the case of an arbitrary distributions of intrinsic frequencies and coupling weights has also been studied in (Jadbabaie et al. 2004). Furthermore, it is also known (Yeung et al. 1999) that considering uniformly delayed interactions (*i.e.* with the substitution $\theta_i \mapsto \theta_i(t - \delta)$ in Eq. 3.3) enhances the behavioural landscape of this model; in particular, a bistable equilibrium exists, in which the system alternates between synchronised and incoherent states.

The Kuramoto model with non-uniform delays (*i.e.* with the substitution $\theta_i \mapsto \theta_i(t - \delta_{ij})$) has been applied previously to the modelling of resting-state activity in MEG (Cabral et al. 2014b), taking $\sin(\theta_k)$ as the simulated signal in brain region k, and looking for correspondence between simulated and empirical functional connectivity across frequency-bands. The authors found a range of coupling values, and average delay between units, for which the correspondence was locally optimal (although it was relatively low overall), which was consistent with previous modelling work looking at the effects of delay and coupling on such systems (Deco et al. 2009).

Despite the questionable biophysical relevance of the Kuramoto model in neuroscience (*e.g.* how to interpret the *phase* of a brain region?), it occupies a central place in the theory of **phase-reduction**, which is concerned with the study of synchronisation properties in systems of non-linear coupled limit-cycle oscillators (Nakao 2017). Specifically, phase-reduction methods aim at capturing essential properties of the local oscillatory dynamics (natural frequency and phase-response) with a single *phase* variable. In turn, this simplified formulation allows a direct parallel with the Kuramoto model, and hence enables the analytical treatment of questions regarding synchronisation typically asked in this context.

Nevertheless, synchronisation is not the only feature of interest when looking at brain activity. For example, there is no explicit formulation of amplitude dynamics, which is an important aspect of empirical measurements (see §2.4.4). In the following sections, we explore more detailed models brain activity.

3.3 Wilson-Cowan Model

In contrast with the Kuramoto model presented previously, the Wilson-Cowan model (Wilson et al. 1972, hereon abbreviated WC) is a phenomenological attempt at explaining the electro-physiological oscillations observed empirically, as a result of cycles of excitation and inhibition in large populations of neurons. Below, we analyse the local equations of this model (which describe the activity within a brain region), and extend it to a network of interacting regions with propagation delays.

3.3.1 Local equations

The local equations are formulated, for each population of neurons (excitatory or inhibitory), in terms of the normalised amount of cells firing at each timepoint. The local interactions between excitation and inhibition are regulated by means of **coupling factors** (related to the distribution of synaptic connections within and between the two populations), and the average contribution of pre-synaptic to post-synaptic activity is summarised by a so-called **subpopulation response function**, defined as the cumulative distribution of firing-thresholds within each population of neurons.

This distribution of firing-thresholds is generally assumed unimodal and symmetric (see Fig. 3.3), leading to a sigmoidal cumulative function. In practical terms, this function represents the expected response of an initially quiescent population of neurons to an external input, and is modelled as a logistic sigmoid:

$$\forall x \in \mathbb{R}, \quad \mathcal{S}(x;\, \mu, \sigma) = \frac{1}{1+e^{-\hat{x}}} \qquad \hat{x} = \frac{x-\mu}{\sigma} \tag{3.5}$$

where μ represents the response threshold, and σ controls the width of the dynamic input-range. The choice of a different sigmoid function did not affect the qualitative behaviour

[5]The data can be found at: http://www.neuroelectro.org/ephys_prop/7/data/

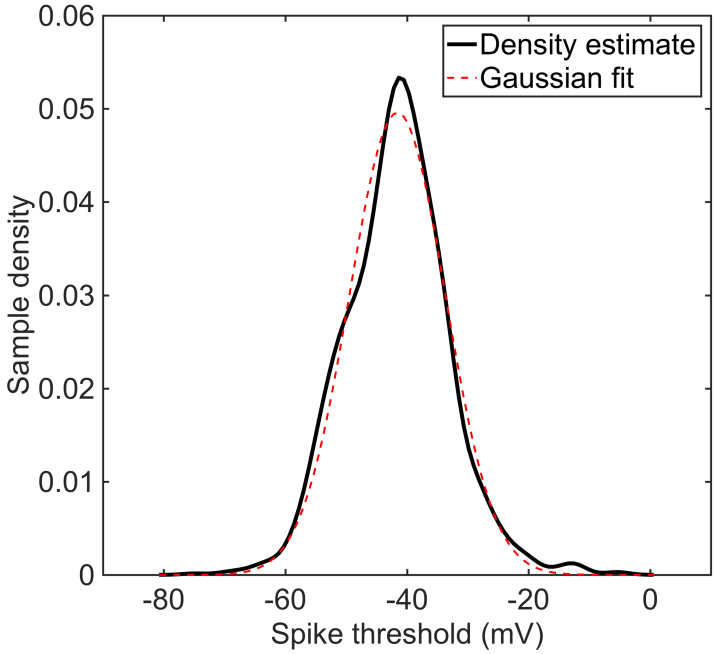

Figure 3.3: Density estimate of spiking-threshold using 1376 samples extracted[5] from the NeuroSynth database (Tripathy et al. 2014), and Gaussian fit ($\mu = -41.6\text{mV}, \sigma = 7.9\text{mV}$). The estimated density is unimodal, but not exactly symmetric. The *subpopulation response function* introduced in the Wilson-Cowan model, and indeed used in most models of neuronal-masses, is a surrogate for the corresponding cumulative density.

of the model in our experiments, but for reference, we provide several alternative choices in Apdx. A.1 (we also propose an original, non-symmetric variant, which may be used to encode asymmetries in the population response function).

Let $E(t)$ denote the ratio of excitatory neurons firing at time t within a brain region (resp. $I(t)$ for inhibitory neurons). The Wilson-Cowan model states that:

$$\begin{aligned} \tau_e \partial_t E &= -E + (1 - r_e E)\mathcal{S}_e\Big(c_{ee}E + c_{ie}I + P_e\Big) \\ \tau_i \partial_t I &= -I + (1 - r_i I)\mathcal{S}_i\Big(c_{ei}E + c_{ii}I + P_i\Big) \end{aligned} \tag{3.6}$$

where lower-case e, i subscripts refer to the excitatory and inhibitory subpopulations, respectively; $\tau_{e,i}$ are decay times; $r_{e,i}$ are refractory periods; $c_{xy} \equiv c_{x \to y}$ is the directional coupling of subpopulation x affecting y; $\mathcal{S}_{e,i}$ are the subpopulation response functions; and $P_{e,i}$ are external inputs controlling the excitability of each subpopulation.

Notice that, although the equations are identical for both subpopulations, the inhibitory coupling coefficients c_{ie} and c_{ii} must be **non-positive** (by definition), while the excitatory coefficients c_{ee} and c_{ei} must be positive, which breaks the apparent symmetry between excitation and inhibition. Furthermore, as noted in (Srinivasan et al. 2013), the factor $(1-rX)$ with $X \in \{E, I\}$ is dimensionally incorrect (X and $\mathcal{S}$ are non-dimensional, but r represents a time-constant), and in practice, r is often set either to 0 or 1 in these equations. However, for the sake of completeness, we keep r in the following analysis as a non-dimensional parameter, taking values in $[0, 1]$ and acting as an **amortisation** constant for the amplitude of the response function.

In summary, each WC unit is composed of two populations of neurons (excitatory and inhibitory), each described by one state variable, and fully determined by **seven** parameters: decay time τ; coupling factors c_{xx} and c_{xy} for $x, y \in \{e, i\}$; response parameters μ and σ; amortisation r and input P.

3.3.1.1 Nullclines and normalisation

As mentioned previously in §3.1.2, the nullclines of a system allow us to characterise the shape of the trajectories in phase-space, and hence the shape of the oscillations when applicable. The nullclines of system 3.6 are obtained by setting $\partial_t E = \partial_t I = 0$:

$$\begin{aligned} c_{ie} I &= -c_{ee} E - P_e + \mathcal{S}_e^{-1}\left(\frac{E}{1 - r_e E}\right) \\ c_{ei} E &= -c_{ii} I - P_i + \mathcal{S}_i^{-1}\left(\frac{I}{1 - r_i I}\right) \end{aligned} \tag{3.7}$$

where

$$\forall x \in (0,1), \quad \mathcal{S}^{-1}(x;\, \mu, \sigma) = \mu + \sigma \ln\left(\frac{x}{1-x}\right) \tag{3.8}$$

is the inverse logistic function (*c.f.* Tab. A.1).

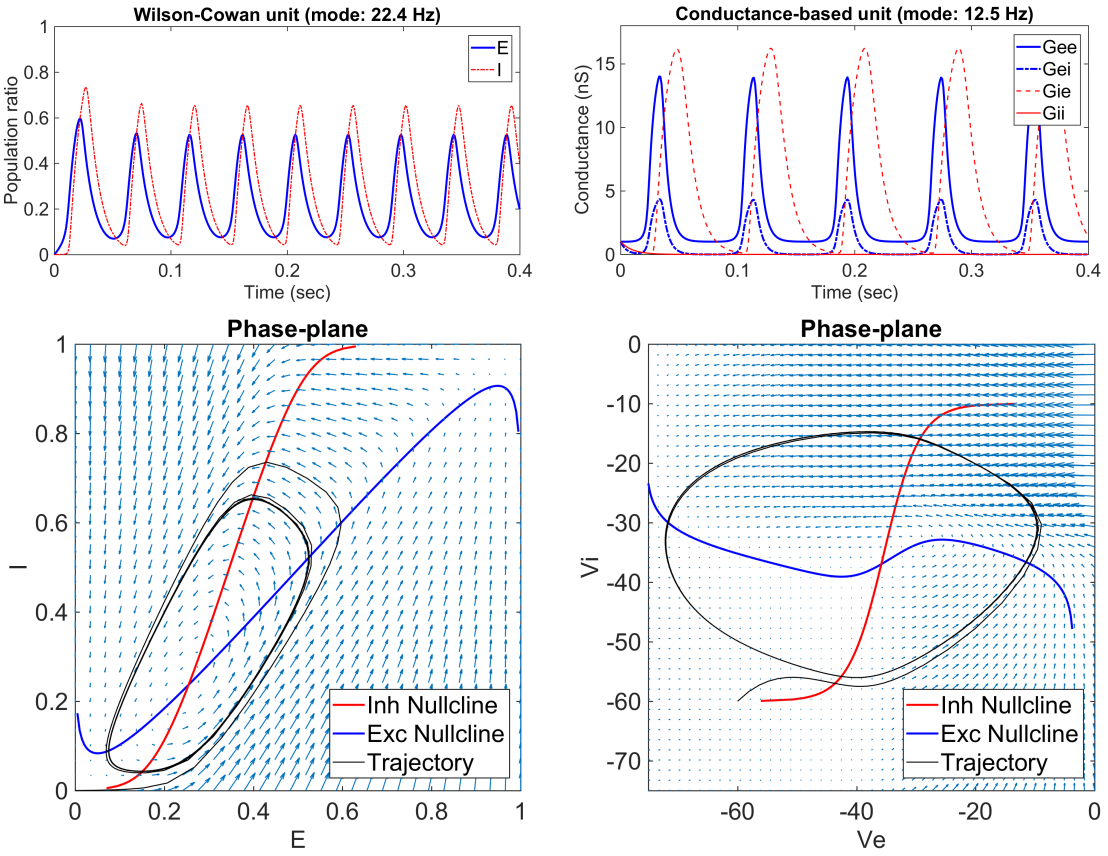

Figure 3.4: Phase-space and example time-courses for the Wilson-Cowan and conductance-based models. The nullclines (blue for excitatory, red for inhibitory) are shown in the bottom-row, as well as a typical oscillatory trajectory (black). The corresponding time-courses are shown in the top row. The Wilson-Cowan model (left) describes the evolution of the ratio of neurons firing at each timepoint separately within an excitatory or inhibitory local subpopulation of neurons. The conductance-based model (right) proposes a biophysically plausible mechanism of oscillations in terms of average membrane potentials and synaptic conductances. Note that the trajectory in the conductance-based model is projected onto the subspace of membrane potentials, and therefore the progression along this trajectory may not be fully explained by the surrounding vector field.

Each of the previous nullclines is a (non-linear) parametric curve in the two-dimensional state-space of the WC model, and these curves may or may not intersect with each-other, depending on their shape and location (controlled by the various parameters), and given their limited domain of definition (constrained by the inverse sigmoid). For example, it is easy to see that the input parameters P_e and P_i act as **translations** parallel to the I and E axes, respectively.

Furthermore, the domain of definition of each nullcline can be expressed in terms of the state variables E and I, by substituting the argument of $\mathcal{S}^{-1}$ in Eq. 3.7 into the logarithmic term in Eq. 3.8:

$$\forall x \in \left(0, \frac{1}{r+1}\right), \quad \mathcal{S}^{-1}(x;\, \mu, \sigma) = \mu + \sigma \ln\left(\frac{x}{1-(r+1)x}\right) \tag{3.9}$$

showing that the domain of definition shrinks as the amortisation r becomes larger. As a consequence, larger values of r effectively limit the range of values accessible to the state variables, and hence the amplitude of the oscillations (if any).

Stable oscillatory regimes are characterised by the presence of closed trajectories, or **limit-cycles**, which in general are not constrained to be either circular or planar. However in two dimensions, these trajectories are necessarily planar, and must enclose a fixed-point located (by definition) at the intersection between the nullclines. An example of such a limit cycle is given in Fig. 3.4.

Finally, note that $\mathcal{S}^{-1}$ is linear in μ and σ, and therefore the nullclines remain unchanged for any simultaneous rescaling of parameters $\{c_{xx}, c_{yx}, P_x, \mu_x, \sigma_x\}$ with $x, y \in \{E, I\}$. We use this degree of freedom within each subpopulation in order to **normalise** the parameters of WC units, specifically:

- we rescale the excitatory parameters by a factor $1/P_e^*$, where P_e^* is defined as the *oscillatory input threshold* (calculated for $P_i = 0$), such that the normalised unit is silent for $P_e < 1$, and oscillating for $P_e \geq 1$;

- we rescale the inhibitory parameters to ensure $\mu_i^{\text{norm}} = \mu_e^{\text{norm}}$, in order to align the responses of both subpopulations.

We propose **four** different choices of unit parameters in Tab. 3.1, and compare the oscillatory behaviour of these units in the next section.

Name	A		B		C		D	
	E	I	E	I	E	I	E	I
μ	4.1	4.1	3.1	3.1	3.1	3.1	4.9	4.9
σ	0.8	0.6	0.6	0.6	0.7	0.7	0.8	0.8
$\lvert c_{xx} \rvert$	16.5	3.3	11	0	11.1	0	45.9	0
$\lvert c_{xy} \rvert$	16.7	12.4	9.2	12.3	5.5	22.2	11.5	57.4
τ	8	8	10	10	5	10	10	10
r	1	1	0	0	0	0	0	0

Table 3.1: Table of normalised Wilson-Cowan parameters for four units (each with a different choice of parameter values), denoted A-D. Each configuration has two columns; left for the excitatory, and right for the inhibitory subpopulation. All parameters are normalised such that the oscillatory input threshold $P_e^* = 1$, and $\mu_e = \mu_i$, and times are given in milliseconds. Unit A corresponds to the parameters given in the original paper (Wilson et al. 1972). Example time-courses can be found in Apdx. A.2.

3.3.1.2 Effect of parameters

We studied the oscillatory behaviour of the WC units given in Tab. 3.1, by varying the excitatory input P_e against particular degrees of freedom listed below, one at a time, and fixing all other parameters. For each combination of parameters, a simulation of time-length equivalent to $120\tau_e$ was run by solving Eq. 3.6, and the interval $[0, 50\tau_e)$ was discarded to ignore transient effects due to the initial conditions, taken as $(E = 0, I = 0)$ in all simulations. The standard deviation and frequency mode of the truncated excitatory time-course were computed, and visualised as a surface-plot in which:

- the x and y axes correspond respectively to the degree of freedom controlled, and the excitatory input P_e;
- the z axis corresponds to the measured standard-deviation;
- the colour corresponds to the the measured frequency mode.

We identified **nine** degrees of freedom (d.o.f.), each affecting one or several parameters at a time:

(D1) scaling all coupling factors, or (D2) only the excitatory ones c_{ee} and c_{ei};

(D3) varying the ratio $c_{ei}/(c_{ee}+c_{ei})$, by controlling c_{ei};

(D4) scaling both sigmoid parameters μ and σ independently within each subpopulation;

(D5) varying the ratio σ/μ in both subpopulations, by controlling σ in each;

(D6) varying the inhibitory input P_i;

(D7) varying the excitatory decay-time τ_e, while maintaining the ratio τ_i/τ_e constant;

(D8) varying the ratio τ_i/τ_e by controlling τ_i;

(D9) and finally varying both amortisation parameters r_e and r_i between 0 and 1.

The results are presented in figures 3.5, 3.6 and 3.7. For completeness, we also provide a one-parameter bifurcation diagram (controlling P_e) in Apdx. A.3. The role of each d.o.f. listed above was consistent across all four units (A,B,C,D), although the profiles of standard-deviation and frequency mode were all noticeably different. These results can be summarised by grouping the d.o.f. in terms of their effect on the *shape* of the amplitude response, or the range of *frequencies*:

- Affecting both shape and frequency: (D2,D3,D5,D9)
- Mainly affecting shape: (D1,D4,D6)
- Affecting frequency only (D7), or frequency and amplitude of oscillations (D8).

This analysis can be used to control specific aspects of the local dynamics, and study their effect at the whole-brain level, when connecting multiple brain regions into a large-scale network. In particular: the range of frequencies can be controlled by scaling both time-constants (D7); shifting τ_i alone also affects the amplitude of the oscillations (D8); the

width of the oscillatory range can be modulated by scaling the coupling coefficients (D1); and the slope of the amplitude response by shifting the inhibitory input, P_i (D6).

Of course, there is no telling how these degrees of freedom might affect the overall dynamics in a network of coupled Wilson-Cowan units, due to the complexity of the system; indeed, this is a particular instance of **emerging** dynamics, and the facts that this system is non-linear, and infinite-dimensional (due to the presence of delays, we will come back to this in §3.5.2.2), makes general analytical predictions infeasible.

3.3.2 Large-scale network model

Extending the previous local equations to a network of interacting brain regions consists in adding coupling terms from those remote regions into the subpopulation response function. The general *node* equation (whether excitatory or inhibitory) in a network of N brain *units* (see Fig. 3.1) therefore becomes:

$$\forall\, 1 \leq k \leq 2N, \quad \tau_k \partial_t X_k = -X_k + (1 - r_k X_k)\, \mathcal{S}_k \left(\sum_{j=1}^{2N} c_{jk} X_j(t - \lambda_{jk}) + P_k \right) \tag{3.10}$$

with the convention that odd indices (*i.e.* $k \in 2\mathbb{N}+1$) correspond to excitatory nodes (resp. even indices for inhibitory nodes), and $X_k(t)$ is the ratio of neurons firing at time t in node k (analogous to the previous state-variables E and I). In this equation, we also introduced **delay** parameters $\lambda_{jk} \equiv \lambda_{j \to k} \in \mathbb{R}_+$ to account for propagation times between distant brain regions, mainly due to axonal conduction and synaptic transmission. These delays typically range from hundreds of microseconds to tens of milliseconds at long-range (highly dependent on the temperature, see Sabatini et al. 1999), and since they are of the same order of magnitude as the decay times of the WC units, they interfere with the local dynamics and cannot be neglected.

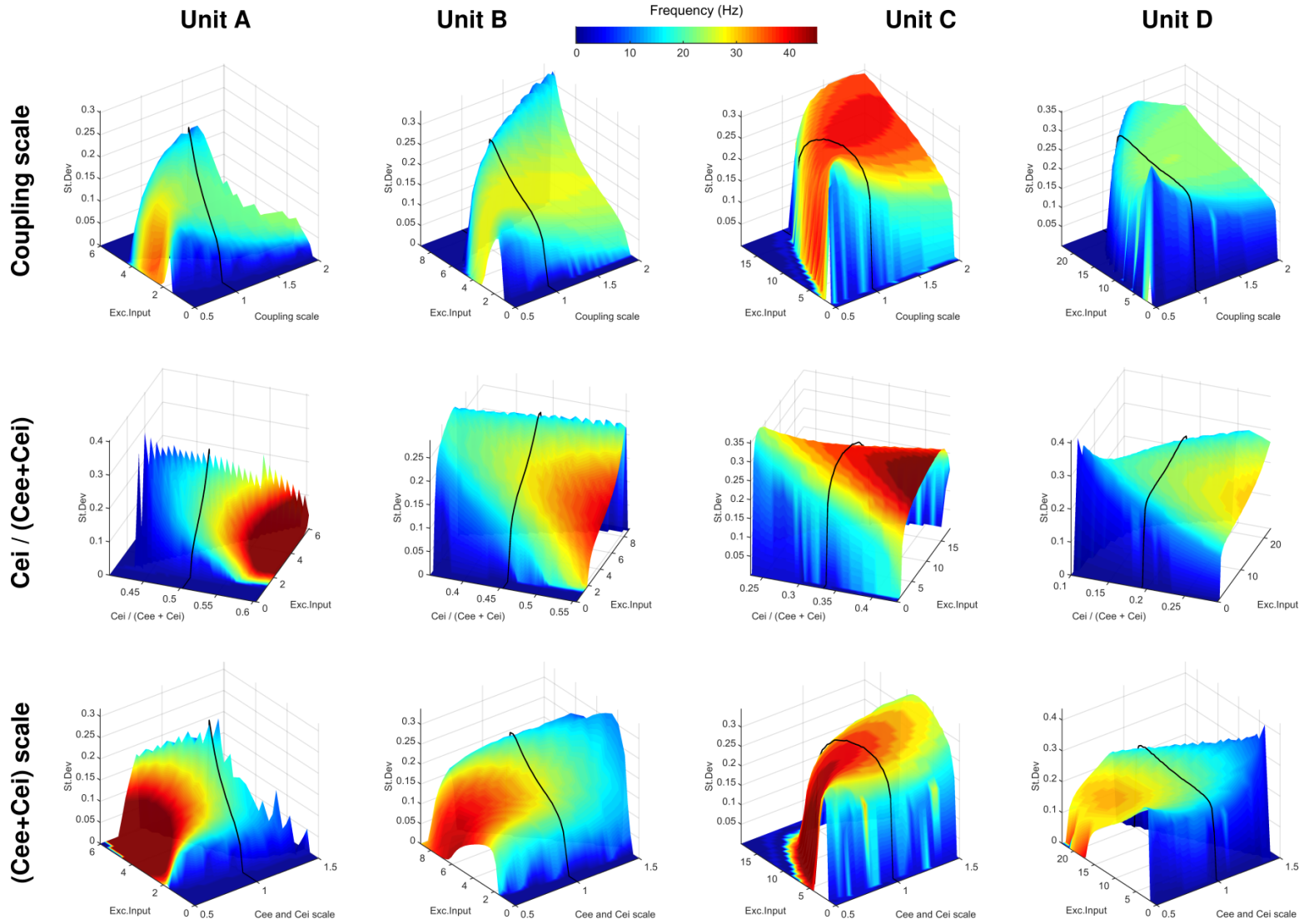

Figure 3.5: Effect of coupling parameters on the oscillatory dynamics of WC units. Black lines indicate baseline values as shown in Tab. 3.1. **Row 1:** the coupling scale (D1) affects mainly the width of the amplitude response, and activity vanishes quickly for low scales. **Row 2:** the E-to-I coupling ratio (D3) affects the width and frequencies of the oscillatory range. **Row 3:** the excitatory coupling scale (D2) affects mainly the frequencies of the oscillatory range.

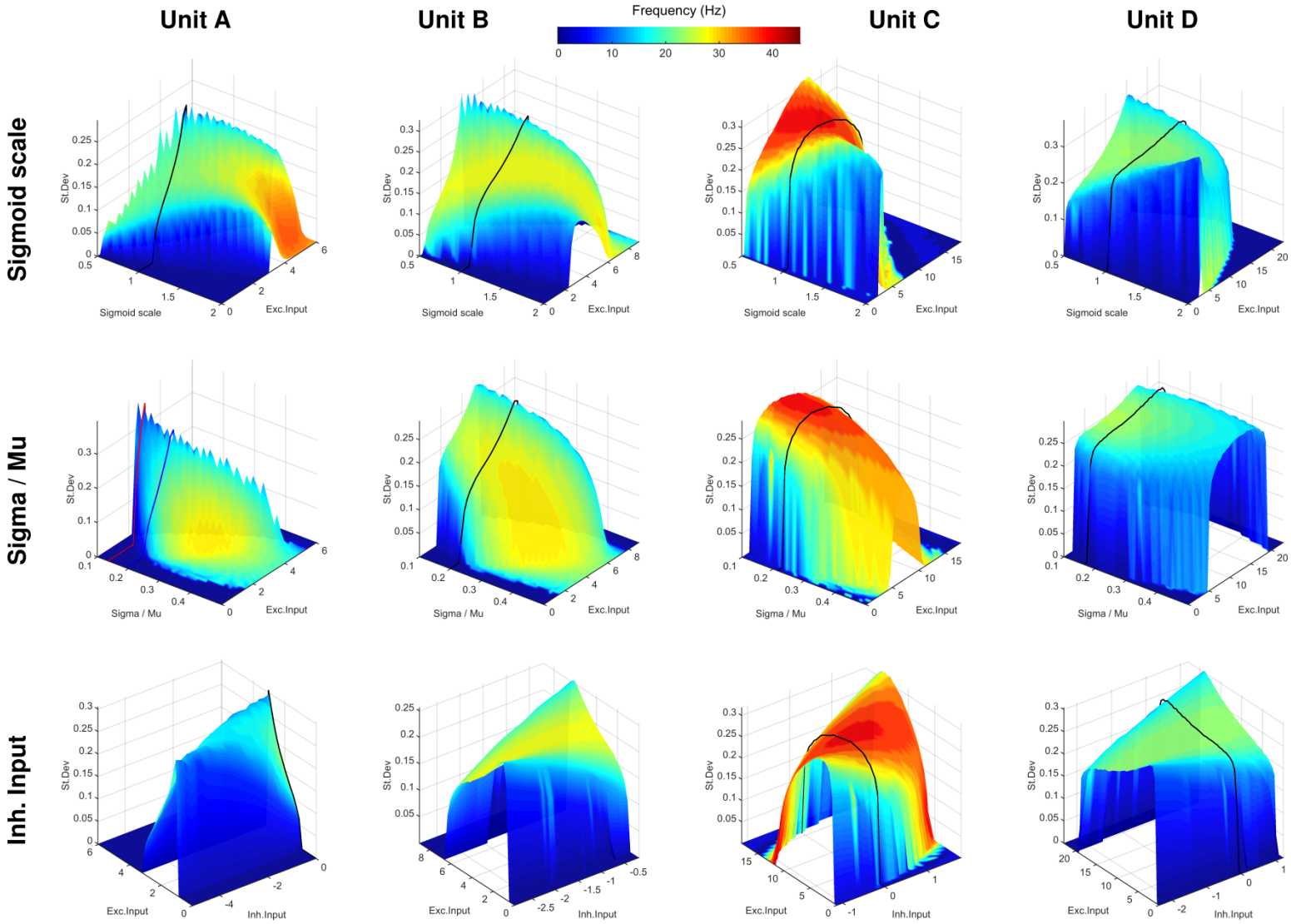

Figure 3.6: Effect of sigmoid parameters and inhibitory input on the oscillatory dynamics of WC units. Black lines indicate baseline values. **Row 1:** the scale of sigmoid parameters (D4) affects the shape, width, and location of the amplitude response. **Row 2:** the ratio σ/μ (D5) affects the frequency range and the width of the amplitude response. **Row 3:** the inhibitory input (D6) was varied implicitly, by controlling the value of the inhibitory nullcline (*c.f.* Eq. 3.7) at $E = 0.5$ between 0.1 and 0.9. It affects the slope of the amplitude response, which is null for $I(E = 0.5) = 0.5$.

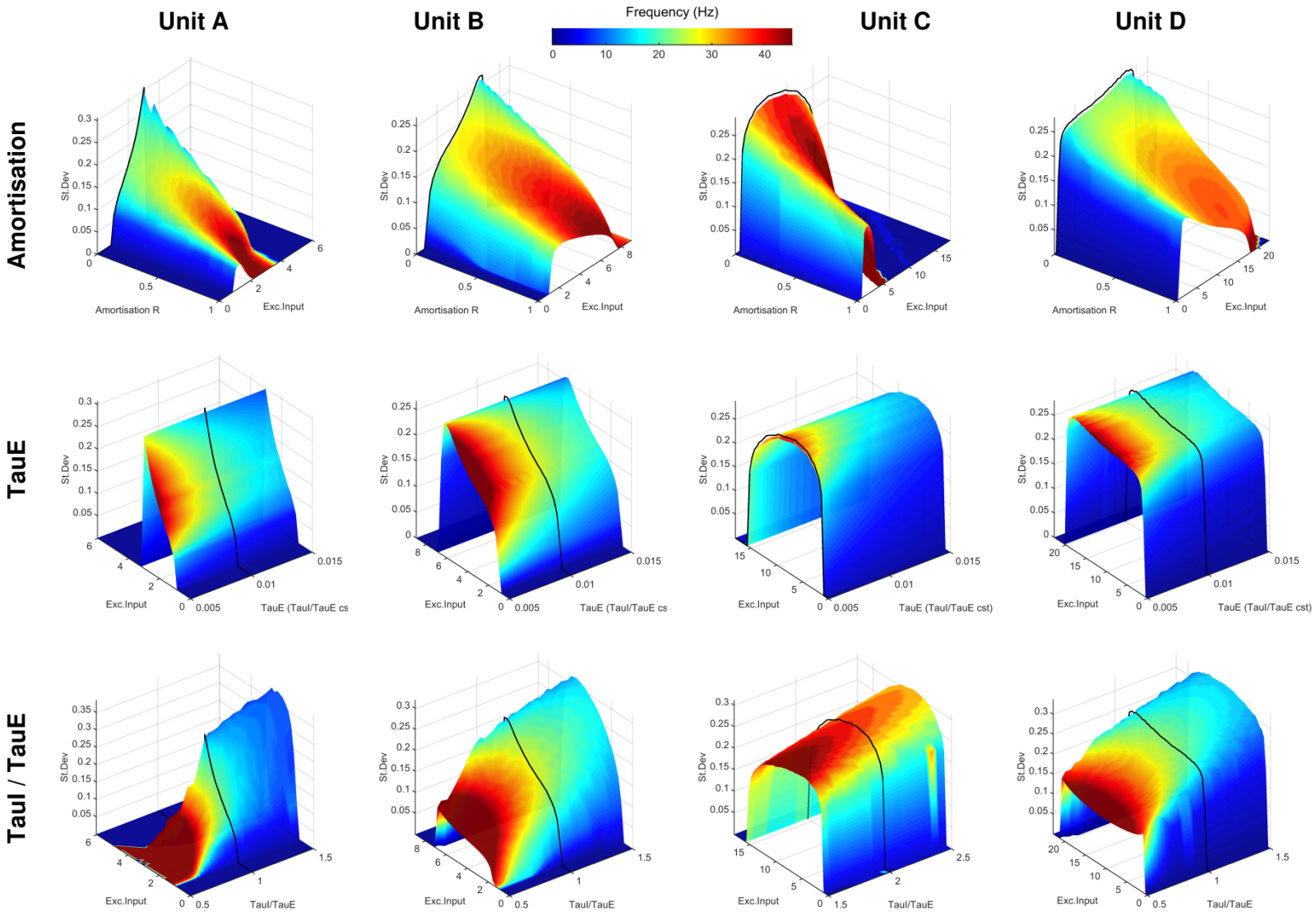

Figure 3.7: Effect of decay times and amortisation on the oscillatory dynamics of WC units. Black lines indicate baseline values. **Row 1:** the amortisation (D9) affects the frequency as well as the shape and width of the amplitude response. **Row 2:** the excitatory decay time (D7) only affects the frequencies of the oscillatory response. **Row 3:** the ratio τ_i/τ_e (D8) affects the frequency and the amplitude of the oscillations (dramatically so for all units except C).

3.3.2.1 Stochastic inputs

We dedicate a section to the inclusion of noise into the previous equations; to our knowledge, the following derivation has not been detailed previously, although there is an abundant literature about the effects of added randomness on neuronal dynamics (**Medvedev2010**; Touboul et al. 2011; Freyer et al. 2011; Bressloff 2010).

There is an issue with the common intuition that adding noise to the right-hand side of a differential system should not fundamentally alter the meaning of these equations. Differentiability relies fundamentally on the assumption of local linearity, but this assumption does not hold for a stochastic function f if the difference between two arbitrarily close timepoints $f(t)$ and $f(t+h)$ does not depend on h (*e.g.* in the case of point-wise white noise). In particular, the ratio $(f(t) - f(t+h))/h$ may not converge when h tends to 0, and in that case writing $\frac{\mathrm{d}f}{\mathrm{d}t}$ is meaningless.

There is also an issue from the perspective of numerical integration; even if the noise process is such that the distribution of $\left\{f(t+h) - f(t)\right\}_t$ depends on h (*e.g.* time-correlated noise), then the choice of a particular time-step for integration may affect the solution obtained. On the other hand, sampling the noise process independently at any timepoint during the integration defeats the purpose of numerical methods taking intermediate steps to increase their precision (*e.g.* Runge-Kutta methods). In fact the idea of *convergence* itself — the fact that numerical solutions become arbitrarily close as we reduce the time-step — is inadequate in the case of stochastic equations.

In summary, including noise into a system of differential equations is not a trivial operation. Stochastic calculus is a mathematical field of its own, aiming to give meaning to operations such as integration and derivation in the presence of noise, along with numerical methods. Notable tools employed previously in neuroscience include: the Fokker-Planck formalism (Breakspear 2017; Deco et al. 2013; Brunel 2000), which models the evolution of probability densities over time as a diffusion process in the

state-space; and the Euler-Maruyama method (Jirsa et al. 2013; Touboul et al. 2011), which is a simple adaptation of the Euler method to the stochastic case.

An excellent introduction to the use of **stochastic differential equations** (SDE) can also be found in (Higham. 2001). For brevity, we summarise the key points below:

- The standard **Wiener process** (a.k.a. random-walk or Brownian motion) is a stochastic process with normally distributed increments, such that:

$$\forall t > s, \quad W(t) - W(s) \sim \sqrt{t-s}\,\mathcal{N}(0,1) \tag{3.11}$$

  where $W(t)$ denotes a random variable, which depends on previous timepoints (though increments are independent), and $\mathcal{N}$ is the normal distribution. Therefore, Gaussian noise on the right-hand side of a differential equation can be interpreted as increments of a Wiener process.

- The Riemann sum can be used to define integration with respect to a stochastic process (under certain conditions):

$$\forall f, \quad \int_0^T f(t)\,\mathrm{d}W(t) = \lim_{N\to\infty} \sum_{k=0}^{N-1} f(t_k)\,(W(t_{k+1}) - W(t_k))$$

  where $t_k = kT/N$ and W is a Wiener process.

- The previous definition leads to the **Itô form** of SDEs, which is written as:

$$\mathrm{d}X = D(X)\mathrm{d}t + V(X)\mathrm{d}W \tag{3.12}$$

  where D and V are called respectively the *drift* and *volatility* functions; X is a (multidimensional) stochastic state-variable; and $\mathrm{d}W$ denotes the infinitesimal increment of a Wiener process. In particular, note that we cannot write $\frac{\mathrm{d}W}{\mathrm{d}t}$, because W is nowhere differentiable.

Coming back to the Wilson-Cowan model; adding noise to Eq. 3.10, for now without regards for the previous discussion, would yield the following equations:

$$\forall k, \quad \tau_k \partial_t X_k = -X_k + (1 - r_k X_k)\mathcal{S}_k \left(\sum_j c_{jk} X_j(t - \lambda_{jk}) + P_k + \eta_k \right) \tag{3.13}$$

where $\eta_k \sim \mathcal{N}(0, \sigma_k^2)$ and σ_k controls the level of noise for node k (independently from other nodes). Note that it would be inconsistent with the model to add noise outside the non-linearity $\mathcal{S}$; random fluctuations may apply to the source of activity, but not to the form of the dynamics itself. In particular, a linear noise term would affect the dynamics equally whether the node is active or not, and could lead to infeasible values of X outside the interval $[0, 1]$. Additionally, there is no reason why measurement noise should interfere with the local dynamics; it should be applied point-wise after integration if needed (*e.g.* as a part of an observation model dependent on X).

With regards to the previous discussion on SDEs, it should be clear that Eq. 3.13 is incorrect; not only because the notation $\partial_t \bullet = \frac{\mathrm{d}\bullet}{\mathrm{d}t}$ cannot be used with stochastic processes, but also because it is not in Itô form, and therefore the system cannot be solved numerically as it stands. To remedy this, the noise term should be extracted from the non-linearity, and appear as a linear term, as in Eq. 3.12. Hence we isolate the feedback term (*i.e.* the argument of the non-linearity) by introducing the two following functions, for all k:

$$Z_k = \sum_j c_{jk} X_j(t - \lambda_{jk}) + \eta_k \tag{3.14}$$

$$F_k = \frac{-X_k + (1 - r_k X_k)\mathcal{S}_k\left(Z_k + P_k\right)}{\tau_k} \tag{3.15}$$

Taking infinitesimal differences in Eq. 3.14, knowing that (see Eq. 3.11):

$$\mathrm{d}\eta_k \sim \mathcal{N}(0, 2\sigma_k^2) \sim \sigma_k \mathrm{d}W \sqrt{\frac{2}{\mathrm{d}t}} \tag{3.16}$$

and recognising that $\mathrm{d}X = F\mathrm{d}t$ (see Eq. 3.10), we then obtain the Itô system:

$$\begin{aligned} \mathrm{d}Z_k &= \left[\sum_j c_{jk} F_j(t - \lambda_{jk})\right] \mathrm{d}t + \sigma_k \sqrt{\frac{2}{\mathrm{d}t}}\, \mathrm{d}W_k \\ \mathrm{d}X_k &= F_k \mathrm{d}t \end{aligned} \tag{3.17}$$

where W_k is an independent standard Wiener process for each k.

Therefore, the stochastic dynamics of a network with N coupled E-I units can be described by a system of $4N$ SDEs, which is different from (although equivalent to, if $\sigma_k = 0$) the deterministic system with $2N$ differential equations derived in Eq. 3.10.

While the system given in Eq. 3.17 can be used in a stochastic integration scheme (*e.g.* Euler-Maruyama or stochastic Runge-Kutta), we did not include noise in the experiments carried out in this thesis, mainly because we found the dynamics to be rich enough in the deterministic case to produce features of interest (*e.g.* broad frequency spectrum and chaotic multi-stability); a typical example is given in Fig. 3.8. In fact, based on our experience with the WC model so far, it seems plausible that deterministic chaos is sufficient to explain key aspects of resting-state activity, and consequently that stochasticity may not be required, despite certain studies supporting this claim (Ghosh et al. 2008).

This last point touches on one of the main focus of our work; claiming that a certain property of a model, or a particular form of equations, is *required* in order to produce a behaviour of interest is a strong claim, and unless a formal proof is possible, it can only be supported in practice by contraposition — that is, by showing that the behaviour of interest **cannot** be produced in the absence of such property or form of equation. In chapter 5, we present methods that we developed in order to assess such claims reliably and efficiently.

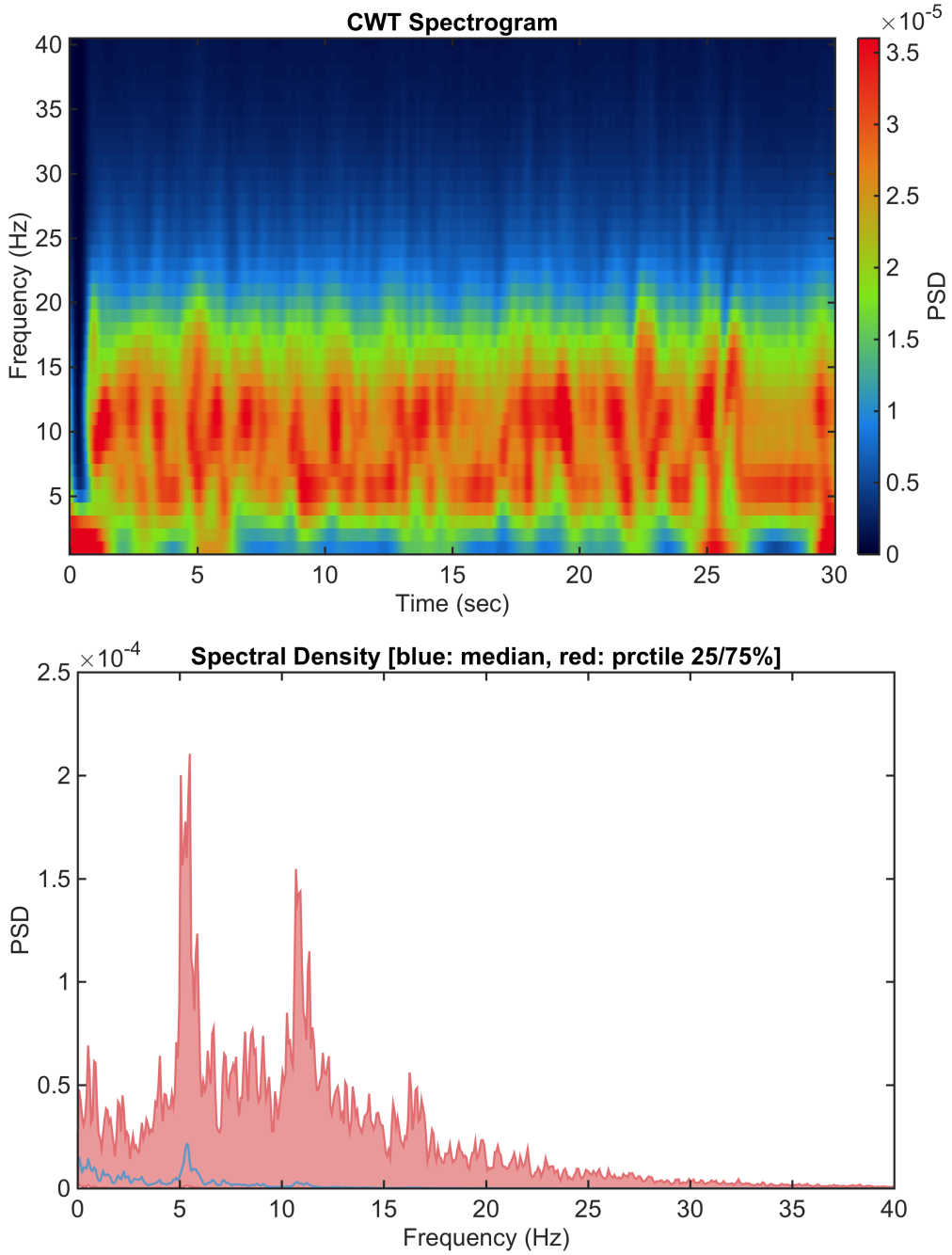

Figure 3.8: Example of a bistable system with broad frequency spectrum produced by the deterministic Wilson-Cowan network model with identical units (*c.f.* Eq. 3.10, and chapter 6 for more details about uniform network simulations). The top row shows the average time-frequency distribution of spectral power (evaluated using the Continuous Wavelet Transform), which displays chaotic transitions between two modes of oscillation, characterised by bursts of activity in alpha and theta bands. The bottom row shows the summary distribution of Power Spectral Density (evaluated using Welch's method), where the blue line indicates the median distribution across network units, and the red patch delineates the 25^{th} and 75^{th} percentiles. Despite noticeable peaks in theta and alpha bands, the spectrum extends broadly across frequencies below 40Hz.

3.4 Conductance-Based Model

Conductance-based models bring us closer to the physiology of neuronal tissues, by modelling the temporal variations of membrane potentials as a function of ionic currents. They have been studied extensively in the literature at the cellular level (spiking models), notably with the Hodgkin-Huxley model (Hodgkin et al. 1952), and branch into a plethora of models focusing on various aspects of membrane potential dynamics, such as integrate-and-fire, voltage-dependent gating and synaptic plasticity (see chapters 5 and 6 of Dayan et al. 2002 for an introduction).

Here, we propose an original derivation of a mean-field conductance-based model (CB), with two subpopulations per brain region (excitatory and inhibitory), and three state variables per subpopulation (membrane potential, excitatory and inhibitory conductances). It is similar to the model presented in (Marreiros et al. 2009), but our derivation is much simpler here, starting with the local dynamics and building up to delay-networks.

The oscillatory mechanism in this model is different from that presented with the Wilson-Cowan model (see our proposed equivalent spring-system in Fig. 3.9), and importantly the mean-field ionic currents relate *directly* to the signal measured with MEG.

3.4.1 Local equations

The local equations of this model describe the evolution of the average **membrane potential** within an excitatory and inhibitory subpopulation of neurons (E and I), as a function of several ionic currents. The intensity of these currents is controlled by synapses, which effectively act as "gates" allowing ionic flows proportional to their **conductance**. As with the Wilson-Cowan model, electro-physiological oscillations are assumed to result locally from the interactions between E and I subpopulations, however this model also proposes a biophysically plausible mechanism for these oscillations.

Denoting $V_{e,i}$ the average excitatory or inhibitory membrane potentials, and $g_{xy} \equiv g_{x\to y}$ the average synaptic conductance from x to y, the local equations are:

$$g_e^{\text{norm}} \tau_e^{\text{pot}} \partial_t V_e = g_e^{\text{leak}} \Delta_e^{\text{leak}} + g_{ee} \Delta_e^{\text{dep}} + g_{ie} \Delta_e^{\text{hyp}} + C_e \tag{3.18}$$

$$\tau_e^{\text{syn}} \partial_t g_{ee} = P_e - g_{ee} + w_{ee} U_e \tag{3.19}$$

$$\tau_i^{\text{syn}} \partial_t g_{ie} = -g_{ie} + w_{ie} U_i \tag{3.20}$$

$$g_i^{\text{norm}} \tau_i^{\text{pot}} \partial_t V_i = g_i^{\text{leak}} \Delta_i^{\text{leak}} + g_{ei} \Delta_i^{\text{dep}} + g_{ii} \Delta_i^{\text{hyp}} + C_i$$

$$\tau_e^{\text{syn}} \partial_t g_{ei} = P_i - g_{ei} + w_{ei} U_e$$

$$\tau_i^{\text{syn}} \partial_t g_{ii} = -g_{ii} + w_{ii} U_i$$

where $g_{e,i}^{\text{norm}}$ are **norm**alisation constants; $g_{e,i}^{\text{leak}}$ are conductances modelling ion leakage through the cell membranes; $\tau_{e,i}^{\text{pot/syn}}$ are decay times for the **pot**ential and **syn**aptic variables; $C_{e,i}$ are input currents, and $P_{e,i}$ are synaptic inputs; $w_{xy} \equiv w_{x\to y} \geq 0$ are synaptic strengths (or coupling factors); $\Delta_y^X = R^X - V_y$ is a potential relative to the so-called *reversal* potential R^X, where $X \in \{$**leak**age, **dep**olarising, **hyp**er-polarising$\}$; and $U = \mathcal{S}(V; \mu, \sigma)$ is a sigmoidal population response function, which tends to 1 if $V - \mu \gg \sigma$, or 0 if $\mu - V \gg \sigma$.

Note that for homogeneity, the potentials V, R and Δ should be in Volts, the conductances g_{xy} and couplings w_{xy} should be in Siemens, and U should be dimensionless. As previously, $\mathcal{S}$ is taken as the logistic function (see Apdx. A.1), and without loss of generality, we assume $g_e^{\text{norm}} = g_i^{\text{norm}} = 1$ nS in the remainder.

In this model, oscillatory activity is due mainly to the decay times of membrane potentials; indeed, V_e and V_i interact only indirectly via their effects on the synaptic conductances, and since conductances vary at least as fast as potentials, the mechanism of oscillations boils down to the non-instantaneous reaction of the inhibitory subpopulation to local excitation, causing hyper-polarising currents to lag behind depolarisation events in the

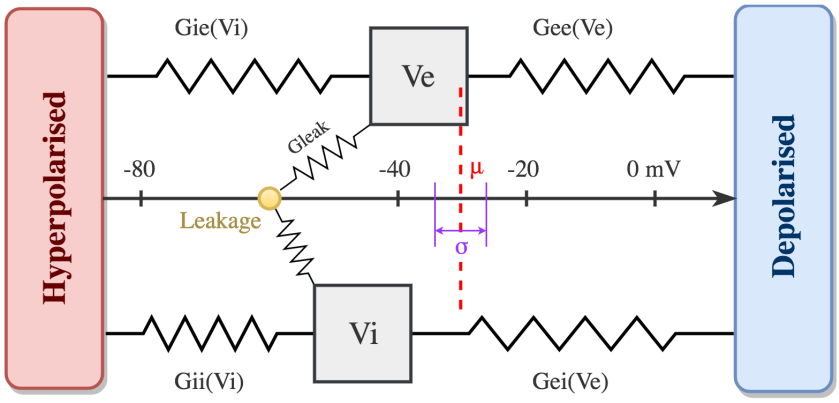

Figure 3.9: Equivalent spring-system to the local conductance-based model (*c.f.* §3.4.1), illustrating the "moving target" behaviour of this system. Conductances, denoted G_{xy} in this figure, are analogous to the strength of the springs. Importantly, these conductances depend on the membrane potentials, in the form of a sigmoid function centred at μ (here -30 mV) and with dynamic range σ. For example, if V_e comes within a neighbourhood $\mu \pm \sigma$, the excitatory conductances G_{ee} and G_{ei} become non-zero, which in turn attracts V_i nearer to μ, eventually causing G_{ie} to pull V_e back towards a hyper-polarised state.

excitatory subpopulation. The synaptic strengths ensure that this negative feedback is strong enough to stop and reverse the depolarisation.

To get a better intuition of this mechanism, we propose a novel equivalent spring-system in Fig. 3.9, which should hopefully save us from cumbersome explanations. There are two additional points worth mentioning:

1. There are two different types of input in this model; the input currents $C_{e,i}$, and the synaptic inputs $P_{e,i}$. As we will see later on, controlling $P_{e,i}$ is best to study the oscillatory behaviour in a context relevant to large-scale networks.

2. Whereas previously in the WC model, the state-variables did not relate to physical quantities that could be measured directly, the **synaptic currents** in this model (of the form $g(R-V)$) are *proportional* to the magnetic field measured by MEG (*c.f.* §2.4.1). Indeed, this magnetic field is produced by charged particles moving through ion channels in dendrites, as given by the Maxwell-Ampere equation.

3.4.1.1 Nullclines and normalisation

Given that the local equations depend on six state variables, the nullclines lie *a priori* in a six-dimensional state space. However in this particular case, looking for example at the potential nullcline $\partial_t V_e = 0$ *implies* a steady-state of the conductances g_{ee} and g_{ei} (provided that the various inputs are fixed), which can therefore be substituted with $P + wU = P + w\mathcal{S}(V)$ back into the potential nullcline.

The same argument applies to the inhibitory potential V_i, and therefore the nullclines of the membrane potentials are actually **embedded** in a two-dimensional space. Nevertheless, note that oscillatory trajectories in this system may *not* be embedded in that subspace (although they will have to intersect each of the previous nullclines at least twice per cycle), and that local extrema of the membrane potentials do not necessarily correspond to local extrema of the conductance variables. An example of nullclines and (projected) oscillatory trajectory is given in Fig. 3.4.

Following this discussion, the following substitutions can be made in the nullclines of membrane potentials:

$$g_{ee} \to P_e + w_{ee}U_e \qquad g_{ei} \to P_i + w_{ei}U_e \qquad g_{ie} \to w_{ie}U_i \qquad g_{ii} \to w_{ii}U_i \tag{3.21}$$

which leads to the following embedded formulas:

$$\begin{aligned} \partial_t V_e = 0 \iff & \quad -w_{ie}\mathcal{S}_i(V_i)\Delta_e^{\text{hyp}} = g_e^{\text{leak}}\Delta_e^{\text{leak}} + (P_e + w_{ee}U_e)\Delta_e^{\text{dep}} + C_e \\ \iff & \quad V_i = \mathcal{S}_i^{-1}\left(\frac{g_e^{\text{leak}}\Delta_e^{\text{leak}} + (P_e + w_{ee}U_e)\Delta_e^{\text{dep}} + C_e}{-w_{ie}\Delta_e^{\text{hyp}}}\right) \end{aligned} \tag{3.22}$$

$$\begin{aligned} \partial_t V_i = 0 \iff & \quad -\left(Pi + w_{ei}\mathcal{S}_e(V_e)\right)\Delta_i^{\text{dep}} = g_i^{\text{leak}}\Delta_i^{\text{leak}} + w_{ii}U_i\Delta_i^{\text{hyp}} + C_i \\ \iff & \quad V_e = \mathcal{S}_e^{-1}\left(\frac{g_i^{\text{leak}}\Delta_i^{\text{leak}} + w_{ii}U_i\Delta_i^{\text{hyp}} + P_i\Delta_i^{\text{dep}} + C_i}{-w_{ei}\Delta_i^{\text{dep}}}\right) \end{aligned} \tag{3.23}$$

Similarly to the WC model, there is a degree of freedom in these nullclines; any simultaneous rescaling of parameters $\left\{g_x^{\text{leak}}, C_x, P_x, w_{xx}, w_{yx}\right\}$ leaves the argument of the inverse sigmoid unchanged, and we use this to **normalise** the parameters of conductance-based units such that $g_e^{\text{leak}} = g_i^{\text{leak}} = 1\text{nS}$.

The effects of the various parameters on the oscillatory behaviour (in terms of frequency and standard-deviation) were consistent across a range of configurations we tried in our experiments, and therefore it seems there is not much added value in providing multiple different units for this model, as we did for the WC model. Instead, we give the parameters of a typical unit in Tab. 3.2, and analyse its behaviour in the next section.

Name	μ	σ	w_{xx}	w_{yx}	τ^{pot}	τ^{syn}
E	-30	3	10	20	15	5
I	-30	3	1	5	15	10

Table 3.2: Table of parameters for a typical conductance-based unit. Parameters are normalised such that $g_i^{\text{leak}} = g_e^{\text{leak}} = 1$, and decay times are given in milliseconds. The reversal potentials were set to $R^{\text{leak}} = -60\text{mV}$, $R^{\text{hyp}} = -80\text{mV}$ and $R^{\text{dep}} = 0\text{mV}$ in all experiments.

3.4.1.2 Effect of parameters

We studied the oscillatory behaviour of the conductance-based unit given in Tab. 3.2 (page 66), by varying the **synaptic input** P_e against particular degrees of freedom listed below, one at a time, and fixing all other parameters. For each combination of parameters, a simulation of time-length equivalent to $120\ \tau_e^{\text{pot}}$ was run by solving the local equations, and the interval $[0, 50\ \tau_e^{\text{pot}}\ )$ was discarded to ignore transient effects due to the initial conditions, taken as $(V_e = V_i = R^{\text{leak}}, g_{xy} = 1)$ in all simulations. As previously with the WC model, the standard deviation and frequency mode of the truncated time-course of excitatory conductance $g_e e$ were computed and visualised as a surface-plot.

It is worth noting that, although both the synaptic inputs $P_{e,i}$ and the input currents $C_{e,i}$ lead to an oscillatory regime beyond a certain **threshold value**[6], they do so in slightly different ways: synaptic inputs force the conductance's steady-state to a non-zero value, which causes the "synapses" to always be active; whereas input currents shift the potential's steady-state near the dynamic range of the response functions. Both affect the steady-state of the conductances, but the latter depends on parameters μ and σ, whereas the former does not.

We chose to vary the synaptic input P_e, rather than the input current C_e, because it corresponds to the effects of remote connections in the large-scale model that will be derived in the next section. In fact, for (reasonable) sub-threshold values, the input currents had **no effect** on the local dynamics at all, but as we will see they allow to control the *sensitivity* of each unit in a large-scale context. The fact that the sensitivity to inputs can be controlled independently from the inputs themselves in this model, is a remarkable difference with the WC model, where parameters μ and P were controlling the exact same degree of freedom.

For this model, we identified the following **twelve** d.o.f., affecting one or several parameters at a time:

(D1-3) scaling all coupling factors w_{xy}, or only the excitatory ones w_{ex}, or only the inhibitory ones w_{ix};

(D4-6) varying the coupling factors w_{ei}, w_{ie} and w_{ii} individually;

(D7-8) varying the sigmoid parameters μ and σ, simultaneously in both E and I subpopulations;

(D9-10) varying the potential decay-times by controlling either τ_e^{pot} while maintaining $\tau_i^{\mathrm{pot}}/\tau_e^{\mathrm{pot}}$ constant, or varying this ratio by controlling τ_i^{pot};

(D11-12) similarly for the synaptic decay-times.

[6] Oscillations can also be triggered by shifting μ_e or increasing σ_e.

The results are presented in Fig. 3.10 and summarised below:

- the coupling scales (D1-2) and response width (D8) seem to have similar effects, and can be chosen to maximise the width of the oscillatory range;
- the inhibitory coupling scale (D3) has (non-surprisingly given that w_{ii} is small) similar effects to that of w_{ie} (D5), in controlling the slope of the amplitude response;
- w_{ei} (D4) affects mainly the amplitude of oscillations, and increasing values of w_{ii} (D6) lead to a reduced width of the oscillatory range, steeper negative slope of the amplitude response, and higher maximum frequency;
- the response threshold μ (D7) should take values between -20 and -30 mV;
- the potential decay-times (D9) control the width of the oscillatory range, whereas the synaptic decay times (D11) affect (dramatically) the range of frequencies;
- finally the inhibitory decay times (D10, D12) have similar effects in controlling the range of frequencies, but τ_i^{syn} seems to do so without side-effects.

For completeness, we also provide a one-parameter bifurcation diagram (controlling P_e) in Apdx. A.3.

3.4.2 Large-scale network model

Extending these local equations to include input currents from remote brain regions at the whole-brain level consists in adding voltage-gated terms (of the form $g_{xy}\Delta_y^X$) to the potential equation Eq. 3.18. Although this is straightforward mathematically, it results in a significant computational burden if implemented naively. Indeed in a non-sparse network with N units, there is now one conductance equation **per edge** (corresponding to each "synapse" with a remote region), leading to an overall complexity of $\mathcal{O}(N^2)$ in *both* time (number of operations) and space (amount of memory) in order to evaluate the system at each time-step.

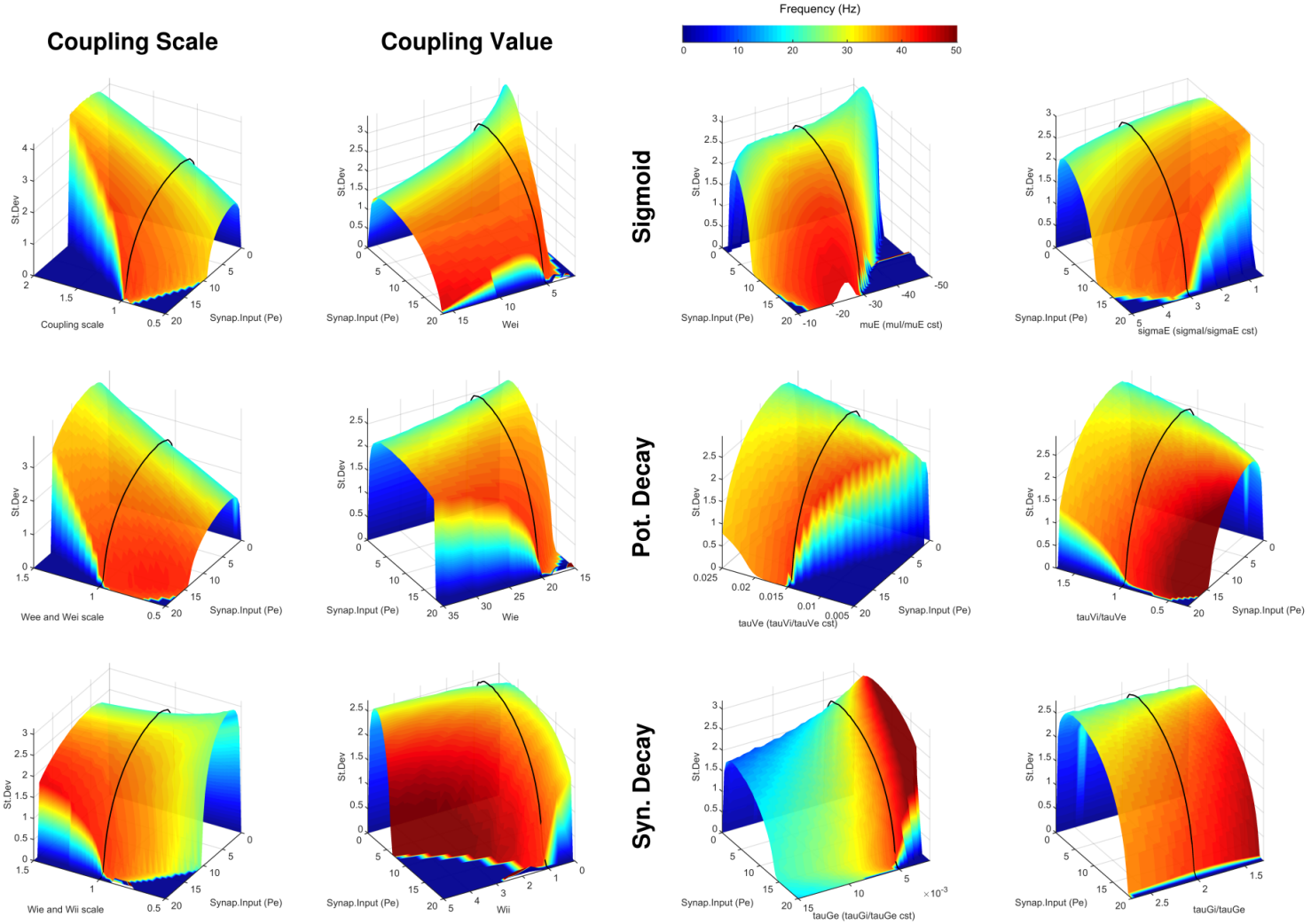

Figure 3.10: Effect of model parameters on the oscillatory dynamics of conductance-based units. Black lines indicate baseline values. Notably, w_{ei} and w_{ie} control respectively the amplitude of oscillations, and the slope of the amplitude response; larger potential decay-times lead to a wider oscillatory range; the inhibitory synaptic decay-time controls the frequency range without side-effects; and there seems to be a preferred range of response threshold μ between -20 and -30 mV. Interestingly, the effect of w_{ii} is also reminiscent of the amortisation in the WC model (*c.f.* Fig. 3.7 page 56).

Here, we derive an equivalent formulation which scales *linearly in space* with the number of units, under the assumption that synaptic decay-times $\tau_{e,i}^{\text{syn}}$ be identical across the network.

For a given node k (either excitatory or inhibitory), let Ω_k^E denote the set of indices of all pre-synaptic excitatory subpopulations (remote or local), and similarly Ω_k^I for pre-synaptic inhibitory subpopulations. Adapting the local equation for the potential V_k to include input currents from remote regions yields, after factorisation:

$$\tau_k^{\text{pot}} \partial_t V_k = g_k^{\text{leak}} \Delta_k^{\text{leak}} + \left(\sum_{j \in \Omega_k^E} g_{jk} \right) \Delta_k^{\text{dep}} + \left(\sum_{j \in \Omega_k^I} g_{jk} \right) \Delta_k^{\text{hyp}} + C_k \tag{3.24}$$

Furthermore, with the assumption that all excitatory synapses have the same decay-time τ_E^{syn}, we can then write:

$$\tau_E^{\text{syn}} \partial_t \left(\sum_{j \in \Omega_k^E} g_{jk} \right) = \sum_{j \in \Omega_k^E} \tau_E^{\text{syn}} \partial_t g_{jk} = - \sum_{j \in \Omega_k^E} g_{jk} + \sum_{j \in \Omega_k^E} w_{jk} U_j(t - \lambda_{jk})$$

where we used the local equations 3.19 and 3.20 for each conductance in the sum, and introduced propagation delays $\lambda_{jk} \equiv \lambda_{j \to k} \in \mathbb{R}_+$ from population j to population k.

The same applies to the inhibitory conductances, and hence we define the **macro-conductances**:

$$g_k^E = \sum_{j \in \Omega_k^E} g_{jk} \qquad g_k^I = \sum_{j \in \Omega_k^I} g_{jk} \tag{3.25}$$

which, after substitution in the previous equation 3.24, leaves us with **only two** conductance equations for node k, instead of one conductance equation per edge. In summary,

the large-scale equations of the conductance-based model for node k are:

$$\tau_k^{\text{pot}} \partial_t V_k = g_k^{\text{leak}} \Delta_k^{\text{leak}} + g_k^E \Delta_k^{\text{dep}} + g_k^I \Delta_k^{\text{hyp}} + C_k \tag{3.26}$$

$$\tau_E^{\text{syn}} \partial_t g_k^E = -g_k^E + \sum_{j \in \Omega_k^E} w_{jk} U_j(t - \lambda_{jk}) \tag{3.27}$$

$$\tau_I^{\text{syn}} \partial_t g_k^I = -g_k^I + \sum_{j \in \Omega_k^I} w_{jk} U_j(t - \lambda_{jk}) \tag{3.28}$$

Note in these equations, that there is no synaptic input term $P_{e,i}$; their purpose in the local equations was to emulate the effects of remote inputs, which are gathered into summation term in equations 3.27 and 3.28. This is important for at least one reason; whereas in the local equations, we could control directly the steady-state of the conductances, here this control is only indirect; through the input current C_k, *and* (as we will see in chapter 6) by scaling the synaptic strengths w_{jk}.

Note that we use *and* truly as a conjunction here; since the synaptic strengths are *outside* the non-linearity (another difference with the WC model), their effect is nil as long as the remote pre-synaptic potentials V_j are far from their respective activation thresholds μ_j, because the activation function U_j is then effectively zero. Therefore the corresponding input currents C_j must be used *together* with a scaling of the synaptic strengths. Hence the previous discussion about the sensitivity of a CB unit, and the difference between synaptic inputs and input currents in the local equations.

Finally, noise in this system should be applied as a linear additive term to the *potential* equations (noisy conductances would make an isolated unit oscillate spontaneously, which is unrealistic). This would yield an Itô system without further complications — although note that for the reasons explained earlier, adding noise will be ineffective unless the input currents bring the potentials close enough to the response threshold in the first place.

3.5 Software Implementation

At the time we started this work, there were very few software packages that seemed relevant to our objective; NEST (Gewaltig et al. 2007; Eppler 2008) and GENESIS (Bower et al. 2013) are optimised for simulations of large networks of spiking neurons, and the recently published Virtual Brain (Sanz Leon et al. 2013; Sanz-Leon et al. 2015) seemed a very large software project, with an accent on feature-rich user-interfaces, rather than in providing a stable library for modelling and simulation. Retrospectively, it is possible that our project would have benefited from an all-encompassing framework like the Virtual Brain, although it may not have been: flexible enough for deploying on a Sun Grid Engine computing cluster without significant work; modular enough to allow extending the underlying models, routines and solvers without chain-dependency issues; configurable enough to avoid generating enormous amounts of data[7]; stable enough to avoid version breakage over the course of this project; and finally performant enough to envisage exploring the landscape of large-scale network behaviour beyond conventional delay-coupling grid-searches (Deco et al. 2009).

We developed our own software package for the simulation of large-scale neuronal systems. Although there were many obstacles on the way, overcoming them led to a better understanding of the typical issues involved with such simulations, as well as of the underlying numerical methods, and of the models themselves. In this section we describe the key aspects of our contribution, and we argue that the resulting framework is a lighter, simpler, more performant and more flexible alternative to existing software.

[7] A typical simulation weighs up to a few hundred mega-bytes, and an experiment can involve thousands of simulations. Counting in hundreds of giga-bytes can be difficult to manage in the long run.

3.5.1 Design considerations

We developed this framework from the bottom-up, entirely in C++ and without any other dependency than the standard library (C++11). Third-party dependencies can be difficult to maintain, and complicate the use of a library in practice (*e.g.* due to version incompatibilities or platform-specific issues); our aim was to avoid such issues, and ensure cross-platform compatibility[8].

3.5.1.1 Assumptions and requirements

It is difficult, if not impossible or impractical, to create a framework for the simulation of *any* large-scale neuronal system; there is always a trade-off between the number of assumptions that can be made about the system to be simulated, the complexity of the underlying code-structure, and the resulting performance in terms of runtime and memory management. In our case, we reduced the number of assumptions about the system to the following:

- deterministic systems should be in canonical form (*i.e.* first-order equations);
- stochastic systems should be in Itô form;
- the state-variables should be real-valued;
- delays should be non-negative;
- the dependency structure between state-variables should be a multigraph (*i.e.* multiple edges between two nodes are allowed).

The strongest assumption is perhaps that the state-variables be real-valued; even though it is always possible to separate complex equations into their real and imaginary parts (or else their moduli and arguments), a non-obvious limitation is that of quotient sets, such

[8] To date, this software compiled without warning on several versions of OSX and Linux distributions, with the GNU and LLVM compilers alike (g++ and clang++), and used with several versions of Matlab.

as $\mathbb{R}/2\pi\mathbb{Z}$ for instance, in the case of 2π-periodic state-variables. The issue then has to do with the interpolation of delayed terms, and may be tackled in future developments. The remaining assumptions are very permissive, and in particular our software supports arbitrarily complex interaction structures (*e.g.* nested hierarchies or time-varying delays).

In addition to these assumptions, for all practical purposes, the system should not exceed a thousand state-variables, or a hundred thousand delay-edges, per CPU core. The current performance is on the order of **five thousand delay-edges per millisecond per core** on modern CPUs[9], and typical network simulations in our experiments (several hundred state-variables and 5k delay-edges) ran twice as slow as real-time with three threads.

3.5.1.2 Architecture

At the highest level, our software consists of **three libraries** built on-top of each other:

- The first library[10] provides mainly utilities (allocators, timers, random generators, special functions, *etc*.), numerical data-structures for multi-dimensional arrays with shared and/or non-contiguous memory layouts, and an interface with Matlab/Mex.
- The second library[11], provides high-performance solvers for large systems of ordinary or stochastic delay-differential equations.
- Finally, the third library[12] provides a simple framework for the definition of large-scale neuronal network models.

The architecture of an object-oriented software is best described as a **class-diagram**, in which the various entities (*e.g.* data-structures, solvers and models) are considered in relation with each-other; for example, a solver may depend on the definition of a problem, stored in some data-structure. In the following sections, we describe the architecture of the second and third library mentioned above.

[9] The largest delay does not matter in practice.
[10] Available from: `https://bitbucket.org/jhadida/drayn`
[11] Available from: `https://bitbucket.org/jhadida/osd`
[12] Available upon request from: `https://bitbucket.org/jhadida/nsl`

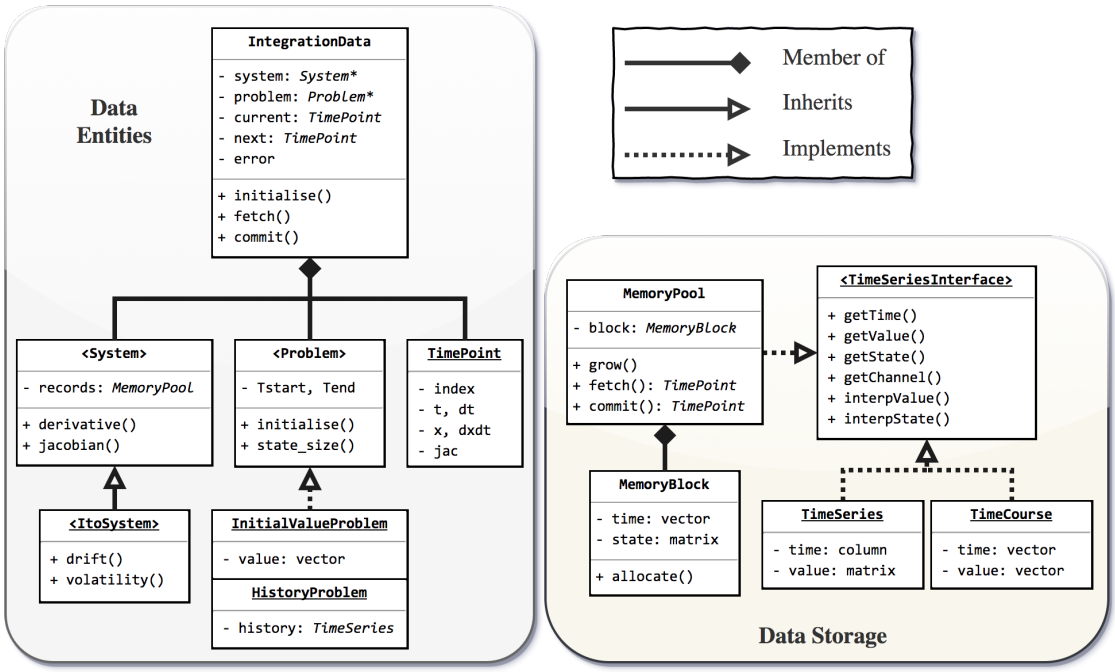

Figure 3.11: Main data-entities in our software library. *Memory pools* allocate storage by blocks of a few thousand timepoints at a time (to avoid successive allocations at each time-step), and collate these blocks internally to be manipulated as contiguous time-series (useful for interpolation). Note that preallocating the entire time-course is not possible with adaptive stepping schemes, and block allocation also allows for downsampling on-the-fly (useful for very long integrations). The *integration data* stores all necessary information to propagate the system one step forward: the system itself (along with the memory of past states to compute delayed terms); the problem to be solved (including information about initialisation and termination); the current state of the system; and allocated storage for the next state to be computed.

3.5.1.3 Numerical integration

There are many available libraries for the integration of non-linear ODEs, fewer for the integration of SDEs, and to our knowledge there is none publicly available for the integration of large stochastic delay-differential systems. Our implementation was inspired by the Boost library "odeint", the main differences being the inclusion of utilities for delay-differential equations, as well as the definition of **events** at several stages during the integration, allowing for **plugins** to be implemented and attached to the system for flexible monitoring (*e.g.* range constraints) or enhancement (*e.g.* synaptic plasticity), with a negligible overhead[13].

[13]Events are implemented following a publish/subscribe pattern, using lambda-closures as callback delegates, and using unordered-sets as storage. The overhead is therefore essentially that of a for-loop.

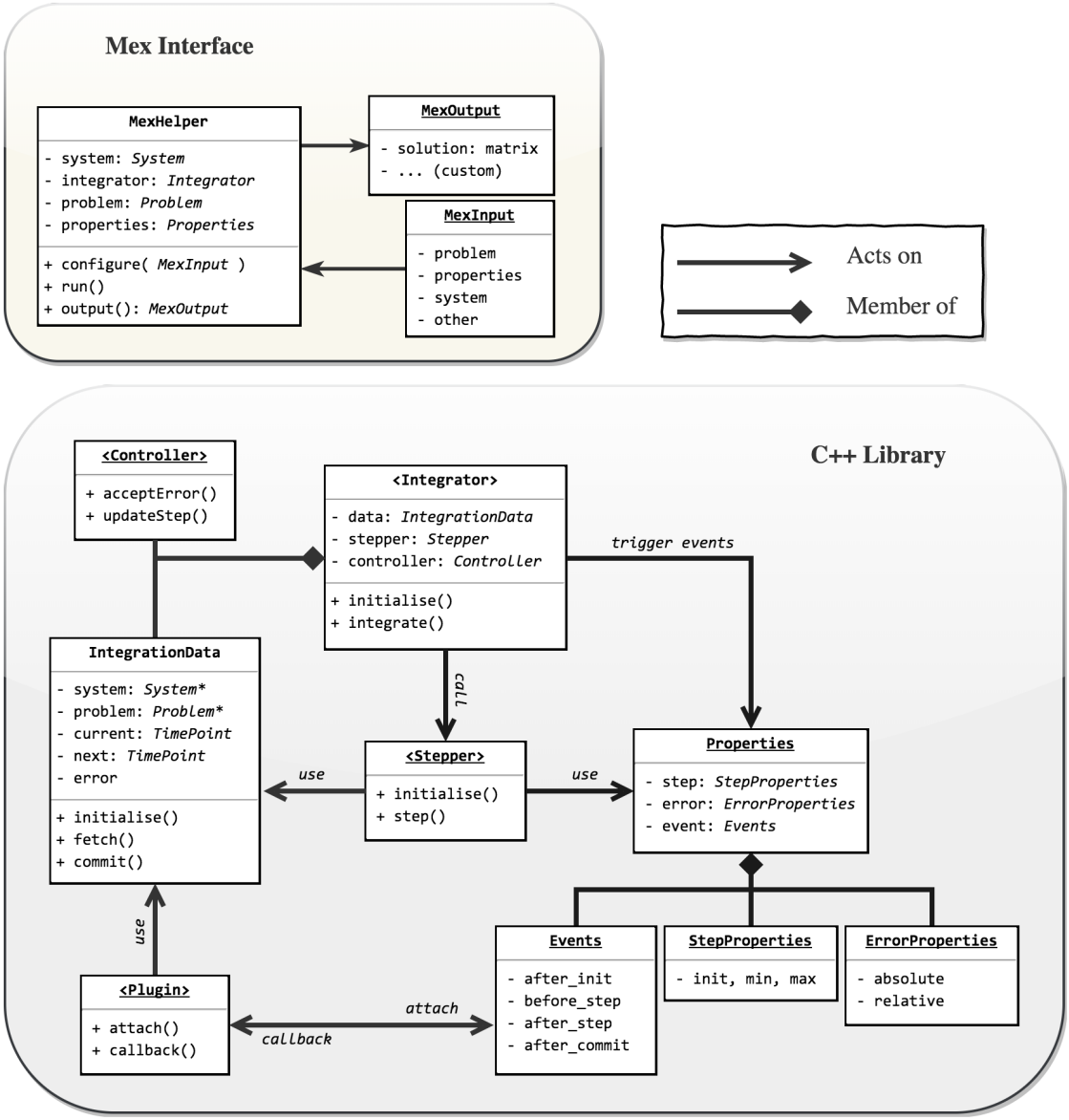

Figure 3.12: Integration process and interface with Matlab/Mex. The IntegrationData (*c.f.* Fig. 3.11) is passed on to the Integrator, which propagates the System forwards in time until the last timepoint (as specified by the Problem), by calling the Stepper sequentially in accordance with the StepProperties. In the case of adaptive stepping schemes, each step requested by the Integrator yields an estimation of the error made, which is evaluated with respect to the ErrorProperties. The Controller monitors failed stepping attempts, and is in charge of updating the time-step adequately (in particular, avoiding oscillations). Finally, Events are triggered at multiple stages during the integration, and can be attached to several Plugins, which may modify the IntegrationData. For example, plugins can be used to ensure that the state variables remain finite, or within a feasible range during the integration (in which case they should be called after each step).

In order to understand the structure of our library, it is important to first identify the main **data-entities** at play. These are described in Fig. 3.11, and we summarise the key points below:

- Memory allocation by block is more efficient than allocating at each step in the case of adaptive stepping methods, and allows for downsampling on-the-fly in the case of very long integrations.
- The integration data holds all necessary information in order to propagate the system one step forward.
- The computed timepoints are stored in the system itself, and this storage can be manipulated as a time-series, which allows delay-terms to be computed easily.
- Stochastic systems extend ordinary ones by providing methods to compute the drift and volatility terms (instead of the derivative).

The **integration process** can then be described as a series of operations which manipulate the previous entities. This is illustrated in Fig. 3.12, and summarised below:

- The Integrator propagates the IntegrationData, one step at a time, from the first to the last timepoint specified by the Problem.
- The initialisation consists of a chain of calls originating in the Integrator, and propagating all the way down to the Problem, in order to setup all entities involved (in particular, the initial conditions are copied to the memory pool).
- In the case of adaptive stepping schemes, the Controller is in charge of monitoring failed stepping attempts, and of updating the time-step accordingly.
- Events are triggered at multiple stages during the integration, and can be used to implement features as Plugins. This favours a modular architecture, which is useful for testing and experimenting with a model, allowing extensions without altering the original implementation.

Finally, this library provides Mex bindings in order to be called directly from Matlab (see Fig. 3.13), such that the simulation of any system can be configured with a simple structure.

3.5.1.4 Neuronal systems

This library is built on top of the previous one, and provides a framework for the definition of large-scale biophysical networks. Specifically, within this framework, any simulation is entirely defined by the following information:

- a given model, integrator and stepping scheme (and additional plugins);
- a list of **nodes** with model-specific parameters (*e.g.* sigmoid and decay-times);
- a list of **edges** with interaction parameters (*e.g.* delay and coupling);
- additional **options** for the system (*e.g.* the number of threads);
- an integration **problem** (*e.g.* initial state and time-span);
- and finally, a set of integration **properties** (*e.g.* integration time-step).

Note that the parameters contained within the nodes, or the information stored within the options is entirely model-dependent, and therefore imposing this structure is not limiting in any way. In fact, it allows for the implementation of a **template network** class, which can be used to streamline the definition of neuronal systems. Additionally, a collection of sigmoid functions and stimuli are implemented to further facilitate the definition of such models. With these utilities, the definition of any large-scale network model boils down to the following:

- Implementation of a structure to store the various options (utilities are provided to parse these options from the input Matlab structure).
- Implementation of a class to store the node properties, as well as the sigmoid and stimulus functions. In particular, stimuli can be specified as time-courses, which

will be interpolated automatically during integration in order to assess input values at specific timepoints.

- Implementation of the derivative, as required by the previous library for numerical integration (*c.f.* System in Fig. 3.11).

To date, we used this framework to implement **eight different models** without needing to change anything in the framework itself. The simplicity of this design allows for the implementation of a new model within hours, and the fact that the data required to run simulations reduces essentially to a set of nodes and edges, means that we are free to parametrise our networks in any imaginable way. Furthermore, we implemented a Matlab interface with this framework (see Fig. 3.13) to facilitate the implementation of different network parametrisations (*e.g.* with identical unit parameters across brain regions or not, with or without subcortical regions, or noise, *etc.*), and the analysis of the corresponding simulation outputs. The details of the analysis pipeline are covered in §4.2.

Importantly, this simplicity and flexibility do *not* come at the cost of performance; as mentioned previously, the ball-park figure is of 5k delay-edges per millisecond per CPU core (although multi-threading causes non-negligible overhead), and a comparison with the Virtual Brain suggests that our framework is slightly faster[14]. With the use of adaptive-step methods, this performance increases further to typical runtimes only twice as slow as real-time.

[14]The experiment suggested in (Sanz Leon et al. 2013) consists of a network of 72 nodes (number of edges unspecified), with delays up to 20ms, and fixed time-steps of 0.065ms using a Runge-Kutta method of order 4 (we assumed with a single-thread). The times reported are of 16 sec average runtime for each second of simulation, whereas we achieved 14.6 sec in our framework (and 7.8 sec with three threads).

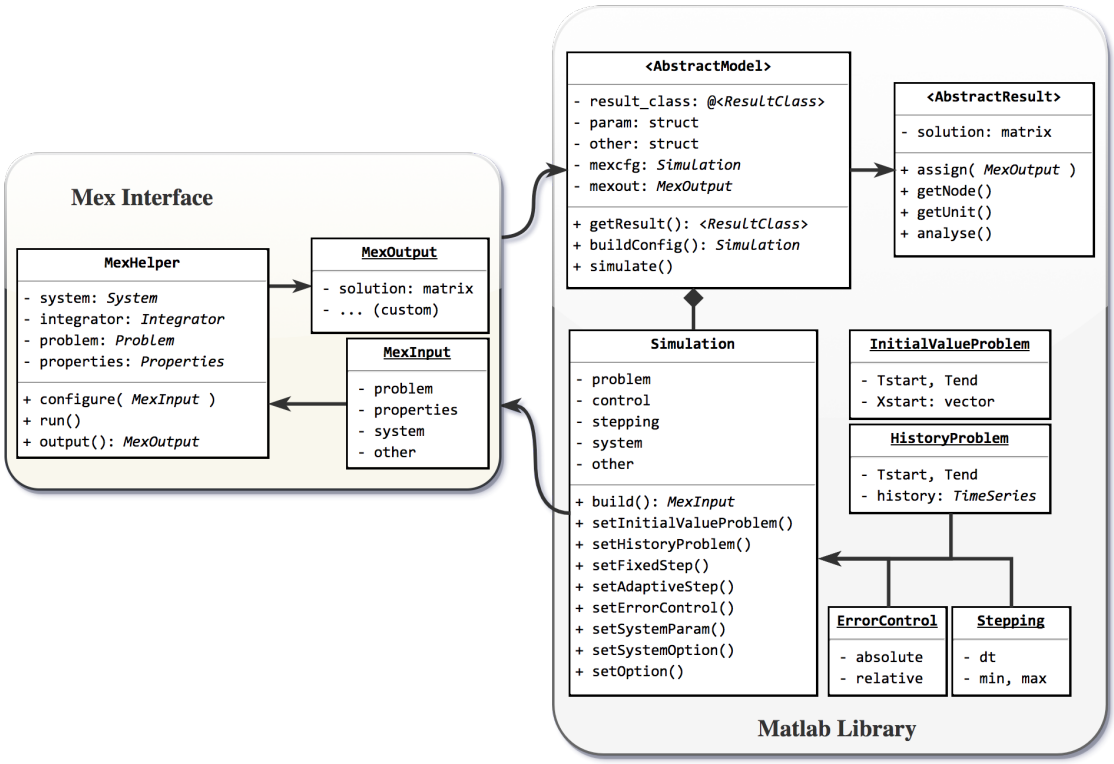

Figure 3.13: Matlab interface with simulation library. Each neuronal-mass network model implements the AbstractModel interface, allowing different parametrisation of the network (*e.g.* with identical unit parameters across brain regions or not, with one or several subpopulations within each unit, with or without subcortical regions, time-varying inputs, coloured noise *etc.*) to be converted into a valid configuration for simulation. The AbstractResult interface wraps around the output of the simulation — mainly, a matrix with successive *states* of the system in rows — to provide semantic access (*e.g.* the state time-courses of a particular unit, or of the excitatory subpopulation, or only the excitatory conductances *etc.*).

3.5.2 Numerical methods

The main computational bottleneck in the simulations of networks of neuronal-masses is due to the number of feedback terms to be computed at each time-step. Since the coupling between the different brain regions, derived from the anatomical connectivity matrices (*c.f.* Fig. 2.3), is not sparse, the complexity of *each* time-step is quadratic in the number of nodes in the network.

Furthermore, most of the feedback terms are delayed, meaning that they depend on past states of the system which may need to be interpolated[15], therefore adding to the complexity of the integration. Finally, the resting-state dynamics measured empirically with MEG are known to span multiple time-scales (*c.f.* §2.4.4), and the models presented are large non-linear systems which are likely to exhibit chaotic behaviour (see Fig. 3.8); the numerical integration of such systems is difficult, and requires advanced methods to compute solutions faithful to the equations while avoiding prohibitively small time-steps.

3.5.2.1 Stepping schemes

Stepping schemes are numerical methods that allow to propagate a system defined by differential equations forwards in time. The choice of a particular method depends on the problem at hand; for instance, the methods used for deterministic or stochastic systems are different. The deterministic methods for ODEs can be divided into two main categories:

- **Explicit** methods evaluate the system of equations at present and past states, in order to estimate future states. The forward Euler method is the simplest example, based on a Taylor approximation of order one:

$$\partial_t x = F(x,t) \quad \Rightarrow \quad x_{n+1} \approx x_n + hF(x_n,t_n)$$

  where x represents the state variables, F is the so-called right-hand side, and $h = t_{n+1} - t_n$ is the time-step. Many other methods exist within this category, improving upon the previous Euler scheme with better accuracy (*e.g.* Runge-Kutta methods) and/or stability (*e.g.* multi-step methods) for an equivalent step-size.

- **Implicit** methods equate values of the system at an unknown future state, to a function of the present (and past) states, and proceed to calculating the unknown

[15] Even if the delays are all multiples of the integration time-step (a.k.a. *commensurate* delays), many numerical integration methods require the right-hand side to be evaluated at multiple fractions of the time-step in order to gain precision (*e.g.* Runke-Kutta methods).

state using zero-finding algorithms. Similarly, the backward Euler method is the simplest example:

$$\partial_t x = F(x,t) \quad \Rightarrow \quad x_{n+1} \approx x_n + hF(x_{n+1}, t_{n+1})$$

where now the right-hand side is evaluated at a future timepoint t_{n+1} with the unknown state x_{n+1}. Although these methods require more work at each step, they are typically more stable than explicit methods for an equivalent time-step, and are particularly suited to problems mixing slow and fast time-scales of variations (see Press et al. 2007, section 17.5). It is worth noting that so-called **semi-implicit** methods are much more common in practice, due to a linearisation of the previous equation involving the Jacobian of the system:

$$\begin{aligned}
x_{n+1} &\approx x_n + hF(x_{n+1}) \\
&\approx x_n + h\left[F(x_n) + \overbrace{\partial_x F(x_n)}^{J(x_n)}\,(x_{n+1} - x_n)\right] \quad \Rightarrow \\
\Big[1 - hJ(x_n)\Big]x_{n+1} &\approx \Big[1 - hJ(x_n)\Big]x_n + hF(x_n) \quad \Rightarrow \\
x_{n+1} &\approx x_n + h\Big[1 - hJ(x_n)\Big]^{-1} F(x_n)
\end{aligned}$$

where we dropped the dependence of F on t (*i.e.* the autonomous case) to illustrate our point; $J(x_n)$ is a matrix denoting the Jacobian of F evaluated at state x_n; and $[1 - hJ(x_n)]^{-1}$ denotes the matrix-inverse.

Although the stability of implicit methods in the case of mixed time-scales dynamics would be a desirable property in our case, these methods are simply too costly in comparison with explicit methods, for systems with hundreds of coupled equations, and without explicit formula for the Jacobian. Indeed in our case, if N is the number of nodes in the network, and $V \propto N$ is the number of state-variables (at least one per

node); then a numerical estimation of the Jacobian requires $\mathcal{O}(V)$ evaluations of the system, each with $\mathcal{O}(N^2)$ coupling terms to be computed, and the matrix inversion has a complexity of $\mathcal{O}(V^3)$. Overall, this yields a complexity of $\mathcal{O}(N^3)$ for each time-step, which is much more costly than using a few direct evaluations of the system (complexity $\mathcal{O}(N^2)$) with an explicit scheme.

We implemented **five explicit** methods within our framework (*c.f.* §3.5.1.3), all Runge-Kutta schemes of increasing order, namely: RK2 (mid-point), RK4, RK6 (Luther 1968), the Dormand-Prince method of order 4 (`DOPRI5`) and a method of order 8 (`DOP853`) adapted from the ForTran routines given in (Hairer et al. 1993). The *order* of these methods relates to their precision for a given step-size; the higher the order, and usually the more precise the step (except for stiff systems), meaning that computing a solution is either faster (fewer steps needed, though each more costly), or more likely to be accurate (less error accumulated over time). Notably, the higher-order methods also include explicit estimates of the precision achieved at each step, which can be used to implement adaptive step-size control (see Press et al. 2007, section 17.2), such that the time-step is adjusted dynamically during integration.

For the sake of completeness, we also implemented **two implicit** methods, namely the method proposed in the appendix of (David et al. 2006), and the Rosenbrock method `RODAS` (Hairer et al. 1996). Although we did not conduct a systematic benchmark so far, preliminary experiments confirmed that these methods reached a similar precision compared to the explicit methods, with a larger time-step, but at the cost of much longer computations.

3.5.2.2 Delay induction

Similarly to the addition of noise discussed previously in §3.3.2.1, introducing delays $\left\{\lambda_k\right\}_{k=1..L}$ into a system of differential equations fundamentally alters their properties. To understand why, it is good to look at the initialisation of such systems; whereas typical

initial-value problems only require a single state (typically $x(t_0)$) in order to make the first step, delay-systems additionally require all the states at timepoints $(t_0 - \lambda_k)_{k=1..L}$ in order to evaluate the system of equations. Immediately after the first step (the step-size is typically smaller than the smallest delay), another set of delayed timepoints is required, and yet another one for any intermediate step (*e.g.* with Runge-Kutta methods of order at least 2); in fact, the *state* of the system at time t is no longer defined by a single timepoint $x(t)$, but indeed by a *continuum* of timepoints defined over the range $[t - \lambda_{\max}, t]$. Therefore, any delay-system is infinite-dimensional, regardless of how many state-variables there are, and an **initial function** is required for initialisation.

One of the consequences is as follows; whereas without delays, it is usually simple to choose an initial state that is *feasible* (*i.e.* for which the system of equations is defined), in the case of delay-systems the initial function should itself satisfy the equations (to avoid causing discontinuities in the solution), but the solution to these equations is unknown, and in fact most often non-analytical. This makes the initialisation of delay-systems a circular problem; the initial function should satisfy the system of equations, but we cannot solve this system without an initial function.

To our knowledge, there is no solution to this problem. In our experiments, we opted for a simple work-around, initially removing the delay-terms from the equations, and re-introducing them once the system settled into an equilibrium for a long-enough time (*i.e.* at least as long as the largest delay). Obviously, this is only possible if the system without delay-terms actually converges towards a fixed-point equilibrium, and we ensured that this was the case (*c.f.* §6.2.2.1). The removal and re-introduction of delayed-terms was done implicitly, by modulating the corresponding coupling coefficients (*c.f.* Eqs.3.10, 3.27 and 3.28) either with a step-function, or with a compact sigmoid (see Apdx. A.1).

3.5.2.3 Delay interpolation and caching

As discussed previously, the computation of delayed interactions at each time-step is the main bottleneck of our simulations. We were able to reduce the simulation times significantly, when using single-step solvers (multi-step solvers were not implemented in our library), with the following approximation.

For a given timepoint t and step-size h, single-step solvers (like the Runge-Kutta methods) may evaluate the system at any point within the interval $[t, t+h]$. In our experiments, we required that the smallest delay be larger than the (largest) step-size during integration, such that all delayed terms relative to the system at time $t+h$ would refer to timepoints prior to t, and could therefore be interpolated[16].

We then isolated the delayed terms for each state-variable (when applicable) in the systems of ODEs, such that:

$$\forall 1 \leq k \leq N, \quad D_k^{\mathrm{WC}}(t) = \sum_{i \in \Omega_k} c_{ik} X_i(t - \lambda_{ik}) \qquad \text{(see Eq.3.10)}$$

$$D_k^{\mathrm{CB}}(t) = \sum_{i \in \Omega_k} w_{ik} \mathcal{S}_k\Big(V_i(t - \lambda_{ik})\Big) \qquad \text{(see Eqs.3.27, 3.28)}$$

where N denotes the number of nodes in the network; the superscripts WC and CB indicate the model; and $\Omega_k = \Big\{ i \;\Big|\; \lambda_{i,k} > 0 \Big\}$ is the set of remote nodes coupled to node k with positive delay. Prior to the step, these variables were computed for each node at time t and $t+h$ (using multiple threads for further acceleration), and used subsequently during each intermediate step[17] for linear interpolation:

$$\forall 0 \leq a \leq h, \quad D(t+a) = (1-w)D(t) + wD(t+h)$$

where $w = a/h \in [0, 1]$.

[16] When using adaptive-step methods, the interpolants were located using dichotomic search amongst past timepoints.

[17] For example, the method `DOPRI853` evaluates the system 11 times per step.

Most people use analytics the way a drunk uses a lamppost;
for support rather than illumination.

— David Ogilvy

4

Analysis Methods

Contents

4.1 Introduction

The biophysical models presented in chapter 3 aim at relating brain structure and function: the *structural* information is derived from diffusion tractography (see §2.3), and serves to parametrise the interactions between different brain regions (coupling strength and propagation delay); whereas the *functional* information is derived from MEG resting-state data (see §2.4), and serves as a reference to be compared against simulations. This last step is crucial to the modelling process, as it allows to assess the relevance of certain choices (*e.g.* using the same local parameters in all brain regions, or using different seeding methods for tractography), so they can be subsequently revised in an incremental fashion.

The comparison between simulated and empirical data depends on a set of analytic methods, not only to characterise the features of interest (*e.g.* FC matrices or spectral contents), but also to define reliable measures of similarity. In this chapter, we briefly describe the main ideas and methods that were used in our experiments, in particular with regards to characterising the oscillatory dynamics of empirical and simulated signals of brain activity, and measuring their functional connectivity.

4.2 Oscillatory Dynamics

Electro-physiological measurements of brain activity are generally considered to be well characterised as oscillatory (see §2.4.4), it is therefore relevant to dwell on mathematical and numerical methods that allow us to manipulate and characterise such signals. In this section, we focus on the spectral properties of oscillatory signals, and specifically on the estimation of the so-called **instantaneous phase and frequency**.

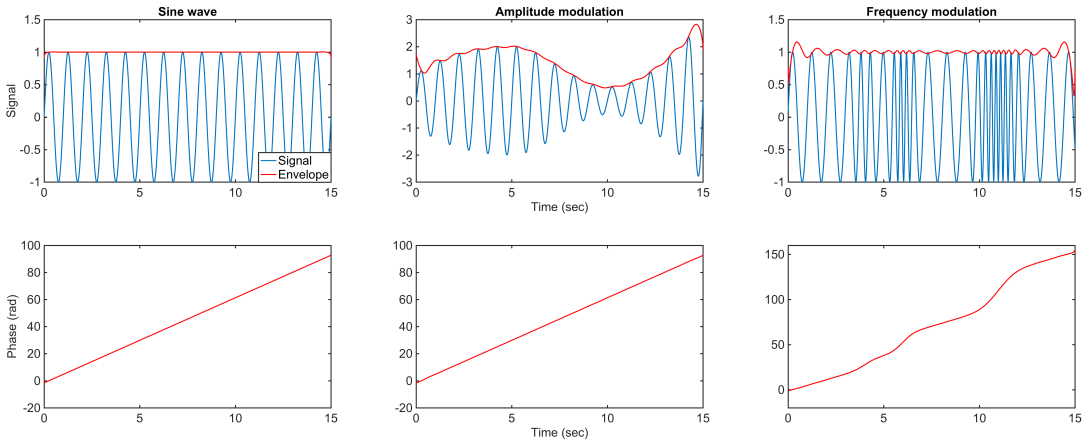

Figure 4.1: Different types of oscillatory activity, and corresponding analytic signals. The so-called Hilbert envelope and phase are shown respectively in red, and on the second row. Although ripple-artefacts are noticeable in the case of amplitude and frequency modulations, the analytic signal is a remarkably flexible representation of oscillatory dynamics.

4.2.1 Mathematical representation

The phenomenon of *oscillation* can be described as a repetitive variation (over time) of a quantity about a central value. In the case of periodic oscillations, the same variation is repeated indefinitely with exactly the same shape (or *waveform*), such that it is sufficient to describe a single period in order to fully characterise the signal. More generally however, oscillatory signals are characterised in terms of their **amplitude** and **phase**, which indicate respectively the size of the excursion from the central value, and the degree of progression through a single oscillation (typically between 0 and 2π).

Formally, if $x(t)$ denotes a real-valued function of time exhibiting oscillatory behaviour, we associate the corresponding complex-valued function of time:

$$\forall t, \quad \widetilde{x}(t) = a(t)e^{i\phi(t)} \tag{4.1}$$

where $i = \sqrt{-1}$, and a and ϕ are respectively the amplitude and phase of the signal. Note that the amplitude is always non-negative, *i.e.* $\forall t, a(t) \geq 0$.

This is a generic definition; in practice, there are several methods to estimate the functions a and ϕ, leading to non-equivalent concrete definitions of $\widetilde{x}$. The **continuous wavelet transform** (CWT) is one example of such a method, which requires the choice of a particular waveform (*e.g.* the Morlet wavelet), and can only be computed at specific frequencies (by scaling the waveform in time). The **analytic signal** is another example relying on the Hilbert transform, as introduced previously in §3.1.3.

In the context of brain activity measurements, both methods have their limitations. The Hilbert transform is capable of representing different types of oscillatory activity, including frequency modulation (see Fig. 4.1), as well as different waveforms (see next section), provided that the underlying signal be "pure" (also called *mono-component* or *narrow-band*), meaning that it should **not** be a superposition of different oscillatory processes. This is ensured in practice either by filtering the signals into different frequency-bands (see §2.4.5), or more rigorously by decomposition into a set of so-called intrinsic-mode functions (IMF, see Huang et al. 1998). By comparison, the wavelet approach is able to deal with the summation of several oscillatory processes. However, it requires the choice of a suitable waveform, it is computationally costly (both in runtime and memory) because it needs to be computed for each frequency individually, and it usually suffers from poor temporal resolution in lower frequencies due to the increasing size of the convolution kernel (time-dilated waveform).

4.2.2 Instantaneous frequency

The notion of instantaneous frequency — in other words, defining the frequency of a signal as a smooth function of time — is somewhat controversial in the literature. As discussed in (Huang et al. 1998, section 3), this controversy is due mainly to two reasons:

- The meaning of a frequency usually relates to some periodicity in the data, and the existence of a period implies the repetition of a particular waveform. In practice,

signals measured experimentally are not truly periodic (often even non-stationary), and their frequency distribution then typically relates to a Fourier decomposition over a large time-frame. From this perspective, adapting the idea of frequency to be defined at each timepoint is challenging; not only is it difficult to consider smooth frequency variations between different waveforms, but by continuity this also implies frequency variations within a single period, which can be confusing.

- Expanding further on the idea of decomposition, signals measured empirically often result from a combination of multiple oscillatory processes, especially in the case of brain activity for instance. Therefore, even if we agree on a definition of the instantaneous frequency for a particular oscillatory process, a single value at each time-point is not sufficient to characterise *all* "sub-processes". Hence, several authors require the signal to be mono-component (Cohen 1995) or narrow-band (Schwartz et al. 1995) in order to preserve the meaning of the Hilbert transform; although to our knowledge, no clear specification of either of these requirements has been given to this date.

Looking at the frequency modulation panel in Fig. 4.1, we see that the slope of the Hilbert phase varies with the frequency of the oscillations. This example provides intuition for the following definition of the **Hilbert frequency**:

$$\forall t, \quad \omega(t) = \frac{1}{2\pi}\frac{\mathrm{d}\phi}{\mathrm{d}t} \tag{4.2}$$

This definition is widely used, and yields a time-resolved frequency which usually behaves as expected in simple cases. However, there are at least two important caveats with this method: **i)** this quantity effectively represents the "velocity" along the trajectory of each oscillation, but in practice there is no guarantee that this velocity should be constant, especially in the case of non-sinusoidal oscillations; and **ii)** empirical measurements are typically noisy, and the derivative is a high-frequency operator, therefore accurate estimations of this quantity from the data can be difficult in practice.

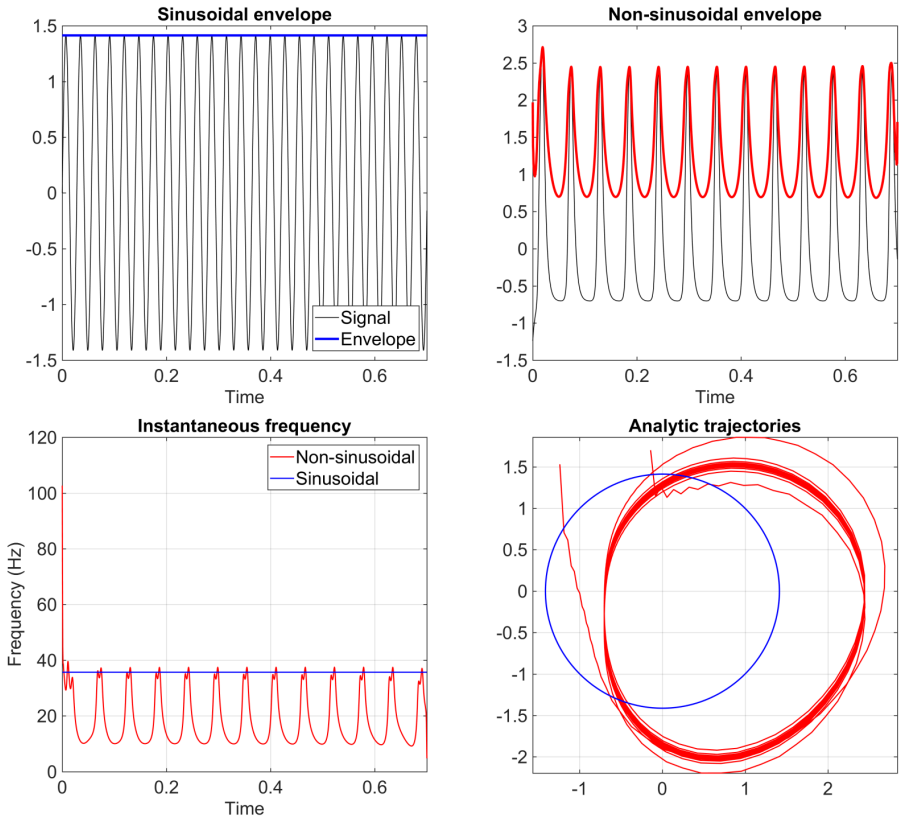

Figure 4.2: The analytic signal in the case of non-sinusoidal oscillations. **First row.** Sinusoidal wave oscillating at 40Hz on the left, and non-sinusoidal oscillations on the right, simulated using the conductance-based model presented in §3.4.1, and normalised to zero mean and unit variance. The corresponding Hilbert envelopes are shown respectively in blue and red. Note that although both signals are periodic, non-sinusoidal oscillations lead to envelope distortions, which cannot be easily distinguished from amplitude modulations (see Fig. 4.1). **Second row.** Trajectories of the corresponding analytic signals (see Eq. 3.2, p.42) in the complex plane (right), and instantaneous frequencies taken as the derivative of the Hilbert phase (left). Non-sinusoidal oscillations are characterised by a non-circular trajectory in the complex plane, along which the signal may not progress steadily. Variations of angular velocity along this trajectory correspond to variations in the phase's derivative, leading to oscillations in the instantaneous frequency.

The consequence of the first caveat is illustrated in Fig. 4.2, with non-sinusoidal oscillations generated using the conductance-based model presented in §3.4.1. The trajectory of the corresponding analytic signal is non-circular, due to distortions of the Hilbert envelope. In addition, the angular velocity along this trajectory is not constant, which leads to oscillations in the instantaneous frequency, as defined in Eq. 4.2. Such oscillations are often undesirable, because they lead to frequency variations even in the case of perfectly periodic signals (and within single oscillations). We propose a simple method to remove them in Apdx. B.2.

The second caveat relates to our discussion about stochastic differentiation in §3.3.2.1: the derivative relies fundamentally on the assumption of local linearity, which does not hold in the presence of noise. In practice, this means that naive differentiation schemes such as forward or backward differences, or using local interpolation, should be avoided. Instead, we propose a linear filtering approach in Apdx. B.1, inspired by the so-called "max-flat" design developed by (Selesnick 2002); this approach consists in estimating the coefficients of an FIR filter subject to tangency constraints imposed in the frequency domain.

4.3 Functional Connectivity: Measure and Comparison

Functional connectivity (FC), as introduced previously in §2.4.5, aims at quantifying the relationships between different time-courses (*e.g.* corresponding to the activity within different brain regions), by measuring statistical dependencies between them. In this section, we first introduce a few measures commonly used in the analysis of resting-state MEG data, which we categorise as "*cosine metrics*". We then propose a new metric combining information about both the instantaneous amplitude and frequency, discuss its relevance within the framework of *communication through coherence*, and demonstrate its performance on real MEG data. Finally, we introduce several metrics for the comparison of functional connectivity matrices between empirical and simulated data, which will be used in chapters 6 and 7.

4.3.1 Cosine similarity metrics

In the following, $f, g \in L^2\left(U \mapsto \mathbb{C}\right)$ denote two complex-valued functions defined on the finite domain U, over which their squared magnitude is integrable. The **inner-product**

between these two functions is defined as:

$$\langle f, g \rangle = \int_U f(u) g^*(u) \, \mathrm{d}u$$

where g^* denotes the complex-conjugate, and this product induces a **norm** $\|f\| = \sqrt{\langle f, f \rangle}$. Equivalently in the discrete case where f and g are defined by N timepoints:

$$\langle f, g \rangle = \sum_{k=1}^{N} f_k g_k^*$$

Given these definitions, we measure the similarity between f and g as their cosine:

$$\cos(f, g) = \frac{\langle f, g \rangle}{\|f\| \, \|g\|} \tag{4.3}$$

Note that this is a complex number in general. This formulation simplifies the definition of various connectivity measures used in practice, assuming that f and g correspond to signals in different brain areas (*e.g.* simulated using LSBMs, or parcellated from source-reconstructed MEG), for example:

- The **envelope correlation** (EC) corresponds to the choice of $f = |\widetilde{x}| - \overline{|\widetilde{x}|}$, where $\widetilde{x}$ corresponds to the analytic signal, and $\bar{\cdot}$ denotes the average over time. See (Brookes et al. 2011a) for an example application in the analysis of MEG.
- The **coherency** corresponds to the choice of $f = \mathcal{F}[x](\omega)$, where $\mathcal{F}$ denotes the Fourier transform, and in that case the domain U corresponds to frequencies (not time). The magnitude of the coherency is commonly called the *coherence*, and its imaginary part is also used as a connectivity measure (Nolte et al. 2004).
- The **phase-coherence** (Mormann et al. 2000) corresponds to the choice of $f = e^{i\phi(t)}$ (*i.e.* the *phasor*), where ϕ denotes the Hilbert phase. Note that this is different from the measure of *synchrony*, previously defined in Eq. 3.4 p.44; in that case, the phasor was averaged across brain regions at each time-point (*i.e.* as a scalar-valued

metric), whereas here we consider the average phase difference over time between pairs of regions (*i.e.* as a matrix-valued metric).

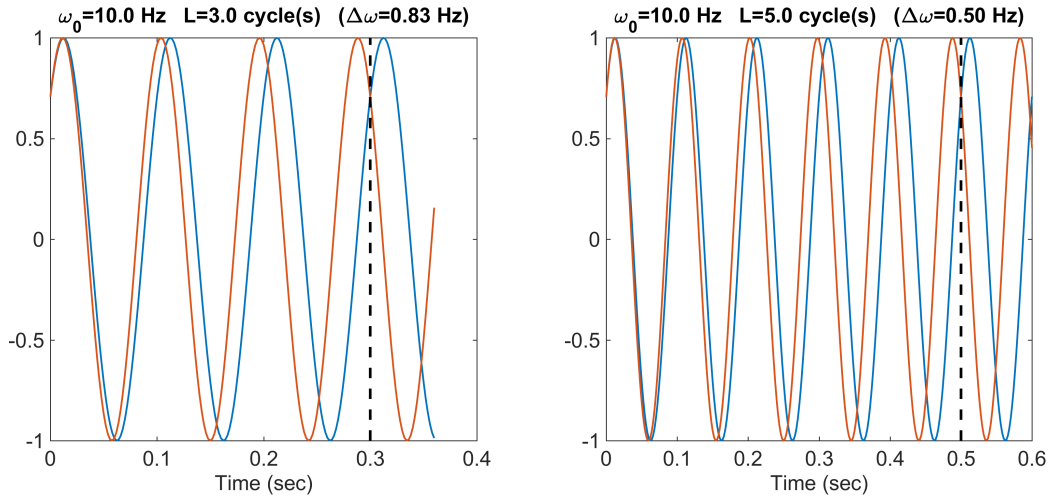

Figure 4.3: Illustration of the desynchronisation length (black dashed line) between two sinusoidal waves (red and blue plain lines). The length is specified as a number of cycles, and corresponds to the amount of time required for two initially synchronised signals with different frequencies to reach phase-opposition. The longer this time, and the smaller the frequency-difference between the two waves.

4.3.2 Communication through coherence

The principle of *communication through coherence* (Fries 2015) postulates that two populations of neurons communicate most effectively when they oscillate at the same frequency (Deco et al. 2016). This follows from the intuition that two coherent electromagnetic waves interfere with each other in an orderly manner, and this predictable order can be exploited to encode information.

In this section, we propose an alternative connectivity measure, which we call "coherence-weighted correlation". It consists in correlating the Hilbert envelopes between two signals (as with EC mentioned previously), but does so by down-weighting the time-points at which the corresponding Hilbert frequencies are different. In order to quantify this difference in an intuitive manner, we introduce the idea of **desynchronisation length**, as illustrated in Fig. 4.3.

For two periodic signals x_1 and x_2, initially in-phase, and respectively oscillating at frequencies ω_0 and $\omega_0 + \Delta\omega$ (in Hertz), the desynchronisation length corresponds to the minimum amount of time needed for the two signals to reach phase-opposition (*i.e.* $|\Delta\phi| = \pi/2$). This time-length, denoted L, is expressed in number of cycles relative to the frequency ω_0. Formally, L and $\Delta\omega$ are related by:

$$2\pi T\Delta\omega = \frac{\pi}{2} \quad \Longleftrightarrow \quad T\Delta\omega = \frac{1}{4} \quad \Longleftrightarrow \quad L\Delta\omega = \frac{\omega_0}{4} \tag{4.4}$$

where $T = L/\omega_0$ is the corresponding time-length in seconds. Note that this relation can be used either to determine the desynchronisation length from a given difference of frequency between two signals, or conversely to determine the maximum frequency difference if the two signals should remain approximately synchronised during a given amount of time.

Assuming now that x_1 and x_2 be any oscillatory signals, and considering the previous definitions of the Hilbert envelope, phase and frequency (Eqs. 4.1 and 4.2), we introduce the following definition of the **coherence weight**:

$$W_{1,2}^{(L)} = W_{2,1}^{(L)} = \exp\left[-\left(\frac{\omega_1 - \omega_2}{\frac{\omega_1+\omega_2}{8L}}\right)^2\right] = \exp\left[-\left(\frac{8L(\omega_1 - \omega_2)}{\omega_1 + \omega_2}\right)^2\right]. \tag{4.5}$$

This quantity equals 1 when both signals are perfectly coherent (*i.e.* $\omega_1 = \omega_2$), and decreases towards 0 as the difference $|\omega_1 - \omega_2|$ becomes large in comparison to a given synchronisation bandwidth $B = (\omega_1 + \omega_2)/8L$. This bandwidth was derived from Eq. 4.4, by taking the average frequency $(\omega_1 + \omega_2)/2$ as a reference, and leaving the desynchronisation length L to be controlled as a tolerance factor. Finally, this leads to the following measure of **coherence-weighted correlation** (CWC):

$$\mathrm{CWC}_{1,2}(L) = \frac{\int_U a_1 a_2 \, W_{1,2}^{(L)} \, dt}{\|a_1\|\|a_2\|} \tag{4.6}$$

which, as explained previously, is a simple measure of envelope correlation in which time-points corresponding to low coherence are down-weighted. The resulting band-specific FC matrices computed on resting-state MEG data are shown in Fig. 4.4.

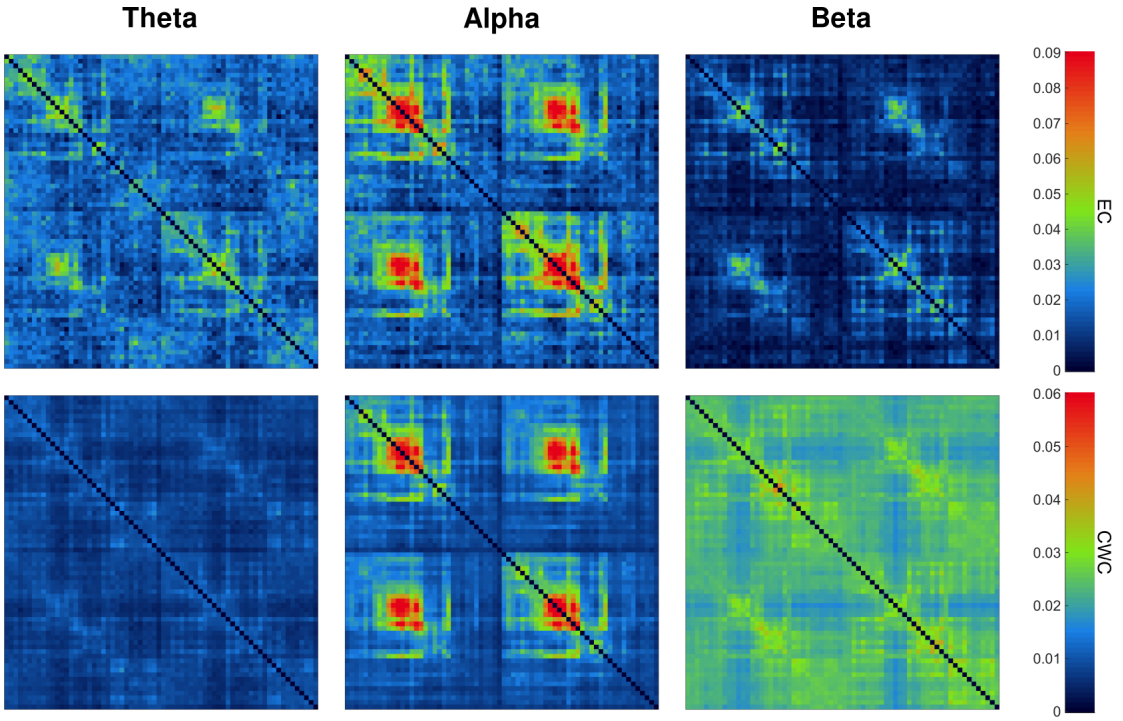

Figure 4.4: Band-specific functional connectivity matrices obtained using envelope correlations (EC, top-row) and coherence-weighted correlations (CWC, bottom-row) with $L = 3$ (see Eq. 4.5), and averaged across 28 subjects in our MEG dataset.

We found that this metric improved the consistency of band-specific resting-state FC matrices across subjects in our MEG dataset. This improvement was tested with a so-called "split-half reliability" approach: the 28 subjects were randomly assigned to one of two equal-sized groups, and the similarity between average FC matrices within each group was taken as the correlation between their lower-triangular values. This procedure was repeated 100 times, in order to estimate a distribution of similarity score insensitive to the particular groupings. The FC was measured either with EC or CWC, in six overlapping frequency-bands:

$$[4,8]\ [6,10]\ [8,13]\ [10,20]\ [13,30]\ [20,40]\text{Hz}$$

and the 100 groupings of the subjects were identical for both connectivity measures. The results of this test are presented in Fig. 4.5, and suggest that FC measurements using the proposed metric are more reliable than with EC.

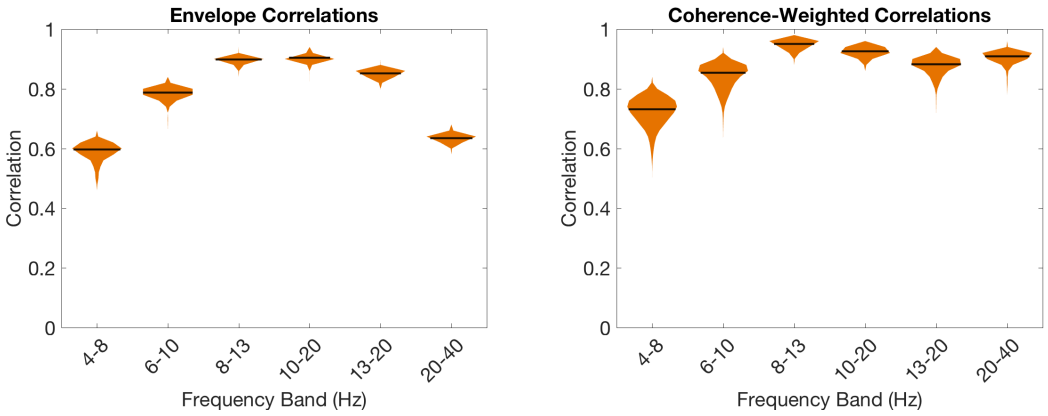

Figure 4.5: Consistency across subjects of envelope correlations (EC, left) and coherence-weighted correlations (CWC, right) with $L = 3$ (see Eq. 4.5). The 28 subjects in our dataset were split randomly into two equal-sized groups, and the FC was computed and averaged within each group, using either EC or CWC, in six overlapping frequency-bands (see §4.3.2). The correlation between the lower triangular values of these FC matrices in each group was computed, and the procedure was repeated 100 times in order to estimate a distribution of correlation insensitive to the particular groupings. Overall, CWC improved the average correlation between groups across bands compared to EC, although the spread of the distribution was also larger.

4.3.3 Comparing functional connectivity

Whatever measure of FC is used to quantify the dependencies between the activity in different brain regions (see §4.3), we also need to evaluate the similarity between the resulting matrices in the empirical and simulated data. This is particularly important in the context of optimisation, as we will see in the next chapters, with regards to the choice of an objective function; if the objective is not specific enough, or does not capture all of the features of interest, the search for a best fit might be ineffective, or even inaccurate. In this section, we present a few measures of similarity that were tested in our experiments, and discuss potential future work in this direction.

4.3.3.1 Modified correlations

The first obvious similarity metric between FC matrices is to correlate their elements. Most metrics in practice are non-directional, and self-similarity is often not of interest; hence FC matrices are usually symmetric, and their diagonal should be ignored. In that case, correlations should be computed between the lower (or upper) triangular values only.

Additionally, in the context of resting-state MEG (see §2.4) or LSBM simulations (see chapter 3), connectivity analyses are typically carried out in different frequency-bands. The similarity between empirical and simulated data should then combine these band-specific similarity scores. However, a simple average across frequency-bands misses an important aspect of the data; the magnitude of the FC varies across the different bands (*e.g.* the EC is stronger in alpha band), and certain bands are more "important" than others with regards to model-fitting (*e.g.* alpha vs. gamma). Furthermore, the absolute magnitude of the FC should be expected to vary between empirical and simulated data (*e.g.* due to noise), hence the valuable information is in the *relative* amounts of connectivity in the different frequency-bands.

This information can be factored into the similarity metric by including a term which explicitly compares those magnitude patterns. Denoting $M_{1..n}$ the FC matrices in n different frequency-bands, we define the vector of **relative connectivity magnitudes** as:

$$u = \left[\frac{\mu_k}{\max_j |\mu_j|} \right]_{k=1..n} \tag{4.7}$$

where μ_k is the average off-diagonal correlation coefficient in matrix M_k. By definition, the largest element in this vector has magnitude 1 (*e.g.* in alpha band), and the magnitude of each element gives the amount of connectivity in one band compared to the principal one (*e.g.* in theta compared to alpha).

Finally, this leads to a similarity metric which combines the average correlation across bands, with a comparison of the relative amount of connectivity between them:

$$\left[1 - \mathrm{RMS}\left(\frac{u^{\mathrm{emp}} - u^{\mathrm{sim}}}{2} \right) \right] \cdot \frac{1}{n} \sum_{k=1}^{n} \mathrm{TrilCorr}\left(M_k^{\mathrm{sim}}, M_k^{\mathrm{emp}} \right) \tag{4.8}$$

where $\mathrm{TrilCorr}$ denotes the correlation between lower-triangular elements; superscripts refer to the simulated or empirical data; and the first factor is a normalised measure of similarity (in $[0, 1]$) based on a root-mean-square (RMS) metric, which is 1 when $u^{\mathrm{ref}} = u^{\mathrm{sim}}$, and decreases towards 0 as the distance between them increases. The multiplication of these two terms corresponds to a logical conjunction; we preferred this choice to that of an addition, because it penalises cases where only one of the criteria is met.

4.3.3.2 Riemannian metrics

The modified correlation presented previously combines information about the similarity within and between bands. In general, it is a good idea to enrich the similarity metric with several complementary criteria, in order to make it more specific to the particular features of interest. However, there are fundamental shortcomings about the correlation as a measure of similarity between FC matrices; while it is important to characterise the

variation of connectivity values around their mean in a statistical manner (the correlation is a cosine between z-scores), ultimately it does not capture explicitly the **patterns** within these matrices. Doing so requires some interpretation of the connectivity values, for example as the adjacency of a graph, or as the extents of a geometric shape in some higher dimensional space.

Riemannian metrics adopt the latter perspective: they have been used in the past to measure distances between covariance matrices by exploiting geometric features induced by their structure (Smith 2005). Below we propose a short introduction starting from basic considerations in linear algebra (skip to Eq. 4.9 if you already know about this), which allows us to highlight key aspects of the distance formula typically used in practice. Based on these remarks, we introduce a novel similarity metric, with desirable properties in the context of model optimisation.

The geometric properties of a matrix can be characterised by its **eigenspectrum**: the set of eigenvectors can be interpreted as a transformation of the original basis by a series of rotations and reflections, and the eigenvalues correspond to spatial extents in the resulting transformed space. In particular, covariance matrices, and more generally symmetric positive definite (SPD) matrices[1], always have positive eigenvalues, and correspond to convex functions in analysis (the Hessian matrix of convex functions is SPD).

In order to compare two different matrices A and B in terms of their geometric properties, we need to relate their eigenspectra. This can be done either by calculating each spectrum independently, and comparing both *a posteriori*, or more generally by solving the so-called **generalised eigen-decomposition** problem. This decomposition yields a set of *shared* eigenvectors V (in column), and a set of eigenvalues D (on-diagonal) representing the *relative* contribution of each eigenvector to the structure of B compared to A, such that $AV = BVD$.

[1] By definition, a matrix M is positive-definite if $\forall z \neq 0,\ z^t M z > 0$. In that case, $\forall z \neq 0,\ z^t M z = z^t P^{-1} D P z = (Pz)^t D (Pz) > 0$, where $P^{-1}DP$ is the eigen-decomposition of M (such that D is diagonal and $P^t P = I$), implies that all eigenvalues are positive.

By requiring the structure of A and B to be described by the same components, we can easily measure structural differences by looking only at the generalised eigenvalues.

The overall contribution of each generalised eigenvector to the structure described by both matrices is encoded in their norm. And each generalised eigenvalue is a factor by which A and B differ in weighting the corresponding eigenvector:

- If it equals 1, then both matrices extend equally along this direction;
- If it equals $x \neq 1$, then B extends x times more than A along this direction, and equivalently A extends $1/x$ times less.

In order to penalise differences equally for reduction or increase, the logarithm is the ideal function to use, since $\log(x) = -\log(1/x)$. However, this requires the eigenvalues to be positive. Hence the definition of the Riemannian distance between SPD matrices A and B:

$$d(A, B) = \sqrt{\sum_k (\log \lambda_k)^2} \tag{4.9}$$

where $\lambda_k > 0$ denotes the k^{th} generalised eigenvalue (see Smith 2005, eq. 65). If all generalised eigenvalues are 1, then this distance is 0. Otherwise, whether B varies x times more or less than A along a direction, the contribution to the squared distance is the same, namely $(\log x)^2$.

In this metric however, we treat all eigenvalues equally, regardless of how important the associated eigenvector is. Furthermore the distance is unbounded, which makes it difficult to work with when combined with other metrics, *e.g.* for multi-criteria optimisation. We address both of these issues by introducing a **novel similarity metric** from this definition, in which each generalised eigenvector contributes proportionally to its norm, and maximally when the associated eigenvalue is 1.

This way, larger eigenvectors have more influence in quantifying the similarity between the two matrices:

$$S(A,B) = \frac{\sum_k w_k \|v_k\|}{\sum_k \|v_k\|} \quad \text{where} \quad \forall k,\ w_k = \frac{1}{1+|\log \lambda_k|^{1/\alpha}} \tag{4.10}$$

where v_k denotes the k^{th} generalised eigenvector associated with λ_k, and $\alpha > 0$ controls the **sensitivity** to small structural changes[2].

4.4 Future Work

There are important topics that were not mentioned in this chapter, for the sake of brevity. For example about time-windowed analysis, which leads to the study of fast transient connectivity patterns using hidden Markov models (HMM), currently the object of active research (Baker et al. 2014; Vidaurre et al. 2016). From the perspective of FC measurements, there is a notable interest in the application of information-theoretic measures (*e.g.* transfer-entropy) to electrophysiological data (Wollstadt et al. 2014; Dimitriadis et al. 2016). Finally, the so-called empirical mode decomposition (EMD, see Huang et al. 1998) is gradually attracting attention in the context of time-frequency analysis, for its ability to circumvent several issues encountered in practice with current methods (*e.g.* the ambiguity introduced by harmonics in Fourier analysis, or the compromise of time/frequency resolution with wavelets).

It will be interesting to see future developments in the characterisation of fast dynamics in resting-state MEG, and more generally in the study of transient behaviour (*e.g.* measures of chaos and meta-stability).

[2] Since $\log(1+x) \underset{x=0}{\sim} x$, we have $w_k \sim 1/(1+|1-\lambda_k|^{1/\alpha})$ when λ_k is close to 1. And because the function $1/(1+x)$ is flat around 0, this measure is poorly sensitive to small changes when $\alpha \leq 1$.

On a different note, the shortcomings of the correlation as a measure of similarity between FC matrices needs to be addressed; Riemannian metrics (as presented previously) may bring some improvement, but ultimately an explicit generative model formulated in terms of *patterns* (for example Aicher et al. 2014) is needed in order to derive meaningful measures of similarity, and characterise differences between individuals.

Overall, the reliability of MEG resting-state FC analyses across subjects is relatively poorly characterised to date, although this should soon be addressed through large-scale studies like the Human Connectome Project (Larson-Prior et al. 2013; Colclough et al. 2016), project OMEGA (Niso et al. 2016), and the MEG UK Partnership (Grant: MR/K005464/1). From a modelling perspective, the wealth of data available, as well as the fine temporal time-scales in electrophysiology, are definitely a strength. However, the lack of consensus about the practical implementation of advanced analysis methods (such as transient connectivity analysis), as well as the computational costs usually associated with their use, is currently an impediment to the development of LSBMs and associated fitting methods.

A Bayesian is one who, vaguely expecting a horse, and catching a glimpse of a donkey, strongly believes he has seen a mule.

— Karl Pearson

5

Bayesian Optimisation

Contents

5.1 Introduction

Large-scale biophysical models (LSBMs), as most other phenomenological models, are **generative** in nature. This means that they typically model the observed data from the bottom-up, and consider the effects of various parameters (controlling the "environment") on the underlying physical system. This is consistent with the usual reductionist approach in sciences, whereby empirical measurements are explained in terms of some combination of underlying causes; in the case of scientific modelling, the set of causes and the ways in which they interact form the hypothesis to be tested against evidence. The generative aspects of these models stems from their bottom-up approach; it is usually much easier to produce an output for a given set of parameters, than it is to infer the parameters causing a certain output to be observed.

This reverse approach is known as **model inversion**, or as the "inverse problem". In practice this can be very difficult to do, depending on the number of parameters, the complexity of the model, and the amount of information in the observed data. Nevertheless, model inversion is essential, because empirical measurements are often a proxy for certain properties of interest, which cannot be measured directly (*e.g.* diffusion-weighted imaging to estimate fibre orientations, or computed-tomography to infer tissue density). In practice, inverse problems are often reformulated as **optimisation** problems, where the goal is to maximise the similarity between synthetic data generated by the model, and real observations, by varying certain parameters of interest. The output of such optimisation is a set of inferred values for the parameters — any subsequent interpretation of these values depends on the plausibility of the model itself, and on the success of the optimisation procedure.

In general, efficient optimisation methods exploit the structural properties of the objective (*e.g.* convexity) in order to devise a strategy which guarantees rapid convergence to a solution. However in the case of LSBMs, these properties cannot be theoretically determined, due to the complexity of the system (non-linear coupled delay-differential equations) and to the features being compared (*e.g.* band-specific functional connectivity). Furthermore, these models are computationally costly to simulate; not only because of the numerics (see §3.5.2), but also because reliable estimates of functional connectivity require large time-spans (∼1 min of data). Therefore, any suitable optimisation method will need to restrict the exploration of the search-space to a minimum, in order to remain computationally tractable. This excludes in practice all methods which rely on the gradient or Hessian (because numerical estimates require many function evaluations), but also stochastic sampling methods (*e.g.* MCMC, particle filters or genetic algorithms) which typically rely on large numbers of samples (either for diversity or statistical validity).

In this chapter, we present an optimisation method designed to tackle problems for which a global solution is sought, but where the objective function is expensive to evaluate, and analytics (*e.g.* the objective's gradient) are not available. In particular, this method is suitable for the inversion of LSBMs, with many more parameters than previously attempted in the literature. We adapted the work of (Kawaguchi et al. 2016) in the field of Bayesian optimisation, and further improved upon this method to reach factorial convergence rates, which is unprecedented to our knowledge. It is worth noting that none of the materials in this chapter is specific to the biophysical models presented previously, and may therefore be applied to any other problem with similar constraints.

5.2 Gaussian-Process Surrogate Optimisation (GPSO)

Bayesian optimisation methods (Brochu et al. 2010) operate under the assumptions that the objective function cannot be easily analysed, and/or that it is computationally costly to evaluate. They are able to tackle such difficult problems by *learning* the objective function, through iterative cycles of exploratory sampling and information consolidation. The method presented here is able to explore high-dimensional parameter spaces simultaneously at multiple scales, allowing local optima to compete for the best solution, all the while building and maintaining a smooth map of uncertainty which is used to prioritize the exploration of unknown regions. The rest of this section covers the general ideas behind this method and explains the specific components that are key to its implementation in practice.

5.2.1 Relation with sequential filtering

For a given black-box function F (*e.g.* a non-analytic function) with parameters $\theta \in \Theta$, where the search-space Θ is **bounded**, consider the problem of finding the global maximum $F(\theta^*)$. The most naive approach based on random sampling would be to draw a large sample of candidate points $\{\theta_i\}_{i=1..N}$ uniformly distributed across Θ, and take $\widetilde{\theta^*} = \arg\max_i F(\theta_i)$ as a crude approximation to the global optimum.

Although this approximation is very likely to be inaccurate, if we can assume that F is at least Lipschitz-continuous and that our sample is sufficiently large, then we can gain confidence knowing that any sample $F(\theta_i)$ is representative of some (possibly small) neighbourhood of θ_i; that is, the assumption of continuity can be used for **knowledge propagation** in the search-space. This idea is at the core of Bayesian filtering methods in the context of optimisation; the set of values $\{F(\theta_i)\}_{i=1..N}$ can be used to infer regions of interest in the search-space, and we can iteratively refine this knowledge by resampling

preferentially near known regions of interest, and subsequently reassess our belief about the location and shape of these regions.

With particle filters (Djuric et al. 2003; Liu et al. 2016), the pairs $\left\{\left(\theta_i, F(\theta_i)\right)\right\}_{i=1..N}$ are called *particles*, and this iterative approach is known as **sequential importance resampling**. Specifically, at any given iteration, each particle is assigned a resampling probability proportional to some non-negative increasing function G of their score:

$$\forall 1 \leq i \leq N, \quad w_i = \frac{G(F(\theta_i))}{\sum_k G(F(\theta_k))} \tag{5.1}$$

For example, if F is non-negative, then taking $G = \mathrm{Id}$ (the identity function) leads to resampling probabilities proportional to the scores. If F is signed or unbounded, then it can always be rescaled for any finite ensemble of particles, and in that case G is a different rescaling at each iteration.

We can then carry out N draws (with replacement) according to these probabilities, such that the best particles have a better chance of being selected. Resampling a given particle $(\theta_i, F(\theta_i))$ consists in taking a new point in the neighbourhood of θ_i, typically by sampling from the normal distribution $\mathcal{N}\left(\theta_i, \Sigma\right)$, where the covariance matrix Σ is a hyper-parameter controlling the size and shape of the neighbourhood considered. The objective function F is then evaluated at these new points, and a new iteration can begin. An example of particle-filter optimisation is shown in Fig. 5.1.

Particle filters, as most stochastic sampling methods, are attractive in the context of optimisation because: they make very few assumptions about the objective function; they work in an intuitive manner that is simple to implement and tweak for particular purposes; and they will eventually converge to the global optimum in a bounded search-space. However in practice, their stochastic nature means that the convergence is not reliable unless the number of particles is very large, and this becomes prohibitive in higher-dimensions. Furthermore, it is implicitly assumed that the objective function is

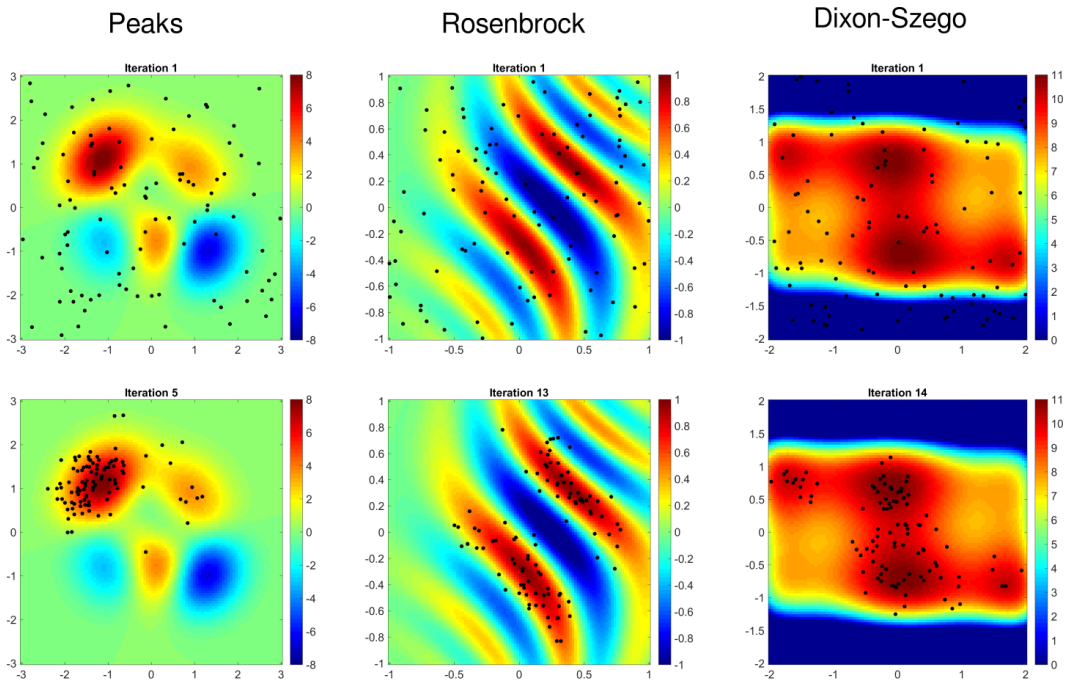

Figure 5.1: Demonstration of particle-filter optimisation on three different test functions (Matlab's peaks function, Rosenbrock, and Dixon-Szego). All optimisations were run for 20 cycles using 100 particles (shown as black dots). We used a normal distribution for resampling, with a relative scale of $1/30$ in each dimension (*i.e.* the covariance matrix is diagonal, and the standard deviation in a given dimension corresponds to the size of the search-space divided by 30). At each iteration, the scores were linearly rescaled such that the particle with the lowest score was assigned a resampling probability zero. Note that particle filters are able to deal with multiple local extrema; in fact, the internal representation of the objective function can be seen as a Gaussian mixture with as many modes as there are of particles.

cheap to evaluate, because sampling methods rely fundamentally on the idea of "strength in number". Indeed, particle filters require as many function evaluations as there are of particles, *at each iteration*.

Overall, sequential filtering methods often suffer from weak information consolidation over iterations (*e.g.* due to the Markov assumption), and from a poorly constrained exploration strategy, which tends to be "wasteful" in higher dimensions. These weaknesses are addressed in what follows, respectively by: accumulating evidence over iterations using a Gaussian-Process in order to gain consistency; and formulating a deterministic exploration strategy in order to gain efficiency.

5.2.2 Optimism in the face of uncertainty

The previous discussion about particle-filters uncovered an important balance in the design of any optimisation method relying on a sampling strategy; the balance between the **exploration** of the search-space, in order to discover new places of interest with respect to the objective, and the **exploitation** of the knowledge accumulated over past iterations, in order to refine the search preferentially in places of known interest.

The balance between exploration and exploitation is best studied within the framework of game theory, where computing time is seen as a limited resource, and we seek to invest this resource as wisely as possible in order to maximise the expected reward (*i.e*. find the highest value of the objective function). In this context, the simplest instance of the exploration-exploitation dilemma is the so-called **multi-armed bandit** problem (MAB) (Auer et al. 2002).

In brief, the MAB problem consists in picking iteratively from a finite set of possible choices, with repetitions allowed, where the outcome of each choice is random with unknown distribution. For any fixed number of picks, the goal is to maximise the cumulative outcome, by taking the best-known choice as often as possible (exploitation), while regularly trying out unknown or uncertain choices (exploration). A posteriori, the difference between the outcome achieved and the best possible outcome is called the *regret*; minimising the regret or maximising the reward is equivalent.

In this case, a successful balance between exploration and exploitation can be achieved by adopting an *optimistic* strategy, whereby at each turn, the best possible outcome for each choice is considered, given an estimate of uncertainty from previous trials. We then iteratively pick the choice with the best expected outcome, and update our uncertainty according to the result obtained. This strategy is known as the **upper confidence-bound** method (UCB), see (Bubeck et al. 2012) for more details.

5.2.3 Surrogate objective function

The first incongruence in the analogy between the MAB problem and continuous optimisation, is that the former applies to finite sets of choices, whereas the latter considers continuous search-spaces where each point is a candidate solution. The second difference is that the objective function is deterministic; evaluating a candidate point does not yield a probabilistic outcome. Reconciling the two contexts (discrete-probabilistic and continuous-deterministic) can be done as follows: **the uncertainty about the outcome of a choice in the MAB problem, is related to the uncertainty about the local topography of the objective function near a candidate point, in the case of continuous optimisation**.

The essence of this relation stems from the assumption of smoothness about the objective function, which induces spatial correlations. In fact, by **partitioning** a given bounded search-space into different areas, and considering the evaluation of the objective function at random points within those areas, the analogy becomes clear; the finite set of choices in the MAB corresponds to the different areas partitioned, and the uncertainty about the outcome of a choice stems from the variations of the objective function within those areas.

This analogy does not solve the issue of efficiency, though. First, naively partitioning high-dimensional search-spaces would yield a prohibitively large number of areas to consider, in the same way that grid-search is intractable in higher dimensions. Second, the assumption of smoothness is not really being exploited by randomly picking points within each area; it would be good to consider spatial uncertainty, as well as expected reward, in order to pick candidate points more wisely.

Estimating smooth maps of uncertainty from a finite sample of points using explicit formulations of spatial correlations is the hallmark of Gaussian Processes (GPs, see Rasmussen et al. 2006), and indeed they have been used previously in the context of Bayesian optimisation for this reason (Freitas et al. 2012). Moreover, GPs provide an

efficient representation of the objective function, based on the evidence accumulated. As additional points become available throughout the search, the parameters of the GPs can be optimised incrementally in order to integrate new information parsimoniously, thereby consolidating our belief about the topography of the objective function in a Bayesian fashion. In fact, GPs can be used as a cheap alternative to the objective function, or **surrogate function**, in order to identify regions of high expected score in the search-space, and devise an effective exploration strategy.

However, the issue remains of partitioning high-dimensional search-spaces into a manageable set of subregions. In the next section, we address this issue by introducing **partition functions**, which break down the search-space into arbitrarily deep hierarchies of non-overlapping areas.

5.2.4 Partition function

The role of the partition function in the context of **GP surrogate optimisation** (GPSO) is to break down the search-space into distinct subregions that can be explored independently. The optimisation algorithm oversees this process at a higher level: it decides which regions should be explored based on the GP surrogate function (which encodes all available evidence); subsequently refines the partition in the selected regions; evaluates the true objective function in these regions to acquire new evidence; and integrates this evidence into the GP surrogate to update its belief about the objective function. This iterative process is summarised in Fig. 5.2, although we will come back to the specific substeps later in §5.2.5. Below, we discuss the general requirements of partition functions in the context of GPSO, and present the solution originally chosen by (Kawaguchi et al. 2016). We will improve upon this solution in §5.3.

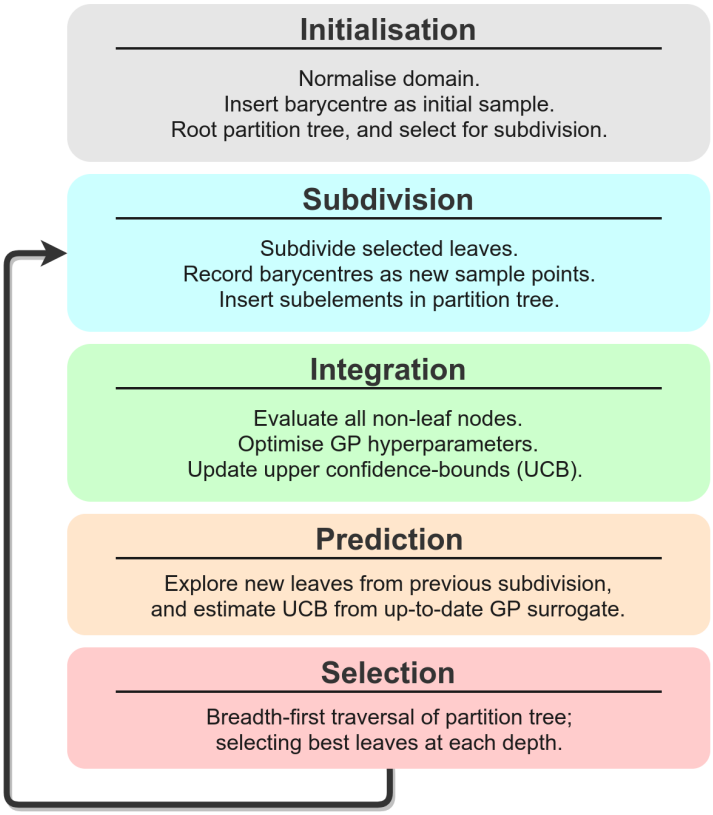

Figure 5.2: Algorithmic summary of Gaussian-Process Surrogate Optimisation (GPSO). The search-space is initially rescaled to normalise the bounds in each dimension to $(0,1)$. The iterations of the algorithm can be summarised in four steps; **i)** *subdivision*, where selected regions are partitioned, and the barycentre of children subelements are registered as new GP-based sample points; **ii)** *integration*, where the true objective function is evaluated in now-partitioned parent subregions, and the GP surrogate is updated accordingly; **iii)** *prediction*, where the expected score in children subregions is assessed using the latest GP surrogate; and **iv)** *selection*, where subregions are selected for further refinement based on the previous predictions.

5.2.4.1 Properties

The choice of any particular partition function is suitable as long as it satisfies the following properties:

- it should be **recursive** (*i.e.* it can always be applied to its own outputs), such that partitioned subspaces can be refined at will in places of interest;
- it should be **covering** (*i.e.* it does not create holes), to ensure that every point in the search-space can be reached.

The recursive property induces a hierarchical structure amongst subregions according to their size, which can be represented as a **partition tree**[1]. Each node in this tree corresponds to a region of the search-space (the size of which decreases strictly with the depth, meaning that we can reach arbitrarily high resolutions), and the children of a node correspond to the subregions obtained by applying the partition function to the parent node. The set of *leaf nodes* (*i.e.* those nodes without children, which may be at different depths) corresponds to the current **state** of the subdivision, and the ancestry information encoded by the tree is a way to **navigate** efficiently the search-space down to these different subregions. In summary, the partition function allows us to identify regions in the search-space, with arbitrary resolution, and since there are only a discrete number of nodes at each depth in the partition tree, the UCB strategy can be applied at each level in a multi-scale fashion.

Furthermore, and although this is not required, it is desirable to restrict our choice to partition functions that are **exactly covering**, in which case any point in the parent region belongs to one and only one subregion after partition (*i.e.* the subregions are non-overlapping). This ensures that there is only one path converging to any specific point in the search-space, and prevents unnecessary competition between nodes during optimisation.

5.2.4.2 Ternary splits

The partition function chosen in (Kawaguchi et al. 2016) applies to hyper-rectangular search-spaces (defined by taking one interval of values for each parameter), and recursively splits the largest dimension (in normalised coordinates) into three equal-sized subintervals. We refer to this partition function as "ternary split" in the remainder. In general N-ary splits confer exponential convergence towards regions of interest. The

[1] A parallel can be drawn with partition refinements in set-theory, where the relation "finer-than" induces an ordering between any given partition and its refinements (*i.e.* the set of partitions is a poset).

choice of $N = 3$ is not trivial; it satisfies two desirable properties with regards to the optimisation, in addition to recursivity and exact covering:

- First, the centre of the parent node is also the centre of the second child, which saves us an evaluation of the objective function at each split;
- And second, because of this conserved point, we can guarantee that the children of a node do not recede, meaning that the progression within a branch is monotonic.

An example of optimisation using this partition function is given in Fig. 5.4, and the corresponding partition tree is shown below in Fig. 5.3. We propose a different partition function in §5.3 below, which improves the convergence rate from exponential to *factorial* in the number of iterations.

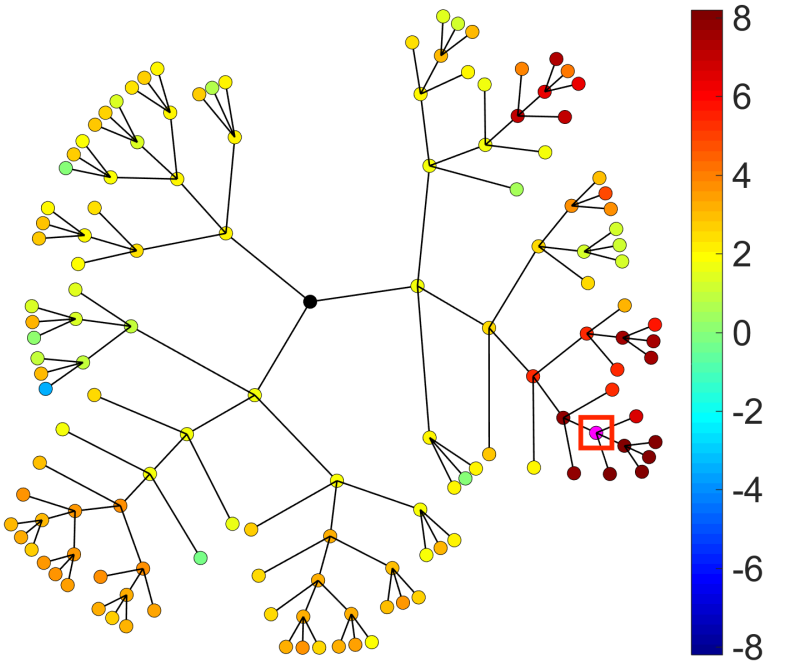

Figure 5.3: Ternary partition tree obtained by running GPSO on Matlab's peaks function (see Fig. 5.4). Nodes correspond to subintervals of the search-space; colours show the associated scores (upper-confidence bounds); and edges represent set inclusion (parent intervals are the union of their children); in particular, deeper intervals are smaller. The root (initial normalised domain) is shown in black, and the region with the best score is marked with a red square. Deeper orange branches at the bottom/left correspond to the local maximum found initially, and red branches on the right correspond to the highest peak.

5.2.5 Concrete implementation

The main challenge of global optimisation methods, as opposed to local methods, is to deal with local extrema in the objective function. This challenge can be efficiently tackled by carrying out multiple local searches in a sequential (*e.g.* simulated annealing, Metropolis-Hastings) or parallel (*e.g.* particle filters, genetic algorithms) manner. The method proposed here implements a special case of the parallel approach, which organises candidate solutions hierarchically using the partition tree introduced in the last section.

The algorithm proceeds iteratively, as summarised in Fig. 5.2. At each iteration, the partition tree is traversed in a breadth-first manner (BFS), in order to select the leaf with maximal expected score **at each level** (unless there is no leaf). Selected leaves are then partitioned in the next iteration. Note that, because we only ever select one leaf node per level in the partition tree, and that each leaf is (by definition) on a branch of its own, the algorithm considers simultaneously at each iteration regions located in different parts of the search-space, and at multiple scales. In fact, a slight improvement can be made to this selection process; since it is pointless to explore regions at a smaller scale, if some region at a larger scale has a better expected score, **any selected leaf at a given depth is discarded if it does not improve on the selection at previous depths**. In effect, this introduces competition between the different scales, and prevents dwelling around local extrema.

Given the previous explanations, there are three points left to clarify in order to get a concrete implementation:

1. For any point x in the search-space, the upper-confidence bound is defined as:

$$\mathrm{UCB}(x) = \mu(x) + \varsigma\sigma(x) \tag{5.2}$$

   where $\mu(x)$ corresponds to the expected value of the objective function f at point x given by GP regression, $\sigma(x) \geq 0$ is the associated standard deviation (*i.e.* the

uncertainty about the predicted score), and $\varsigma \geq 0$ controls our optimism[2].

2. Each leaf-node in the partition tree is labelled as being either: **evaluated**, meaning that the objective function was evaluated at its barycentre; or **GP-based**, meaning that its associated score was estimated by UCB using the GP surrogate function. Specifically, the UCB assigned to a GP-based leaf corresponds to the maximal bound obtained amongst N points sampled within the corresponding region of the search-space, as given by the **sampling function** (see next point). Later on during optimisation, if a GP-based leaf is selected for further refinement, the true objective function is evaluated at its barycentre, and it is relabelled as such.

3. At any stage during the optimisation, the sampling function can be invoked for a given node, and returns a list of N points within the corresponding subregion in the search-space. These points can either be randomly sampled (*e.g.* following a uniform distribution), or deterministically sampled by applying the partition function for a given number of recursions.

Once again, this method is illustrated in Fig. 5.4; it is useful to return to this figure in the light of the previous explanations, before moving on to the next section.

[2]For a GP with Gaussian likelihood kernel, the upper bound of a $p\%$ confidence interval on the expected value corresponds to $\varsigma = \mathrm{erfc}^{-1}(p/100)$, where erfc is the complementary Gauss error function.

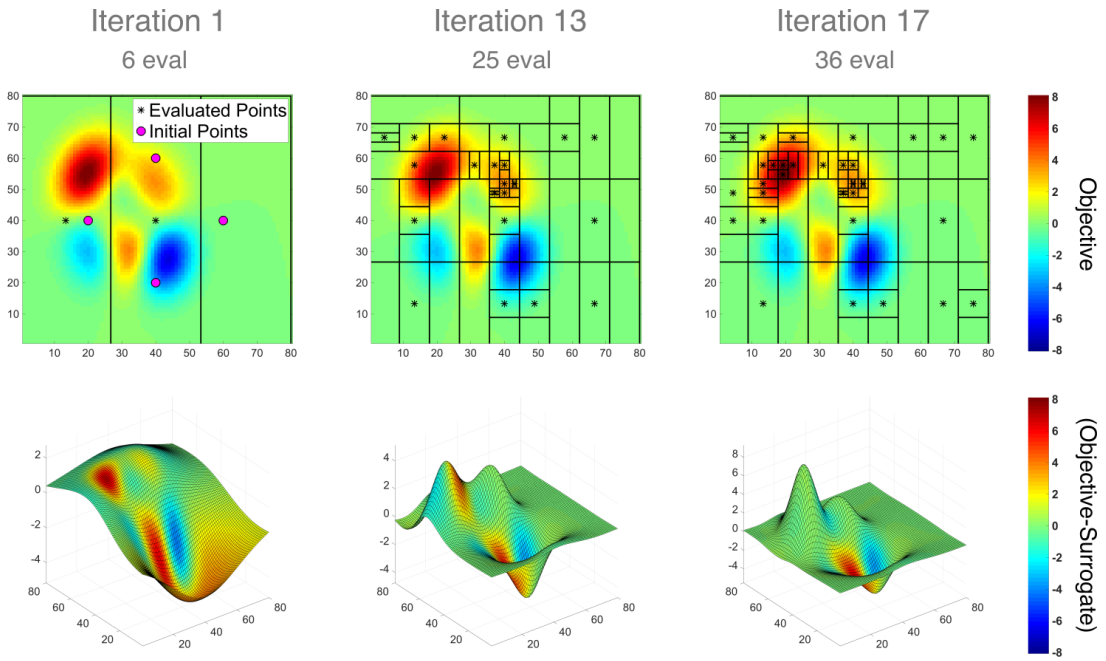

Figure 5.4: Demonstration of GPSO with ternary splits on Matlab's peaks function. The partition of search-space and the GP surrogate function are shown for three different iterations, respectively in the top and bottom row. The boundaries of the partition are shown overlaid on top of the objective function (black lines over coloured background). The surfaces show the predicted mean of the GP surrogate, and colours indicate differences with the true objective: red means that the true objective is higher (resp. lower for blue). **Iteration 1.** Initial sample and 2 points evaluated in the first iteration; the top and bottom initial points are near a peak and a trough, hence the slope of the surrogate. **Iteration 13.** The algorithm initially finds a local maximum, and converges rapidly to its peak by refining the partition around it. Meanwhile, exploration at larger scales hits the slope of the highest peak; the surrogate function shows that the corresponding peak is misaligned (red patch between the two peaks), but it is already higher than the previous peak. **Iteration 17.** The discovery of a higher peak at a larger scale froze the subdivision near the first local maximum. The algorithm converged to the global optimum after 4 iterations. The surrogate peaks are now both aligned with the truth (green colour).

5.3 Simplicial Tessellations

In this section, we present a new partition function which improves upon the ternary splits proposed in (Kawaguchi et al. 2016), by allowing *factorial* convergence rates w.r.t. the number of iterations. To our knowledge, this level of convergence is unprecedented in the literature.

5.3.1 Definitions

In the following, we consider a set $V = \{v_0, v_1, \ ..., v_d\}$ of $d+1$ points in $\mathbb{R}^d$.

These points are said to be in **general position** if they do not lie on some lower-dimensional subspace, which is equivalent to saying that the square matrix $[v_1 - v_0, \ v_2 - v_0, \ ..., \ v_d - v_0]$ (with coordinates in column) has full rank. In that case, the geometric object created by linking every pair of points in V is called a **simplex** (plural: simplices). The space contained within a simplex is **convex**; if two points lie within that space, then so does any point between them. In fact, the simplex is the smallest possible convex subspace which contains V, also known as the **convex hull** of V.

A simplex is a special kind of **polytope**. Polytopes generalise the idea of two-dimensional polygons to higher dimensions, and describe any geometric object with flat faces. In dimension d, the **faces** of a polytope describe features of all dimensions, and are therefore usually prefixed by their dimensionality; for example, a 3-face refers to some 3-dimensional face of a polytope. By convention, the only d-face is the polytope itself, 0-faces are the vertices, 1-faces are called edges, and $(d-1)$-faces are called **facets**. In a simplex, any pair of vertices is connected by an edge, and any subset of d vertices defines a facet (hence, there are $\binom{d+1}{d} = d+1$ facets).

5.3.2 Partial barycentric subdivision

Barycentric subdivision is an algorithm that partitions any d-dimensional simplex into $(d+1)!$ distinct sub-simplices, by recursively replacing vertices in V with the barycentre of those vertices which have not yet been replaced. For example, each of the $d+1$ vertices in V can be replaced with the barycentre of the initial simplex, and therefore the algorithm first branches into $d+1$ different cases, each corresponding to a different sub-simplex. It can be shown that these sub-simplices are non-overlapping and that they cover exactly

the original simplex[3]. The same logic applies at the next recursion, where only d original vertices remain in each of the previous sub-simplices, leading to a further d possible subcases. Similarly over the next recursions, until only one of the original vertices remains, hence a total count of $\prod_{k=0}^{d-1}(d+1-k) = (d+1)!$ sub-simplices after d recursions.

We use the word *recursion* instead of *iteration* on purpose here; a given subelement cannot be easily identified with a single index (as in S_k), but rather by considering the series of subcases which led to it (as in $S_{a,b,c,...}$). More formally, each subelement at recursion k is defined by $d+1-k$ original vertices, and k intermediate barycentres. We denote the corresponding sets of points respectively $U = \{u_1,\ ..., u_{d+1-k}\} \subseteq V$ and B. As explained previously, each barycentre in B corresponds to a p-face for $d+1-k \leq p \leq d$. From the simplex $U \cup B$, the subdivision at recursion $k+1$ yields the following sub-simplices:

$$\left\{U_{\setminus i} \cup (B \cup \overline{U}),\ i = 1\ ..\ d+1-k\right\} \tag{5.3}$$

where $U_{\setminus i} = U \setminus \{u_i\}$, and $\overline{U}$ denotes the barycentre of U. The same process can be applied to each of the resulting sub-simplices, until only one of the original vertices remains, in which case a new cycle of d subdivisions can be initiated by considering each subelement as an original simplex.

A simple implementation is given in Alg. 1. It is worth noting that barycentric subdivision is *not* equivalent to recursive barycentric splits (which is itself not suitable for optimisation, due to multiple issues); a visual comparison is provided in Fig. 5.5. The hierarchy of subcases can be represented as a tree, which is analogous to the partition tree in GPSO (see §5.2.3). Each node in this tree corresponds to a subelement created during subdivision, and each level corresponds to a recursion. The main difference here, is that the number of children for each node depends on the depth: counting from 0 at the root (initial simplex),

[3]Each sub-simplex differs from every other by only one original vertex, which means that it shares a different facet with each of its siblings (of which there are d). Furthermore, its last facet is unique, as one of the $\binom{d+1}{d}$ possible combinations, and belongs to the original simplex.

Algorithm 1 Recursive implementation of barycentric subdivision in Matlab.

```
function S = barycentric_subdivision( V, B )
%
% Barycentric subdivision of the simplex defined by the vertices in V.
% DO NOT RUN THIS CODE IN DIMENSION > 10 !
%
% The first input V is a dx(d+1) matrix of vertices (coordinates in column).
%
% The second input B is used internally for recursive calls, and carries the
% list of intermediate barycentres for each subcase. The number of intermediate
% barycentres corresponds to the depth of the recursion, and in particular the
% total number of points in V and B is always d+1.
%
% The output S is a cell array, in which each cell is a dx(d+1) matrix
% corresponding to a sub-simplex.

   if nargin < 2
      B = [];
      assert( ismatrix(V) && diff(size(V))==1, 'Bad input dimensions.' );
      assert( rcond(bsxfun(@minus, V(:,2:end), V(:,1))) > eps, ...
        'Input points are not in general position.' );
   end

   n = size(V,2);
   if n == 1
      S = [V,B];
   else
      S = {};
      B = [B, mean(V,2)];

      for i = 1:n
         U = V(:,setdiff(1:n,i));
         S = [S, barycentric_subdivision(U,B)];
      end
   end

end
```

all nodes at depth h have $d+1-p$ children where $p \equiv h \pmod{d}$. This corresponds to the number of remaining "original vertices" relative to the latest subdivision cycle.

Finally, since the subdivision of any given subelement is independent from the others (it only depends on the sequence of subdivisions leading to it), we can avoid considering all $(d+1)!$ subelements at each iteration of GPSO, which would be intractable. Instead, by carrying information about the remaining original vertices in each subelement, we can explore individual branches in the partition tree, corresponding to the leaves selected during optimisation (see Fig. 5.2) — a process that we call **partial barycentric subdivision** (PBS).

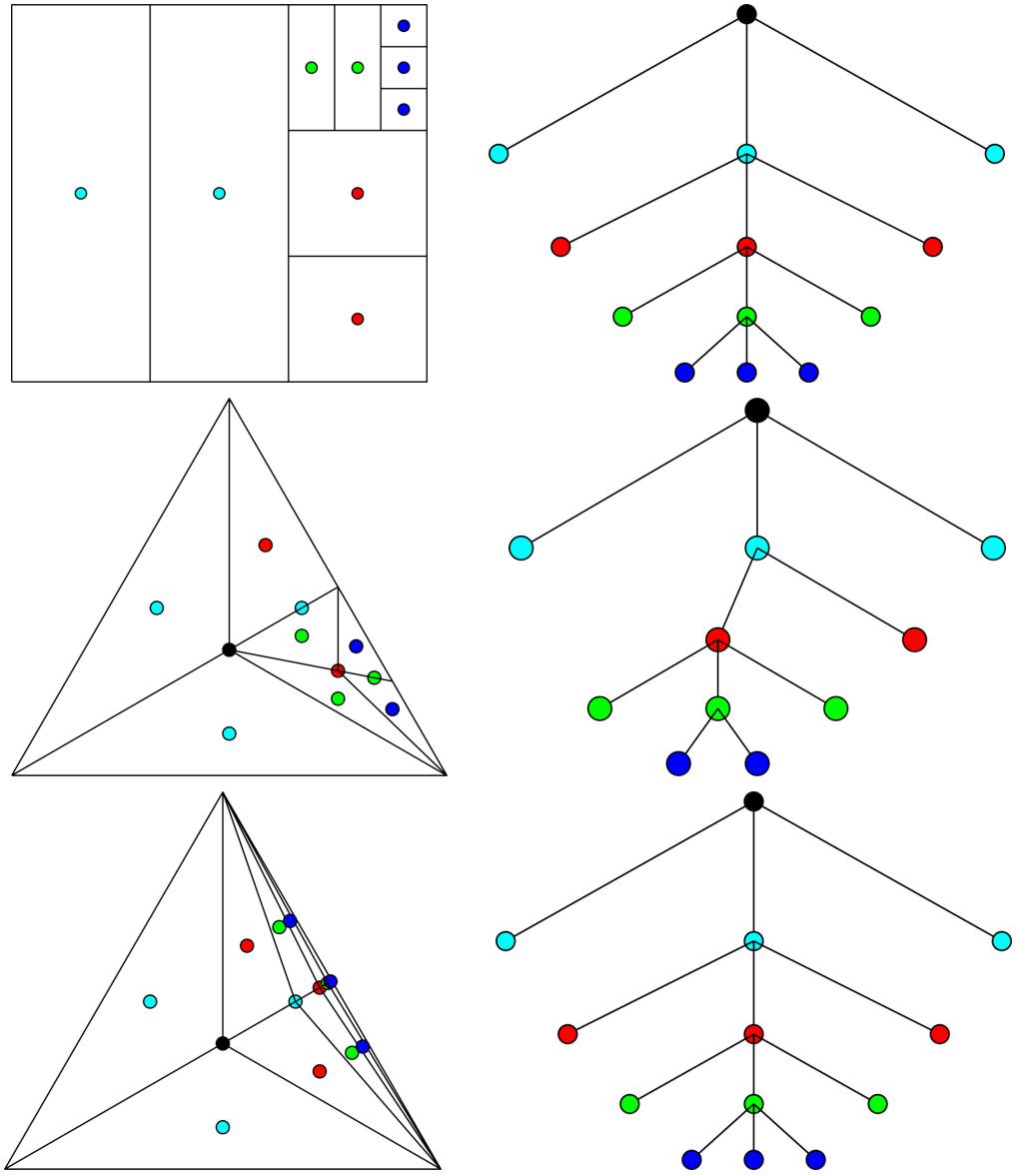

Figure 5.5: Comparison of partial barycentric subdivision (middle-row) to ternary (top) and barycentric (bottom) splits. Geometric illustrations of the subdivisions are shown on the left, and corresponding partition trees are on the right. Colours indicate the depth (0:black, 1:cyan, 2:red, 3:green, 4:blue), and bullet points on the left indicate the barycentre of each subelement (where the objective function is either evaluated or estimated by the surrogate). PBS is *not* equivalent to recursive barycentric splits (see bottom rows); the latter suffers from "flattening" issues, which prevent a suitable coverage of the search-space during optimisation. In contrast, ternary splits cover the search-space in a very orderly manner, but only explore one dimension at a time (alternating with the depth). PBS considers all dimensions at each step, and produces similar-shaped subelements across depths.

5.3.3 Comparison with n-ary splits

Here we compare the efficiency of n-ary splits on d-cubes (with $n, d \geq 2$), to that of PBS on d-simplices. In the context of Bayesian optimisation, the efficiency of a partition function should quantify its ability to reduce the size of the search-space by a certain factor, while evaluating as few candidate points as possible in the process. Denoting F and N respectively this reduction factor and the number of evaluated points, we measure the **efficiency** of a partition function simply with the ratio F/N. Note that this ratio is independent of the geometric properties of the initial search-space (in particular, its shape and size); we will discuss this in the next section §5.3.4.

In the case of regular n-ary splits proceeding sequentially in each dimension of the search-space (as described previously with the ternary splits), after d recursions, the size of the search-space is reduced by a factor $F_{\text{n-ary}} = n^d$. Counting the minimum number of function evaluations is tedious, because at each iteration of GPSO, there is one function evaluation at each level of the partition tree, unless all nodes at this level have already been evaluated (which happens in the first levels if d is large enough). Furthermore, if n is odd and we keep subdividing the middle child, we save one evaluation at each iteration. Skipping over the derivation of this formula, the least possible number of evaluations required to reach a depth d in the partition tree is given by:

$$N_{\text{n-ary}} = \sum_{k=0}^{d-1} \min \Big[n^k, d-k \Big] - (d-1) \tag{5.4}$$

where we subtract $d-1$ only if n is odd.

In the case of PBS, the search-space is reduced by a factor $F_{\text{pbs}} = (d+1)!$ after d recursions. Counting the minimum number of evaluations to reach this depth is equally tedious here, with the added complexity that the number of children varies with the depth in the partition tree. After derivation, the least possible number of evaluation after d recursions of GPSO+PBS is:

$$N_{\text{pbs}} = \sum_{k=0}^{d-1} \min\left[\frac{n!}{(n-k)!}, d-k\right] - 1. \tag{5.5}$$

A comparison of the log-efficiency between both methods (see Fig. 5.6) shows that **PBS is increasingly more efficient with the number of dimensions of the search-space**, and in particular it outperforms ternary splits from dimension 3 upwards.

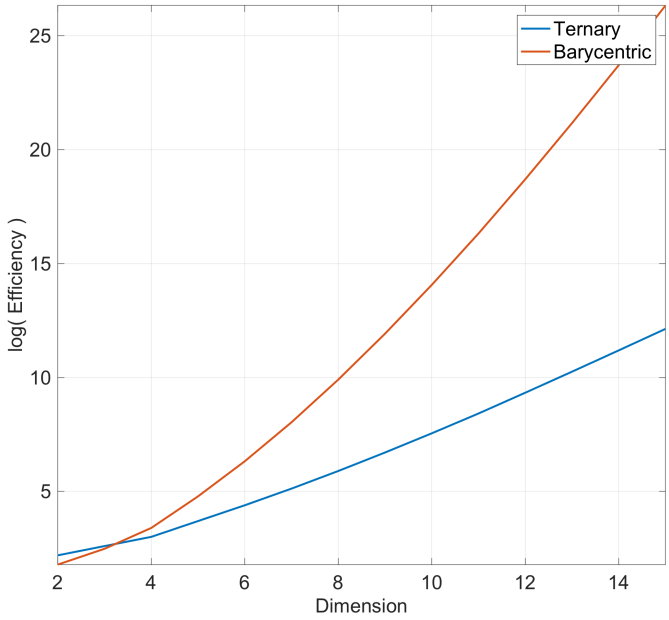

Figure 5.6: Log-efficiency of the partial barycentric subdivision process (red), plotted against that of ternary splits (blue) for an increasing number of dimensions. PBS is increasingly more efficient than ternary splits with the number of dimensions of the search-space. In particular, it performs better from dimension 3 upwards.

5.3.4 The initialisation problem

GPSO considers problems in **bounded search-spaces** only; these bounds are typically specified dimension-wise with an open interval for each parameter. The resulting search-space is a hyper-rectangle, and can be easily normalised to a hyper-cube, by rescaling each dimension affinely between 0 and 1. However, this can be a practical constraint for the choice of a partition function, because all subdivision processes make their own assumptions about the required geometric properties of the search-space (mainly imposed by their recursive nature). In particular, barycentric subdivision, as defined previously, operates on *simplices* and not hyper-cubes; hence there is an immediate issue for initialisation.

This is not a trivial problem. Firstly, it is not sufficient to claim that any hyper-cube is contained within some larger simplex, because the bounds of the search-space may enforce: domain constraints for the objective function (*i.e*. the objective may not be defined outside of these boundaries); or feasibility constraints for the problem at hand (*i.e*. parameters beyond these boundaries might yield irrelevant system configurations). Therefore, considering candidate solutions outside of the specified bounds may not always be possible, or relevant. Secondly, considering a naive auxiliary subdivision process specially for initialisation may result in prohibitive performance hits. For example, taking all possible simplices defined by the vertices of a hyper-cube in dimension d would yield a set of $\binom{2^d}{d+1}$ overlapping simplices, which is utterly inefficient and intractable.

5.3.4.1 Barycentric subdivision of convex polytopes

Although we defined it previously *for* simplices, barycentric subdivision can also be used to partition arbitrary convex polytopes *into* non-overlapping simplices (and from there, we can subdivide recursively using PBS).

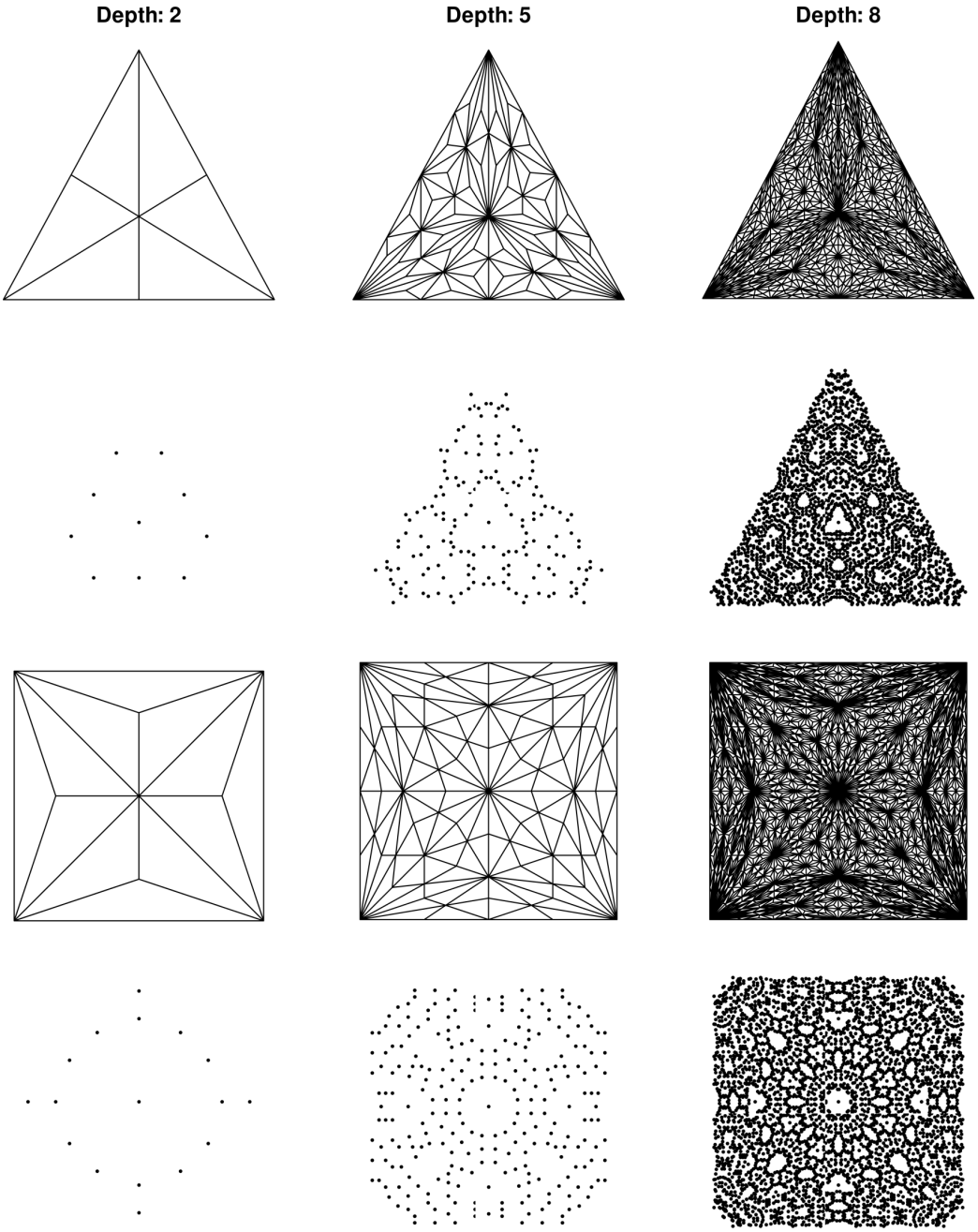

Figure 5.7: Full barycentric subdivision of an initial triangle (top rows) and square (bottom rows), computed respectively for 2, 5 and 8 recursions from left to right. Rows 1 and 3 show the subelements themselves by drawing their edges, whereas rows 2 and 4 show the barycentres of these subelements (*i.e.* the points that are actually used during GPSO). The algorithm in the case of an initial triangle is given in Alg.1, and an extension is given in §5.3.4.1 in the case of an initial rectangle. Notice that the distribution of points (rows 2 and 4) follows a pattern containing "holes"; this violates the requirement for the partition function to be covering (see §5.2.4), and therefore precludes PBS to be used with GPSO as it stands. This will be object of future work.

This involves an equivalent but more general formulation, which does not affect the previous analysis. Specifically, the partition of any given d-dimensional polytope proceeds as follows:

1. Subdivide the initial polytope by associating its barycentre with each facet. This yields as many new polytopes as there are of original facets, although their shape may differ from the original one (*e.g.* different number of vertices).

2. Subsequently, after recursion $k < d$, any sub-polytope is the union of some $(d-k)$-face belonging to the original polytope, with the set of intermediary barycentres B carried until then, which contains k points. This subelement can be partitioned (independently from all others) by adding its barycentre to the set B, and forming new polytopes as the union of B with each facet of the original $(d-k)$-face (that is, a subset of the $(d-k-1)$-faces before partition).

After $d-1$ recursions, the sub-polytopes are the union of $d-1$ intermediate barycentres with some edge of the original polytope, and since these points are linearly independent by construction (the barycentre of a convex polytope cannot be on its facets), the resulting sub-polytopes are d-simplices. This process is illustrated in Fig. 5.7, where we compare the full barycentric subdivisions starting either from an initial triangle, or a square, in two dimensions.

In the case of an initial d-cube, all p-faces are also p-cubes, and therefore the subdivision discards 2^{d-k} original vertices at recursion k [4]. Crucially, since the vertices of a p-cube are only sparsely connected, the number of facets to consider at each recursion is only $2p$, which is at most **linear** in the number of dimensions, and in particular much smaller than the 2^p vertices of the p-cube. In other words, the number of subcases to consider at each recursion is still tractable in the case of an initial d-cube.

[4] One can easily verify that $\sum_{k=1}^{d-1} 2^{d-k} = \sum_{k=1}^{d-1} 2^k = 2^d - 2$, and hence only two of the original vertices are left after $d-1$ recursions of barycentric subdivision on a d-cube.

5.3.4.2 Practical issues with high-dimensional sub-polytopes

The last point raised in the previous paragraph about the large number of vertices in d-cubes hints at another practical issue; calculating the barycentre of arbitrary polytopes can be intractable, if they have a large number of vertices. In fact, this is the case for most of the sub-polytopes generated by the subdivision of a d-cube, because they have exactly $2^p + d - p$ vertices for $p \in \{1 \,..\, d\}$. However, we need the coordinates of these barycentres, not only for the subdivision process itself, but also for evaluating leaf-candidates during GPSO (either using the true objective function or the GP surrogate). In addition, listing the facets of a p-cube in terms of their vertices is equally intractable. Fortunately both of these problems can be solved efficiently, using a suitable representation of these polytopes. We give the corresponding implementations, as well as high-level explanations, in Apdx. C.

5.4 Software Implementation

5.4.1 Existing software

We improved upon the implementation of IMGPO (Kawaguchi et al. 2016), by addressing a number of issues and extending the algorithm in several ways. Our implementation is a complete refactoring of the original version, and is made freely available at the following address: `https://gitlab.com/jhadida/gpso`.

Our main **contributions** with respect to this implementation, aside from proposing a new partition function, are:

1. Updating the upper-confidence bounds following updated of GP hyper-parameters at each iteration, in order to propagate information across the partition tree; the original implementation did not update the bounds of leaf-nodes in the tree, and this resulted in incorrect selection.

2. Enabling the exploration of candidate leaves using uniformly random samples in the corresponding subregion of the search-space (only with ternary splits); the original implementation only explored a subset of the dimensions[5] by applying the partition function for a few recursions.

3. Decoupling the optimisation, surrogate and partition logics with an object-oriented implementation.

4. Implementing events at key points during the optimisation, allowing to monitor, and interact with, intermediate states.

5. Implementing serialisation, allowing to save intermediate states, or stop and resume the optimisation at any stage.

5.4.2 Design considerations

Although certain components of GPSO can be easily implemented on their own (*e.g.* GP regression, ternary split, or BFS traversal), the full implementation of the algorithm requires some consideration about the entities involved throughout the various steps listed in Fig. 5.2. In most cases, the design of a software proceeds from the bottom-up, by identifying the essential *data* being manipulated, the main *operations* being performed on this data, and the key *actors* performing these operations. The aim is to isolate the logic pertaining to each of these levels, and formalise the interactions between the different entities; this limits the effects of particular choices (*e.g.* using specialised data-structures) on the rest of the implementation, and makes it easier to add features incrementally (*e.g.* vary the optimism for UCBs during optimisation).

[5] See Fig. 5.6 for an illustration in two dimensions. Note that using PBS instead of ternary splits eliminates this issue; the subdivisions at each iteration involve all dimensions.

In our case, there are **three essential data entities** being manipulated throughout the optimisation process:

- The various **subregions** of the search-space (including the search-space itself), which contain information about the position and geometric shape of the region, but also the "state" of that region with regards to the partition function (*e.g.* the sets V and B in simplicial PBS, see Eq. 5.3).

- The **sample points**, which contain information such as: the normalised parameter values (coordinates); the mean and uncertainty of associated GP-predictions (surrogate data); the optimism associated with that point; and a label indicating whether it is GP-based or evaluated (see §5.2.5).

- The **partition tree**, which contains ancestry information for each subregion, and encodes the current subdivision of the search-space.

Furthermore, our implementation is structured around **four key components**, each of which can be replaced without affecting the rest of the code. This allowed us to explore the benefits of various partition functions for instance, or different ways of predicting the surrogate scores, but also to test these components outside of an optimisation context:

- The **partition function** implements any recursive and covering subdivision algorithm (see §5.2.4).

- The **surrogate function** maintains a parametric representation of the knowledge accumulated throughout the iterations, which can be used to make predictions about the objective. This typically relies of an underlying implementation of GP-regression, which is used to update the hyper-parameters every time new points are evaluated using the true objective function.

- The **sampling function** explores any given subregion and yields a set of points to be evaluated using the surrogate function.

- Finally, the **optimism function** quantifies the potential of a newly partitioned subregion to improve on the score of its parent. It was taken constant during our experiments so far, but constitutes one of the possible improvements to be explored in future work.

5.5 Comparison with Monte-Carlo Sampling

In this section, we compare the performance of GPSO against sequential Monte-Carlo sampling in dimension 5. We emphasize, as stated in (Hadida et al. 2018), that:

*[...] the two methods differ fundamentally in their approach, and **this comparison is not intended, and should not be interpreted, as a competition**; random sampling methods are built around the property of ergodicity (i.e. the probability of sampling any open subspace is positive, hence any region will eventually be sampled), whereas space-partitioning methods like GPSO implement a multi-scale "divide-and-conquer" philosophy, relying on the smoothness of the objective function.*

In order to carry out this comparison, and assess the ability of GPSO to converge towards the global optimum even in the presence of local extrema, we considered several mixtures of isotropic Gaussians with five modes randomly placed in $(0,1)^5$, and proceeded to finding the coordinates of the highest point in each case.

Without further constraints, and even with perfect knowledge of the location, height and width of each mode, it is non-trivial to locate the highest point analytically (Pulkkinen et al. 2013), and therefore to determine the success of the optimisation. To remedy this, we constructed each mixture by adding one mode at a time, with a rejection scheme in order to ensure the following constraints were always satisfied:

- The location of a new mode is invalid if it is within a distance σ of the closest border, where σ is the width of the new mode.

- The location of a new mode is invalid if the height at that location, considering all previous modes, exceeds a threshold $H_{\max}$.
- The new mode is invalid if, considering this mode alone, the height at the location of any previously accepted mode exceeds $H_{\max}$.

This ensured in practice that each mode would correspond to a peak of the mixture, and hence that the highest point would simply correspond to the highest mode.

We constructed ten different mixtures following this procedure, and ran GPSO on each of them, using either the ternary partition function (see §5.2.4.2), or barycentric subdivision (see §5.3.2). The success of each optimisation was assessed according to the following criteria:

- The optimisation was considered successful if the closest mode to the best sample was the highest one, and unsuccessful otherwise.
- The distance to the closest mode, and the difference between the height of that mode, and the best score achieved (a.k.a. the *regret*), were recorded.
- Similarly with the highest mode.

Finally, we compared the results obtained with GPSO to those obtained with a sequential Monte-Carlo method, namely particle-filter optimisation (Djuric et al. 2003; Liu et al. 2016). Briefly, after an initialisation with a certain number of samples (a.k.a. *particles*), this method iterates sequentially over the following steps:

- Remove a certain amount of the worst samples, and replace them with new uniformly sampled particles.
- Resample the remaining particles, by associating a probability of selection proportional to their score (with replacement); this is known as **importance sampling**.
- Add isotropic noise to the resampled particles.

Due to the stochastic nature of this algorithm, we repeated the particle-filter optimisation three times for each mixture, and report the results for each repeat independently, in order to compare fairly with GPSO. The various parameters controlled for this experiment were as follows:

- The parameters for GPSO were chosen as given in Tab. 6.1, in particular, we allowed a maximum of 800 evaluations of the objective function.

- As mentioned previously, the mixtures were constructed with five modes, with a rejection scheme to ensure a good separation of the peaks. The location of each peak was taken uniformly at random in $(0,1)^5$, the width (standard-deviation of the mode) was sampled uniformly between $0.1 - 0.2$, and the height was sampled uniformly between $1 - 5$. We set $H_{\max} = 0.6$.

- For particle filtering, we initialised with 800 particles uniformly located at random in $(0,1)^5$. The bottom 25% were removed at each iteration, and the noise added to the resampled particles had a standard-deviation of 0.1.

The results are summarised in Tab. 5.1. It is worth noting that GPSO required approximately 25 min to complete on average, whereas particle-filter optimisation consistently required less than a second. This illustrates the fact that GPSO is only valuable in the case of costly objective functions, for which the time required to carry out the optimisation is negligible compared to the time required to evaluate the various samples.

5.6 Limitations and future work

Below is a list of limitations currently associated with GPSO.

	Success	Closest	Highest	RegretC	RegretH	Time (sec)
Ternary	0.600	0.085	0.522	0.724	1.499	1321.850
Barycentric	0.800	0.002	0.659	-0.011	0.389	1588.205
PFilt1	0.600	0.075	0.712	0.501	1.509	0.783
PFilt2	0.500	0.098	0.698	0.883	1.290	0.783
PFilt3	0.500	0.073	0.622	0.486	1.112	0.783

Table 5.1: Summary results of the comparison between GPSO and sequential Monte-Carlo sampling. **Success:** the average number of successes across the 10 mixtures. **Closest,RegretC:** the distance between the best sample and the closest mode, and the corresponding difference between its height and the best score, averaged across all 10 mixtures. **Highest,RegretH:** similarly with the highest mode, averaged across failed mixtures only. **Time:** the average runtime, across all 10 mixtures.

5.6.1 Evaluating convergence

It is not currently possible to systematically evaluate the convergence of the optimisation. This is mainly because at every iteration, multiple areas of the search-space are being explored at multiple scales, which means that a lack of improvement in the best score obtained (typically a criterion for convergence) over several iterations is no guarantee that there will not be a substantial improvement at the next iteration. However, one can define several relevant termination criteria, such as: the number of evaluations of the objective function (used in our experiments), the number of iterations, the depth of the partition tree, *etc*.

5.6.2 Prior over parameter values

It is not currently possible to define priors over the parameters being optimised, in order to initially bias the search towards regions of known interest. Note that this cannot be done via the mean function of the GP, because hyper-parameters are revised at each iteration (and making the prior insensitive to hyper-parameters would also make it insensitive to evidence accumulated by simulations, which would corrupt the objective function).

Instead, this could be done in two ways:

- Provided that the uncertainty from GP predictions can be normalised between 0 and 1 (or else, the covariance function could be used to assess the proximity with evaluated samples), we could replace the UCB estimate (see Eq. 5.2) with:

$$(1-\nu)\mu(x)+\nu\pi(x)+\varsigma\sigma(x)$$

  where π denotes the prior defined over the search space, and ν denotes the normalised measure of uncertainty at location x.

- Better still, for a given set of prior samples $\left\{\left(x_k,\ \pi(x_k)\right)\right\}_{k=1..p}$, these points could be inserted into the surrogate function, such that they would initially be used to train the GP hyper-parameters, and would subsequently be *disabled* one-by-one as the true objective function is evaluated in a close neighbourhood. This would essentially be equivalent to introducing "ghost nodes" arbitrarily deep into the partition tree, waiting to be discovered by subdivision.

5.6.3 Ghost nodes

The first bottleneck in GPSO is to retrain the GP hyper-parameters after every iteration. The second bottleneck is to explore candidate sub-regions using the sampling function; if the region is a hyper-rectangle (*e.g.* when using ternary splits as a partition function), then it is easy to sample points uniformly randomly, but random sampling within arbitrary convex polytopes is not trivial (Dyer et al. 1991). Therefore in general, the exploration of subregions is done by applying the partition function for a small number of recursions, and taking the barycentres of the resulting subelements as sample points to be evaluated using the surrogate function.

Hence, the algorithm could be improved by inserting these subelements into the partition tree as "ghost nodes". We would need to relax the constraint that all non-leaf nodes should be evaluated using the true objective function at each iteration (see Fig. 5.2), but this would be beneficial for several reasons:

- The purpose of the exploration step is to assess the potential of all leaf-subelements in the partition tree, in order for their subsequent selection to be carried out fairly. Once the selection is done, however, all sample points are forgotten, and this often penalizes larger subelements. Indeed, if a node was not selected at a given iteration, because it did not obtain the largest UCB at its level, but that it contains a "good" subregion at one of its extremities (far from the barycentre), then it may not be considered again for many iterations. This is because the information about its subparts is lost, and the updates of UCBs only consider the barycentre of leaf-subelements. In that case, keeping the explored children as ghost nodes, and backtracking their updated UCBs at each iteration to the parent subregion, would both prevent the loss of information and improve the fairness of the selection.
- Keeping explored subregions as ghost nodes would also reduce the complexity of subsequent exploration step, because many of them currently end up being recomputed at every iteration. That being said, since the total number of leaves in the partition tree would increase considerably, so would the complexity of updating UCBs at each iteration.

5.6.4 Other limitations

It is worth noting that because we only ever select those nodes with maximal UCB in the partition tree, areas of the search-space with lower expected scores are the last to be evaluated at each level of the tree, and therefore the resolution of the surrogate is lower there. This is an intended consequence of prioritising exploration in places of high expected reward, but it also means that the surrogate will in general not be reliable when the objective function is low; such is the price to pay for efficiency, this is not primarily an exploration method.

Finally, and although this is purely a technical limitation, the GP library we used so far (GPML Rasmussen et al. 2006) is limited in the number of samples it can handle for regression; in practice, the regression becomes prohibitively slow beyond a few thousand samples, which means that we cannot reasonably explore parameter spaces beyond 10 dimensions. This can be solved indirectly, by selecting only a limited number of evaluated samples for training the GP; for instance, up to a certain depth in the partition tree, and randomly beyond that depth, up to a certain amount.

6

Optimising Uniform LSBMs

Contents

6.1 Introduction

In this chapter, we use GPSO (see chapter 5) to fit the parameters of networks of Wilson-Cowan (WC) units with delays (see §3.3.2) to band-specific MEG resting-state FC matrices (see §2.4.5). For simplicity, we assume that all units in the network have the same local parameters, which reduces the overall number of parameters to consider in our large-scale models. The benefits of considering variations of local parameters across the cortex will be explored in the next chapter.

We present the results of two experiments, which illustrate the benefits of GPSO in the context of LSBMs. The first experiment is a proof of concept in a two-dimensional case (similarly to Fig. 5.4), which allows results to be visualised and compared with exhaustive search, in order to demonstrate global convergence. The second experiment considers a model with five parameters; we provide a detailed analysis of the results, and discuss how such analysis can be used to refine large-scale models iteratively. This work was published in NeuroImage (Hadida et al. 2018).

We find that GPSO is able to converge to regions of high functional similarity across frequency bands with empirical MEG data; that two of the four methods used to estimate AC matrices (see §2.3.2) yield systematically better similarity results; that inter-hemispheric connectivity is likely to be underestimated by these methods; and that either local dynamics or connectivity (or both) from the frontal lobe may require special treatment in large-scale models.

6.2 Problem Definition

The large-scale models presented in chapter 3 describe the activity of N brain regions, or *units*[1], connected into a network with propagation delays. Specifically, the WC model considers two populations of neurons (or *nodes*) per brain region, each described by a single equation. This leads to a system of $2N$ coupled state-equations (see Eq. 3.10), in most of which there are $\mathcal{O}(N)$ non-zero coupling terms (the structural connectivity between regions is not sparse); hence the high computational costs associated with simulations in practice.

As it stands, this system also has $\mathcal{O}(N^2)$ parameters because of the coupling and delay matrices, which we denote respectively $C = [c_{i,j}]$ and $\Lambda = [\lambda_{i,j}]$ in the remainder. Fitting such a large number of parameters is impractical; below, we propose a more parsimonious parametrisation, controlling key structural and functional aspects of the system with five parameters. These parameters can be inferred from empirical MEG data using GPSO.

6.2.1 Assumptions

The experiments presented in this chapter rely on the following assumptions:

1. All units across the network are identical.
2. E and I subpopulations have the same response function and decay-time.
3. The coupling between units is from and to excitatory subpopulations only.
4. Neuronal activity propagates throughout the brain at constant and uniform velocity.
5. We only consider cortico-cortical connections (*i.e.* no subcortical structures).
6. The network has hemispheric symmetry: each region belongs to one and only one hemisphere, and has a homologous region in the other hemisphere.

[1] See Fig. 3.1 p.39 for the terminology used in our models.

Assumptions 1 and 2 greatly reduce the number of parameters to consider in the network. Excluding inputs, each WC *node* is normally defined by six parameters (see §3.3.1), and since there are two nodes (E and I) per *unit*, this leads to $12N$ local parameters in total. Assumption 1 brings this number down to only 12 parameters, and assumption 2 further reduces it to **9 parameters**: τ, μ, σ for both E and I subpopulations, and r_x, c_{xx}, c_{xy} with $x, y \in \{e, i\}$ for each of them. Note that these assumptions only affect the *local* parameters of our models; the networks can still be *globally* heterogeneous, due to the different coupling weights and delays assigned to their edges.

Considering two nodes per unit also means that the connectivity and delay matrices have a 2-block structure. In the coupling matrix, all on-diagonal blocks (containing the local couplings) are identical following assumption 1, and off-diagonal blocks only have **one non-zero entry** following assumption 3:

$$\underbrace{\begin{pmatrix} c_{ee} & c_{ei} \\ c_{ie} & c_{ii} \end{pmatrix}}_{\text{On-diagonal}} \qquad \underbrace{\begin{pmatrix} c_{i,j} & 0 \\ 0 & 0 \end{pmatrix}}_{\text{Off-diagonal}}$$

Propagation delays are neglected within any brain region, and therefore the delay between two regions is the same regardless of which subpopulations are considered. Hence, all on-diagonal blocks in the delay-matrix are zero, and off-diagonal blocks are given by:

$$\lambda_{i,j} \begin{pmatrix} 1 & 1 \\ 1 & 1 \end{pmatrix}$$

where $\lambda_{i,j}$ (positive for $i \neq j$) is proportional to the distance between units i and j, following assumption 4. In this chapter, the distance between units is taken as the **Euclidean distance** between their respective barycentres[2].

[2]The tract-lengths (see §2.3.3) were unavailable at the time we ran these experiments.

Assumption 5 relates partly to the choice of the neuronal-mass model[3], and partly to the choice of the anatomical parcellation (see §2.2). This is perhaps the most questionable assumption, and we intend to explore the effects of different structural choices in future work.

Finally, assumption 6 implies that the network can be divided into two (connected) subnetworks, each with $N/2$ units, which induces an additional N-block structure in the network matrices. This is useful for two reasons:

- to our knowledge, there is no evidence for one hemisphere driving brain activity more than the other, or for a lateral bias in the AC between hemispheres, therefore requiring both to have the same size ensures that the overall AC within and between hemispheres is structurally unbiased;
- from a purely practical perspective, the assumption of hemispheric symmetry makes it easier to manipulate connections within and between them.

6.2.2 Parametrisation

In this chapter, the local parameters of WC units are taken as those of **unit D** in Tab. 3.1 p.51. These parameters were chosen mainly such that local couplings verify $c_{ee}/(c_{ee}+c_{ei}) = 0.8$ (80% of self-excitation), and $c_{ee}+c_{ei} = c_{ie}+c_{ii}$ (equal strength of excitation and inhibition). Furthermore, we select the **excitatory input** P_e, and the **decay-time** τ (identical for E and I, following assumption 2), as key parameters to control the local dynamics during optimisation; the former allows to bring individual units closer to their oscillatory threshold, while the latter influences their frequency response to external inputs from remote regions (see Fig. 3.7).

Controlling the network parameters (*i.e.* the coupling and delay matrices) requires additional work. For a given parcellation of the brain into N different regions (*e.g.*

[3]For example, see (Roberts et al. 2012) for a model considering cortico-thalamic connections.

$N = 68$ in the DK parcellation, see §2.2), let A be the AC matrix obtained from diffusion tractography using one of the methods in §2.3.2, and D the matrix of pairwise Euclidean distances between the barycentres of the corresponding regions.

Both matrices are $N \times N$, and by convention the diagonal of A is set to zero. We also identify excitatory and inhibitory nodes using indices between 1 and $2N$, respectively with odd and even numbers (*i.e.* odd indices correspond to excitatory nodes).

Given these notations and conventions, the coupling and delay matrices, C and Λ, are parametrised as follows:

$$C = \underbrace{\gamma A \otimes \begin{pmatrix} 1 & 0 \\ 0 & 0 \end{pmatrix}}_{\text{non-local}} + \underbrace{\mathrm{I}_N \otimes \begin{pmatrix} c_{ee} & c_{ei} \\ c_{ie} & c_{ii} \end{pmatrix}}_{\text{local}} \tag{6.1}$$

$$\Lambda = \frac{\overline{\lambda}}{\overline{D}} D \otimes \begin{pmatrix} 1 & 1 \\ 1 & 1 \end{pmatrix} \tag{6.2}$$

where $\otimes$ is the Kronecker product; I the identity matrix; $\overline{D}$ the average pairwise distance; and we introduced the following parameters:

- γ the **global coupling strength**, controlling the amount of non-local coupling;
- and $\overline{\lambda}$ the **average propagation delay**, controlling the speed of interactions.

Note that although matrix A is typically be symmetric, C is *not*; the element in row i column j corresponds to the edge from node i to node j (not unit), and therefore **each column can be seen as a coupling vector for the corresponding node**.

Finally, we introduce a fifth parameter controlling the magnitude of inter-hemispheric couplings in matrix A; probabilistic tractography methods have an inherent bias towards shorter connections (see Fig. 2.3 and §2.3.2), and therefore connectivity between distant regions is generally lower. This reflects to a degree a biological reality (Donahue et al. 2016), but it is unclear whether the same decrease in connectivity applies equally within

or between hemispheres. The **inter-hemispheric (IH) scaling**, denoted h, allows us to account for such potential bias by scaling off-diagonal blocks in matrix A before substitution in Eq. 6.1:

$$A \leftarrow\!\shortmid A \odot \left[\mathbf{1}_{N/2} \otimes \begin{pmatrix} 1 & h \\ h & 1 \end{pmatrix} \right] \tag{6.3}$$

where $\odot$ is the Hadamard product (element-wise) and $\mathbf{1}$ is a full matrix of ones.

Equations 6.1, 6.2 and 6.3 determine entirely the network structure, and we considered **five parameters** to be optimised (listed in Tab. 6.1), which control key structural and functional aspects of our model.

6.2.2.1 Relative variants

The five parameters considered in the previous paragraph will be optimised by GPSO so as to maximise the similarity between simulated and empirical resting-state activity. To do so, GPSO requires a search-interval for each parameter (the search-space is always bounded). However, these intervals are not always easy to define; for example, determining the range of coupling strengths for which a given network model oscillates is not analytically tractable, and depends on the excitatory input P_e, as well as on the AC matrix, and therefore on the IH scaling h. Choosing an interval large enough to accommodate all cases implies spending valuable time evaluating systems which are either silent or saturated, and makes it difficult to compare results obtained with different AC matrices.

We know that Wilson-Cowan units oscillate for excitatory inputs beyond a certain threshold value P_e^* (see §3.3.1.1). Similarly at the network level, we know that oscillations occur for coupling values beyond a certain threshold value γ^* (which is null if the units intrinsically oscillate on their own). Normalising the input and coupling parameters with respect to their threshold values would help, not only to compare them across different

models, but also to easily control the state of the network (oscillating or silent) and focus on the oscillating regimes during optimisation. Hence, we define the following **relative parameter variants** instead:

$$\widetilde{P_e} = P_e / P_e^* \qquad \widetilde{\gamma} = \gamma / \gamma^* \tag{6.4}$$

and use them throughout our experiments. With these definitions, we know for example that $\widetilde{P_e} < 1$ corresponds to brain units below oscillatory threshold, and that networks are in oscillatory regime only when $\widetilde{\gamma} > 1$. And we can enforce these conditions during optimisation by choosing the parameter ranges accordingly.

As explained previously, determining the threshold value γ^* for any given network model is not trivial. In our experiments, for any candidate set of parameters (including $\widetilde{P_e}$ and $\widetilde{\gamma}$), both threshold values were estimated prior to simulation by dichotomic search (with 3 significant digits), in order to determine the corresponding values of P_e and γ required to build the network. The overhead introduced, in terms of runtime, was on the order of a minute per candidate set of parameters (largely dominated by the search for γ^*; the search for P_e^* always took less than a second).

The search-intervals considered for the five parameters (with relative variants) are given in Tab. 6.1.

Symbol	Description	Short-name	Range
$\widetilde{P_e}$	Relative input	Input	$(0.6, 1)$
$\widetilde{\gamma}$	Relative coupling	Coupling	$(1, 3)$
$\overline{\lambda}$	Average delay (ms)	Delay	$(1, 50)$
h	Inter-hemispheric scaling	IH Scaling	$(0, 4)$
τ	Decay-time (ms)	Tau	$(4, 16)$

Table 6.1: Network parameters controlled during optimisation. The ranges correspond to the boundaries of the search space (required by GPSO). The parameter variants $\widetilde{P_e}$ and $\widetilde{\gamma}$ are defined in Eq. 6.4. Short names are used in figures 6.1, 6.4 and 6.5.

6.2.3 Objective function

The *optimal* parameters should maximise the similarity between biophysical simulations and real MEG data, and this similarity should be assessed using characteristic features of resting-state dynamics. In this chapter, we consider a simple objective function comparing FC matrices (taken as envelope correlations, see §4.3.1) across six overlapping frequency-bands:

$$[4,8]\ [6,10]\ [8,13]\ [10,20]\ [13,30]\ [20,40]\ \text{Hz}$$

As excitatory pyramidal cells contribute most strongly to EEG/MEG signals, we associate activity in the excitatory subpopulations of our models with signals measured experimentally (Buzsáki et al. 2012). Importantly, the simulated time-series of different cortical regions are orthogonalised prior to computing Hilbert envelopes (using the Procrustes method from Colclough et al. 2015), in order to replicate the effects of leakage correction on source-reconstructed MEG data (see §2.4.3). Envelope correlations are then computed in each band (see §2.4.3), and compared using the modified correlation defined previously in §4.3.3.1. The resulting similarity score constitutes the objective to be maximised by GPSO.

The various settings for GPSO used during our experiments are listed in Tab. 6.2.

Function	Hyperparameter	Value
UCB	ς	1.98
Constant mean	μ	0
Gaussian likelihood	σ	0.001
Isotropic Matèrn covariance (order 5)	Length	0.25
	Magnitude	1

Table 6.2: GPSO hyperparameters and initial values used for all experiments. The optimism parameter ς corresponds to confidence bounds of 99.5% (*i.e.* $\text{erfc}^{-1}(0.005)$), which was found to strike a good balance between exploration and exploitation.

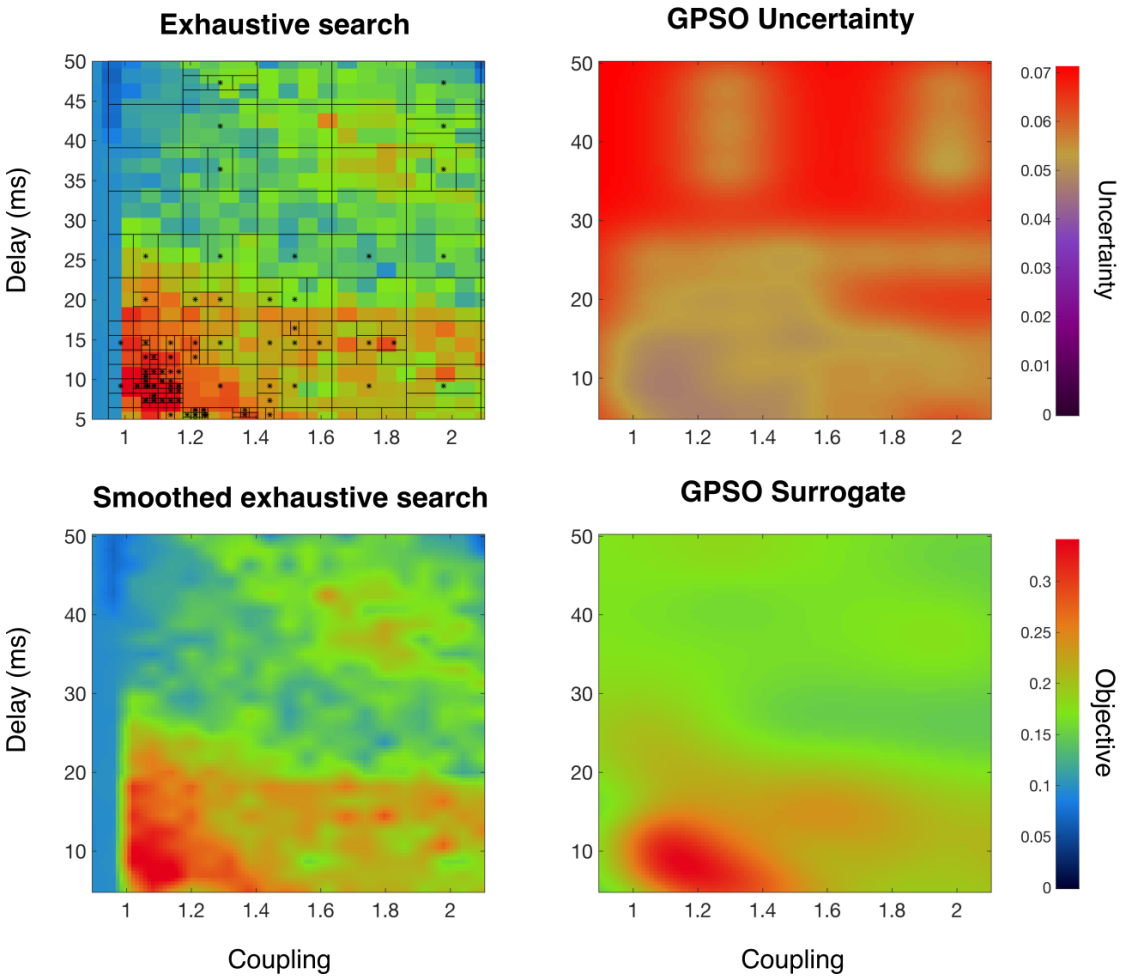

Figure 6.1: Exhaustive grid-search with 525 simulations, compared against GPSO with 100 simulations, controlling 2 parameters (average delay $\overline{\lambda}$ and relative coupling $\widetilde{\gamma}$). See §6.3 for details. **Top-left:** exhaustive search (background image) and partition tree from the GPSO (black lines). Black asterisks indicate the samples evaluated during optimisation (see §5.2.5 for details about GP-based samples). Each pixel corresponds to a 63 sec simulation, analysed and compared with reference MEG data. The partition is refined in places where the objective function is higher, and the optimisation converged rapidly to the global optimum. **Bottom-row:** surrogate function (predicted mean) learned by GPSO, to be compared against the smoothed exhaustive search (ground-truth) on the left. **Top-right:** surrogate uncertainty (predicted st-dev.), driving the compromise between exploration and exploitation during optimisation.

6.3 Two-Dimensional Example

In this experiment, the similarity between simulated and reference MEG data was maximised according to the objective function defined in the previous paragraph, by optimising just **two parameters**; the average delay $\overline{\lambda}$, and the relative network coupling $\widetilde{\gamma}$. The remaining parameters (see Tab. 6.1) were set to: $\widetilde{P_e} = 0.85, h = 1, \tau = 10\text{ms}$, and we used the `conn1_mean` AC matrix (see Fig. 2.3 p.17) to connect the network units. The timespan of each simulation was 63 seconds, and we discarded the first 3 seconds to get rid of transient effects before analysis. The results are shown in Fig. 6.1.

The performance of GPSO was assessed by comparison with an exhaustive grid search, which is computationally tractable in two dimensions and can be easily visualised. The grid search required 525 simulations, considering respectively 25 and 21 equally spaced points across the search-intervals of the delay and coupling parameters. In comparison, GPSO was run with 100 simulations, with which it successfully converged to the optimum, while learning a surrogate objective function defined smoothly across the search space, along with a map of uncertainty. These results demonstrate the efficiency of the method in a restricted two-dimensional context of LSBM optimisation. See also §5.5 for a comparison against sequential Monte-Carlo sampling.

6.4 Five-Dimensional Analysis

In this second experiment, we consider all five parameters listed in Tab. 6.1, and all four AC matrices shown in Fig. 2.3. For each AC matrix, an optimisation was run with 800 samples (*i.e.* evaluations of the objective functions), which took approximately 1.5 day to run on a computing cluster with four threads. In comparison, an exhaustive search run sequentially with just 20 values per dimension would take over 18 years to complete.

The five-dimensional results cannot be displayed as in the previous two-dimensional case; instead we summarise below key aspects of the analysis, illustrating the type of information made available by this new method.

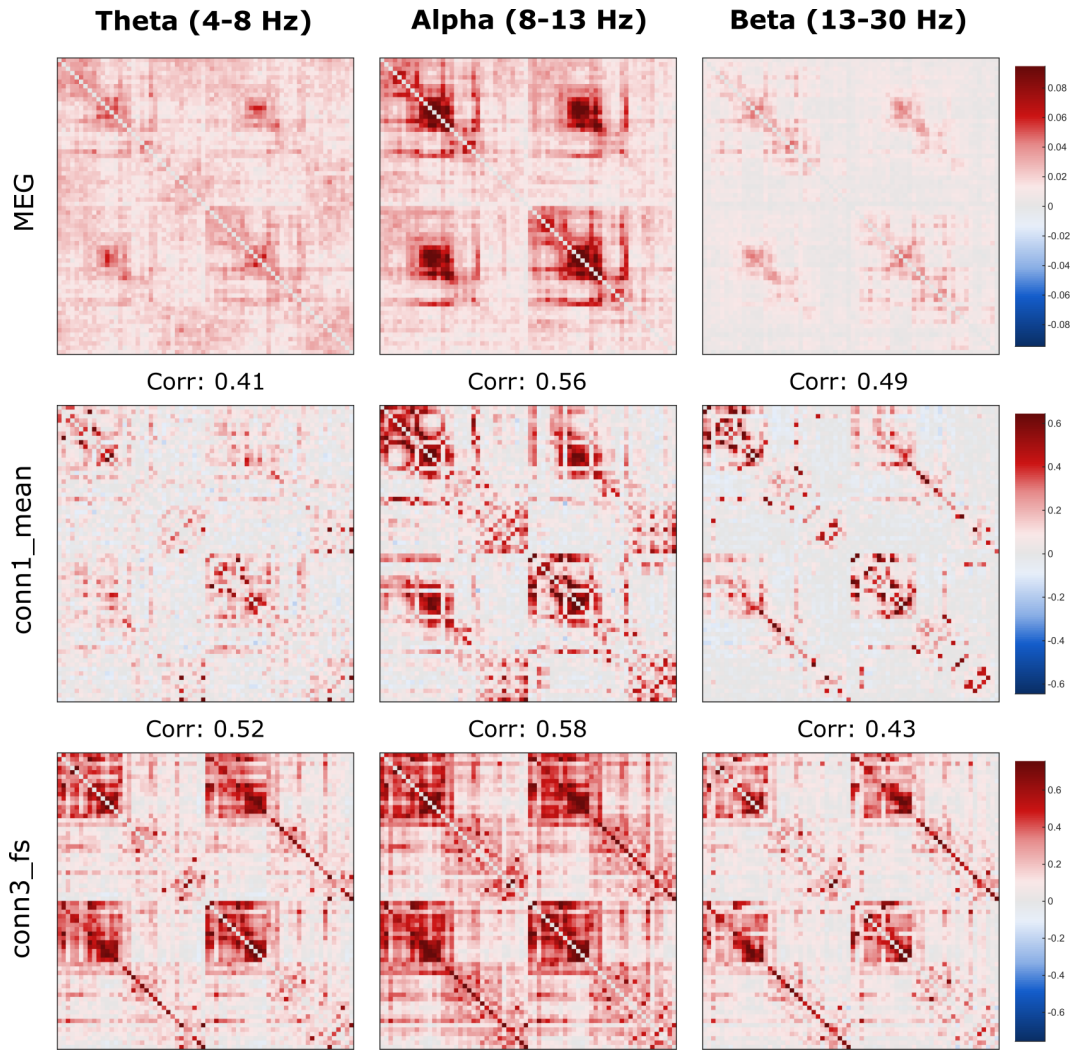

Figure 6.2: Comparison between simulated and reference FC matrices in theta, alpha and beta bands. Reference matrices are shown in the first row, followed by the best results obtained with connectivity `conn1_mean` (row 2), and the second best results obtained with `conn3_fs` (row 3). The correlation between each simulated FC matrix and the corresponding reference is indicated on top of the matrix. The FC patterns obtained with `conn1_mean` connectivity are strikingly similar to the reference, except in the frontal lobe (lower-right block in each quadrant). Note that although results obtained with `conn3_fs` achieved better correlations on average, they had a lower similarity score than the results obtained with `conn1_mean`, because their variation across bands was poor (see Fig. 6.3).

6.4.1 Summary results

The best results were obtained with AC matrices `conn1_mean` and `conn3_fs`, and are shown in Fig. 6.2. Interestingly, both matrices have almost exactly the same distribution of connectivity strength as a function of the distance between regions (see Fig. 2.3 p.17, third row, right), which suggests that **the distribution of connectivity vs. distance is a key aspect of LSBMs**.

It is also worth noting that the best results according to the modified correlation defined in §4.3.3.1 were associated with `conn1_mean` connectivity, but the best envelope correlations (*i.e.* without controlling for the variation of FC magnitude across bands) were obtained with `conn3_fs` connectivity. Looking at the corresponding FC matrices (bottom-row in Fig. 6.2), we see that the same pattern (high FC throughout the temporal and occipital lobes) is repeated across bands with little magnitude variation, whereas those patterns vary and are better defined in the second row, where `conn1_mean` connectivity is used. In Fig. 6.3, the best results obtained after optimisation with each of the four AC matrices are summarised and compared, using both modified correlations and envelope correlations. These results suggests that **using detailed, multi-criteria objective functions, can be beneficial for optimisation**.

6.4.2 Preferred parameter values

Looking at the distribution of parameter values for the best samples found during optimisation tells us about "preferred" values for each parameter; that is, parameter values for which the corresponding networks produce dynamical activity most similar to MEG resting-state data. Fig. 6.4 shows a comparison between the marginal parameter distributions computed independently for each of the four AC matrices.

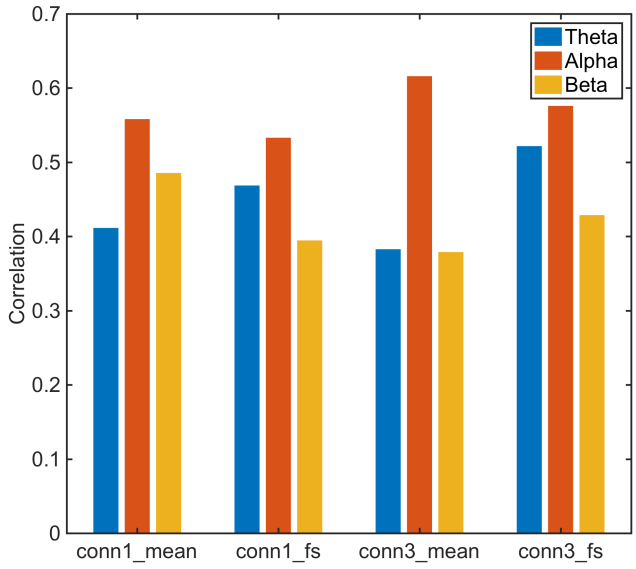

	conn1_mean	conn1_fs	conn3_mean	conn3_fs
Objective	0.42	0.39	0.39	0.40
EC	0.49	0.47	0.46	0.51

Figure 6.3: Best results obtained with the four AC matrices given in Fig. 2.3. The bar plot shows the similarity between simulated and reference FC matrices in theta, alpha and beta bands, as evaluated by the objective function during optimisation (see §6.2.3). The table reports these similarity scores, as well as the average envelope correlations (EC) across bands. These results suggests that using multi-criteria objective functions can be beneficial for optimisation: see §6.4.1 for explanations.

These distributions correspond to the 90^{th} percentile of all evaluated samples (ranked according to their similarity score). The narrower the distributions, the stronger the preference for a specific parameter value. And the more overlap between distributions, the better the consensus across experiments with different connectivities.

Our results suggest a good consensus across AC matrices with regards to the first three parameters (input, coupling, delay), and in particular for the average network delay around 10ms, but the comparisons for the inter-hemispheric scaling h and decay-time τ are more mitigated. This is not surprising; the connectivity matrices control the interactions between the different brain regions, and structurally different networks should not be expected to agree on parameter values in general.

That being said, three out of the four AC matrices (all except `conn3_mean`) indicate clearly that **the strength of inter-hemispheric connections should be increased at least two-fold**. This is consistent with the known bias for shorter connections in probabilistic tractography, but it is also remarkable to be able to estimate the amount of "missing" connectivity purely from simulations.

Finally, the results for the temporal parameters (average delay and time-constant) are somewhat surprising. We would not expect network delays to be lower on average than the characteristic time of variation within each brain region, because these delays are caused by axonal conduction over long distances, and local oscillations (caused by cycles of local excitation and inhibition) are not subject to propagation issues. This particular result might change with a more accurate estimation of the delays in our model (*e.g.* using tract-lengths from tractography instead of Euclidean distances, see Fig. 2.4); this will be explored in the next chapter.

6.4.3 Topography near the optimum

Here we take a closer look at the best results obtained using `conn1_mean` connectivity. The optimal parameters correspond to a single point in the search space; in order to study the shape of the objective function near the optimum, we computed the conditional distributions of the GP surrogate on orthogonal slices going through that point. These slices are shown in Fig. 6.5.

A local maximum can be seen in the conditional surrogate coupling vs. input (row 2 column 1), which indicates that **the objective function is not unimodal**. Note that this is by no means a complete picture; for example, it is impossible to know about local optima located elsewhere in the search space based on this information only. Instead, the partition tree from GPSO can be used in combination with these conditional distributions, to identify local extrema and explore the topography of the search space around them.

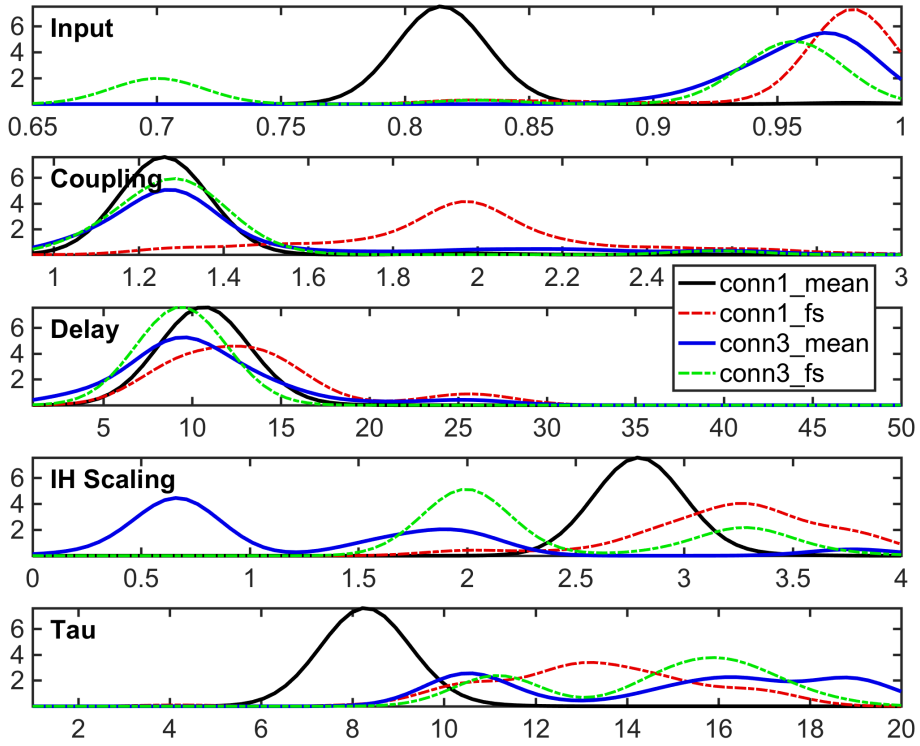

Figure 6.4: Marginal parameter distributions corresponding to the 90th percentile of all evaluated samples, for the four AC matrices (see Fig. 2.3). Higher distribution values (y-axes) indicate parameter values (x-axes) which were consistently associated with the best scores for a given AC matrix. **Input:** all but `conn1_mean` indicate that the excitatory input should be just below units' oscillatory threshold. **Coupling:** all but `conn1_fs` indicate that coupling scale should be just above network oscillatory threshold. **Delay:** general consensus that average delay should be around 10ms. **Scaling:** no clear consensus, but all except `conn3_mean` indicate an upscale by a factor of 2 or more. **Tau:** `conn1_mean` centred around 8ms, and others above 10ms.

Additionally, the marginally-weighted means and standard-deviations of the similarity scores obtained during optimisation are shown on the diagonal of Fig. 6.5, computed within each dimension across *all* samples in eleven bins covering the corresponding parameter range[4]. These statistics are consistent with the parameter distributions previously shown in Fig. 6.4, although we previously only considered the 90^{th} percentile of all samples.

[4]The weights were defined for each bin as $w(x) = \exp\big(-3|x-c|/w\big)$ where c, w are respectively the centre and width of the bin.

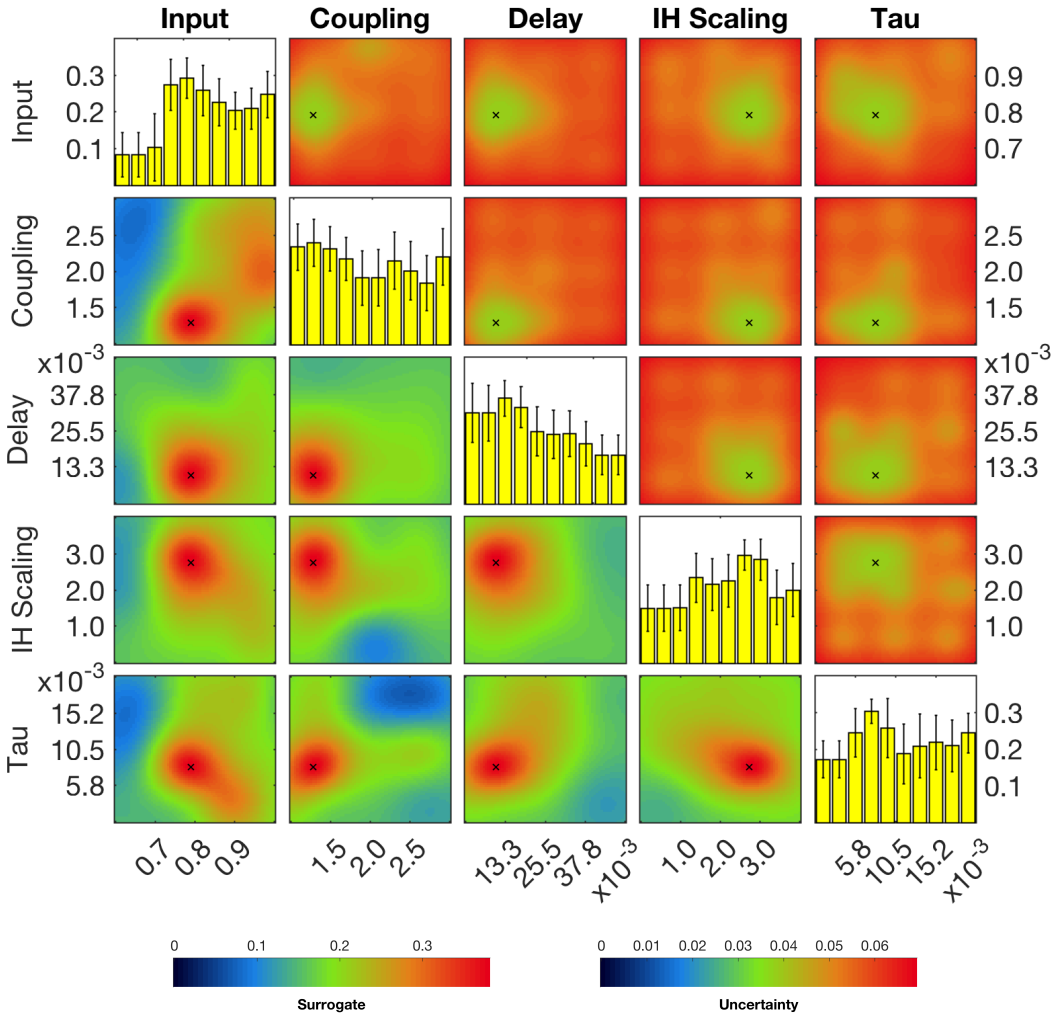

Figure 6.5: Conditional surrogate distributions (off-diagonal) and marginally weighted means and st-dev. (on-diagonal) around the best sample (black cross). These results correspond to the best experiment, using AC matrix `conn1_mean` (see Fig. 6.3). Note that y-axes in the first and last on-diagonal bar-plots indicate similarity scores, whereas all other axes indicate parameter values. **Lower-triangle:** surrogate similarity (predicted mean) computed on orthogonal slices of the search space, going through the best sample for each pair of dimensions. **Upper-triangle:** associated surrogate uncertainty (predicted st-dev.) showing lowest uncertainty around the best sample, which is a good indicator of convergence. **Diagonal:** weighted mean and st-dev. of evaluated scores, calculated within each dimension across all samples. Higher bars indicate "preferred" values for the corresponding parameters (similar to the distributions shown in Fig. 6.4, but considering all samples).

6.4.4 Region-wise similarity

The correspondence between simulated and reference FC matrices shown in Fig. 6.2 can be explored further, by correlating each row of these matrices independently, in order to get a region-wise similarity score in each frequency-band. This comparison is illustrated in Fig. 6.6, by associating these correlations with a colour in each brain region and in each band. **We find a very good correspondence across frequency bands in the temporal and occipital lobes, and systematically lower correlations in the frontal lobe, especially in the OFC.**

The signal-to-noise ratio in the OFC is known to be rather poor in MEG (Goldenholz et al. 2009), but the fact that the bad correspondence extends throughout the entire frontal lobe may relate to the work of (Chaudhuri et al. 2015), which introduced gradients of excitatory inputs in the frontal areas, in order to account for higher dendritic spine counts compared with primary sensory areas. This modification affects the frequency response of the frontal lobe, and therefore its properties of synchronisation within the whole-brain network, which could be the cause of the anti-correlation observed in the alpha band. We explore the benefits of considering different local parameters across brain regions in the next chapter.

Whether gradients of excitatory inputs improve the correspondence with real data or not, however, it is remarkable to be able to point to such specific modelling aspects, with reasonable confidence that no other configuration of the current system could yield a better result by tweaking the five parameters considered. These results tell us that a change to the *model* is required, and specifically one that will affect dynamics in the frontal areas. This type of information is invaluable, and demonstrates how GPSO can be used to inform modelling choices incrementally.

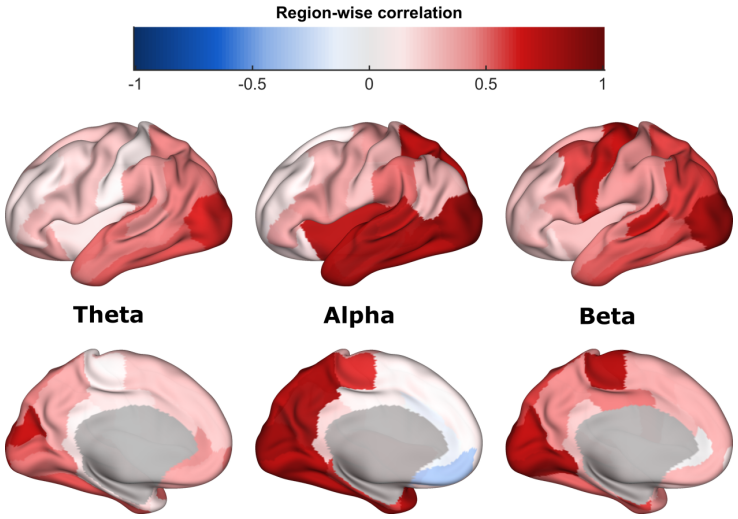

	Theta	Alpha	Beta	Average
Temporal	0.40	0.68	0.48	0.52
Occipital	0.59	0.83	0.78	0.73
Parietal	0.33	0.48	0.52	0.45
Frontal	0.29	0.09	0.28	0.22

Figure 6.6: Band-specific region-wise correlation, calculated between matching columns of simulated and reference FC matrices, for the best simulation with `conn1_mean` connectivity (see Fig. 6.2). The average band-specific correlations within each lobe are reported in the table underneath the surfaces. The correspondence between simulated and reference data is: very good in the occipital lobe; good in the temporal lobe, although driven mostly by the alpha band (>1.5 times better than other bands); consistently worse in the frontal lobe; and the average correspondence in the frontal+parietal lobes is twice as low as in the temporal+occipital lobes.

6.5 Discussion

The limitations associated with GPSO were covered previously in §5.6. Here, we discuss the results obtained in the five dimensional experiment presented in the last section.

6.5.1 Influence of local parameters

There is no doubt that the parameters governing the local dynamics (see Tab. 3.1 p.51) will, in general, affect the characteristics of the network activity; in fact, this is the premise of our work. The problem of systematically predicting network activity from local properties

is currently unsolved, although this is an active area of research (see Stroud et al. 2015 for instance). The purpose of this first set of experiments was to demonstrate the ability of GPSO to maximise the similarity between simulated and empirical resting-state data, by manipulating a relatively small number of parameters (yet larger than previously attempted in the literature), in reasonable computation time.

In order to properly assess the influence of local parameters, we should conduct the same experiment with many different unit parameters, and compare the results obtained, in order to determine empirically how choices at the local level may affect large-scale dynamical features. Alternatively, it could be envisaged to optimise the local parameters themselves (beyond the input and decay-time considered in this chapter), in order to determine the best configuration.

Ultimately however, these results depend not only on the choice of a particular oscillatory model (here, the Wilson-Cowan model), but also on the coarse assumption that all units in the network are identical (*c.f.* §6.2.1). With regards to the choice of an oscillatory model, we have carried out preliminary work with the conductance-based model proposed in §3.4, and intend to investigate this model further in the future. In the next chapter, we consider varying the local parameters across the cortex using a smooth spatial parametrisation relying on spherical harmonics.

6.5.2 Influence of structural information

The functional properties measured at the whole-brain level depend fundamentally on the underlying definition of different brain regions (Smith et al. 2011; Fornito et al. 2013). The task of defining cortical parcellations reliably across subjects and modalities is extremely difficult, and is still the object of active research (Harrison et al. 2015; Glasser et al. 2016); in fact, whether or not individual structural connectomes are better predictors of their own functional connectomes than averaged ones is currently an open

question. Moreover in the case of MEG, the "leakage" of spatial information, due to the ill-posed nature of source-reconstruction (see §2.4.2), adds to the difficulty in delineating different brain regions (Farahibozorg et al. 2017).

We have no definite answer to these questions, and the effects of the anatomical parcellation, as well as potential predictions of subject-specific characteristics, will be the object of future work.

Nevertheless, we would like to point out that several connectivity matrices (produced using different seeding and normalisation methods) were compared in the results presented, based on their ability to produce network dynamics of interest. In particular, the two best results obtained, using `conn1_mean` and `conn3_fs` AC matrices, indicate that inter-hemispheric connections should be between two and three times as strong (see Fig. 6.4). In other words, GPSO allowed us to assess *structure* (the AC matrix) from *function* (band-specific FC); this is an exciting perspective, and one with a different emphasis to previous work relating structure and function through biophysical models (Stephan et al. 2009; Deco et al. 2014).

6.5.3 Overfitting concerns

While overfitting is generally an important consideration in modelling and inference, we do not think it is an issue in this particular case.

First, in order to reduce the effects of measurement noise in the definition of our objective, we used an established analysis pipeline to estimate empirical functional connectivity (FC) matrices in several relevant frequency bands, and further averaged these matrices across subjects in our dataset to increase the signal-to-noise ratio (see §2.4.5).

One way to assess the risk of overfitting during optimisation is to look at the consistency of the averaged FC across subjects; if there were not enough subjects for the mean to "converge" to a representative value, then splitting the dataset into two groups, and

running the optimisation separately within each group, could yield significantly different results. However, based on the split-half tests shown previous on Fig. 4.5 p.98, we see that between-groups correlations is on the order of 75% across frequency bands (for the average envelope-based FC on the left), and up to 90% in the alpha band, with very low variance. These scores are much higher than the similarity achieved between simulations and empirical data (see figure 8), and therefore it is unlikely that optimising two groups of subjects independently would yield higher similarity within-group than between them.

More fundamentally, the empirical data is much richer than the models allow; especially from the perspective of spectral contents, and variability of functional connectivity over time. Our five-parameters model, with its restrictive assumptions (e.g. uniform local parameterization) is far too simple to capture the full richness of the MEG data.

6.5.4 Objective function and parametrisation

The objective function proposed in §4.3.3.1 combines a measure of envelope correlations with a comparison of connectivity-magnitude variations across frequency-bands. We highlighted in §6.4.1 the potential benefits of considering multi-criteria objective functions in the context of LSBM optimisation. However, the different ways in which these criteria can be combined into a single value (*e.g.* arithmetic, geometric or harmonic averaging, L^p norms, *etc.*) may affect the performance of the optimisation in the best case (if they affect the shape of the objective function while preserving extrema), or in the worst case even alter the objective itself. Similarly, the choice of equivalent parameters (*e.g.* §6.2.2.1) may affect the performance, or the success, of the optimisation.

Characterising the relationship between parametrisation, objective function (particularly when combining different criteria) and optimisation procedure, in order to determine the properties that work best together, is a difficult task. Further experiments will be conducted in the future in order to investigate this relationship.

7

Optimising Non-Uniform LSBMs

Contents

7.1 Introduction

In this chapter, we present the results of preliminary experiments aimed at exploring the benefits of allowing the local parameters of LSBMs (*i.e.* the unit's parameters) to vary across different regions. The assumption that all units should be identical across the cortex (made in the previous chapter) is overly simplistic, and it has been shown previously that allowing their parameters to vary across different regions can give rise to richer temporal dynamics (Chaudhuri et al. 2014). In order to avoid the tedious task of specifying manually the parameters in each region, we propose to encode these variations as a continuous map of modulation across the cortex using spherical harmonics (SH). Similar uses of SH to encode information on the cortical surface have been proposed in the literature (Chung et al. 2007). This provides us with a flexible representation of spatial patterns while controlling only a few parameters, which can be optimised by GPSO in the context of LSBMs.

Several additional changes are made in comparison with the previous experiments, including: the use of tract-lengths instead of Euclidean distances to estimate the delays between different regions; the inclusion of spectral constraints into the objective function; and the use of different unit parameters (see Tab. 3.1 p.51).

We find that the inclusion of spectral constraints into the objective leads to simulated time-courses with striking similarity compared with MEG resting-state data. The similarity between band-specific functional connectivity (FC) matrices improves considerably compared with the previous results, which may be due to several reasons, including the more accurate estimation of network delays (affecting the timing of interactions between regions). Allowing units' parameters to vary across regions improved the correspondence in the frontal lobe by almost 50% (in terms of functional connectivity), but remains poor overall with a best correlation of 0.3 on average across frequency bands, and only 0.15 in alpha band (see Fig. 7.6). This suggests that perhaps a more fundamental change

to our models is required, such as the inclusion of subcortical structures, or the use of a more detailed oscillatory model (see §3.4).

7.2 Problem Definition

7.2.1 Assumptions

In comparison with the previous chapter, and as explained in the following paragraphs, we relax assumptions 1 and 2, which state respectively that units are identical across the networks, and that excitatory and inhibitory subpopulations have the same response function and decay-times.

Specifically, assumption 1 is relaxed by modulating the units' excitatory couplings across the network. This is inspired by the work of (Chaudhuri et al. 2014), in which the authors associate such modulation with a so-called "intrinsic hierarchy" between different brain regions — correlated with dendritic spine counts reported in (Elston 2007) — and demonstrate its importance in shaping realistic FC matrices from biophysical models (see Figure 8A in the paper). In that paper, the modulation is implemented as a multiplicative factor $(1+\eta h)$ to the excitatory coupling terms, where η is a scaling parameter (similar to γ in our case, see §6.2.2), and h is the intrinsic hierarchy parameter (between 0 and 1). In our experiments, we implement this modulation using spherical harmonics to encode spatial variations. Our aim is to investigate the benefits of allowing local parameters to vary across the cortex (especially in the frontal areas, see Fig. 6.6) by letting GPSO tweak the modulation maps so as to maximise the functional similarity with resting-state MEG data.

Assumption 2 is relaxed partially by **allowing the local excitatory and inhibitory populations to have different decay-times**. This follows from physiological evidence that inhibitory decay-times are typically longer than excitatory ones (Tripathy et al. 2014),

and from the results of complementary experiments (not shown for brevity) which suggest that doing so can improve the spectral contents of LSBM simulations.

Finally, we also used **tract-lengths instead of Euclidean distances** (see §2.3.3) in order to estimate the propagation delays between different brain regions more accurately.

7.2.2 Spherical harmonic mapping

Similarly to the decomposition of functions defined on the real line as series of sines and cosines with increasing frequencies (*i.e.* the discrete Fourier transform), functions defined on the 2-sphere can be decomposed as series of so-called *spherical harmonics* (SH) with increasing angular frequencies. These are functions of the azimuth and inclination angles[1], respectively $\varphi \in [0, 2\pi)$ and $\theta \in [0, \pi]$, and parametrised by their **order** $m \geq 0$ which characterises their angular frequency. There are $2m+1$ SH of order m, defined by:

$$S_{m,k}(\varphi,\theta) = \begin{cases} C_{m,|k|} N_{m,|k|}(\theta)\ \sin(|k|\varphi) & : -m \leq k < 0 \\ N_{m,0}(\theta) & : k = 0 \\ C_{m,k} N_{m,k}(\theta)\ \cos(k\varphi) & : 0 < k \leq m \end{cases} \tag{7.1}$$

with the notation:

$$\forall\ 0 \leq k \leq m, \quad N_{m,k}(\theta) = P_{m,k}(\cos(\theta))\sqrt{\frac{2m+1}{4\pi}} \quad \text{and} \quad \frac{C_{m,k}^2}{2} = \frac{(m-k)!}{(m+k)!}$$

where $P_{m,k} : [-1,1] \mapsto [-1,1]$ is the associated Legendre polynomial of order m and degree k.

The cortical surfaces made available by the HCP (Van Essen et al. 2012a) exist in several forms of triangulated meshes, including a fully inflated form in which the cortical vertices corresponding to each hemisphere independently have been mapped onto a sphere. We

[1] The azimuth angle is measured counter-clockwise from the x-axis in the xy-plane, and the inclination is measured from the positive z-axis. The elevation, measuring the angle from the xy-plane, corresponds to $\pi/2 - \theta$.

used this surface in order to define smooth maps on the cortical surface, encoded as a weighted sum of SH functions.

For a given upper-bound $M \geq 0$ on the order parameter, we consider patterns of modulation defined as a truncated sum of $\sum_{m=0}^{M} 2m+1 = (M+1)^2$ harmonic functions, where the component $S_{0,0}$ corresponds to an offset value across the whole sphere, and the higher order components correspond to "high frequency" information (*i.e.* more spatially refined).

Denoting $\left\{w_{m,k}\right\}_{m=0..M,\ k=-m..m}$ the weights associated with each component, and $\{v_i\}_{i=1..V}$ the cortical vertices of the left hemisphere mapped onto a sphere (the modulation was mirrored on the right hemisphere), the value at any vertex is given by:

$$\forall\, i \in \{1..V\}, \quad v_i = (r_i, \phi_i, \theta_i) \;\mapsto\; \sum_{m=0}^{M} \sum_{k=-m}^{m} w^*_{m,k} S_{m,k}(\phi_i, \theta_i) \tag{7.2}$$

where $w^*_{m,k} = w_{m,k} \,\Big/ \max_i \left|S_{m,k}(\phi_i, \theta_i)\right|$ is a normalised weight corresponding to the actual maximal absolute contribution of component $S_{m,k}$ across all vertices. **In our experiments, we control these normalised weights directly**; the normalising factor is computed internally for each harmonic component across vertices, prior to computing the weighted sum.

The resulting cortical map is then summarised within each region of the DK parcellation (shown in Fig. 2.1 p.11), by averaging the values associated with all vertices belonging to this region. An example of the parcellated maps obtained is shown in Fig. 7.1 for $M = 1$ (4 components).

7.2.3 Parametrisation

In this chapter, we present the results of four experiments considering two different unit parameters (units B and C given in Tab. 3.1 p.51), and two AC matrices (`conn1_mean`

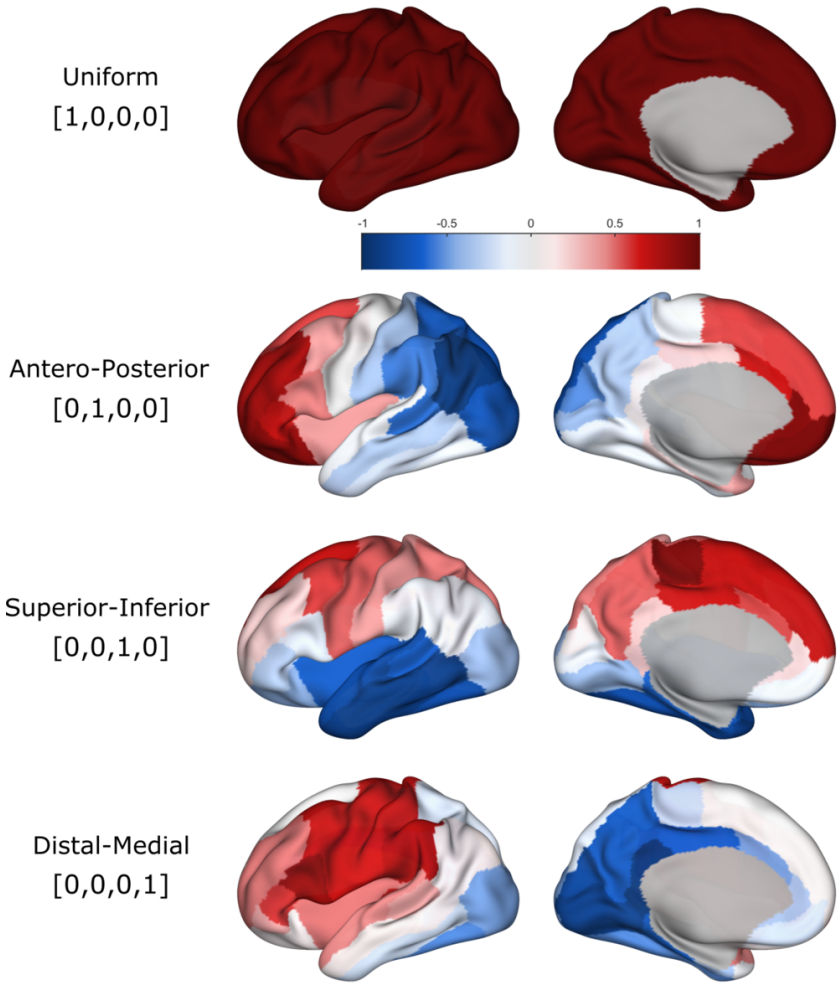

Figure 7.1: Example of parcellated cortical maps using spherical harmonics (left hemisphere; right hemisphere is mirrored). We used the spherical meshes from the HCP (Van Essen et al. 2012a) to assign a value to each cortical vertex as a weighted sum of spherical harmonic functions, here up to order 1 (4 components). The weights shown on the left correspond to the normalised weights defined in Eq. 7.2; the first weight is simply an offset for all vertices, and the remaining weights ($w^*_{1,-1}, w^*_{1,0}$, and $w^*_{1,1}$) correspond respectively to the antero-posterior (AP), superior-inferior (SI) and distal-medial (DM) directions. Using negative weights instead would yield the same pattern but with opposite signs (*i.e.* the opposite direction).

and `conn3_fs`). As mentioned previously, the decay-times within the E and I populations of neurons were allowed to vary independently in these experiments (uniformly across all regions), by **controlling τ_e as a baseline value, and the ratio τ_i/τ_e**. The effects of these parameters on the local dynamics can be seen in Fig. 3.7.

The local excitatory couplings c_{ee} and c_{ei} were modulated in each region of the DK parcellation using spherical harmonics. For the sake of simplicity, and in order to keep the optimisation times reasonable, we restricted ourselves to four harmonics (*i.e.* $M = 1$), and only controlled **three normalised weights** during optimisation: the AP weight $w_{\text{AP}} = w^*_{1,-1}$, the SI weight $w_{\text{SI}} = w^*_{1,0}$, and the DM weight $w_{\text{DM}} = w^*_{1,1}$ (shown in Fig. 7.1). By choosing search-intervals centred around 0 for these weights, and setting $w^*_{0,0} = 1$, we obtained a parametrisation in which **non-zero values result in a non-uniform cortical map, and all three values being zero yields a map equal to 1 everywhere**. Centred search-intervals also ensured that any non-uniform map had an opposite achievable by GPSO. With this parametrisation, the excitatory couplings (c_{ee} and c_{ei}) in each unit were **scaled** by the value obtained in each brain region for a given choice of weights (w_{AP}, w_{SI}, w_{DM}). The effects of such scaling on the local dynamics are shown in Fig. 3.5 p.54 (last row second column).

Finally, the network equations given in the previous chapter (Eqs. 6.1 and 6.3) remain unchanged. However, we change the definition of the relative coupling from a multiplicative, to an **additive form**:

$$\tilde{\gamma}^{\,\text{old}} = \gamma/\gamma^* \quad \Rightarrow \quad \tilde{\gamma} = \gamma - \gamma^* \tag{7.3}$$

This is because the coupling threshold γ^* was found to be highly dependent on the input P_e; as a consequence, the range of actual coupling values γ spanned for a fixed interval $\tilde{\gamma}^{\,\text{old}} \in (1,3)$ became very small for values of $\widetilde{P_e}$ close to 1. By choosing an additive form instead, we ensure that the effective width of the search-interval is independent of the excitatory input.

In total, there are now **nine parameters** being controlled by GPSO, and we give the corresponding search-intervals in Tab. 7.1.

Symbol	Description	Short-name	Range
$\widetilde{P_e}$	Relative input	Input	$(0.7, 1)$
$\widetilde{\gamma}$	Relative coupling	Coupling	$(0, 3)$
$\overline{\lambda}$	Average delay (ms)	Delay	$(1, 50)$
w_{AP}	Antero-posterior weight	AP weight	$(-0.5, 0.5)$
w_{SI}	Superior-inferior weight	SI weight	$(-0.5, 0.5)$
w_{DM}	Distal-medial weight	DM weight	$(-0.5, 0.5)$
h	Inter-hemispheric scaling	IH scaling	$(0, 5)$
τ_e	Decay-time (ms)	Tau	$(5, 20)$
τ_i/τ_e	Decay-time (ms)	Tau	$(0.5, 3)$

Table 7.1: Network parameters controlled during optimisation. The ranges correspond to the boundaries of the search space (required by GPSO). Note that the definition of the relative coupling $\widetilde{\gamma}$ is additive, not multiplicative, in this chapter (see Eq. 7.3).

7.2.4 Objective function

In this chapter, we consider both the band-specific FC matrices (taken as envelope correlations) *and* the time-frequency contents of the activity within each region, as features to be compared between simulated and reference data. As in the previous chapter, we consider six overlapping frequency-bands, and the simulated time-courses are orthogonalised prior to computing the features of interest, in order to normalise for the potential artefacts introduced by leakage correction on source-reconstructed MEG data.

We denote $M_{1..6}$ the band-specific FC matrices, and P_μ, P_σ respectively the temporal mean and standard-deviation of the wavelet time-courses computed between 4 and 40 Hz for each time-course. The FC matrices are all of size $N \times N$, and the matrices P_μ, P_σ are both of size $37 \times N$ (where N is the number of regions, and $37 = 40 - 4 + 1$).

With these notations, the similarity between simulated and reference MEG data is taken as:

$$\bigotimes \left[\frac{1}{6} \sum_{k=1}^{6} \mathrm{TrilCorr}(M_k^{\mathrm{ref}}, M_k^{\mathrm{sim}}),\ \mathrm{Corr}(P_\mu^{\mathrm{ref}}, P_\mu^{\mathrm{sim}}),\ \mathrm{Corr}(P_\sigma^{\mathrm{ref}}, P_\sigma^{\mathrm{sim}}) \right] \tag{7.4}$$

where $\mathrm{TrilCorr}$ denotes the correlation between lower-triangular elements; Corr denotes the correlation between **vectorised** matrices, which in this case allows to account for power-level differences across brain regions; and $\bigotimes$ denotes the **signed geometric mean**, such that $|\bigotimes(a_1, a_2, ..., a_n)| = |\prod_{k=1}^{n} a_k|^{1/n}$, and the result is negative if one *or more* factors are negative. This ensures that positive scores correspond necessarily to samples which do well with respect to all three criteria.

7.3 Results

We present the results of four experiments, considering two different unit parameters, and two AC matrices:

Experiment	Unit	Connectivity
1	B	`conn1_mean`
2	B	`conn3_fs`
3	C	`conn1_mean`
4	C	`conn3_fs`

In the following, **we abbreviate the names of the AC matrices as `c1m` and `c3fs` for short**.

GPSO was run with similar hyper-parameters as given in Tab. 6.2, except for the use of an anisotropic Matèrn covariance kernel (order 5 with automatic relevance determination), and using the improved partition function presented in §5.3. Optimisation was run with nine parameters given in Tab. 7.1, and a budget of 3000 simulations per experiment. Each

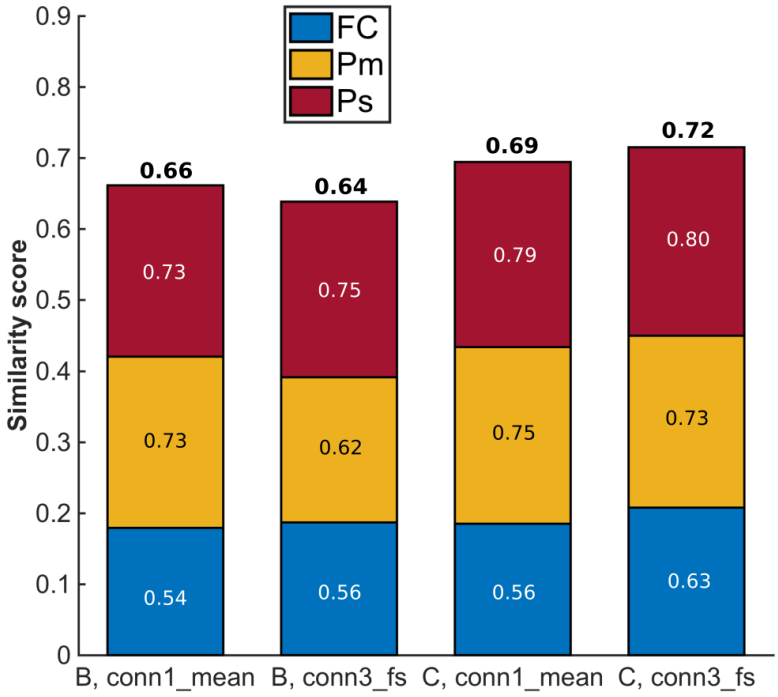

Figure 7.2: Break-down of the best scores obtained for the four experiments considered in this chapter. The similarity score used as an objective function during the experiments is shown on top of each bar, and the factors entering in its definition (see Eq. 7.4) are shown underneath: in blue for the average correlation of FC matrices; in yellow for the correlation of average wavelet-power P_m (aka spectral mean); and in red for the correlation of temporal deviations of wavelet-power P_s (aka spectral deviation). The performance of unit B is noticeably inferior to that of unit C, although its performance in terms of FC similarity is better than the results presented in the previous chapter (see Fig. 6.3 p.152), although these results cannot be compared directly (different parameters, objective and delays).

experiment took approximately six days to run; by comparison, an exhaustive search with just 20 values per dimension would take just shy of two million years to complete.

7.3.1 Summary results

The best scores achieved for each of the four experiments are compared in Fig. 7.2, along with a break-down of the contributions in terms of the factors defined in Eq. 7.4 (*i.e.* average FC similarity, spectral-mean similarity, and spectral-deviation similarity). Overall, simulations with unit C led to better results than with unit B, although the correspondence in terms of average FC is significantly better than in the previous chapter

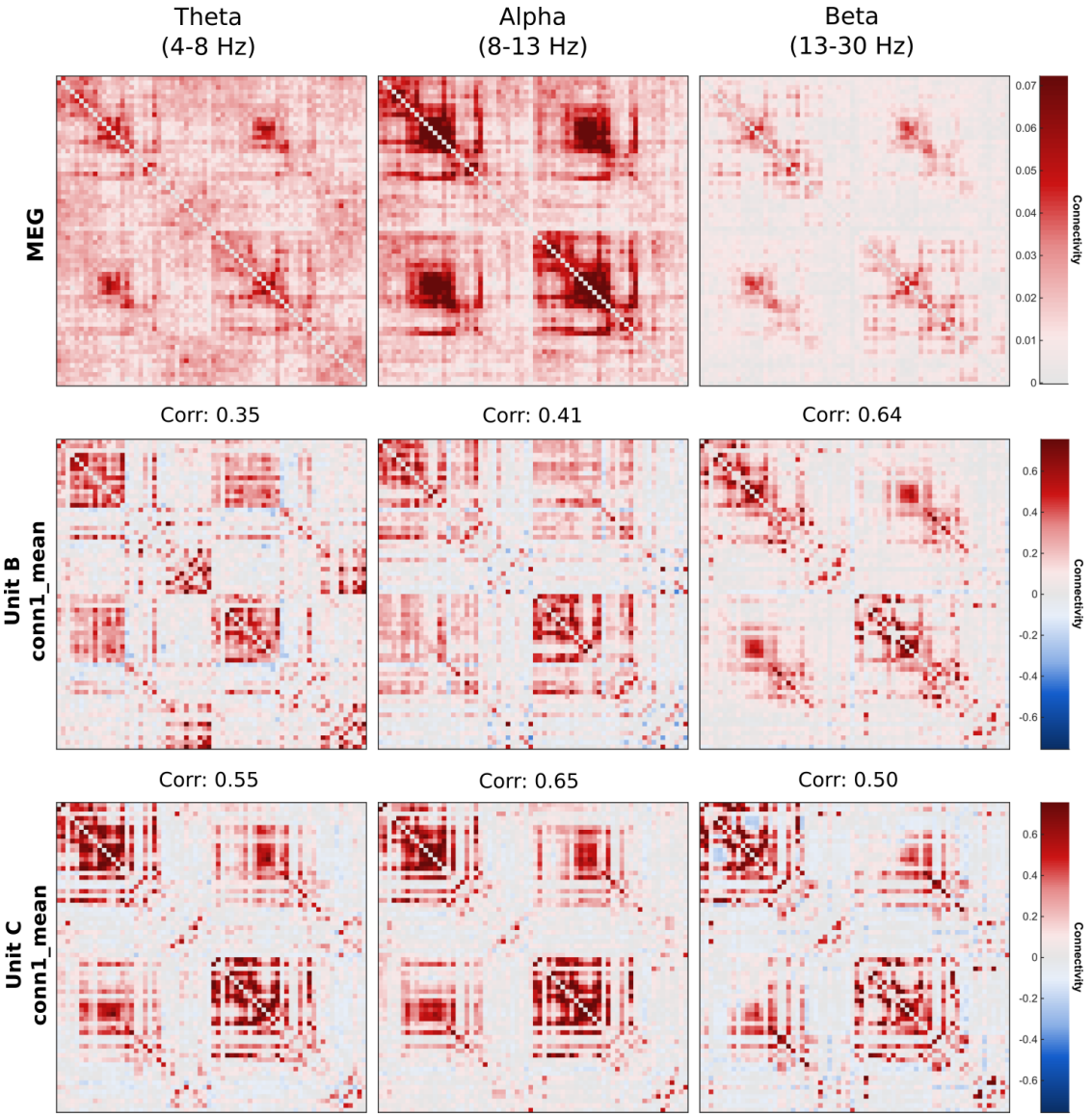

Figure 7.3: Functional connectivity matrices corresponding to the best simulations in experiments 1-3 (unit D was excluded from this panel due to its lower performance, see Fig. 7.2). The correspondence with real MEG data is slightly degraded in the alpha band compared to the previous results (see Fig. 6.2), though better overall across bands. There is also a noticeable difference in the FC patterns between the results obtained with `conn3_fs` (row 2) and `conn1_mean` (rows 3-4) connectivities, which can be described as a "clear-cut" separation between temporal+occipital and parietal+frontal lobes in the case of `conn3_fs`.

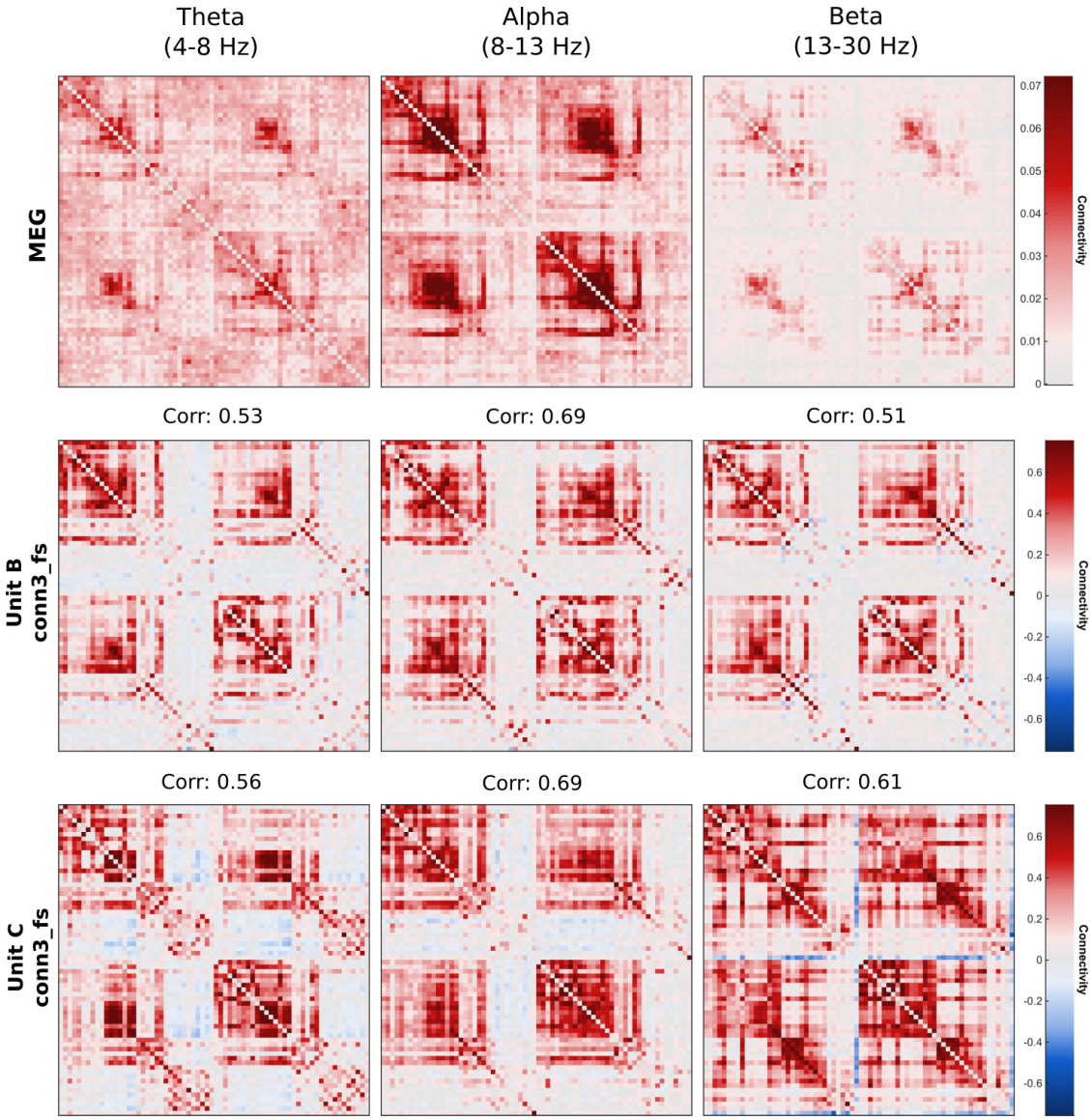

Figure 7.4: Functional connectivity matrices corresponding to the best simulations in experiments 1-3 (unit D was excluded from this panel due to its lower performance, see Fig. 7.2). The correspondence with real MEG data is slightly degraded in the alpha band compared to the previous results (see Fig. 6.2), though better overall across bands. There is also a noticeable difference in the FC patterns between the results obtained with `conn3_fs` (row 2) and `conn1_mean` (rows 3-4) connectivities, which can be described as a "clear-cut" separation between temporal+occipital and parietal+frontal lobes in the case of `conn3_fs`.

in both cases. The comparison between the two AC matrices, `c1m` and `c3fs` is less clear; the summary scores obtained with unit B suggest that `c1m` connectivity is superior, whereas it is the contrary with unit C.

Taking a deeper look at the results in terms of correspondence localised on the cortical surface, for each criterion contributing to the objective function, clarifies the picture. `c3fs` connectivity seems to yield a more consistent correspondence across bands (compared to `c1m` connectivity) in terms of FC in the temporal and occipital lobes (see Fig. 7.6), and simulations with unit C yield noticeably better correspondence (compared to unit B) in terms of spectral features (see Fig. 7.7).

The FC matrices corresponding to the best simulations in each experiment (figures 7.3 and 7.4) reveal an impressive pattern-variability across bands in the case of experiments 1 and 4. However, we note that the correspondence in terms of alpha connectivity in the frontal lobe is still very poor in all cases, which suggests that the problem uncovered in the previous chapter is not only due to assumption of coupling-uniformity across the cortex.

Lastly, the marginal parameter distributions corresponding to the best samples in each experiment are shown in Fig. 7.5. A consensus with regards to the "preferred" parameter values is achieved for most parameters, with a few notable exceptions:

- The spherical-harmonic weight in the AP direction was unused by most experiments, except in the case of experiment 3, with a strong preference for values around $w_{\mathrm{AP}} = -0.4$, corresponding to larger excitatory couplings in the posterior areas. It is unclear what the effects of this choice are, when looking at the various features contributing to objective function.

- There is no clear consensus with regards to the relative excitatory input $\widetilde{P_e}$ (row 1), or the ratio of decay-times τ_i/τ_e (row 9), though all experiments suggest that τ_i should be larger with a factor roughly between 1.5 and 3.

The preferred value of the average propagation delay between regions (row 2) is now between 15 and 35 ms (compared to 10 ms in the previous chapter), which fits better with our expectations (see discussion in §6.4.2); though it is unclear whether this is due to the use of tract-lengths instead of Euclidean distances, the inclusion of spectral constraints in the objective function, or to the difference allowed between τ_i and τ_e. Finally, the results obtained across experiments suggest that the search-interval for the relative coupling parameter $\widetilde{\gamma}$ (row 3) was too narrow[2]. This is surprising, because it seems at odds with the hypothesis of *criticality* in the literature, which suggests that LSBMs should sit near their oscillatory thresholds (here $\widetilde{P_e} = 1$ and $\widetilde{\gamma} = 0$) in order to produce meta-stable activity most similar to empirical measurements (Deco et al. 2011).

7.3.2 Region-wise similarity

Here, we evaluate the correspondence between the best simulations and reference MEG data within each region of the DK cortical parcellation. This region-wise correspondence is established separately with regards to the band-specific FC, and to the spectral contents.

As shown in Fig. 7.6, the FC correspondence in theta band is significantly higher in these experiments than in the previous chapter. The reasons for this unusual spectral distribution may be due to the use of a different delay-structure, or the choice of different excitatory and inhibitory decay-times, and more generally considering unit parameters varying across the network. The correspondence in the frontal lobe remains low compared to other lobes, especially in alpha band.

As shown in Fig. 7.7, the correlation between simulated and reference spectral contents (temporal mean and standard-deviation of wavelet time-courses) is very high across experiments, though noticeably lower in experiments 1 and 2 (using unit B), particularly in the frontal lobe in the case of the spectral mean.

[2] Again! This is the second run of the experiment, and the size of this interval was doubled compared to the previous run.

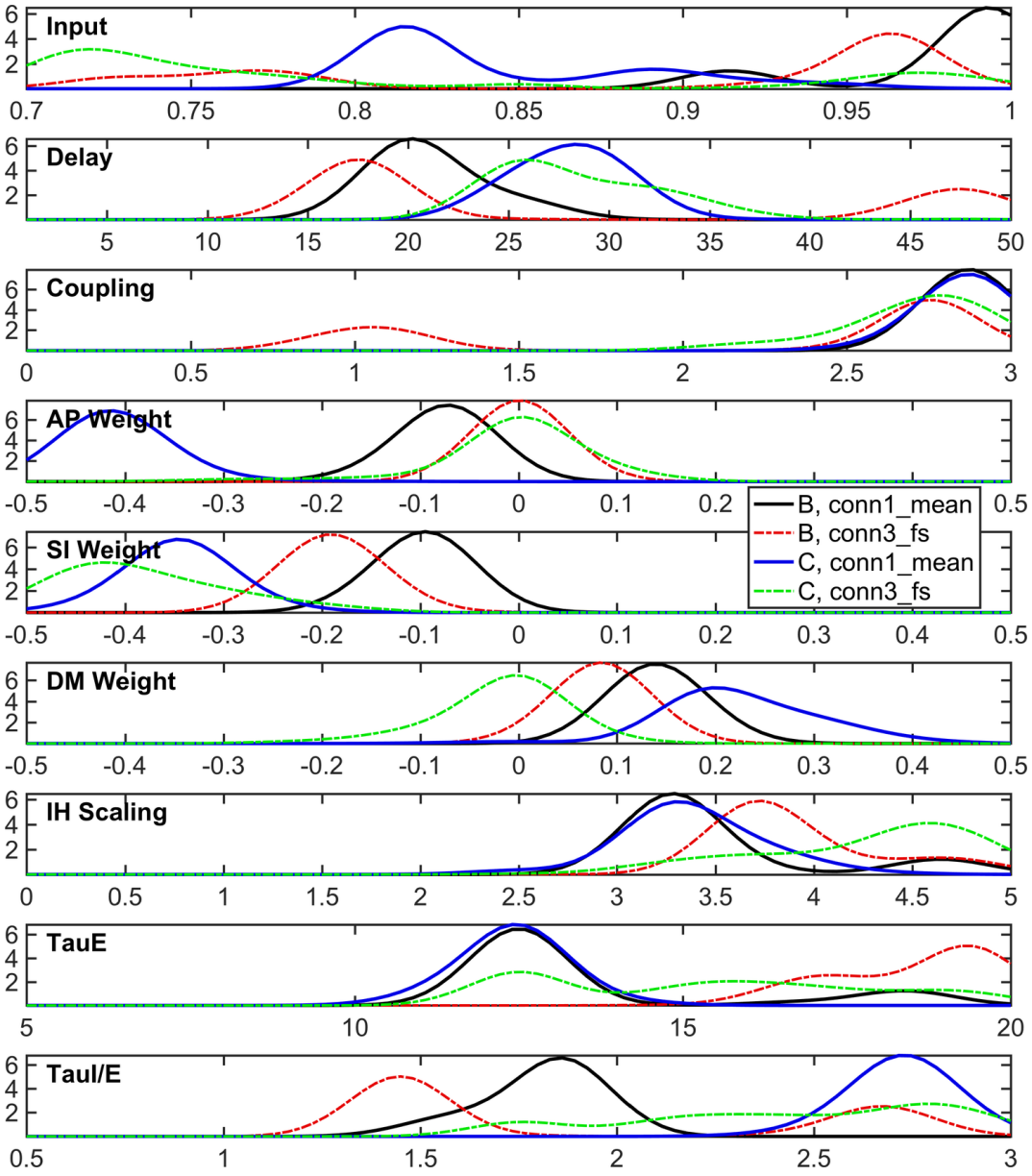

Figure 7.5: Marginal parameter distributions corresponding to the 90th percentile of all evaluated samples, for each experiment. To be compared with Fig. 6.4 in the previous chapter. The range of relative coupling $\widetilde{\gamma}$ considered (row 3) may have been too narrow for these experiments, given the clear preference for larger coupling. There is also no clear consensus as to how close the excitatory input $\widetilde{P_e}$ should be to the oscillatory threshold ($\widetilde{P_e} = 1$). The average network delay is now placed between 15 and 35 ms, instead of 10 ms previously. All experiments suggest that inter-hemispheric couplings should be increased 2-5 fold, which is consistent with the previous results. Finally, the spherical-harmonic modulation seems to be unhelpful in the AP direction (row 4, except for experiment 3), but there is a clear preference for a modulation towards inferior regions (row 5), and a noticeable bias for distal modulation (row 5).

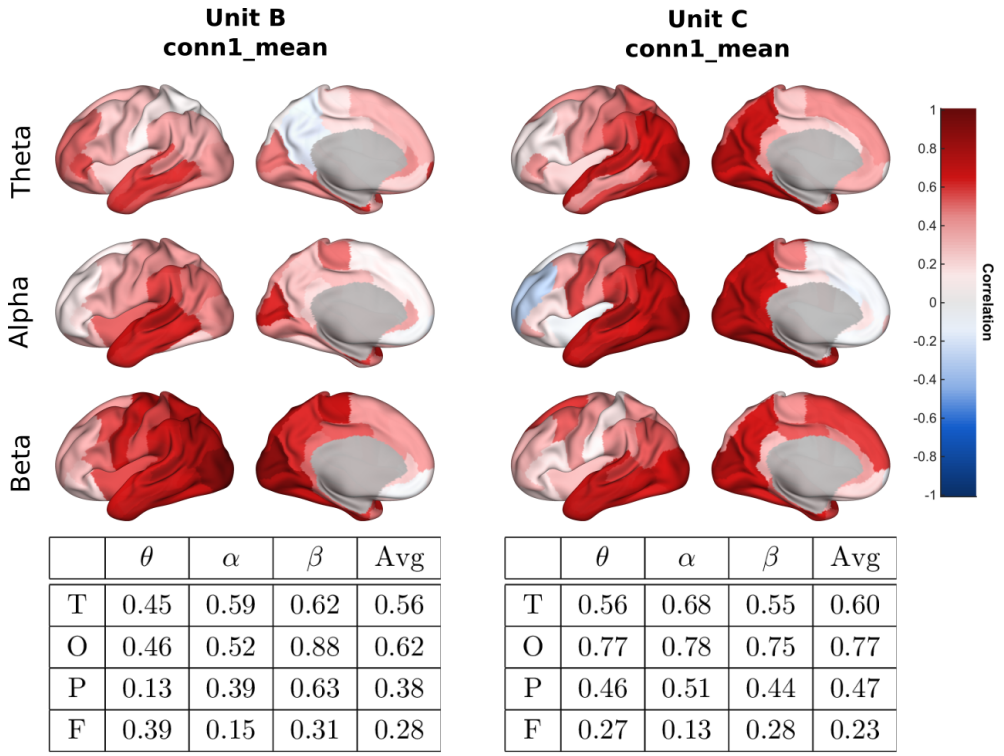

	θ	α	β	Avg
T	0.45	0.59	0.62	0.56
O	0.46	0.52	0.88	0.62
P	0.13	0.39	0.63	0.38
F	0.39	0.15	0.31	0.28

	θ	α	β	Avg
T	0.56	0.68	0.55	0.60
O	0.77	0.78	0.75	0.77
P	0.46	0.51	0.44	0.47
F	0.27	0.13	0.28	0.23

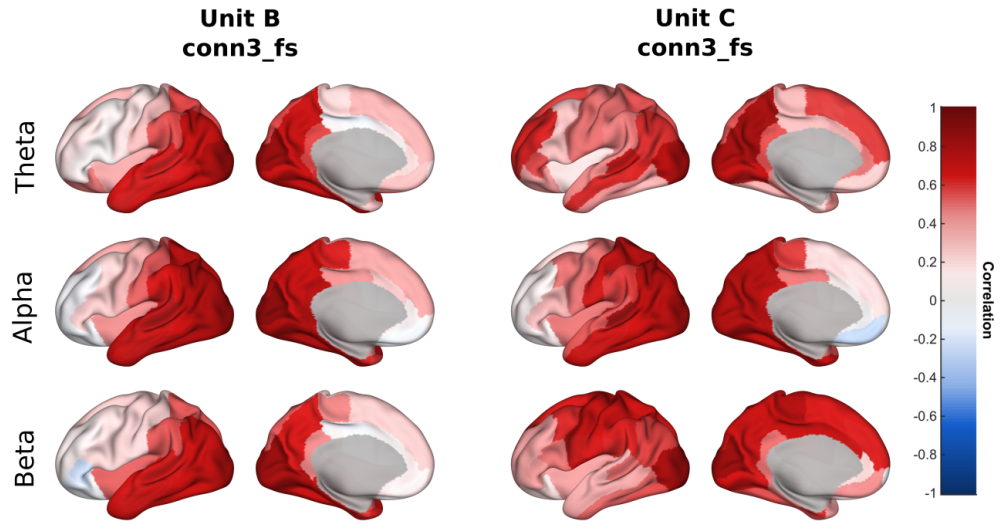

	θ	α	β	Avg
T	0.52	0.64	0.56	0.57
O	0.81	0.86	0.82	0.83
P	0.40	0.61	0.40	0.47
F	0.19	0.06	0.08	0.11

	θ	α	β	Avg
T	0.48	0.70	0.53	0.57
O	0.78	0.79	0.78	0.79
P	0.52	0.65	0.66	0.61
F	0.38	0.14	0.37	0.30

Figure 7.6: Band-specific functional similarity within each brain region, obtained by correlating matching columns of the corresponding FC matrices. To be compared with the results obtained previously in Fig. 6.6. The spherical harmonic modulation did not help as we had hoped with functional correspondence in the frontal lobe, particularly in alpha band where the correspondence is still very poor. However, the similarity is noticeably higher than previously in theta bands.

The spectral correspondence is lowest in the case of experiment 2, and highest in the case of experiment 4; this can also be seen when looking at the simulated time-courses, and indeed the similarity between the best simulation in experiment 4 (see Fig. 7.8) and real MEG data (see Fig. 2.6 p.27) is visually striking.

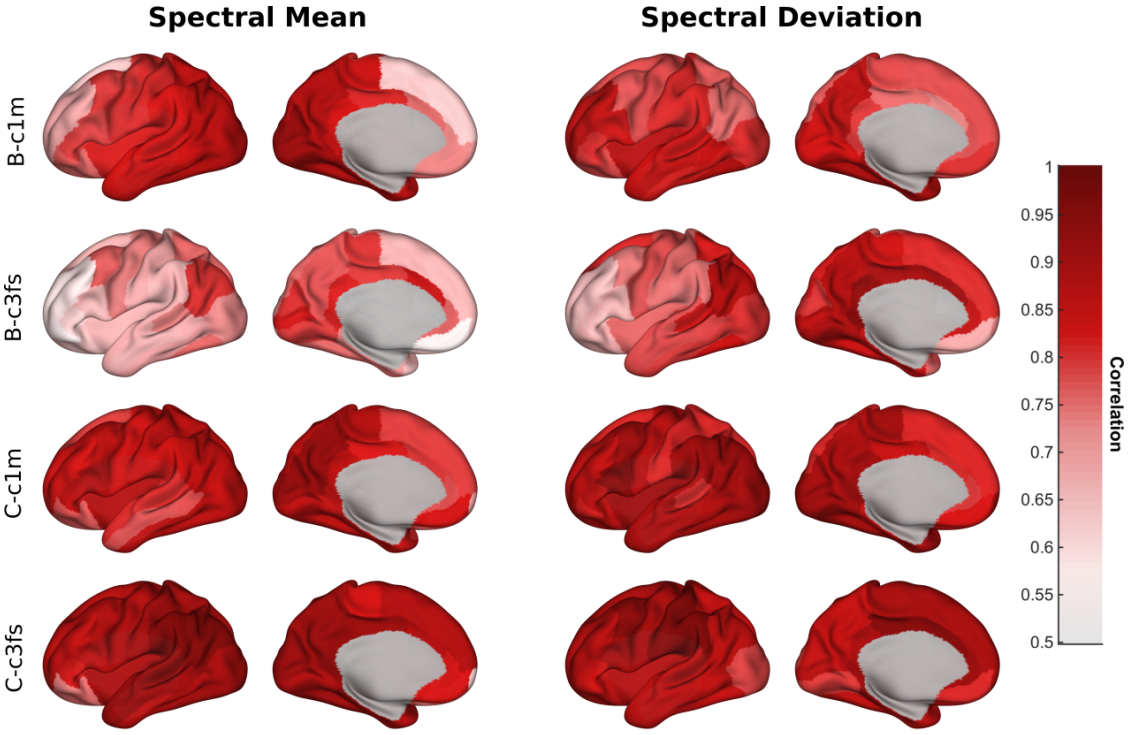

Exp	1	2	3	4
T	0.86	0.80	0.89	0.88
O	0.83	0.85	0.91	0.83
P	0.80	0.84	0.88	0.91
F	0.79	0.73	0.87	0.88
Avg	0.82	0.80	0.89	0.88

Exp	1	2	3	4
T	0.85	0.69	0.84	0.92
O	0.91	0.78	0.89	0.92
P	0.84	0.76	0.86	0.92
F	0.74	0.66	0.81	0.81
Avg	0.84	0.72	0.85	0.89

Figure 7.7: Spectral similarity within each brain region, obtained by correlating matching columns in matrices P_m (spectral mean) and P_s (spectral deviation), as defined in §7.2.4. The spectral similarity is excellent overall (note the colour-range), both in terms of temporal average or standard-deviation, and markedly higher in experiments with unit C; an example of simulated time-series is shown in Fig. 7.8.

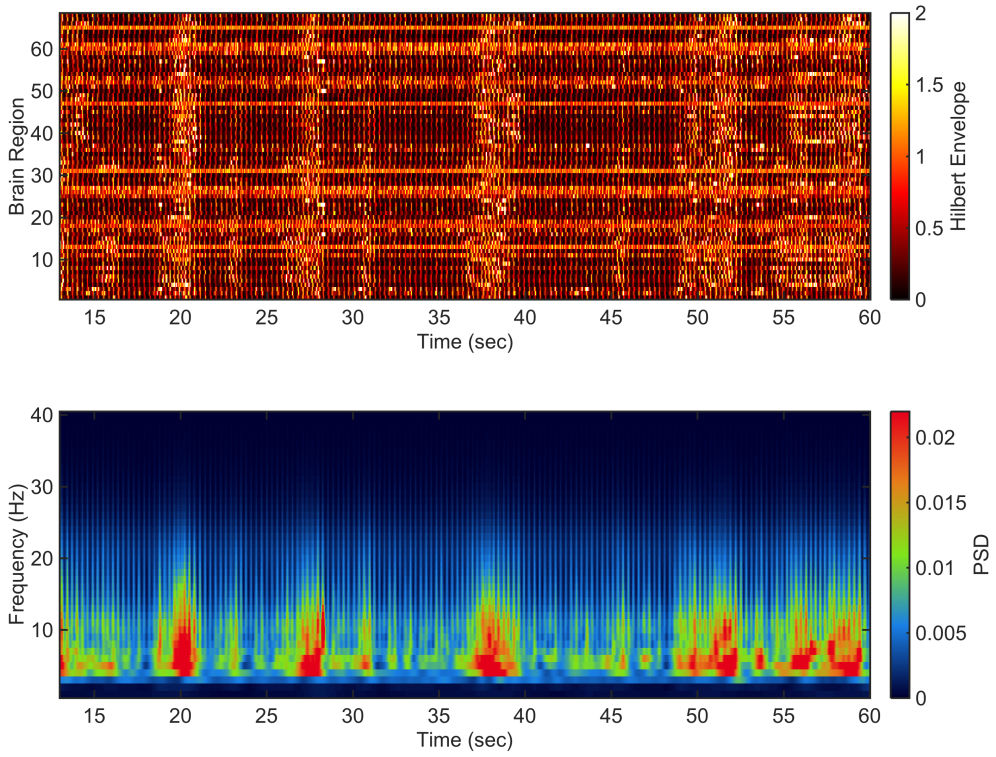

Figure 7.8: Best simulated time-courses with `conn3_fs` connectivity and unit C, to be compared against real MEG data in Fig. 2.6 p.27. The similarity in terms of envelope dynamics is striking, with multiple whole-brain synchronisation events (bright vertical bands) separated by a few seconds, and corresponding with transient bursts of activity spanning the theta and alpha ranges of frequency. Equally striking however, is the lack of spectral power for frequencies below 4 Hz; contrary to real MEG data, the simulations were *not* filtered between 4-40 Hz.

7.4 Discussion

Overall the results presented in this chapter further demonstrate the ability of GPSO to explore relatively high-dimensional search-spaces, and find regions of high functional correspondence with real MEG data. Although there are still improvements to be made (notably in frontal alpha, and frequency contents below 4Hz), the best simulated time-courses shown in Fig. 7.8 exhibit striking similarities with real MEG data, and the correspondence between band-specific functional connectivity matrices suggests that our models capture different patterns of interactions, occurring at different frequencies, between specific regions (particularly for experiments 1 and 4).

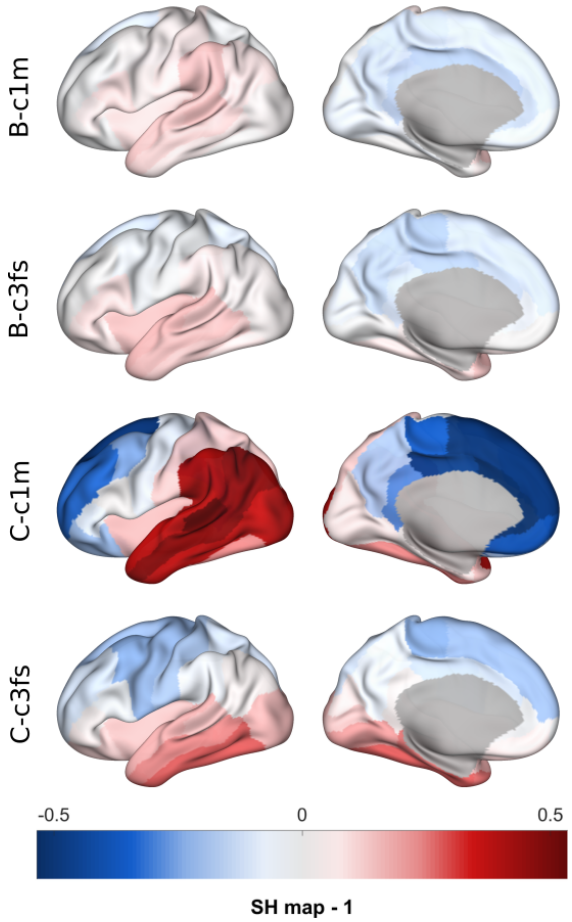

Figure 7.9: Spherical-harmonic modulation maps corresponding to the parameters $(w_{\mathrm{AP}}, w_{\mathrm{SI}}, w_{\mathrm{DM}})$ for the best results obtained in all experiments. The corresponding modulation of local excitatory couplings was on the order of $\pm 40\%$ in experiment 3, and $\pm 30\%$ in experiment 4 (which achieved the best results); those are very large variations, and perhaps requiring that the modulation balance-out across the surface (some regions with positive, and some with negative modulation) is unreasonable in such cases.

7.4.1 Benefits of parameter modulation

The spherical-harmonic modulation maps corresponding to the best simulations in each experiment are shown in Fig. 7.9. The largest modulations of local excitatory couplings were on the order of $\pm 40\%$ in experiment 3, and $\pm 30\%$ in experiment 4; such large differences can cause significant variations in terms of frequency responses (see third row in Fig. 3.5 p.54).

As discussed previously, the degrees of freedom introduced in this chapter in order to modulate the units' parameters across the cortex did not yield a major improvement with

regards to FC correspondence in the frontal lobe. This may seem difficult to reconcile with the fact that region-wise spectral similarity was so high (nearly 85% on average across experiments), but it could indicate an issue with the **timing of interactions** between the frontal lobe and other regions, which may be due to a number of reasons, including:

- The insufficient complexity of the oscillatory model considered (*e.g.* replacing the Wilson-Cowan model with the conductance-based model presented in §3.4);
- A fundamental structural deficit in our models, *e.g.* due to neglecting the role of subcortical structures;
- Or perhaps the need to modulate not only local excitatory couplings, but also long-range couplings (*i.e.* applying a block-wise modulation to the AC matrices).

Interestingly, these potential shortcomings could also account for the lack of slow dynamics observed in the best time-courses Fig. 7.8.

The last point relates to the work of (Chaudhuri et al. 2014), in which several modulations of the excitatory couplings are proposed, in accordance with the variation of dendritic spine counts across the cortex, and specifically in the frontal lobe. In our experiments, we adopted the simplest modulation (the so-called "intrinsic hierarchy" argued in the paper on Figure 8A), which only affects local excitatory couplings. The benefits of modulating both local and long-range couplings will be explored in future work.

Finally, it is worth mentioning a potential issue with the spherical-harmonic parametrisation chosen for this experiment. Although it is very convenient to be able to define smooth cortical maps with only three weight-coefficients, **one of the questionable side-effects is that the resulting modulation imposes a "dipole" pattern**, in the sense that for any region with modulation greater than baseline, there is a region with comparable modulation lower than baseline. It would be interesting to investigate instead, a parametrisation in which positive weights would lead to lead to a gradient of modulation from the baseline upwards, and similarly downwards for negative weights.

7.4.2 Questioning the objective

Although the previous results could be improved, should we really expect that a particular model, with specific parameters, would be able to reproduce dynamical features corresponding to an average across subjects?

We know from the analysis of empirical resting-state MEG data, that large variations across subjects are to be expected, and even so within-subjects to a lesser extent (Colclough et al. 2016). This casts uncertainty regarding the meaning of the average patterns observed; the fact that these patterns can be repeated across large groups of subjects indicates that they are characteristic of resting-state activity, but perhaps a pattern is all this is, in which case we should not expect our biophysical models to improve significantly at the population-level, and instead it may be time to consider particular groups of subjects (*e.g.* genetically related individuals, see Colclough et al. 2017), or even individuals, in order to move forward.

8

Conclusion

Summary of contributions

We have presented several computational models capable, with varying degrees of biological plausibility, of generating time-series which exhibit complex properties thought to be characteristic of resting-state activity, as measured by magneto-encephalography (MEG). These models were implemented as part of a novel software framework, which performance compares favourably to that of large established alternatives in the field, while being much lighter and (we argue) more flexible. We proposed two novel analysis methods to measure and compare functional connectivity in (simulated or empirical) parcellated brain activity, and demonstrated that the measure proposed improves the replicability across subjects, in an admittedly small dataset of 28 subjects.

We then adapted a method recently developed in the field of Bayesian optimisation, and proposed its use as a generic tool for inference in the context of large-scale biophysical modelling (with consideration for the computational constraints encountered in practice). Furthermore, we proposed an extension of this method involving concepts at the cross-roads between geometry and combinatorics, and demonstrated formally that it drastically improved convergence in higher-dimensional spaces. Here as well, these methods were implemented as part of a novel software package, improving on alternative implementations to date in terms of efficiency, resilience and flexibility.

Finally, we applied this optimisation method to fit the parameters of two large-scale biophysical models of resting-state activity (respectively with 5 and 9 parameters), using structural connectivity information derived from diffusion tractography, by comparing band-specific functional connectivity patterns as well as spectral properties with empirical MEG data. The proposed optimisation method was able to efficiently and reliably explore the parameter-spaces in each case, yielding results with high levels of correspondence with resting-state MEG. Through a detailed and systematic analysis of those results, we further demonstrated the benefits of using this method in a modelling context, looking at marginal parameter distributions across high-performing samples to reveal preferred parameter ranges; conditional distributions around the optimum to study the local topography of the objective function; and cortical maps of the correspondence between simulations and empirical data in order to guide potential improvements to our models.

So what matters?

The results presented in this thesis, and the experience accumulated throughout our research, suggest that the following modelling aspects matter:

- The parameters governing the local activity (*i.e*. the unit parameters). In particular:
  - the characteristic decay/response-time;
  - the presence of a fast excitatory, and slower inhibitory subpopulation;
  - the fact that inputs to a given unit modulate both its amplitude and frequency response;
- The modulation of unit parameters across different regions;
- The shape of the distribution of long-range coupling strength as a function of the distance between brain regions;
- The ratio of inter- vs. intra- hemispheric coupling;
- The average propagation delay between different brain regions.

In addition, the following points correspond to modelling aspects which likely matter, but for which we only have limited evidence so far:

- An accurate estimation of propagation delays, *e.g*. using tract-lengths instead of Euclidean distances between regions, and potentially using MRI myelin maps to modulate conduction velocities;
- The ratio between the average amounts of local vs external coupling, for each individual unit;
- Long-range inhibition, by excitation of remote inhibitory subpopulations.

Finally aspects which, in our experience, do not seem to matter:

- The choice of a particular sigmoid function (*i.e*. logistic, trigonometric *etc*.);

- The rounding of delays to a precision lower than the units' decay-times;
- The presence of decay-times between potential and conductance variables in the conductance-based model.

Future Work

Besides the various extensions to our work mentioned in the previous chapters (*i.e.* in sections 4.4, 5.6, and with regards to using different oscillatory models or including subcortical structures into the networks), below are two potential future works that would be interesting to pursue:

- **Multi-stage objective function:** so far, we have focused on making the simulations of LSBMs computationally efficient (see §3.5), and on developing an optimisation method capable of efficiently exploring high-dimensional spaces (chapter 5). Another unexplored possibility would be to consider an objective function which would *evolve* as a function of the depth in the partition tree; for example, we could consider running short simulations in the first instance, comparing Fourier distributions based on these time-courses, but only computing full-length simulations and associated FC matrices beyond a certain depth. This would require a special treatment of the final score, to ensure a fair selection within deeper levels of the partition tree, but it could accelerate significantly the time required for optimisation.

- **Generative network model:** our assumptions so far with regards to the network parametrisation were fairly simple (uniform parameters, or spherical-harmonics with few degrees of freedom), and we have not explored the effects of the anatomical parcellation on the results obtained. Ultimately, it would be beneficial to merge the definition of various network nodes, with the modulation of unit parameters across the network, into a single generative network model. In concrete terms, this could take the form of a hierarchical clustering of the cortical vertices, based on a criterion derived from dense connectomes for example.

Appendices

A

Modelling

This appendix contains supplementary material for the modelling chapter 3.

A.1 Sigmoid Functions

In this section we provide several possible choices of sigmoid (or "S-shaped") functions, as well as an original derivation of a change of variable allowing for non-symmetric extensions, and a simple (but non-analytic) formulation of a compact sigmoid function.

For reference, four of the most commonly used sigmoid functions are given in Tab. A.1, along with their derivative and inverse.

Name	$f(x)$	$f'(x)$	$f^{-1}(x)$	$f^{-1\prime}(x)$
Logistic	$\frac{1}{1+\exp(-x)}$	$f(x)-f^2(x)$	$\log\left(\frac{y}{1-y}\right)$	$\frac{1}{y(1-y)}$
Gumbel	$e^{-e^{-x}}$	$e^{-x}f(x)$	$\log\left(\frac{-1}{\log(y)}\right)$	$\frac{-1}{y\log y}$
Gaussian	$\frac{1+\operatorname{erf} x}{2}$	$\frac{e^{-x^2}}{\sqrt{\pi}}$	$\operatorname{erf}^{-1}(2y-1)$	$\sqrt{\pi}e^{\left[\operatorname{erf}^{-1}(2y-1)\right]^2}$
Hyperbolic	$\frac{1+\tanh x}{2}$	$\frac{1-\tanh^2 x}{2}$	$\tanh^{-1}(2y-1)$	$\frac{1}{2y(1-y)}$

Table A.1: Formulas for various sigmoid functions, with their derivatives and inverses.

A.1.1 Rescaling and asymmetry

All sigmoid functions (and in particular those given in Tab. A.1) can be rescaled smoothly by composition[1] with

$$x \mapsto \hat{x} = \frac{x-\mu}{\sigma} \tag{A.1}$$

where μ affects the location of the inflexion point, and σ the sharpness of the transition.

Smooth asymmetries can also be introduced for all sigmoid functions, by smoothly altering the slope of the rescaling before and after μ. We introduce the shape parameter a, and propose a different rescaling function below, ensuring that the slope before μ is $1/\sigma$, and $(1+a)/\sigma$ after, the main difficulty being to ensure a smooth transition between the two slopes. This can be achieved simply by defining the rescaling function itself as the integral of a sigmoid, because the slope before and after the inflexion point can be chosen arbitrarily with an offset and scaling factor. For example, the following function

$$r(x) = \frac{1}{\sigma}\int_{-\infty}^{x}\left(1+\frac{a}{1+e^{-\hat{t}}}\right)dt \tag{A.2}$$

is equivalent to x/σ when $x \ll \mu$, and to $(1+a)x/\sigma$ when $x \gg \mu$.

[1] We recall that for two functions f and g we have $(f\circ g)' = g'\ (f'\circ g)$ and $(f\circ g)^{-1} = g^{-1}\circ f^{-1}$, where $\circ$ is the composition.

Furthermore, we can obtain an analytic form by expanding the integral:

$$r(x) = \frac{x}{\sigma} + \frac{a}{\sigma} I_1 + C_1 \tag{A.3}$$

where

$$I_1 = \int \frac{dt}{1+e^{-\hat{t}}} = x + \sigma \int \frac{\frac{-1}{\sigma} e^{-\hat{t}}}{1+e^{-\hat{t}}}\, dt = x + \sigma \ln(1+e^{-\hat{x}}) + C_2 \tag{A.4}$$

which leads to

$$r(x) = (1+a)\frac{x}{\sigma} + a \ln(1+e^{-\hat{x}}) + C_3 \tag{A.5}$$

where $C_{1,2,3}$ are constant integration constants.

Finally, choosing C_3 such that $r(\mu) = 0$ yields

$$\begin{aligned} r(x) &= (1+a)\hat{x} + a \ln\left(\frac{1+e^{-\hat{x}}}{2}\right) \\ &= \left(1+\frac{a}{2}\right)\hat{x} + a \overbrace{\left[\frac{\hat{x}}{2} + \ln\left(\frac{1+e^{-\hat{x}}}{2}\right)\right]}^{g(\hat{x})} \\ &\boxed{= \left(1+\frac{a}{2}\right)\hat{x} + a\left[\frac{|\hat{x}|}{2} + \ln\left(\frac{1+e^{-|\hat{x}|}}{2}\right)\right]} \end{aligned} \tag{A.6}$$

where the last equality (which ensures numerical stability) holds because g is symmetric

$$g(-u) = -\frac{u}{2} + \ln\left(e^{u}\frac{e^{-u}+1}{2}\right) = g(u). \tag{A.7}$$

Given this definition, we can simply compose any previous sigmoid function with r in order to control location, sharpness and asymmetry respectively with parameters μ, σ and a.

A.1.2 Compact sigmoid

Sigmoid functions typically map the real line smoothly to some finite interval, with an S-shaped function (null derivatives at the bounds, strictly increasing otherwise, with a single inflexion point). However, it is sometimes required to achieve such a mapping from a finite domain instead. Unfortunately, it can be proven that no such analytic function exists (derivatives cannot all be null at the bounds).

We propose the following non-analytic function to achieve the mapping $[-1,1] \to [0,1]$ smoothly with a sigmoid shape:

$$\forall x \in [-1,1], \quad \mathcal{C}(x) = \frac{I(x)}{I(1)} \qquad I(x) = \int_{-1}^{x} e^{\frac{1}{t^2-1}} \, \mathrm{d}t \tag{A.8}$$

A.2 Example Time-Courses

Example time-courses for the four Wilson-Cowan units listed in Tab. 3.1 are shown in Fig. A.1. See also Fig. 3.4 p.49 for an example time-course of the conductance-based unit given in Tab. 3.2.

A.3 Bifurcation Diagrams

We provide one-parameter bifurcation diagrams for each of the four Wilson-Cowan units listed in Tab. 3.1, as well as the conductance-based unit listed in Tab. 3.2. These diagrams were computed using the MatCont software package (Dhooge et al. 2008), and are shown respectively in figures A.2 and A.3.

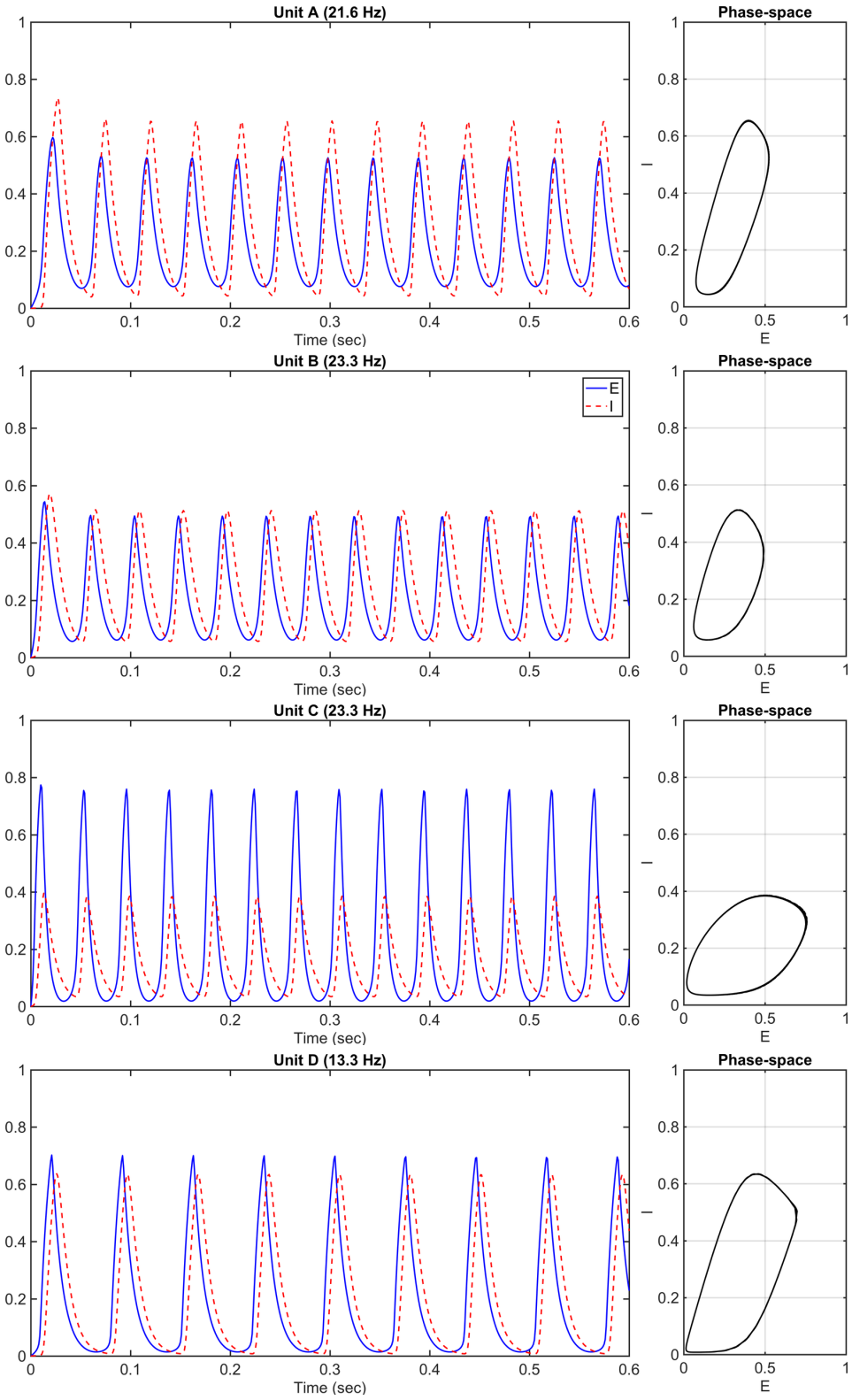

Figure A.1: Example time-courses for the different Wilson-Cowan units. Time-courses for the excitatory and inhibitory subpopulations are shown on the left, and the corresponding orbit in the phase-space is shown on the right. See Tab. 3.1 for the corresponding parameters.

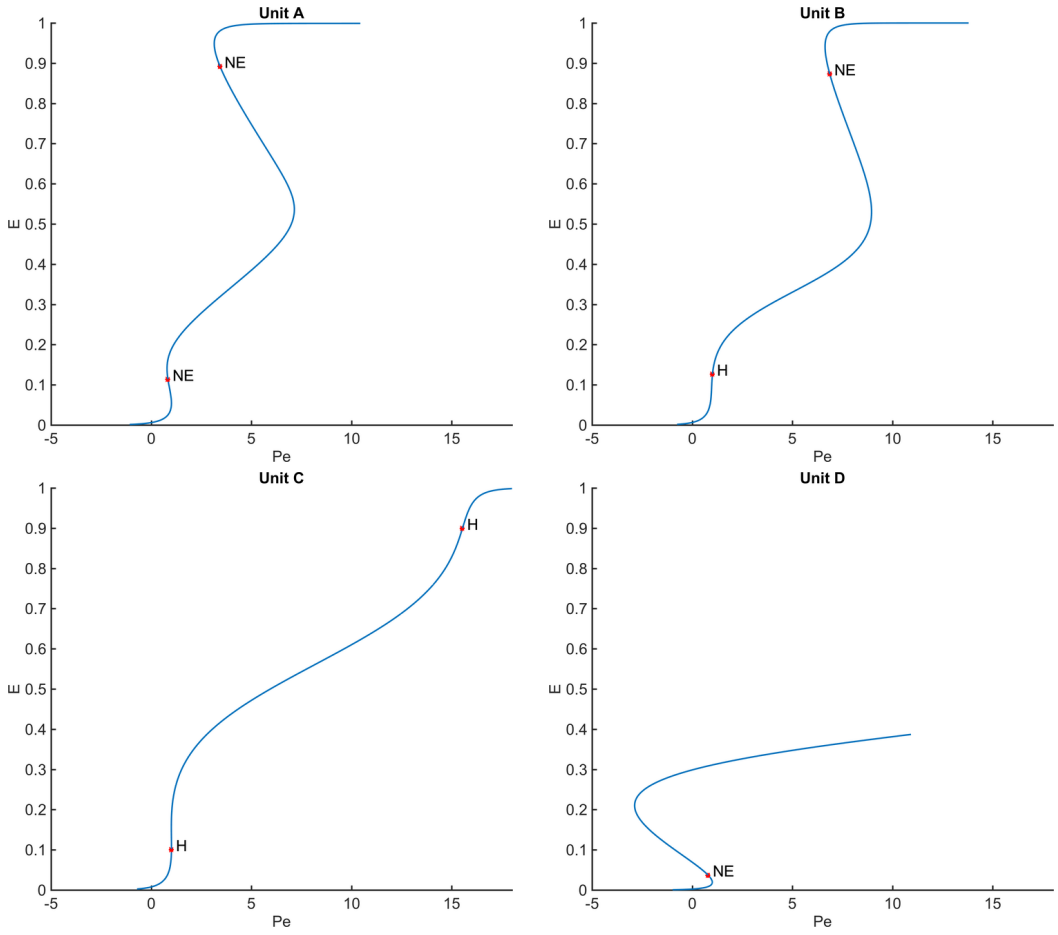

Figure A.2: Bifurcation diagrams for the different Wilson-Cowan units. The label H denotes a Hopf bifurcation (from a fixed-point to a limit-cycle), and NE denotes a neutral equilibrium. See parameters in Tab. 3.1.

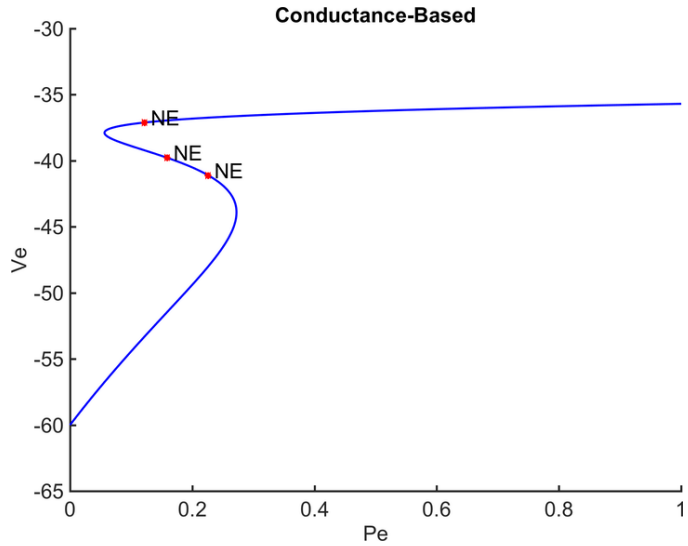

Figure A.3: Bifurcation diagrams for the conductance-based unit. The label NE denotes a neutral equilibrium. See parameters in Tab. 3.2.

B

Instantaneous Frequency

This appendix provides methodological details relevant to the estimation of *instantaneous frequency* from empirical data (see §4.2.2).

B.1 Noise-Robust Differentiation

The numerical differentiation of noisy signals is a difficult problem in practice; the derivative relies fundamentally on the assumption of local linearity, but this assumption does not hold in the presence of noise. In the following, we propose a practical solution to this problem based on the so-called "max-flat" filter design method developed by (Selesnick 2002).

Specifically, we want to estimate the finite impulse response (FIR) coefficients $\{c_k\}_{k=1..N}$ of a differential filter based on central differences:

$$\forall\, t, \quad x'(t) \approx \frac{1}{h} \sum_{k=1}^{N} c_k (x_k - x_{-k}) \tag{B.1}$$

where $x_k = x(t+kh)$, h is the time-step of the digital signal (assumed fixed for simplicity), and N is the **width** of the filter, which determines its order $2N+1$.

Next, we enforce constraints on the **frequency response** of the corresponding linear filter:

$$\forall\, \omega \in [0,\pi], \quad F(\omega) = 2i \sum_{k=1}^{N} c_k \sin(k\omega) \tag{B.2}$$

where ω denotes the normalised frequency, such that it behaves as a perfect differentiator ($F_d(\omega) = i\omega$) for low frequencies

$$\partial_\omega F(0) = i \quad \text{and} \quad \forall\, 1 \le p \le M_0, \quad \partial_\omega^{2p+1} F(0) = 0$$

and attenuates the signal as much as possible for higher frequencies

$$\forall\, 0 \le p \le M_\pi, \quad \partial_\omega^{2p+1} F(\pi) = 0$$

where M_0 and M_π control the degree of **tangency** for low and high frequency constraints.

The previous constraints yield a system of equations, which can be solved to determine the coefficients $\{c_k\}_{k=1..N}$ uniquely for any choice of triplet (N, M_0, M_π) such that $M_0 + M_\pi = N - 2$, and knowing that:

$$\forall\, \omega \in [0,\pi], \quad \forall\, p \ge 0, \quad \partial_\omega^{2p+1} H(\omega) = 2i(-1)^p \sum_{k=1}^{N} k^{2p+1} c_k \cos(k\omega).$$

In our experiments, we used $(N, M_0, M_\pi) = (4,1,1)$ (filter of order 9), for which the optimal coefficients are $[27, 16, -1, -2]/96$.

B.2 Non-Sinusoidal Oscillations

As discussed in §4.2.2, and as shown in Fig. 4.2, variations of the angular speed within a single period of oscillation (which typically occurs with non-sinusoidal waveforms) cause the instantaneous frequency to vary, even if the signal is perfectly periodic. This is consistent with the definition given in Eq. 4.2, but perhaps unintuitive, and it may be desirable to remove such oscillations in practice. We propose a simple method to do so, based on a sequence of interpolations:

- Choose $n+1$ equally spaced points between 0 and 2π:

$$\forall\, 0 \leq k \leq n, \quad p_k = 2k\pi/n$$

- Interpolate the points $\left\{ \left(t_j, \phi(t_j)\right) \;\middle|\; \left|\measuredangle\left(\phi(t_j), p_k\right)\right| < \eta \right\}$ over time for each p_k, where ϕ is the unwrapped Hilbert phase, $\measuredangle$ denotes the angular distance, and $0 < \eta < \pi$ should be chosen reasonably small depending on the sampling rate.

- Average the resulting $n+1$ interpolated time-courses as a smooth estimate of the phase, and differentiate it to obtain the corresponding instantaneous frequencies.

C

Partition Functions

This appendix provides implementation details for sections §5.2.4 and §5.3.

C.1 Working with Polytopes

Simplices in dimension d are defined by $d+1$ vertices in general position. In the context of barycentric subdivision, the sub-simplices are defined as the union of a subset V of "original" vertices, and a set B of intermediate barycentres.

Hyper-cubes, and more generally hyper-rectangles (or d-boxes), are defined by 2^d vertices. However, with regards to implementation, it is inefficient to use such a representation in practice. Instead, they can be defined by a lower-bound and an upper-bound in each dimension, which can be stored as two vectors of d coordinates. In the context of ternary subdivision, all subelements are hyper-rectangles, and can therefore be stored like this. In the context of barycentric subdivision, all subelements are defined as the union of a p-box embedded in dimension d (the lower and upper bounds have $d-p$ coordinates in common), and a set B of intermediate barycentres. We call these subelements "sub-rectangles".

In light of these explanations, simplices and sub-rectangles are defined as follows in our implementation (sets of points are stored as a $n \times d$ matrices with coordinates in row):

```
% create new simplex
function P = make_simplex( vert, bary )
   if nargin < 2, bary=[]; end
   P = struct( 'type', 'simplex', 'v', vert, 'b', bary );
end

% create new subrectangle
function P = make_subrec( lower, upper, bary )
   if nargin < 3, bary=[]; end
   P = struct( 'type', 'subrec', 'lo', lower, 'up', upper, 'b', bary );
end
```

Furthermore, the barycentre of these elements can be computed efficiently (that is, in $\mathcal{O}(d)$ time) using these representations. In particular, the barycentre of a hyper-rectangle is also the centre of its lower and upper bounds, and the barycentre of a sub-rectangle with a p-box base can be computed as:

$$\frac{(d-p)\overline{B} \; + \; 2^p \; \frac{L+U}{2}}{2^p + d - p} \tag{C.1}$$

where L and U denote respectively the lower and upper bounds, and $\overline{B}$ is the barycentre of the set B.

Finally, the partition of sub-rectangles involves listing the facets of embedded p-box bases (which are themselves $(p-1)$-boxes). This can also be computed efficiently (in $\mathcal{O}(d)$ time) with the following routine:

```
function [fac,p] = list_facets(pbox)

   % the bounds of an embedded p-box only differ by p coordinates
   m = pbox.lo ~= pbox.up;
   p = sum(m);
   k = find(m);

   % a p-box has 2p facets
   fac = repmat(pbox,1,2*p);
   for i = 1:p
      ki = k(i);
      fac(i).up(ki) = pbox.lo(ki);
      fac(p+i).lo(ki) = pbox.up(ki);
   end

end
```

This routine can be summarised in two main points:

- The bounds of a p-box embedded in any larger-dimensional space only differ by p coordinates (which is the dimensionality of the subspace it spans);
- The facets of a hyper-rectangle are obtained by collapsing its bounds over each dimension, one at a time.

C.2 Ternary Splits

The partition function originally introduced for GPSO is a recursive ternary split along the largest dimension of the subspace considered (hyper-rectangular by construction). See §5.2.4.2 for details. We used the following recursive implementation in our work:

```
function sub = ternary_subdivision(rec,r)

   if nargin < 2, r=1; end
   if r == 0
      sub = rec;
      return;
   end

   % parent bounds
   Plo = rec.lo;
   Pup = rec.up;

   % split along largest dimension
   [~,s] = max(Pup - Plo);

   % children bounds
   Lup = Pup;
   Rlo = Plo;
   Mlo = Plo;
   Mup = Pup;

   Lup(s) = (2*Plo(s) + Pup(s))/3.0;
   Rlo(s) = ( Plo(s) + 2*Pup(s))/3.0;
   Mlo(s) = Lup(s);
   Mup(s) = Rlo(s);

   % recursion
   sub = [ ...
      ternary_subdivision(make_subrec(Plo,Lup), r-1), ... left
      ternary_subdivision(make_subrec(Mlo,Mup), r-1), ... middle
      ternary_subdivision(make_subrec(Rlo,Pup), r-1) ... right
   ];

end
```

C.3 Barycentric Subdivision

Here, we extend algorithm listed in Alg. 1 in two ways:

1. The subdivision can be computed for an arbitrary number of recursions. Primarily, this is used in the context of GPSO to compute single recursions, in order to explore only a few branches of interest in the partition tree. In other words, this is the core routine for the implementation of *partial* barycentric subdivision (see §5.3.2). Note that it can also be used to subdivide simplices over several cycles of d recursions, although we warn that this is completely intractable beyond a few dimensions.

2. Second, the initial search space can be a hyper-rectangle, which enables the practical use of PBS as a partition function for GPSO (see §5.3.4). After $d-1$ recursions, the algorithm transitions seamlessly to the subdivision of simplices. Of course the initial search space can also be a simplex if needed.

The corresponding code is given below:

```
function sub = barycentric_subdivision(poly,r)

   if nargin < 2, r=1; end

   % polytope can be either a subrectangle or a simplex
   switch poly.type

      case 'simplex'

         b = [poly.b; mean(poly.v)];
         n = size( poly.v, 1 );

         if n == 2
            % intermediate barycentres become original vertices
            sub = [ ...
               make_simplex([b; poly.v(1,:)]), ...
               make_simplex([b; poly.v(2,:)])
            ];
         else
            % facets are defined by their opposite vertex
```

```
21              sub = repmat(poly,1,n);
22              for i = 1:n
23                 sub(i).b = b;
24                 sub(i).v = poly.v(setdiff(1:n,i),:);
25              end
26           end
27
28        case 'subrec'
29
30           % subrectangles have a p-box base, we can list its facets
31           [sub,p] = list_facets( poly );
32           n = numel(sub);
33           b = (poly.lo + poly.up)/2;
34
35           if p == 2
36              % transition to simplicial subelements
37              sim = cell(1,n);
38              for i = 1:n
39                 sim{i} = make_simplex([ sub(i).b; b; sub(i).lo; sub(i).up ]);
40              end
41              sub = [sim{:}];
42           else
43              % children subrectangles have a (p-1)-box base
44              for i = 1:n
45                 sub(i).b = [sub(i).b; b];
46              end
47           end
48
49     end
50
51     % recursion
52     if r > 1
53        sub = arrayfun( @(s) barycentric_subdivision(s,r-1), sub, ...
54           'UniformOutput', false );
55        sub = [sub{:}];
56     end
57
58  end
```

References

Aicher, C., A. Z. Jacobs, and A. Clauset (2014). "Learning Latent Block Structure in Weighted Networks". In: pages 1–28. arXiv: 1404.0431 (cited on page 104).

Andreasen, N. C., D. S. O'Leary, T. Cizadlo, S. Arndt, K. Rezai, G. L. Watkins, L. L. B. Ponto, and R. D. Hichwa (1995). "Remembering the past: two facets of episodic memory explored with positron emission tomography". In: *American Journal of Psychiatry* 152.11, pages 1576–1585 (cited on page 3).

Ashwin, P., S. Coombes, and R. Nicks (2016). "Mathematical Frameworks for Oscillatory Network Dynamics in Neuroscience". In: *The Journal of Mathematical Neuroscience* 6.1, page 2. arXiv: arXiv:1506.05828v1 (cited on page 4).

Auer, P., N. Cesa-Bianchi, and P. Fischer (2002). "Finite-time Analysis of the Multiarmed Bandit Problem". In: *Machine Learning* 47.2/3, pages 235–256 (cited on page 111).

Baillet, S. (2017). "Magnetoencephalography for brain electrophysiology and imaging". In: *Nature Neuroscience* 20.3, pages 327–339 (cited on pages 23, 24).

Baillet, S., J. Mosher, and R. Leahy (2001). "Electromagnetic brain mapping". In: *IEEE Signal Processing Magazine* 18.6, pages 14–30. arXiv: 1053-5888 (cited on page 25).

Baker, A. P., M. J. Brookes, I. a. Rezek, S. M. Smith, T. Behrens, P. J. P. Smith, and M. Woolrich (2014). "Fast transient networks in spontaneous human brain activity". In: *eLife* 2014.3, pages 1–18 (cited on pages 4, 37, 103).

Basser, P., J. Mattiello, and D. LeBihan (1994). "MR diffusion tensor spectroscopy and imaging". In: *Biophysical Journal* 66.1, pages 259–267 (cited on page 13).

Beckmann, C. F., M. DeLuca, J. T. Devlin, and S. M. Smith (2005). "Investigations into resting-state connectivity using independent component analysis." In: *Philosophical transactions of the Royal Society of London. Series B, Biological sciences* 360.1457, pages 1001–1013 (cited on page 5).

Behrens, T. E. J., H. J. Berg, S. Jbabdi, M. F. S. Rushworth, and M. Woolrich (2007). "Probabilistic diffusion tractography with multiple fibre orientations: What can we gain?" In: *NeuroImage* 34.1, pages 144–155 (cited on page 15).

Behrens, T., M. Woolrich, M. Jenkinson, H. Johansen-Berg, R. Nunes, S. Clare, P. Matthews, J. Brady, and S. Smith (2003). "Characterization and propagation of uncertainty in diffusion-weighted MR imaging". In: *Magnetic Resonance in Medicine* 50.5, pages 1077–1088 (cited on page 16).

Behrens, T. E. and H. Johansen-Berg (2013). *Diffusion MRI, Second Edition: From Quantitative Measurement to In vivo Neuroanatomy*. Elsevier, page 632 (cited on pages 13, 19).

Biswal, B. B., J. Van Kylen, and J. S. Hyde (1997). “Simultaneous assessment of flow and BOLD signals in resting-state functional connectivity maps.” In: *NMR in biomedicine* 10.4-5, pages 165–70 (cited on page 3).

Biswal, B., F. Z. Yetkin, V. M. Haughton, and J. S. Hyde (1995). “Functional connectivity in the motor cortex of resting human brain using echo-planar MRI.” In: *Magnetic resonance in medicine* 34.4, pages 537–41 (cited on pages 3, 5).

Bower, J. M., H. Cornelis, and D. Beeman (2013). “GENESIS, The GEneral NEural SImulation System”. In: *Encyclopedia of Computational Neuroscience*. Edited by D. Jaeger and R. Jung. 2. New York, NY: Springer New York, pages 1–8. arXiv: 1501.01854 (cited on page 72).

Breakspear, M. (2017). “Dynamic models of large-scale brain activity”. In: *Nature Neuroscience* 20.3, pages 340–352 (cited on pages 4, 6, 57).

Bressloff, P. C. (2003). “Spatially periodic modulation of cortical patterns by long-range horizontal connections”. In: *Physica D: Nonlinear Phenomena* 185.3-4, pages 131–157 (cited on page 38).

– (2010). “Metastable states and quasicycles in a stochastic Wilson-Cowan model of neuronal population dynamics”. In: *Physical Review E* 82.5, page 051903 (cited on page 57).

Bressloff, P. C. and S. R. Carroll (2015). “Laminar Neural Field Model of Laterally Propagating Waves of Orientation Selectivity”. In: *PLoS Computational Biology* 11.10, pages 1–26 (cited on page 38).

Brochu, E., V. M. Cora, and N. de Freitas (2010). “A Tutorial on Bayesian Optimization of Expensive Cost Functions, with Application to Active User Modeling and Hierarchical Reinforcement Learning”. In: *ArXiv*, page 49. arXiv: 1012.2599 (cited on page 108).

Brookes, M. J., J. R. Hale, J. M. Zumer, C. M. Stevenson, S. T. Francis, G. R. Barnes, J. P. Owen, P. G. Morris, and S. S. Nagarajan (2011a). “Measuring functional connectivity using MEG: Methodology and comparison with fcMRI”. In: *NeuroImage* 56.3, pages 1082–1104 (cited on page 94).

Brookes, M. J., E. L. Hall, S. E. Robson, D. Price, L. Palaniyappan, E. B. Liddle, P. F. Liddle, S. E. Robinson, and P. G. Morris (2015). “Complexity Measures in Magnetoencephalography: Measuring "Disorder" in Schizophrenia”. In: *PLOS ONE* 10.4. Edited by S. Doesburg, e0120991 (cited on page 26).

Brookes, M. J., M. Woolrich, H. Luckhoo, D. Price, J. R. Hale, M. C. Stephenson, G. R. Barnes, S. M. Smith, and P. G. Morris (2011b). “Investigating the electrophysiological basis of resting state networks using magnetoencephalography.” In: *Proceedings of the National Academy of Sciences of the United States of America* 108.40, pages 16783–8 (cited on pages 4, 5).

Brunel, N. (2000). “Dynamics of Sparsely Connected networks of Excitatory and Inhibitory Spiking Neurons”. In: *Journal of Computational Neuroscience* 8.3, pages 183–208 (cited on page 57).

Bubeck, S. and N. Cesa-Bianchi (2012). “Regret Analysis of Stochastic and Nonstochastic Multi-armed Bandit Problems”. In: *arXiv.org* cs.LG, page 138. arXiv: 1204.5721 (cited on page 111).

Buckner, R. L. (2012). "The serendipitous discovery of the brain's default network". In: *NeuroImage* 62.2, pages 1137–1145 (cited on page 3).

Bullmore, E. and O. Sporns (2009). "Complex brain networks: graph theoretical analysis of structural and functional systems". In: *Nature Reviews Neuroscience* 10.3, pages 186–198. arXiv: arXiv:1011.1669v3 (cited on page 4).

Buzsáki, G., C. a. Anastassiou, and C. Koch (2012). "The origin of extracellular fields and currents — EEG, ECoG, LFP and spikes". In: *Nature Reviews Neuroscience* 13.6, pages 407–420. arXiv: NIHMS150003 (cited on page 147).

Cabral, J., M. L. Kringelbach, and G. Deco (2014a). "Exploring the network dynamics underlying brain activity during rest". In: *Progress in Neurobiology* 114, pages 102–131 (cited on page 6).

Cabral, J., H. Luckhoo, M. Woolrich, M. Joensson, H. Mohseni, A. Baker, M. L. Kringelbach, and G. Deco (2014b). "Exploring mechanisms of spontaneous functional connectivity in MEG: how delayed network interactions lead to structured amplitude envelopes of band-pass filtered oscillations." In: *NeuroImage* 90, pages 423–35 (cited on page 45).

Chaudhuri, R., A. Bernacchia, and X.-J. Wang (2014). "A diversity of localized timescales in network activity". In: *eLife* 3, e01239 (cited on pages 162, 163, 180).

Chaudhuri, R., K. Knoblauch, M.-A. Gariel, H. Kennedy, and X.-J. Wang (2015). "A Large-Scale Circuit Mechanism for Hierarchical Dynamical Processing in the Primate Cortex". In: *Neuron* 88.2, pages 419–431 (cited on page 156).

Childs, C. (2008). "Human brain temperature: regulation, measurement and relationship with cerebral trauma: Part 1". In: *British Journal of Neurosurgery* 22.4, pages 486–496 (cited on page 19).

Chung, M. K., K. M. Dalton, and R. J. Davidson (2007). "Encoding Neuroanatomical Information using Weighted Spherical Harmonic Representation". In: *2007 IEEE/SP 14th Workshop on Statistical Signal Processing*. Cos 0. IEEE, pages 146–150 (cited on page 162).

Cohen, L. (1995). *Time-frequency Analysis: Theory and Applications*. Upper Saddle River, NJ, USA: Prentice-Hall, Inc. (cited on page 91).

Colclough, G. L., S. M. Smith, T. E. Nichols, A. M. Winkler, S. N. Sotiropoulos, M. F. Glasser, D. C. Van Essen, and M. W. Woolrich (2017). "The heritability of multi-modal connectivity in human brain activity". In: *eLife* 6, pages 1–19 (cited on page 181).

Colclough, G., M. Brookes, S. Smith, and M. Woolrich (2015). "A symmetric multivariate leakage correction for MEG connectomes". In: *NeuroImage* 117, pages 439–448 (cited on pages 26, 147).

Colclough, G., M. Woolrich, P. Tewarie, M. Brookes, A. Quinn, and S. Smith (2016). "How reliable are MEG resting-state connectivity metrics?" In: *NeuroImage* 138, pages 284–293 (cited on pages 104, 181).

Coombes, S. (2010). "Large-scale neural dynamics: Simple and complex". In: *NeuroImage* 52.3, pages 731–739 (cited on page 6).

Coombes, S., P. beim Graben, R. Potthast, and J. Wright (2014). *Neural Fields*. Edited by S. Coombes, P. beim Graben, R. Potthast, and J. Wright. Berlin, Heidelberg: Springer Berlin Heidelberg (cited on page 38).

Damoiseaux, J. S., S. a. R. B. Rombouts, F. Barkhof, P. Scheltens, C. J. Stam, S. M. Smith, and C. F. Beckmann (2006). "Consistent resting-state networks across healthy subjects". In: *Proceedings of the National Academy of Sciences* 103.37, pages 13848–13853 (cited on pages 4, 5).

David, O., S. J. Kiebel, L. M. Harrison, J. Mattout, J. M. Kilner, and K. J. Friston (2006). "Dynamic causal modeling of evoked responses in EEG and MEG." In: *NeuroImage* 30.4, pages 1255–72 (cited on page 83).

Dayan, P. and L. Abbott (2002). *Theoretical Neuroscience: Computational and Mathematical Modeling of Neural Systems*. MIT Press (cited on page 62).

De Luca, M., C. Beckmann, N. De Stefano, P. Matthews, and S. Smith (2006). "fMRI resting state networks define distinct modes of long-distance interactions in the human brain". In: *NeuroImage* 29.4, pages 1359–1367 (cited on pages 4, 5).

Deco, G., A. R. McIntosh, K. Shen, R. M. Hutchison, R. S. Menon, S. Everling, P. Hagmann, and V. K. Jirsa (2014). "Identification of Optimal Structural Connectivity Using Functional Connectivity and Neural Modeling". In: *Journal of Neuroscience* 34.23, pages 7910–7916 (cited on page 159).

Deco, G., V. Jirsa, A. R. McIntosh, O. Sporns, and R. Kotter (2009). "Key role of coupling, delay, and noise in resting brain fluctuations". In: *Proceedings of the National Academy of Sciences* 106.25, pages 10302–10307 (cited on pages 21, 45, 72).

Deco, G., V. K. Jirsa, and A. R. McIntosh (2011). "Emerging concepts for the dynamical organization of resting-state activity in the brain." In: *Nature reviews. Neuroscience* 12.1, pages 43–56 (cited on page 174).

Deco, G. and M. L. Kringelbach (2016). "Metastability and Coherence: Extending the Communication through Coherence Hypothesis Using A Whole-Brain Computational Perspective". In: *Trends in Neurosciences* 39.3, pages 125–135 (cited on page 95).

Deco, G., A. Ponce-Alvarez, D. Mantini, G. L. Romani, P. Hagmann, and M. Corbetta (2013). "Resting-State Functional Connectivity Emerges from Structurally and Dynamically Shaped Slow Linear Fluctuations". In: *Journal of Neuroscience* 33.27, pages 11239–11252 (cited on pages 36, 57).

Desikan, R. S., F. Ségonne, B. Fischl, B. T. Quinn, B. C. Dickerson, D. Blacker, R. L. Buckner, A. M. Dale, R. P. Maguire, B. T. Hyman, M. S. Albert, and R. J. Killiany (2006). "An automated labeling system for subdividing the human cerebral cortex on MRI scans into gyral based regions of interest". In: *NeuroImage* 31.3, pages 968–980 (cited on pages 11, 12).

Dhooge, A., W. Govaerts, Y. A. Kuznetsov, H. G. Meijer, and B. Sautois (2008). "New features of the software MatCont for bifurcation analysis of dynamical systems". In: *Mathematical and Computer Modelling of Dynamical Systems* 14.2, pages 147–175 (cited on pages 41, 192).

Dimitriadis, S., Y. Sun, N. Laskaris, N. Thakor, and A. Bezerianos (2016). "Revealing Cross-Frequency Causal Interactions During a Mental Arithmetic Task Through Symbolic Transfer Entropy: A Novel Vector-Quantization Approach". In: *IEEE Transactions on Neural Systems and Rehabilitation Engineering* 24.10, pages 1017–1028 (cited on page 103).

Djuric, P., J. Kotecha, J. Zhang, Y. Huang, T. Ghirmai, M. Bugallo, and J. Miguez (2003). "Particle Filtering". In: *IEEE Signal Processing Magazine* 20.5, pages 19–38 (cited on pages 109, 133).

Donahue, C. J., S. N. Sotiropoulos, S. Jbabdi, M. Hernandez-Fernandez, T. E. Behrens, T. B. Dyrby, T. Coalson, H. Kennedy, K. Knoblauch, D. C. Van Essen, and M. F. Glasser (2016). "Using Diffusion Tractography to Predict Cortical Connection Strength and Distance: A Quantitative Comparison with Tracers in the Monkey". In: *Journal of Neuroscience* 36.25, pages 6758–6770 (cited on pages 15, 18, 144).

Drachman, D. A. (2005). "Do we have brain to spare?" In: *Neurology* 64.12, pages 2004–2005. arXiv: arXiv:1011.1669v3 (cited on page 23).

Dyer, M., A. Frieze, and R. Kannan (1991). "A random polynomial-time algorithm for approximating the volume of convex bodies". In: *Journal of the ACM* 38.1, pages 1–17 (cited on page 136).

Elston, G. N. (2007). "Specialization of the Neocortical Pyramidal Cell during Primate Evolution". In: *Evolution of Nervous Systems*. Edited by J. H. Kaas. Oxford: Academic Press, pages 191–242 (cited on page 163).

Eppler, J. M. (2008). "PyNEST: A convenient interface to the NEST simulator". In: *Frontiers in Neuroinformatics* 2.January, pages 1–12 (cited on page 72).

Ercsey-Ravasz, M., N. T. Markov, C. Lamy, D. C. Van Essen, K. Knoblauch, Z. Toroczkai, and H. Kennedy (2013). "A Predictive Network Model of Cerebral Cortical Connectivity Based on a Distance Rule". In: *Neuron* 80.1, pages 184–197. arXiv: NIHMS150003 (cited on page 18).

Farahibozorg, S.-R., R. N. Henson, and O. Hauk (2017). "Adaptive cortical parcellations for source reconstructed EEG/MEG connectomes". In: *NeuroImage* (cited on page 159).

Fornito, A., A. Zalesky, and M. Breakspear (2013). "Graph analysis of the human connectome: promise, progress, and pitfalls." In: *NeuroImage* 80, pages 426–44 (cited on pages 12, 158).

Freitas, N. de, A. Smola, and M. Zoghi (2012). "Exponential Regret Bounds for Gaussian Process Bandits with Deterministic Observations". In: *Proceedings of the 29th International Conference on Machine Learning (ICML-12)*, pages 1743–1750. arXiv: 1206.6457 (cited on page 112).

Freyer, F., J. A. Roberts, R. Becker, P. A. Robinson, P. Ritter, and M. Breakspear (2011). "Biophysical Mechanisms of Multistability in Resting-State Cortical Rhythms". In: *Journal of Neuroscience* 31.17, pages 6353–6361 (cited on pages 6, 57).

Fries, P. (2015). "Rhythms for Cognition: Communication through Coherence". In: *Neuron* 88.1, pages 220–235 (cited on page 95).

Gewaltig, M.-O. and M. Diesmann (2007). *NEST (NEural Simulation Tool)* (cited on page 72).

Ghosh, A., Y. Rho, A. R. McIntosh, R. Kötter, and V. K. Jirsa (2008). "Noise during Rest Enables the Exploration of the Brain's Dynamic Repertoire". In: *PLoS Computational Biology* 4.10. Edited by K. J. Friston, e1000196 (cited on page 60).

Glasser, M. F., T. S. Coalson, E. C. Robinson, C. D. Hacker, J. Harwell, E. Yacoub, K. Ugurbil, J. Andersson, C. F. Beckmann, M. Jenkinson, S. M. Smith, and D. C. Van Essen (2016). "A multi-modal parcellation of human cerebral cortex." In: *Nature* 536.7615, pages 171–8. arXiv: NIHMS150003 (cited on pages 12, 158).

Glasser, M. F., S. N. Sotiropoulos, J. A. Wilson, T. S. Coalson, B. Fischl, J. L. Andersson, J. Xu, S. Jbabdi, M. Webster, J. R. Polimeni, D. C. Van Essen, and M. Jenkinson (2013). "The minimal preprocessing pipelines for the Human Connectome Project". In: *NeuroImage* 80.6, pages 105–124. arXiv: NIHMS150003 (cited on pages 16, 21).

Goldenholz, D. M., S. P. Ahlfors, M. S. Hämäläinen, D. Sharon, M. Ishitobi, L. M. Vaina, and S. M. Stufflebeam (2009). "Mapping the signal-to-noise-ratios of cortical sources in magnetoencephalography and electroencephalography". In: *Human Brain Mapping* 30.4, pages 1077–1086 (cited on page 156).

Greicius, M. D., B. Krasnow, A. L. Reiss, and V. Menon (2003). "Functional connectivity in the resting brain: a network analysis of the default mode hypothesis." In: *Proceedings of the National Academy of Sciences of the United States of America* 100.1, pages 253–258 (cited on page 4).

Greicius, M. D., K. Supekar, V. Menon, and R. F. Dougherty (2009). "Resting-state functional connectivity reflects structural connectivity in the default mode network." In: *Cerebral cortex (New York, N.Y. : 1991)* 19.1, pages 72–8. arXiv: 1 (cited on page 36).

Gros, C. (2015). *Complex and Adaptive Dynamical Systems*. Cham: Springer International Publishing (cited on page 41).

Hadida, J., S. Sotiropoulos, R. Abeysuriya, M. Woolrich, and S. Jbabdi (2018). "Bayesian Optimisation of Large-Scale Biophysical Networks". In: *NeuroImage* 174, pages 219–236 (cited on pages 132, 140).

Hafting, T., M. Fyhn, S. Molden, M. B. Moser, and E. I. Moser (2005). "Microstructure of a spatial map in the entorhinal cortex". In: *Nature* 436.7052, pages 801–806. arXiv: /dx.doi.org/10.1038/nature01964 [http:] (cited on page 5).

Hairer, E., S. P. Nørsett, and G. Wanner (1993). *Solving Ordinary Differential Equations I*. Springer, Berlin (cited on page 83).

Hairer, E. and G. Wanner (1996). *Solving Ordinary Differential Equations II*. Springer, Berlin (cited on page 83).

Hansen, E. C., D. Battaglia, A. Spiegler, G. Deco, and V. K. Jirsa (2015). "Functional connectivity dynamics: Modeling the switching behavior of the resting state". In: *NeuroImage* 105, pages 525–535 (cited on page 6).

Hansen, P., M. Kringelbach, and R. Salmelin, editors (2010). *MEG: An Introduction to Methods*. Oxford University Press (cited on page 24).

Harrison, L., W. Penny, and K. Friston (2003). "Multivariate autoregressive modeling of fMRI time series". In: *NeuroImage* 19.4, pages 1477–1491 (cited on page 37).

Harrison, S. J., M. W. Woolrich, E. C. Robinson, M. F. Glasser, C. F. Beckmann, M. Jenkinson, and S. M. Smith (2015). "Large-scale probabilistic functional modes from resting state fMRI." In: *NeuroImage* 109, pages 217–31 (cited on page 158).

Heuvel, M. P. van den and H. E. Hulshoff Pol (2010). "Exploring the brain network: A review on resting-state fMRI functional connectivity". In: *European Neuropsychopharmacology* 20.8, pages 519–534 (cited on pages 4, 5).

Heuvel, M. van den, R. Mandl, and H. Hulshoff Pol (2008). "Normalized Cut Group Clustering of Resting-State fMRI Data". In: *PLoS ONE* 3.4. Edited by B. Brembs, e2001 (cited on page 5).

Higham., D. J. (2001). "An Algorithmic Introduction to Numerical Simulation of Stochastic Differential Equations". In: *SIAM Review* 43.3, pages 525–546 (cited on page 58).

Hodgkin, A. L. and A. F. Huxley (1952). "A quantitative description of membrane current and its application to conduction and excitation in nerve". In: *The Journal of Physiology* 117.4, pages 500–544 (cited on pages 4, 62).

Honey, C. J., O. Sporns, L. Cammoun, X. Gigandet, J. P. Thiran, R. Meuli, and P. Hagmann (2009). "Predicting human resting-state functional connectivity from structural connectivity". In: *Proceedings of the National Academy of Sciences* 106.6, pages 2035–2040 (cited on pages 4, 31, 36).

Huang, N. E., Z. Shen, S. R. Long, M. C. Wu, H. H. Shih, Q. Zheng, N.-C. Yen, C. C. Tung, and H. H. Liu (1998). "The empirical mode decomposition and the Hilbert spectrum for nonlinear and non-stationary time series analysis". In: *Proceedings of the Royal Society A: Mathematical, Physical and Engineering Sciences* 454.1971, pages 903–995 (cited on pages 90, 103).

Izhikevich, E. M. (2006). "Polychronization: Computation with Spikes". In: *Neural Computation* 18.2, pages 245–282 (cited on page 5).

Izhikevich, E. M. and G. M. Edelman (2008). "Large-scale model of mammalian thalamocortical systems." In: *Proceedings of the National Academy of Sciences of the United States of America* 105.9, pages 3593–3598 (cited on page 38).

Jadbabaie, A., N. Motee, and M. Barahona (2004). "On the Stability of the Kuramoto Model of Coupled Nonlinear Oscillators". In: *2004 American Control Conference*, pages 1–16 (cited on page 44).

Jbabdi, S., S. N. Sotiropoulos, S. N. Haber, D. C. Van Essen, and T. E. Behrens (2015). "Measuring macroscopic brain connections in vivo". In: *Nature Neuroscience* 18.11, pages 1546–1555 (cited on pages 12, 15).

Jbabdi, S., S. N. Sotiropoulos, A. M. Savio, M. Graña, and T. E. J. Behrens (2012). "Model-based analysis of multishell diffusion MR data for tractography: How to get over fitting problems". In: *Magnetic Resonance in Medicine* 68.6, pages 1846–1855. arXiv: NIHMS150003 (cited on page 16).

Jirsa, V. and V. Müller (2013). "Cross-frequency coupling in real and virtual brain networks". In: *Frontiers in Computational Neuroscience* 7.July, page 78 (cited on page 58).

Jones, D. K. (2011). *Diffusion MRI: Theory, Methods, and Applications*. Oxford University Press, page 784 (cited on page 13).

Kawaguchi, K., L. P. Kaelbling, and T. Lozano-Pérez (2016). "Bayesian Optimization with Exponential Convergence". In: *Neural Information Processing Systems*, pages 1–9. arXiv: 1604.01348 (cited on pages 107, 113, 115, 119, 129).

Kuramoto, Y. (1984). *Chemical Oscillations, Waves, and Turbulence*. Volume 19. Springer Series in Synergetics. Berlin, Heidelberg: Springer Berlin Heidelberg (cited on page 43).

Larson-Prior, L., R. Oostenveld, S. Della Penna, G. Michalareas, F. Prior, A. Babajani-Feremi, J.-M. Schoffelen, L. Marzetti, F. de Pasquale, F. Di Pompeo, J. Stout, M. Woolrich, Q. Luo, R. Bucholz, P. Fries, V. Pizzella, G. Romani, M. Corbetta, and A. Snyder (2013). "Adding dynamics to the Human Connectome Project with MEG". In: *NeuroImage* 80, pages 190–201. arXiv: NIHMS150003 (cited on page 104).

Laule, C., I. M. Vavasour, S. H. Kolind, D. K. B. Li, T. L. Traboulsee, G. R. W. Moore, and A. L. MacKay (2007). "Magnetic resonance imaging of myelin". In: *Neurotherapeutics* 4.3, pages 460–484 (cited on page 21).

Le Bihan, D., E. Breton, D. Lallemand, P. Grenier, E. Cabanis, and M. Laval-Jeantet (1986). "MR imaging of intravoxel incoherent motions: application to diffusion and perfusion in neurologic disorders." In: *Radiology* 161.2, pages 401–407 (cited on page 13).

Liewald, D., R. Miller, N. Logothetis, H.-J. Wagner, and A. Schüz (2014). "Distribution of axon diameters in cortical white matter: an electron-microscopic study on three human brains and a macaque". In: *Biological Cybernetics* 108.5, pages 541–557 (cited on page 19).

Liu, B., S. Cheng, and Y. Shi (2016). "Particle Filter Optimization: A Brief Introduction". In: *Studies in Computational Intelligence*. Volume 248, pages 95–104. arXiv: 9780201398298 (cited on pages 109, 133).

Lücken, L., J. P. Pade, and K. Knauer (2015). "Classification of Coupled Dynamical Systems with Multiple Delays: Finding the Minimal Number of Delays". In: *SIAM Journal on Applied Dynamical Systems* 14.1, pages 286–304 (cited on page 21).

Luther, H. A. (1968). "An explicit sixth-order Runge-Kutta formula". In: *Mathematics of Computation* 22.102, pages 434–434 (cited on page 83).

Markov, N. T., M. M. Ercsey-Ravasz, a. R. Ribeiro Gomes, C. Lamy, L. Magrou, J. Vezoli, P. Misery, a. Falchier, R. Quilodran, M. a. Gariel, J. Sallet, R. Gamanut, C. Huissoud, S. Clavagnier, P. Giroud, D. Sappey-Marinier, P. Barone, C. Dehay, Z. Toroczkai, K. Knoblauch, D. C. Van Essen, and H. Kennedy (2014). "A Weighted and Directed Interareal Connectivity Matrix for Macaque Cerebral Cortex". In: *Cerebral Cortex* 24.1, pages 17–36 (cited on page 18).

Markram, H., K. Meier, T. Lippert, S. Grillner, R. Frackowiak, S. Dehaene, A. Knoll, H. Sompolinsky, K. Verstreken, J. DeFelipe, S. Grant, J.-P. Changeux, and A. Saria (2011).

"Introducing the Human Brain Project". In: *Procedia Computer Science* 7, pages 39–42 (cited on page 38).

Marreiros, A. C., S. J. Kiebel, J. Daunizeau, L. M. Harrison, and K. J. Friston (2009). "Population dynamics under the Laplace assumption". In: *NeuroImage* 44.3, pages 701–714 (cited on page 62).

Meier, J., P. Tewarie, A. Hillebrand, L. Douw, B. W. van Dijk, S. M. Stufflebeam, and P. Van Mieghem (2016). "A Mapping Between Structural and Functional Brain Networks". In: *Brain Connectivity* 6.4, pages 298–311 (cited on page 31).

Meiss, J. D. (2007). *Differential Dynamical Systems*. Society for Industrial and Applied Mathematics (cited on page 41).

Messe, A., H. Benali, and G. Marrelec (2014). "Relating structural and functional connectivity in MRI: A simple model for a complex brain." In: *IEEE transactions on medical imaging* 0062.c, pages 1–11 (cited on page 37).

Michalareas, G., J. M. Schoffelen, G. Paterson, and J. Gross (2013). "Investigating causality between interacting brain areas with multivariate autoregressive models of MEG sensor data". In: *Human Brain Mapping* 34.4, pages 890–913 (cited on page 37).

Mormann, F., K. Lehnertz, P. David, and C. E. Elger (2000). "Mean phase coherence as a measure for phase synchronization and its application to the EEG of epilepsy patients". In: *Physica D: Nonlinear Phenomena* 144.3-4, pages 358–369 (cited on page 94).

Murakami, S. and Y. Okada (2006). "Contributions of principal neocortical neurons to magnetoencephalography and electroencephalography signals". In: *The Journal of Physiology* 575.3, pages 925–936 (cited on page 23).

Muresan, R. C. and C. Savin (2007). "Resonance or Integration? Self-Sustained Dynamics and Excitability of Neural Microcircuits". In: *Journal of Neurophysiology* 97.3, pages 1911–1930 (cited on page 40).

Nakao, H. (2017). "Phase reduction approach to synchronization of nonlinear oscillators". In: 214, pages 188–214. arXiv: 1704.03293 (cited on page 45).

Niso, G., C. Rogers, J. T. Moreau, L.-Y. Chen, C. Madjar, S. Das, E. Bock, F. Tadel, A. C. Evans, P. Jolicoeur, and S. Baillet (2016). "OMEGA: The Open MEG Archive". In: *NeuroImage* 124, pages 1182–1187 (cited on page 104).

Nolte, G., O. Bai, L. Wheaton, Z. Mari, S. Vorbach, and M. Hallett (2004). "Identifying true brain interaction from EEG data using the imaginary part of coherency". In: *Clinical Neurophysiology* 115.10, pages 2292–2307 (cited on page 94).

Pinotsis, D., E. Hansen, K. Friston, and V. Jirsa (2013a). "Anatomical connectivity and the resting state activity of large cortical networks". In: *NeuroImage* 65, pages 127–138 (cited on page 36).

Pinotsis, D. a., M. Leite, and K. J. Friston (2013b). "On conductance-based neural field models." In: *Frontiers in computational neuroscience* 7.November, page 158 (cited on page 38).

Pinotsis, D., P. Robinson, P. beim Graben, and K. Friston (2014). "Neural masses and fields: modeling the dynamics of brain activity". In: *Frontiers in Computational Neuroscience* 8.November, pages 1–3 (cited on page 37).

Pooley, R. A. (2005). "Fundamental Physics of MR Imaging". In: *RadioGraphics* 25.4, pages 1087–1099 (cited on page 14).

Press, W. H., S. A. Teukolsky, W. T. Vetterling, and B. P. Flannery (2007). *Numerical Recipes 3rd Edition: The Art of Scientific Computing*. 3rd edition. New York, NY, USA: Cambridge University Press (cited on pages 82, 83).

Pulkkinen, S., M. M. Mäkelä, and N. Karmitsa (2013). "A continuation approach to mode-finding of multivariate Gaussian mixtures and kernel density estimates". In: *Journal of Global Optimization* 56.2, pages 459–487 (cited on page 132).

Purves, D. (2004). *Neuroscience, 3rd ed.* Edited by D. Purves, G. J. Augustine, D. Fitzpatrick, W. C. Hall, A.-S. LaMantia, J. O. McNamara, and S. M. Williams. Sunderland, MA, US: Sinauer Associates, page 773 (cited on page 19).

Raichle, M. E., A. M. MacLeod, A. Z. Snyder, W. J. Powers, D. A. Gusnard, and G. L. Shulman (2001). "A default mode of brain function". In: *Proceedings of the National Academy of Sciences* 98.2, pages 676–682. arXiv: 0402594v3 [arXiv:cond-mat] (cited on page 3).

Rasmussen, C. E. and C. K. I. Williams (2006). *Gaussian Processes for Machine Learning*. Adaptive Computation and Machine Learning. Cambridge, MA, USA: MIT Press, page 248 (cited on pages 112, 138).

Ritchie, J. M. (1982). "On the relation between fibre diameter and conduction velocity in myelinated nerve fibres." In: *Proceedings of the Royal Society of London. Series B, Biological sciences* 217.1206, pages 29–35 (cited on page 19).

Roberts, J. A. and P. A. Robinson (2012). "Corticothalamic dynamics: Structure of parameter space, spectra, instabilities, and reduced model". In: *Physical Review E* 85.1, page 011910 (cited on page 143).

Robson, S. E., M. J. Brookes, E. L. Hall, L. Palaniyappan, J. Kumar, M. Skelton, N. G. Christodoulou, A. Qureshi, F. Jan, M. Z. Katshu, E. B. Liddle, P. F. Liddle, and P. G. Morris (2016). "Abnormal visuomotor processing in schizophrenia". In: *NeuroImage: Clinical* 12, pages 869–878 (cited on page 26).

Sabatini, B. L. and W. G. Regehr (1999). "Timing of Synaptic Transmission". In: *Annual Review of Physiology* 61.1, pages 521–542 (cited on pages 19, 53).

Salvador, R., J. Suckling, M. R. Coleman, J. D. Pickard, D. Menon, and E. Bullmore (2005). "Neurophysiological Architecture of Functional Magnetic Resonance Images of Human Brain". In: *Cerebral Cortex* 15.9, pages 1332–1342 (cited on page 5).

Sanz Leon, P., S. a. Knock, M. M. Woodman, L. Domide, J. Mersmann, A. R. McIntosh, and V. Jirsa (2013). "The Virtual Brain: a simulator of primate brain network dynamics." In: *Frontiers in neuroinformatics* 7.June, page 10 (cited on pages 72, 79).

Sanz-Leon, P., S. A. Knock, A. Spiegler, and V. K. Jirsa (2015). "Mathematical framework for large-scale brain network modeling in The Virtual Brain". In: *NeuroImage* 111, pages 385–430 (cited on page 72).

Schröder, M., M. Timme, and D. Witthaut (2017). "A universal order parameter for synchrony in networks of limit cycle oscillators". In: *Chaos: An Interdisciplinary Journal of Nonlinear Science* 27.7, page 073119. arXiv: 1704.04130 (cited on page 44).

Schwartz, M., W. R. Bennett, and S. Stein (1995). *Communication Systems and Techniques*. An IEEE press classic reissue. Wiley (cited on page 91).

Selesnick, I. (2002). "Maximally flat low-pass digital differentiator". In: *IEEE Transactions on Circuits and Systems II: Analog and Digital Signal Processing* 49.3, pages 219–223 (cited on pages 93, 195).

Smith, S. (2005). "Covariance, subspace, and intrinsic Cramer-Rao bounds". In: *IEEE Transactions on Signal Processing* 53.5, pages 1610–1630 (cited on pages 101, 102).

Smith, S. M., M. Jenkinson, H. Johansen-Berg, D. Rueckert, T. E. Nichols, C. E. Mackay, K. E. Watkins, O. Ciccarelli, M. Z. Cader, P. M. Matthews, and T. E. Behrens (2006). "Tract-based spatial statistics: Voxelwise analysis of multi-subject diffusion data". In: *NeuroImage* 31.4, pages 1487–1505 (cited on page 15).

Smith, S. M., K. L. Miller, G. Salimi-Khorshidi, M. Webster, C. F. Beckmann, T. E. Nichols, J. D. Ramsey, and M. W. Woolrich (2011). "Network modelling methods for FMRI." In: *NeuroImage* 54.2, pages 875–91 (cited on pages 4, 12, 158).

Sotiropoulos, S. N. and A. Zalesky (2017). "Building connectomes using diffusion MRI: why, how and but". In: *NMR in Biomedicine* April, e3752 (cited on pages 16, 18).

Srinivasan, R., S. Thorpe, and P. L. Nunez (2013). "Top-Down Influences on Local Networks: Basic Theory with Experimental Implications". In: *Frontiers in Computational Neuroscience* 7.April, page 29 (cited on page 48).

Stejskal, E. O. and J. E. Tanner (1965). "Spin Diffusion Measurements: Spin Echoes in the Presence of a Time-Dependent Field Gradient". In: *The Journal of Chemical Physics* 42.1, pages 288–292. arXiv: 1011.1669v3 (cited on page 14).

Stephan, K. E., M. Tittgemeyer, T. R. Knösche, R. J. Moran, and K. J. Friston (2009). "Tractography-based priors for dynamic causal models". In: *NeuroImage* 47.4, pages 1628–1638 (cited on page 159).

Strogatz, S. H. (2000). "From Kuramoto to Crawford: exploring the onset of synchronization in populations of coupled oscillators". In: *Physica D: Nonlinear Phenomena* 143.1-4, pages 1–20 (cited on page 43).

Stroud, J., M. Barahona, and T. Pereira (2015). "Dynamics of Cluster Synchronisation in Modular Networks: Implications for Structural and Functional Networks". In: pages 107–130. arXiv: 1411.2805 (cited on page 158).

Touboul, J., G. Hermann, and O. Faugeras (2011). "Noise-induced behaviors in neural mean field dynamics". In: *SIAM Journal on Applied Dynamical Systems* 11.1, pages 49–81. arXiv: 1104.5425 (cited on pages 57, 58).

Tripathy, S. J., J. Savitskaya, S. D. Burton, N. N. Urban, and R. C. Gerkin (2014). "NeuroElectro: a window to the world's neuron electrophysiology data". In: *Frontiers in Neuroinformatics* 8.April, page 40 (cited on pages 47, 163).

Van Essen, D. C. and K. Ugurbil (2012a). "The future of the human connectome." In: *NeuroImage* 62.2, pages 1299–310 (cited on pages 17, 164, 166).

Van Essen, D., K. Ugurbil, E. Auerbach, D. Barch, T. Behrens, R. Bucholz, A. Chang, L. Chen, M. Corbetta, S. Curtiss, S. Della Penna, D. Feinberg, M. Glasser, N. Harel, A. Heath, L. Larson-Prior, D. Marcus, G. Michalareas, S. Moeller, R. Oostenveld, S. Petersen, F. Prior, B. Schlaggar, S. Smith, A. Snyder, J. Xu, and E. Yacoub (2012b). "The Human Connectome Project: A data acquisition perspective". In: *NeuroImage* 62.4, pages 2222–2231 (cited on page 16).

Van Veen, B., W. Van Drongelen, M. Yuchtman, and A. Suzuki (1997). "Localization of brain electrical activity via linearly constrained minimum variance spatial filtering". In: *IEEE Transactions on Biomedical Engineering* 44.9, pages 867–880. arXiv: 10.623056 [10.1109] (cited on page 25).

Vidaurre, D., A. J. Quinn, A. P. Baker, D. Dupret, A. Tejero-Cantero, and M. W. Woolrich (2016). "Spectrally resolved fast transient brain states in electrophysiological data". In: *NeuroImage* 126, pages 81–95. arXiv: arXiv:1011.1669v3 (cited on pages 37, 103).

Vogels, T. P., H. Sprekeler, F. Zenke, C. Clopath, and W. Gerstner (2011). "Inhibitory Plasticity Balances Excitation and Inhibition in Sensory Pathways and Memory Networks". In: *Science* 334.6062, pages 1569–1573 (cited on pages 5, 40).

Vogels, T. P., K. Rajan, and L. Abbott (2005). "Neural Network Dynamics". In: *Annual Review of Neuroscience* 28.1, pages 357–376 (cited on page 37).

Wang, H., M. Kim, K. P. Normoyle, and D. Llano (2016). "Thermal Regulation of the Brain—An Anatomical and Physiological Review for Clinical Neuroscientists". In: *Frontiers in Neuroscience* 9.January, pages 1–6 (cited on page 19).

Wang, X.-J. (2010). "Neurophysiological and Computational Principles of Cortical Rhythms in Cognition". In: *Physiological Reviews* 90.3, pages 1195–1268 (cited on page 4).

Wilson, H. R. and J. D. Cowan (1972). "Excitatory and Inhibitory Interactions in Localized Populations of Model Neurons". In: *Biophysical Journal* 12.1, pages 1–24 (cited on pages 46, 51).

Wipf, D. and S. Nagarajan (2009). "A unified Bayesian framework for MEG/EEG source imaging". In: *NeuroImage* 44.3, pages 947–966. arXiv: NIHMS150003 (cited on page 24).

Wollstadt, P., M. Martínez-Zarzuela, R. Vicente, F. J. Díaz-Pernas, and M. Wibral (2014). "Efficient Transfer Entropy Analysis of Non-Stationary Neural Time Series". In: *PLoS ONE* 9.7. Edited by D. Marinazzo, e102833. arXiv: arXiv:1401.4068v1 (cited on page 103).

Woolrich, M. W. and K. E. Stephan (2013). "Biophysical network models and the human connectome." In: *NeuroImage* 80, pages 330–8 (cited on pages 6, 10).

Yeung, M. K. S. and S. H. Strogatz (1999). "Time Delay in the Kuramoto Model of Coupled Oscillators". In: *Physical Review Letters* 82.3, pages 648–651. arXiv: 9807030v1 [arXiv:chao-dyn] (cited on page 44).